JRJC 2022 - Journées de Rencontres Jeunes Chercheurs. Book of Proceedings

Elsa Guy, Marie van Uffelen, Johan Loizeau, Jordan Koechler, Antoine Syx, Christopher Alléné, Guillaume Albouy, Benjamin Blancon, Jieun Choi, Christopher Greenberg, et al.

23-29 Octobre 2022

Saint Jean de Monts

Village Club « la Rivière »

JRJC

Journées de Rencontres Jeunes Chercheurs

Théorie

Instrumentation

Physique hadronique

Physique au-delà du modèle standard

Physique nucléaire et interdisciplinaire

Ondes Gravitationnelles

Physique des saveurs

Modèle standard

Astroparticules

Cosmologie

Neutrinos

Secrétariat :

Isabelle Cossin, LPNHE

Isabelle.cossin@lpnhe.in2p3.fr

Tel: +33 (0)1 44 27 68 95

Société Française de Physique

Book of Proceedings

Comité d'organisation :

Pauline Ascher	(LP2i Bordeaux)
François Brun	(CEA Saclay)
Emmanuel Chauveau	(LP2i Bordeaux)
Rachel Delorme	(LPSC)
Romain Gaior	(LPNHE)
Maxime Guilbaud	(SUBATECH)
Julien Masbou	(SUBATECH)
Laure Massacrier	(IJCLab)
Sabrina Sacerdoti	(APC)
Thomas Strebler (*)	(CPPM)
Antonio Uras (*)	(IP2I Lyon)
Dimitris Varouchas	(IJCLab)
Laura Zambelli	(LAPP)

(*) Editors of these proceedings

Secrétariat :

Isabelle Cossin	(LPNHE)

Contents

I Astrophysics and Astroparticle physics **5**

Elsa Guy: ***Study and development of new detectors for the search of light dark matter with EDELWEISS*** **7**

Marie van Uffelen: ***The calibration of a direct search dark matter detector: the TPC of DarkSide-20k*** **13**

Johan Loizeau: ***Spatial Stability of ^{83m}Kr calibration events in XENONnT experiment*** **17**

Jordan Koechler: ***X-rays constraints on sub-GeV dark matter*** **23**

Antoine Syx: ***Calibration of the Virgo Gravitational Waves detector using a Newtonian Calibrator for the upcoming O4 observing run*** **29**

Christopher Alléné: ***Study of the localization of sources identified by the MBTA pipeline for low latency CBC search and Early Warnings*** **33**

II Beyond Standard Model **39**

Guillaume Albouy: ***Search for Beyond the Standard Model physics with Emerging Jets and the ATLAS detector during Run-3*** **41**

Benjamin Blancon: ***Search for a Vector Like Quark T' decaying into a quark top and a Higgs boson in the dileptonic same sign final state with the CMS experiment at the LHC*** **47**

Jieun Choi: ***Jet Calibration and Search for Vector-Like Quarks decaying into top+Higgs in hadronic final states using Run2 CMS data with Neural Networks*** **53**

Christopher Greenberg: ***Searches for CP symmetry violation in the top quark sector with CMS at the LHC, and the tracker Endcap upgrade for the High Luminosity LHC*** **59**

Raphael Haeberle: ***Search for new heavy stable charged particles with the CMS experiment*** **65**

III Cosmology **71**

Leander Lacroix: ***Supernova cosmology with the Zwicky Transient Facility*** **73**

Gregoire Pierra: ***Gravitational Wave Cosmology: Constraints on the Hubble Constant using Dark-Sirens and Binary Black-hole Spins*** **79**

Ting Tan: ***Detection of Baryon Acoustic Oscillations using Lyman-α Forests in eBOSS/DESI*** **85**

IV Hadronic Physics **89**

Rayane Abou Yassine: ***e^+e^- emission in pp at 4.5 GeV with HADES*** **91**

Sarah Herrmann: ***Charged-particle pseudorapidity density in proton-proton collisions at $\sqrt{s}$ = 900 GeV with the ALICE MFT and ITS2*** **97**

Gregoire Pihan: ***Dynamics of the conserved charge fluctuations in an expanding medium*** **101**

Romain Schotter: ***Testing CPT symmetry via the mass difference between anti-hyperons and hyperons in pp collisions with ALICE*** **105**

Afnan Shatat: ***Rapidity-differential J/ψ photoproduction in Pb−Pb collisions with nuclear overlap measured in ALICE at the LHC*** **111**

V Instrumentation 117

Daniil Trofimov[1,2,3], *with Etienne Parizot[1], Pavel Klimov[2] on behalf of JEM-EUSO collaboration*: *Tests and calibration of multi-channel photodetectors for balloon and space-based EUSO missions* **119**

Alexis Doudard: In vitro *dosimetry for assessment of targeted alpha therapy* **125**

Levana Gesson: ***Nuclear data for particle therapy and spatial radioprotection*** **131**

Dingbang Cai: ***Studies of Frisch grid performance and calibration of light measurement in liquid xenon detector for small animal medical imaging*** **137**

Thomas Bouillaud: ***Systematic effects and magnetic field uniformity in the n2EDM experiment.*** **141**

Mojahed Abushawish: ***Machine learning and imaging approaches to improve the AGATA position resolution*** **145**

VI Nuclear Physics & Multidisciplinary Topics 151

Yohannes Molla *with Lydie Giot*: *The Impact of Nuclear Data on Decay Heat Uncertainty Quantification* **153**

Mohamad Chamseddine *with Jérôme Margueron, Guy Chanfray, Hubert Hansen, Rahul Somasundaram*: *Dense matter within Relativistic Hartree-Fock approaches* **159**

VII Standard Model 165

Felicia Volle: ***Angular analysis of the $\Lambda_b^0 \to \Lambda(1520)\mu^+\mu^-$ decays at LHCb*** **167**

Gaelle Khreich: ***Angular analysis of the $B_s^0 \to \phi e^+ e^-$ decay at LHCb*** **173**

Gaya Benane: ***Test of lepton flavor universality using $B^0 \to D^{*-}\tau^+\nu_\tau$ decay at LHCb*** **177**

VIII Theoretical Physics 181

Andreas Goudelis: ***Theoretical Physics Session Introduction*** **183**

Pierre-Yves Duerinck: ***Nucleon-antinucleon annihilation from optical and coupled-channel models*** **187**

José Pablo Linares Fernández: ***Nuclear physics at the edge of stability*** **193**

Part I

Astrophysics and Astroparticle physics

session chaired by Julien MASBOU

Study and development of new detectors for the search of light dark matter with EDELWEISS

Elsa Guy

Institut de Physique des deux Infinis, Lyon

Abstract — The EDELWEISS collaboration performs light Dark Matter (DM) particle searches with high-purity germanium bolometers collecting both charge and phonon signals. Our recent results (PhysRevD.106.062004) using NbSi *Transition Edge Sensor* (TES) equipped detectors operated underground at the *Laboratoire Souterrain de Modane* (LSM) has shown the high relevance of this technology for future dark matter searches. As most cryogenic dark matter experiments, this study was limited by unknown low-energy backgrounds. In this context, the EDELWEISS collaboration, as part of its SubGeV program, is working on a new design of germanium bolometers using NbSi TES : **CRYOSEL**. These innovative TES phonon sensors called *Superconducting Single Electron Device* (SSED) will be sensitive to the athermal phonons induced by the amplification of a single charge drifting in the strong electric field generated in the detector and hence, will be able to discriminate against our main low-energy background, which is not affected by this amplification.

Introduction

As of today, the problem of dark matter (DM) is one of the biggest mysteries of modern physics. Dark matter particles would constitute approximately a quarter of the total energy density of our universe, but they have never been detected. Theoretical models predict DM particle masses to range from 1 eV/c^2, all the way up to 1 TeV/c^2 [1, 2, 3]. While important progress has been made in the search of DM-nuclei interactions in the GeV/c^2 to TeV/c^2 region [4, 5, 6], the absence of signal has led more and more experiments to turn to lighter DM particles detection, down to and below 1 GeV/c^2 [7, 8, 9, 10, 11, 12, 13]. Searching for such light particles gives rise to new challenges in terms of low threshold and of new types of backgrounds [14, 15, 16, 17, 18, 19] in cryogenic detectors. That includes a population of events called heat-only (HO) events, not associated with the production of charges and of yet unknown origin. Recent results [20, 21] have motivated the EDELWEISS collaboration to develop a new generation of Ge detectors named CRYOSEL. Equipped with a Transition Edge Sensor (TES) evaporated on the surface of the crystal, they are no longer subjected to the instrumental background associated with the operation of the Ge-NTD (neutron transmutation doped) heat sensors conventionally used by the collaboration.

The problem of dark matter

Since the 1930s, observations supporting the existence of dark matter have multiplied. Whether it be at galactic scale, with Vera Rubin's work [22], at galaxy clusters scale with Fritz Zwicky's work [23], or at cosmological scale with Planck's observations [24], the conclusion is the same : the luminous mass does not account for all that is observed, there has to be something else and this something else most likely is made of non-baryonic dark matter.

In particle physics, we search for dark matter in the form of *particles*. Based on observations, DM particles must fulfill several constraints. Studies on structures formation in the Universe favor a *bottom-up* mechanism. That means that the big structures like clusters of galaxies originate from the smaller objects like gas or stars[1]. This mechanism is compatible with cold, non-relativistic and thus, massive DM particles. To reproduce the relic density $\Omega_{DM} \approx 0.259$ measured by Planck, the DM annihilation cross section must be of the order of magnitude of the weak interaction, that is $< \sigma_{annihilation} v > \sim 10^{-25}$ cm^3.s^{-1}. Furthermore, DM particles must be stable at the scale of the Universe since gravitational effects are visible. They must also be neutral in charge and color in order not to absorb nor emit any radiations that would have revealed their presence, i.e., they cannot interact through electromagnetic nor strong interactions.

[1] As opposed to *top-down* mechanism where bigger structures sunder to create small objects.

No known particle from the Standard Model (SM) of particle physics can fulfill all the above *and* match observations made at all scales. Hence, this gas is made of a majority of unknown particles from Beyond the Standard Model (BSM).

EDELWEISS and direct detection

Dark matter particles can be detected through three different processes : **production in collider** ($SM + SM \rightarrow DM + DM$) where physicists are looking for missing transverse energy following a collision of two SM particles, **indirect detection** ($DM + DM \rightarrow SM + SM$) where one tries to detect primary or secondary DM annihilation products, and finally **direct detection** ($DM + SM \rightarrow DM + SM$).

The EDELWEISS experiment belongs to the latter category. It is a direct detection experiment using germanium cryogenic bolometers. It searches for interactions of DM particles with the target resulting in either a nuclear or electronic recoil depending on the DM model considered. In both cases, such an interaction undergoes the heat-ionization double readout of EDELWEISS detectors. The *ionization signal* - proportional to the number of electron-hole pairs (e^+/h^-) produced by the collision - is collected by Aluminum electrodes evaporated or lithographed on the surface of the germanium crystal. The *heat signal*, due to the excitation of the crystal lattice via the propagation of phonons, is measured using Ge-NTD sensors. When applying a potential difference ΔV to the electrodes, another contribution to the total measured heat signal arises due to the *Neganov-Trofimov-Luke* (NTL) effect [25, 26]. Indeed, when N electron-hole pairs drift across the crystal on their way to the electrodes under the effect of a potential difference ΔV, they produce additional phonons with a total energy $E_{NTL} = Ne\Delta V$ (where e is the elementary charge) that adds to the recoil energy. Depending on the type of recoil i, the total gain accounting for the NTL effect is $\langle g \rangle_i = 1 + e\Delta V/\epsilon_i$, where $\epsilon_N = 12$ eV for nuclear recoils (NR) and $\epsilon_E = 3$ eV for electronic recoils (ER) are the average ionization energies per electron-hole pair in Ge [27]. While simulations predict two bands of events in the E_{ion} vs. E_{heat} plot, it is actually observed that a third population of events appears, centered at $E_{ion} = 0$ and largely dominant at low energy. These events were named "heat-only" (HO) events from their main characteristic, and are *the* main background in modern cryogenic dark matter experiments.

Heat-only background

Heat-only are a real issue for dark matter search and neutrino physics experiments, many cryogenic experiments also observe similar kind of population which deeply impacts their sensitivy The NbSi-equipped detector presented in [21] (called NbSi209 on Fig 1) demonstrated a reduced HO background relative to previous EDELWEISS detectors (such as RED20 [28] or RED30 [14] on Fig 1). This 200g Ge cylindrical crystal, as opposed to previous detectors equipped with Ge-NTD heat sensors, uses a lithographed Nb_xSi_{1-x} thin film TES [20] as a phonon sensor. The film is maintained at constant temperature $T_C \sim 30$ mK, by a small heater in order to remain in the transition regime, where an event is characterized by an increasing resistance as the temperature rises.

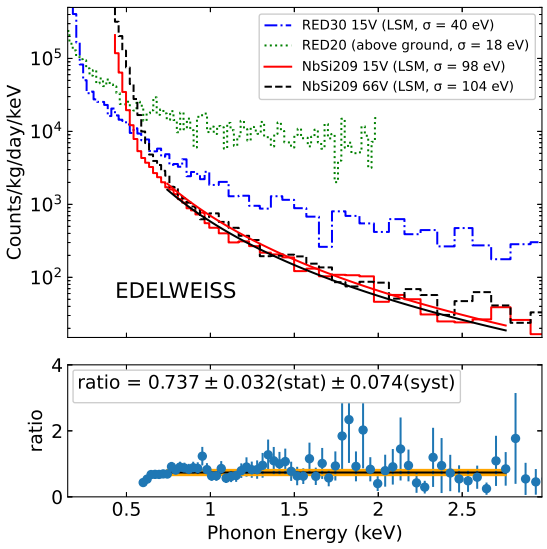

Figure 1: *Top:* The heat energy spectra of events recorded with a 33g Ge detector operated above ground at 0 V (RED20) is plotted in green [28] and events with no ionization ($E_{ion} < 0$) for a 33g Ge detector operated at LSM at 15 V (RED30) are in blue [14]. NbSi209 spectra operated at 15 V (resp. 66 V) and its fitted power law are plotted in red (resp. black). *Bottom:* Ratio of NbSi209 distributions recorded at 15 and 66 V (blue), associated fit of a constant (black line) and its uncertainty band (orange). Fig from [21].

Fig 1 (top) compares the heat energy spectra recorded at 15 V (red) and 66 V (black), requiring $E_{ion} < 0$ keV to better isolate the HO population. In the energy range shown in Fig 1, the ionization resolution does not allow to separate HO from ER events, but the similarity of the two spectra suggests that most of these are not events associated with the creation of charges. Indeed, HO events, by definition, do not produce charges, therefore, they should not be affected by the NTL boost. Comparing energy spectra at various biases is thus very useful to study this type of background. A more quantitative comparison is provided by fitting the distributions with a power law (αE^β). The fitted slopes are identical within uncertainties ($\beta = 3.40 \pm 0.07$), which is further confirmed in the bottom panel of Fig 1 showing a flat ratio of the two distributions as a function of the energy. Assuming that both the HO and the possible electronic backgrounds follow the same power law, a limit on the fraction x of events associated with charges can be set. The resulting upper limit on this fraction is $x < 0.0004$ at 90% C.L. which strongly suggests that, in the en-

ergy range between 0.8 to 2.8 keV, most events are HO events [21].

CRYOSEL detectors

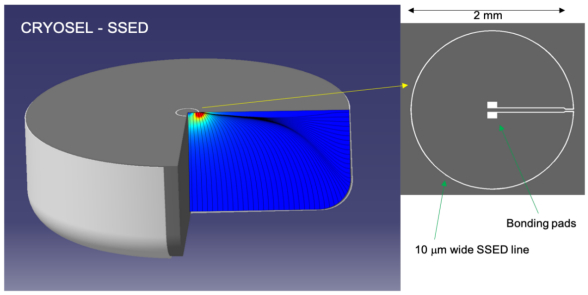

Figure 2: Diagram of the CRYOSEL detector, a 40 g Ge cryogenic bolometer with an encompassing bottom Al electrode and the SSED detector layout including the simulated electric field-lines. The red region under the SSED line corresponds to a high intensity electric field.

Figure 2 shows the innovative design of the CRYOSEL detectors which goal is to reject HO events by tagging the presence of charges down to one electron-hole pair.

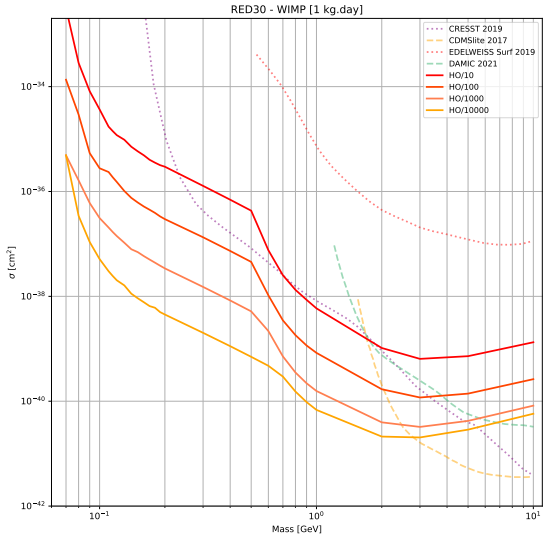

Figure 3: The thick lines (from red to yellow) represent the projected sensitivity for CRYOSEL detectors for WIMP-nucleon SI interactions (90%CL) with 1 kg.d exposure ($\sim$ 1 month with a 40 g detector), for different values of rejection factors (10 to 10^4).

This 40 g Ge detector is equipped with a new type of NbSi phonon sensor, called Super Conducting Single Electron Device (SSED). It is a 10 μm-thin NbSi line evaporated on the surface of the crystal. Operated at high biases ($\sim$ 200 V), it will be sensitive to the athermal phonons induced by the NTL amplification of a single charge drifting in the strong electric field generated in the Ge at the proximity of the line and hence, to discriminate against the HO events which are not affected by this amplification. The Ge detector will also be equipped with a Ge-NTD sensor having a 20 eV phonon resolution (0.3 eV_{ee} considering the NTL amplification).

Simulation of the expected sensitivity from a short exposure (1 month) at LSM of a single CRYOSEL detector for WIMP-nucleon interactions is represented by the thick lines in Fig 3. This detector design will allow to explore areas of the parameters space that have yet to be excluded and to extend the search for DP at masses below those currently accessible by Si detectors, making CRYOSEL a very competitive DM search experiment. The different colors account for different HO suppression factors, from the actual HO rate reduced by a factor 10 in red to a factor 10^4 in light orange. This provides a good overview of the various possible scenarii and how they can limit the sensitivity of the experiment.

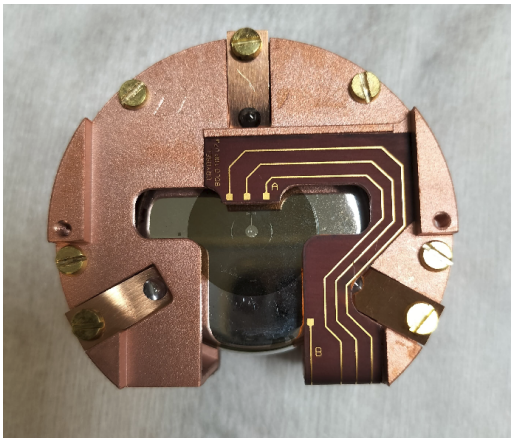

Figure 4: Picture of the fifth prototype of detector with CRYOSEL design called CRYO50. The picture is taken from above, so the top face of the crystal is visible inside its copper casing. The small light grey dot in the middle is the top Al electrode. It is surrounded by a 10 μ-thick SSED NbSi line. The encompassing bottom electrode is the large light grey outer annular region on the crystal. CRYO50 is also equipped with a Ge-NTD, glued on its bottom face.

The Fig 4 shows the latest prototype of CRYOSEL detectors : CRYO50. As opposed to the first design shown in Fig 2, this prototype has two rounded edges to better constrain the field lines towards the SSED and avoid charge trapping at the surface of the crystal. Using this detector, we have observed a transition of the SSED for the first time when coupled to a massive detector. The shape of several signals obtained with the photopeak at 59 keV of an ^{241}Am calibration source can be seen in Fig 5 for the heat channel (top), the ionization channel (middle) and the SSED (bottom).

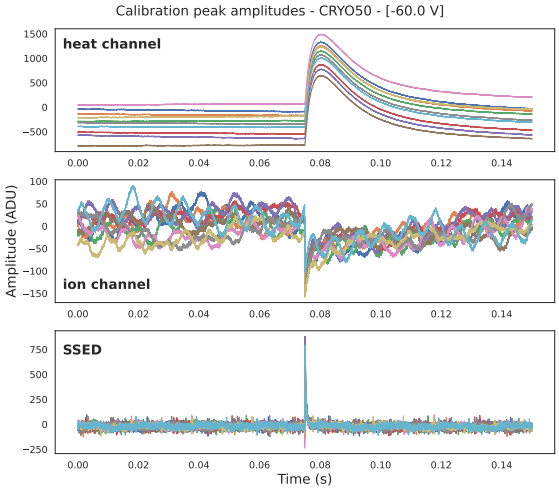

Figure 5: Example of 10 events selected among 59 keV calibration events on the heat channel (*top*), ionization channel (*middle*) and SSED TES (*bottom*).

Although the signals behaviour is well known for NTD heat sensors, SSED events are yet to be characterized. Data were taken with CRYO50 detector between September and October 2022 at IJCLab, Orsay. A LED was used to neutralize free charges in the crystal.

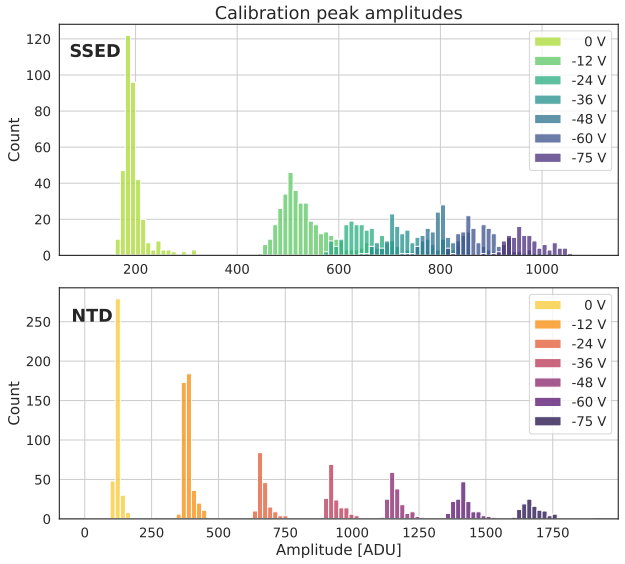

Figure 6: Histogram of 59 keV calibration events amplitudes for the SSED (*top*) and NTD (*bottom*), channels for biases from 0V to -75V.

The analysis of this first run is still ongoing. It has already shown interesting differences in SSED signals depending on the nature of the events. Indeed, a study on the detector response to both the 59 keV and LED events on both NTD and SSED channels was conducted at various biases, from 0V to -75V. Fig 6 shows that the amplitude of NTD events increase linearly as a function of the bias. As expected for the SSED sensor designed to operate in a saturation mode, the increase of sensitivity with bias is less pronounced. Looking at Fig 7 further confirms this observation. The resistance of the SSED and NTD sensors are plotted as a function of the bias applied. This SSED sensor reaches a saturation regime very quickly whereas the NTD resistance behaves following the NTL boost. This can be explained by the fact that the energy of the LED photons is just above the gap of the Ge $\sim$ 0.7 eV. Each 0.7 eV-LED photon creates one e^-/h^+ pair that propagates in various directions before interacting at random positions in the crystal. The LED events excite the SSED more homogeneously and trigger a bigger portion of the SSED line, which ends up saturating it. On the contrary, the photons of ^{241}Am source, placed on the lateral side of CRYO50, need at least an average of 3 eV to create a pair, they do not penetrate much the bulk of the crystal making the calibration events much more localized and causing them to only trigger a small portion of the SSED line.

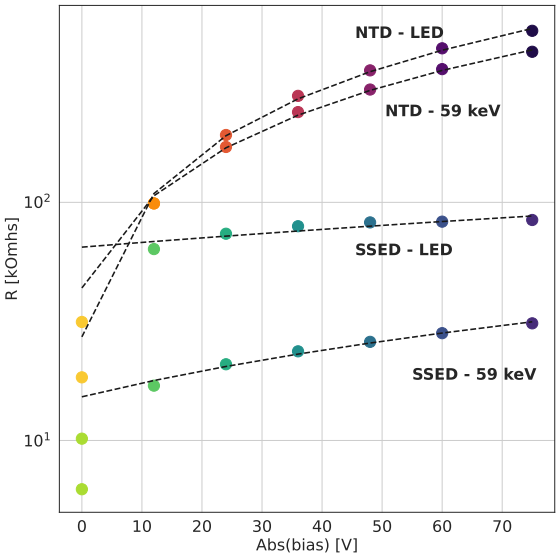

Figure 7: Resistance of the NTD and SSED sensors for 59 keV calibration events and LED events as a function on bias.

Conclusion

EDELWEISS is currently developing new detectors for the search of light dark matter with innovative SSED sensors. Preliminary studies have already allowed us to learn more about the SSED response to different kinds of events compared to the other usual readout technologies. The full characterization of the SSED is crucial to better constrain the HO population in the future in order to greatly enhance our performance. Another data taking is currently in progress at IP2I, Lyon, it will allow us to test the detector in a different environment, with different shielding and a different data taking pipeline. Furthermore, R&D is still ongoing and the CRYOSEL design will continue to improve in the future.

References

[1] Goodman, Mark W. and Witten, Edward Phys. Rev. D. **31**, 3059 (1985)

[2] A. Drukier, L. Stodolsky, Phys. Rev. D. **30**, 2295 (1984)

[3] A. Drukier, K. Freese, D. N. Spergel Phys. Rev. D. **33**, 3495-3508 (1986)

[4] E. Aprile *et al.* (XENON Collaboration), Phys. Rev. Lett. **121**, 111302 (2018)

[5] D. S. Akerib *et al.* (LUX Collaboration), Phys. Rev. Lett. **118**, 021303 (2017)

[6] A. Tan *et al.* (PandaX-II Collaboration), Phys. Rev. Lett. **117**, 121303 (2016)

[7] R. Essig, J. Kaplan, P. Schuster and N. Toro, (2010).

[8] C. Cheung, J. T. Ruderman, L.-T. Wang and I. Yavin, Phys. Rev. D **80**, 035008 (2009)

[9] D. Hooper and W. Xue, Phys. Rev. Lett. **110**, 041302 (2013)

[10] A. Falkowski, J.T. Ruderman and T. Volansky, JHEP **1105**, 106 (2011)

[11] K. Petraki and R.R. Volkas, Int. J. Mod. Phys. A **28**, 1330028 (2013)

[12] K. M. Zurek, Phys. Rep. **537**, 91 (2014)

[13] G. Bertone and T. M. P. Tait, Nature **562**, 51-56 (2018)

[14] Q. Arnaud *et al.* (EDELWEISS Collaboration), Phys. Rev. Lett. **135**, 141301 (2020)

[15] G. Angloher *et al.* (CRESST Collaboration), Eur. Phys. J. C. **76**, 25 (2016)

[16] R. Agnese *et al.* (SuperCDMS Collaboration), Phys. Rev. D **97**, 022002 (2018)

[17] A. Aguilar-Arevalo *et al.* (DAMIC Collaboration), Phys. Rev. Lett. **118**, 141803 (2017)

[18] O. Abramoff *et al.* (SENSEI Collaboration), Phys. Rev. Lett. **122**, 161801 (2019)

[19] Z.Z. Liu *et al.* (CDEX Collaboration), Phys. Rev. Lett. **123**, 161301 (2019)

[20] S. Marnieros *et al.* (EDELWEISS Collaboration), Submitted to JLTP, Special Issue for the 19th International Workshop on Low Temperature Detectors.

[21] Armengaud, E *et al*, Phys. Rev. D **106**, 062004 (2022)

[22] Rubin, Vera C. and Ford, Jr., W. Kent Astrophys. J. **159**, 379–403 (1970)

[23] Zwicky, F. Astrophys. J. **86**, 217–246 (1937)

[24] Ade, P. A. R. *et al.* Astronomy & Astrophysics **594**, (2016)

[25] B. Neganov and V. Trofimov, Otkryt. Izobret. **146**, 215 (1985), USSR Patent No. 1037771.

[26] P. N. Luke, J. Appl. Phys. **64**, 6858 (1988).

[27] G. F. Knoll, Radiation Detection and Measurement, 4th ed. (John Wiley and Sons, New York, 2010).

[28] E. Armengaud *et al.* (EDELWEISS Collaboration), Phys. Rev. D **99**, 082003 (2019). and Semiconductors

The calibration of a direct search dark matter detector: the TPC of DarkSide-20k

Marie van Uffelen

CPPM, Aix Marseille University, CNRS/IN2P3

Abstract — DarkSide-20k will be the next liquid argon TPC built to perform direct search for dark matter under the form of WIMPs. Its calibration to both signal and backgrounds is key as we expect very few events in WIMPs search. In the following proceeding, I present my work around the calibration of the TPC of DarkSide-20k: the simulations of the calibration programs themselves and the simulations of the impact of the calibration system on the rest of the detector (reduction of the light collection efficiency in the veto buffer, induced background by the tubes in the TPC and veto). To finish, the design of the calibration system also has to be mechanically tested and validated at cold, thus I describe my work on the hardware tests of the calibration set-up.

Introduction

Almost a century ago, astrophysics observations lead to the suspicion of dark matter (DM) existence in gravitationally bound astrophysical objects such as our galaxy, the Milky Way. Since then, it became a pillar in modern cosmology. Yet, although many efforts were made to detect it, no DM signal has been firmly established in direct or indirect detection experiments.
There exists many candidates for DM, the most favored being the Weakly Interacting Massive Particle (WIMP). The WIMP is expected to be rather heavy, with a favored mass range from 1 GeV to several TeV. The DarkSide collaboration builds direct detectors of WIMPs, using the TPC technology, operated at cryogenic temperature with liquid argon. Their next detector is DarkSide-20k (20t of liquid argon in the fiducial volume), it should start taking data in 2027 for a decade [1].
Once the detector is built, it is absolutely needed to understand perfectly its response to both signal and backgrounds. Indeed, DM search is in the realm of physics of rare events, thus the separation between background and signal is key. To this respect, the use of Argon double phase TPC is a real asset. Indeed, after an interaction between a particle and the atom of a double phase TPC, the signal collected comes from two physical processes: first, there is scintillation (photons, signal called S1), which travels quasi instantaneously towards the TPC to reach the arrays of photo-detectors located at the top and bottom of the TPC. Second, a ionisation signal (electrons), which drifts towards a gaseous pocket of argon thanks to an electric field. This signal is thus delayed, the travelling time of these ionisation electrons being 4 ms maximum. Once in the gaseous pocket, these electrons are transformed into photons through electroluminescence (signal called S2) under a strong electric field. Then photons are collected by the same photo-detectors as S1. Signal and backgrounds are expected to behave very differently in a TPC. The main (in number of interactions) source of background should come from light particles (photons, electrons, neutrinos), therefore should interact with the cloud electrons of argon atoms (it is called an Electronic Recoil (ER)). This background mainly comes from residual radioactivity of all materials composing the detector. On the contrary, heavy particles mostly interact with the nucleus of Argon (called a Nuclear Recoil (NR)). In this experiment, heavy particles are neutrons (background) and WIMP (signal). The population of S1 and S2 are very different for ER and NR, thus the S1/S2 ratio provides good discrimination between the main sources of background (light particles) and signal. In addition, Argon provides very different scintillation signal shapes for ER and NR, allowing a Pulse Shape Discrimination (PSD) between ER and NR, and reducing the ER contribution by a factor $\approx 10^8$ [2] -however, there is remaining background coming from neutrons, which can dangerously mimic the WIMP signal. The pulse shapes for both types of interaction, the energy and position resolution in the detector and its time stability have to be tested. This is the role of the several calibration programs that will be performed along the 10 years of data taking.
The CPPM laboratory is working on the calibration procedure of the detector, from the construction of the system, to the simulation of the calibration and the signal reconstruction.
In the following, I present my simulation work around the calibration of DarkSide-20k's TPC and the calibration strategy, then I present the feasibility tests done at CPPM with a calibration mock-up.

The calibration of DarkSide-20k's TPC: simulations

DarkSide-20k is a layer detector working at cryogenic temperatures. A cut view of its CAD is shown on figure 1. The outer layer is a cubic cryostat (8.5x8.5x8.5 m^3) filled with liquid Argon ($T_{boil} = -186$ °C). Inside it, there is the inner detector (4.65 m high oval volume), composed of two sub-detectors: a veto buffer (in order to tag residual background before it enters the active search volume) and a TPC (3.5 m high hexagon) inserted inside the latter. The inner detector will be filled with 100t of purified LAr.

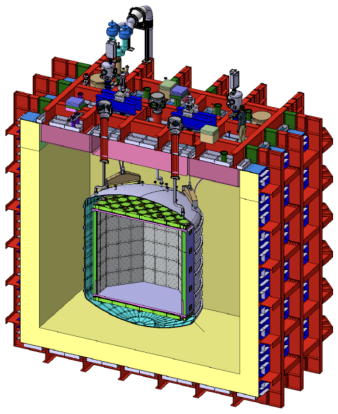

Figure 1: Cut view of the DarkSide-20k experiment, from the cryostat (outer part) to the TPC (inner part). The cryostat is a cube of 8.5 m side, the TPC is a 3.5 m high hexagon.[1]

The actual search for WIMPs will take place in the center volume of the TPC (which we call the fiducial volume). In order to perform the calibration of this TPC, the collaboration has two strategies. On the one hand, it plans to use diffuse radioactive sources with short lifetime and decays chains in order to have a volume and uniform calibration. On the other hand, the collaboration will use external radioactive sources of photons and neutrons, all with well-known initial energy spectra. Both strategies are complementary because the former cannot provide NR calibration while the latter cannot allow calibration in the inner volume of the TPC.
The main challenge for the second calibration is to be able to bring the sources very close to the TPC, i.e. near the very center of the cryostat, inside the veto buffer and at liquid argon temperature. To do so, the CPPM lab builds a guide-tube system [1]. It is composed of two (almost-)U-shape tubes, going around the TPC (thus dived inside the veto buffer) and exiting the detector on top of the cryostat. At each tubes' exists, there is a motor system driving a rope holding the radioactive source and bringing it near the TPC. These tubes will have a diameter of 3 cm and be 3 cm - close to the side of the TPC and 1 cm under the signal - readout system (which is itself at the bottom of the TPC). A cut view of the inner detector with one calibration pipe around the TPC is shown on Figure 2.

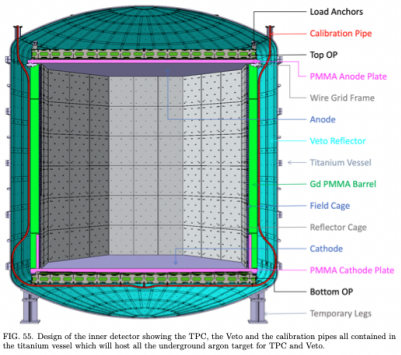

Figure 2: Cut view of the DarkSide-20k inner detector. The outer detector is the veto buffer, aiming at tagging background before it enters the TPC and interacts inside it. The inner part is the TPC, the detetor where the WIMP search will be performed. The calibration pipe (shown in red here) are located outside the TPC and inside the veto. This pipe, exits the veto at its top cap and exits the detector by the top of the cryostat.[1]

Another challenge comes with the calibration procedure: the thickness and materials of the TPC walls. Indeed, in order to remove as much as possible the background coming from residual radioactivity of the detector, the DarkSide collaboration uses thick Gadolinium-loaded acrylic (PMMA) walls. When a neutron crosses the walls, it might interact with an Hydrogen or Gadolinium atom which composes the wall resulting in the moderation (Hydrogen) of the neutron and capture (Gadolinium) producing photons accompanying incoming neutrons. Plus, as these walls are thick, incoming photons deposit their energy inside them before entering the TPC, and might even be absorbed before entering. These walls are huge assets for reducing background (the main enemy in DM search), but they impose constraints on the calibration for the same reasons. This is why the calibration of DarkSide-20k's TPC should be carefully studied before the deployment of the system.
In order to elaborate the calibration strategy, I performed simulations of the TPC response for all the considered radioactive sources. There are sources of neutrons: AmBe, AmC, DD-gun (a Deuteron-Deuteron system providing monochromatic neutrons of 2.45 MeV), and photons: ^{57}Co, ^{133}Ba, ^{22}Na, ^{137}Cs and ^{60}Co. The calibration using photons is used to understand the ER background coming from light particles. Calibration with neutrons sources aims at producing NR, thus understanding both the background coming from neutrons and the WIMP signal. To perform ER and NR calibration prevision, simulations were made with a GEANT4-based software (called g4ds), in which the previously described geometry of the detector and of the calibration system is

implemented. I obtained energy spectra resulting from the interaction of emitted particles and argon of the TPC. An example of spectra following the exposure of one photon source and one neutron source on the side of the TPC is shown in Figure 3. In both plots, the blue line represents all events seen in the TPC, while the red one is after the pure NR (for neutron sources) or pure ER (for photon sources) single scatter selection. Indeed, in addition to NR (or ER) selection, one needs to select single scatters -meaning that there is only one interaction inside the TPC- to mimic the WIMP signature.
These red spectra are the first step to deduce the time needed to perform the calibration at this position. To follow up, one needs to set the right value of source' activity to which the detector is exposed. Indeed, as introduced before, the S2 signal comes from ionization electrons drifting towards the photodetectors thanks to a drift electric field. Therefore, S1 and S2 coming from the same interaction are separated in time. Thus, to avoid pile-ups, the rates of photodetections should be less than $1/4\ ms = 250$ Hz. Yet, in these 250 Hz, 150 Hz are allocated to noise, thus the rate of interactions inside the TPC should be of 100 Hz maximum. Thanks to the blue spectra (representing all events one can see in the TPC) following the exposure of each source, the activity of the source is estimated by computing $A = 100\ Hz \cdot \frac{N_{events,TPC}}{N_{events,simulated}}$.
To finish, the time needed to perform the calibration is computed thanks to the rate of interesting events inside the TPC, the activity of the source and the statistics required to have a reliable study.

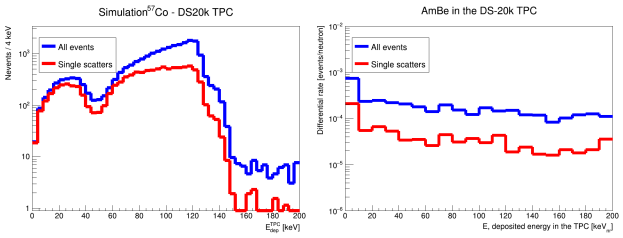

Figure 3: Two examples of energy spectra obtained after the exposure of photon source (here ^{57}Co, left) and neutron source (here AmBe, right) on the side of the TPC.

As the tubes are dived inside the veto buffer and positioned very close to the TPC, they might degrade the performance of the inner detector, either by inducing background in both sub-detectors or by decreasing the light collection efficiency of the veto buffer. Thus, two last sets of simulations were performed in order to study the influence of the tubes on the rest of the detector.
Even if the collaboration performs assays to control the radioactivity of each detector's components material, there is remaining radioactivity in each parts of the detector. The tubes will be in Titanium, which is contaminated by five isotopes: ^{238}U, ^{235}U, ^{232}Th, ^{40}K and ^{46}Sc. All these radio-contaminants produce photons, the three first also produce neutrons. The simulations consisted in the uniform emission of photons and neutrons from the tubes (1e7 simulated decays for each source), with the right energy and the right activity. In the analysis, pure ER (resp. pure NR) single scatters in the fiducial volume, in the energy region of interest and without veto tagging were selected for the ER (resp. NR) background rate estimation.
To finish on the simulation aspects, it was necessary to check the damages caused by the tubes on the veto's Light Collection Efficiency (LCE). Indeed, the veto collects photons from scintillation thanks to photodetectors placed on its walls. The presence of the tubes can lower the LCE by absorbing or badly reflecting photons on their surface. Tubes can also induce an asymmetry of LCE in regions around them. This last work was the simulation of 1e6 photons uniformly distributed inside the veto compared with the number of photons collected by the photodetectors. Without the tubes (thus only with the geometry of the veto), the LCE is of 4 %. In order to decrease as much as possible the effects of the tubes on the veto, different optical boundaries were tested, the best one is reflector (ESR foils) wrapped tubes.

Simulations results

The simulations were performed on the side of the TPC and under the TPC (the materials to cross are different in both positions) for each radioactive sources. T_{calib}, the time needed to perform the calibration was estimated for each position and each source. Then, the time needed to perform the whole calibration run was established considering the operators will take data at six positions on the side of the TPC (three points per side) and three additional under the TPC. The time needed to perform calibration source by source is summarized in table 1. The full time needed to perform the ER calibration is about one week, and one month for the NR calibration. These calibration runs will have to be repeated several times in order to check the time stability of the detector over the 10 years of data taking.

The simulations of the background induced inside the inner detector (TPC and veto) lead to the conclusion that the tubes induce less than 0.01 % of the NR background budget of DarkSide-20k (0.1 events/10 years of data taking). The ER background induced by our system is also fully negligible, and will be ruled out by the PSD and the S1/S2 ratio anyway. The rates of events seen by the photodetectors due to photons and neutrons emitted by the tubes represent 0.04 % (resp. 0.15 %) of the TPC (resp. veto) rate -thus they are very small. To finish on the simulation part, the light collection efficiency simulations shew a very small asymmetry in the veto induced by the pipes (less than 0.5 %) and a relative loss of efficiency of 1% in average

Source	^{57}Co	^{133}Ba	^{22}Na	^{137}Cs	^{60}Co
E (keV)	122	356	511	662	1173
A (kBq)					
Side	18	1.9	0.36	2.2	0.36
Bottom	100	5.0	0.67	4.6	0.6
T_{calib} (d)	0.16	0.78	0.98	1.5	3.1
Source	AmBe	AmC	DD gun		
E (MeV)	[0.2, 12]	[2, 7]	2.45		
A (kBq)					
Side	0.14	0.15	0.19		
Bottom	0.18	0.18	0.23		
T_{calib} (d)	8	8	10		

Table 1: Activity needed and time estimation for the calibration using 10,000 single scatters (NR) and 1,000 single scatters in the photoelectric peak (ER) for the previously presented sources. In such conditions, the overall time needed to perform the NR calibration run is roughly one month, roughly one week for ER calibration.

(this number goes up to 2 % in pipes' regions) if the tubes are wrapped with a reflector foil.

Feasibility tests with a mock-up

In addition to the simulations work made to check the feasibility of the calibration in terms of physics, it is necessary to check the mechanical feasibility of the calibration. Indeed, the tubes will be surrounded by cryogenic liquid at their bottoms and go on top of the cryostat were it is room temperature and where people will handle the radioactive sources. It is possible that moist air enters the tubes and that ice forms on the source path preventing it to circulate. The worst risk would be to stuck the source inside the pipes without being able to remove it. This is why the CPPM created a mock-up of the guide tube system: the goal is to obtain the best conditions for the safe circulation of sources.
This mock-up is composed of a small stainless steel tank in which a Titanium tube (3 cm diameter) is inserted. On the two tubes' exits there is a motor system driving a rope on which a fake source is attached. Thus this fake source can circulate inside the tube so that the precision on the position can be checked. When performing cold tests, the tank is filled with liquid Nitrogen (LN_2, $T_{boil} = -196$ °C) as it is cheaper and more available than liquid argon. During the tests, an operator controls the motors so that they drive the source inside the pipes, at cold. Different conditions were tested, with (resp. without) gas flushing (gaseous N_2) in order to (resp. not to) remove moist inside the pipes and prevent (resp. allow) ice formation.
After several tests with the mock-up of the guide tube system at cold, the first results tend to show that the guide tubes system will permit the calibration without large issues. The source can circulate inside the pipes at cryogenic temperatures if we permanently remove moist in the tubes thanks to gas flushing. The precision on the position of the source is really acceptable ($\approx$ 1cm), even at LN_2 temperature.

References

[1] The Global Argon Dark Matter Collaboration, DarkSide-20k Technical Design Report, Dec 2021. https://darkside-docdb.fnal.gov/cgi-bin/private/ShowDocument?docid=4637

[2] DEAP-3600 Collaboration, "First results from the DEAP-3600 dark matter search with argon at SNOLAB", Phys. Rev. Lett., no 7 (2018). https://doi.org/10.1103/PhysRevLett.121.071801

[3] Aalseth, et al. "DarkSide-20k: A 20 Tonne Two-Phase LAr TPC for Direct Dark Matter Detection at LNGS". The European Physical Journal Plus 133, no. 3 (March 2018): 131. https://doi.org/10.1140/epjp/i2018-11973-4.

Spatial Stability of ^{83m}Kr calibration events in XENONnT experiment

Johan Loizeau

Subatech

Abstract — XENONnT is an experiment for dark matter direct detection using a time projection chamber filled with liquid and gaseous xenon. Its main goal is to detect the collision between WIMPs and xenon nuclei. WIMPs are theoretical particles candidate for dark matter. Due to their low interaction with matter, a low background noise is mandatory in order to observe their collisions with liquid xenon. As the large size of the instrument and the long data taking are some difficulties of the experiment, monitoring is crucial for its proper operating. Moreover, the response of the detector must be perfectly known in order to be able to better reconstruct different events. For this, various calibration sources are used. Among them, the ^{83m}Kr is an internal calibration source emitting gamma at an energy close to the one expected for the WIMP-xenon collision. This work therefore focus on the use of signals from ^{83m}Kr calibrations period to monitor the spatial stability of the detector response.

Introduction

The dark matter discovery is one of the biggest challenge for modern science as astrophysical observation indicate that it composes a significant fraction of the universe [1]. There are numerous theories about dark matter composition. Among them, WIMPs (weakly interacting massive particles) are one of the most promising candidates for a particle explanation of dark matter [2]. It exists a variety of techniques to try to detect these particles expected to interact very rarely.

Dual-phase time projection chambers (TPC) using liquid and gaseous xenon are among the best detector to perform WIMP direct detection [3]. Indeed with its absence of long-lived isotopes and its high stopping power for gamma and beta radiation, liquid xenon provide an excellent self-shielding with low internal radiation making it an ideal WIMP target. Moreover, its large atomic mass (A $\approx$ 131) enhances the expected rate of coherent elastic scattering between WIMPs and xenon nuclei. The WIMP-xenon collision is expected to have an energy around 1 to 100 keV.

In 2004, the XENON collaboration started at the Laboratori Nazionali del Gran Sasso (LNGS) in Italy. Now including 27 laboratories around the world, its goal is to prove the existence of WIMPs via the direct detection of its interaction with liquid xenon target. Three detectors of increasing size, based on the time projection chamber technology, had been operating: XENON10, XENON100 and XENON1T. With more than 1 tonne of liquid xenon as a target, the XENON1T experiment was the biggest dark matter direct detector worldwide which operated until the end of 2019. Now, a detector named XENONnT is currently under data taking at LNGS with a 3 times bigger target mass and a 5 times lower background noise than its predecessor [4].

Moreover, thanks to the experiment low background noise, it's possible to look into more physics. We have for example neutrinoless double beta decay search using ^{136}Xe naturally present in liquid xenon [5] or supernova neutrinos observation.

To control the detector, various calibration source are used. Moreover, due to the size of the detector, spatial stability studies can be perform in order to check the accurate reconstruction of events in the whole TPC and to spot variations. Thus, this work present the spatial stability study of the XENONnT experiments using events from ^{83m}Kr calibration periods.

Xenon dual-phase time projection chamber

When a particle interacts within the xenon target, it will generate either a nuclear recoil (NR) if the particle is a WIMP or a neutron or an electronic recoil (ER) if the particle is a photon, a charged particle or a electronic neutrino [6]. In both scenarios, the recoil will excite and ionize nearby xenon atoms as we can see in fig.1. This will create two signal, one scintillation signal called S1 from the decay of excited xenon and one from free emitted electrons that will generate S2 signal.

In order to detect light and electron emitted during the collision between an incident particle and xenon, the XENON collaboration uses a dual phase time projection chamber (TPC) with liquid and gaseous xenon (rendered in fig.2). This TPC is cylindrical in shape and have two PMT array at the top and bottom of the TPC. In this TPC, the liquid xenon, which corresponds to most of the volume of xenon, is the target to incident particle. Their collision produce the first signal of light S1 with a wavelength of 175 nm that will be immediately detect by PMT arrays. Free electron, for

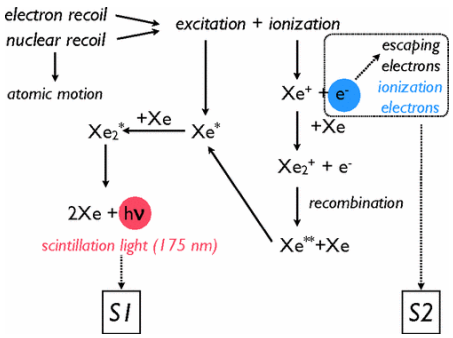

Figure 1: Illustration of the scintillation(S1) and ionization(S2) signals production inside liquid xenon [8].

their part, are drifted to the liquid-gas interface thanks to an electric field. Then they are extracted to the gas phase thanks to a second electric field. Finally, those electrons interact with gaseous xenon producing a second light signal S2 of same wavelength of 175 nm that can therefore be detected by PMT arrays. Due to the gain in the gas phase, S2 signal are way bigger than S1 signal at the same energy. Thus it is possible to distinguish S1 and S2 signals and to spot event pairing them. Moreover, the TPC allows to determine the position of the interaction. Indeed, the x,y coordinates are given by the detection pattern on PMT arrays while the time difference between S1 and S2, corresponding to the drift-time of electron, give us the depth of the interaction and thus the z coordinate.

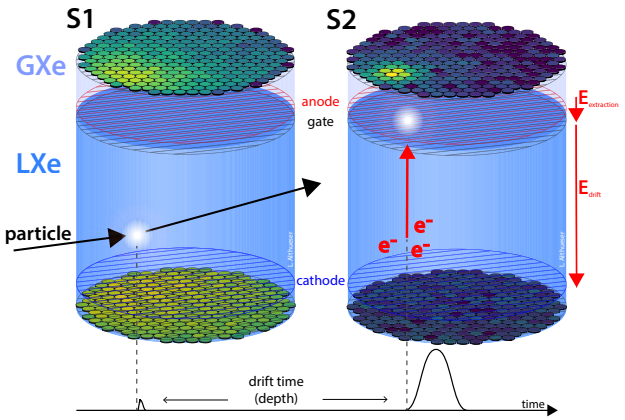

Figure 2: XENON experiment's dual phase detector working principle. (Left) An incident particle collide with LXe atom emitting the first luminous signal S1. (Right) Free electrons are drifted and extracted to GXe phase by electric fields in order to create the second luminous signal S2. Image Credit: Lutz Althüser.

Moreover, as free electrons drift in liquid xenon, the will recombine themselves with ionized xenon producing excited xenon which will contribute to S1 signal. Thus, whatever the incident particle, its collision with xenon nuclei will generate 2 anti-correlated signals. Nevertheless, the detector response will be different to ER and NR [7] as you can see in fig.3. So, the study

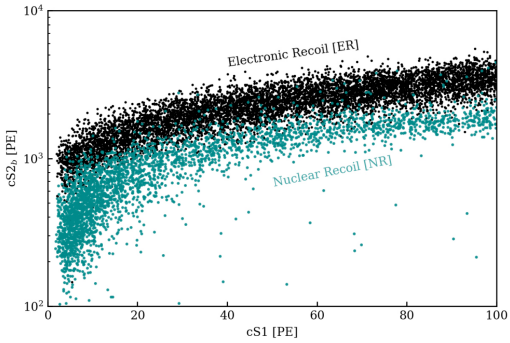

Figure 3: Comparison of the detector response to electronic recoils (black dots) and nuclear recoils (blue dots) in XENONnT. cS1 and cS2 correspond to the reconstructed signal of S1 and S2 respectively

and the good understanding of both ER and NR event allow to distinguish them reducing background noise for WIMP research to only NR background noise.

Using this technology, the XENON collaboration built 4 experiments: XENON10, XENON100, XENON1T and XENONnT.

XENONnT experiment

The XENONnT experiment is composed of various subsystems. Some of them are reused from the XENON1T experiment and some are news.

TPC As previously seen, the TPC is the core of the experiment. The xenon is enclose by 24 polytetrafluoroethylene (PTFE) reflector panels [9]. This active volume is observed at the top and bottom of the TPC by 2 arrays of respectively 253 and 241 PMTs chosen for their low radioactivity [10] and their efficacy at 175 nm [11]. This TPC measures ∼1.5 m in height and ∼1.3 m in diameter. It allows to have an active region of 5.9t liquid xenon as a target. Electrodes consist of parallel wires placed around PTFE panel. The gate (fig. 4) and anode have respectively two and four additional wires perpendicular to other added to counteract deformation of the electrode plane under electrostatic forces.

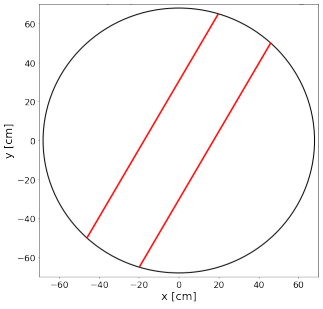

Figure 4: Position of the two perpendicular wire(in red) on the gate

Cryostat The cryostat contains the TPC and is made of two stainless steel vessels. Stainless steel is chosen in order to minimize material radioactivity while having two vessel allow to have some liquid xenon between serving as an additional shielding. A rendering of the cryostat and the TPC is shown on fig.5.

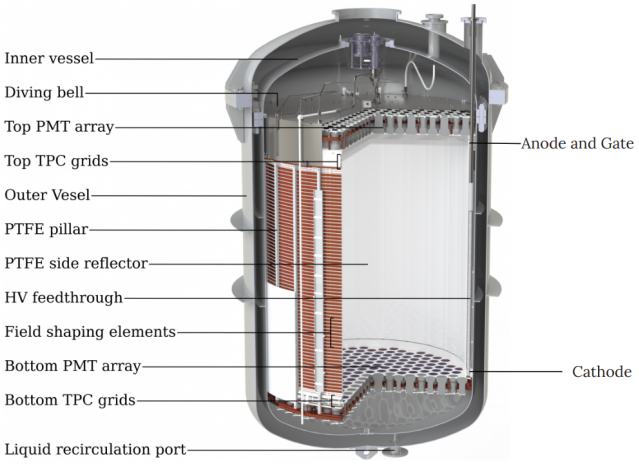

Figure 5: CAD rendering of the XENONnT cryostat and TPC. The TPC has a diameter of ∼1.3 m and is ∼1.5 m-tall. [9]

Water tank The cryostat is placed in a ∼10.2 m-tall and ∼9.6 m-large stainless steel tank inherited from XENON1t. This tank is filled by $\sim 700\,t$ of gadolinium loaded-water serving as a shielding against environmental gamma and neutron radiation. Moreover, the inner walls of the tank are instrumented with PMTs to operates as an active Cherenkov muon veto tagging incoming muons and hadronic showers induced by muons in the cavern rock [12]. Additional PTFE reflective surfaces with additional PMT enclose the cryostat in order to tag neutrons events in the TPC detecting them thanks to the gamma ray cascade following a neutron capture by gadolinium atom [13]. A rendering of the cryostat with both muon and neutron veto is shown on fig.6.

Cryogenic, purification and recovery systems The LXe inside the TPC is at an operating temperature of T_0 = -96°C. To cool xenon to this temperature, a cryogenic system is used [14]. Moreover, various purification system are used in order to reduce impurity and radioactive isotope from xenon. Among them, we have a krypton cryogenic distillation column [15], radon removal column [16] and liquid and gaseous xenon purification systems. Finally, to store the xenon in case of emergency, 2 insulated stainless-steel storage named ReStoX and ReStoX-II are installed.

Selection In order to analyze experimental data, a lot of selections are performed in order to remove background. Among them, we can list the pairing of S1 and

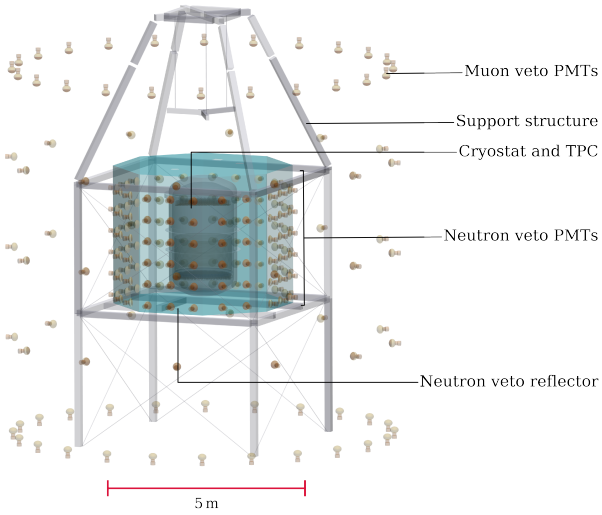

Figure 6: Rendering of the three nested detectors, including muon and neutron veto. The water tank walls, are omitted for clarity. Reflector panels, which optically separate the neutron and muon vetos, are shown as transparent turquoise surfaces. The neutron veto PMT windows face the neutron veto region through openings in the panels. [9]

S2 in order to form events removing so events with lone S1 or S2 or multiple S1 or S2 of close energy. Moreover, we have the fiducial volume selection. It allow to remove events occurring near the edge of the TPC where we have an higher background noise. All selection perform are optimised to keep a good signal-to-noise ratio.

Correction In order to analyze experimental data, we need to correct some effects occurring in the TPC. We have for example the non uniformity of the electric field in the TPC happening near the whole of the TPC and electrodes impacting electron behaviour and thus S2 signals. As previously shown, the gate electrode has 2 perpendicular wires. Those wires have an influence of electric field nearby and can capture drifted electrons passing nearby. We can thus wonder what is the impact of those wires on S2 signals and if it currently well corrected.

Finally, as XENONnT is a large experiment with a long operating time, spatial stability study and monitoring need to be done in order to assure the good operating of the whole detector for all data taking period.

For all of this, calibrations sources are needed. There are various calibration sources used in XENONnT but, in the following, I will only speak of the ^{83m}Kr that was used for this spatial stability study.

Spatial stability method

For the spatial stability study, we use ^{83m}Kr calibration source. This is an internal source and has the

particularity to decay in ^{83}Kr by two electron conversion with energies at 32.2 keV and 9.4 keV [17] in a very short period of time. Its two metastable steps have respective half-life of 1.83 h and 157 ns. These properties translates into major advantages of the ^{83m}Kr source to calibrate the XENON experiments. The energy of these events is very interesting because it sits in the energy window of the WIMP-nucleus recoil expected to $\sim 10keV$ [18] allowing to calibrate ER at this energy. Moreover, the half-life of the ^{83m}Kr of 1.83 h means that, once the source is closed and after a few hours, there won't be many radioactive components left in the TPC. This allows to make short calibration periods during data taking. However, because of the short half-life of 157 ns of the second state and signals having a time dispersion, signals can overlap each other if their dispersion in time are bigger than the decay time. It lead to three possible topologies either both signal can be distinguished or not.:

- Double S1 S2 - Both S1 signals as well as both S2 signals are resolved.
- Double S1 Single S2 - Both S1 signals are still resolved but S2 signals are merged into an unique one corresponding to an energy of 41.6 keV.
- Single S1 S2 - Both S1 are merged as well as both S2 into unique signals of 41.6 keV (fig.7). It the most common topology in XENONnT.

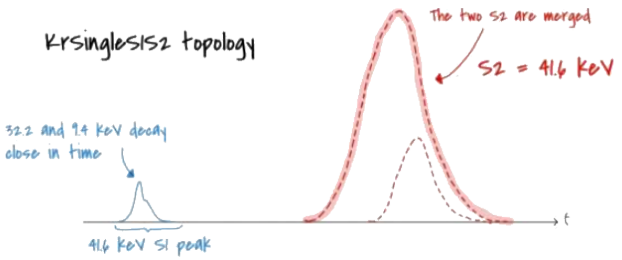

Figure 7: Single S1 S2 topology for ^{83m}Kr calibration events in XENONnT experiment. Both S1 are merged as well as both S2 into unique signals of 41.6 keV

Using Single S1 S2 selections developed by the collaboration, we were able to select $\sim 4.10^7$ Single S1 S2 events during Science Run 0 which lasts from the 1st of May to 10th of December 2021)

In order to check the spatial stability, a cylindrical volume inside the TPC was select with radius below 68 cm and z between -3 and -141 cm. This volume is cut into 48 slices of 2.875 cm high in z. Each of those slice are cut into 192 voxels of same volume arrange in concentric circle. We so to cut the total volume into 9216 voxels of same volume with each $\sim 4.10^3$ Single S1 S2 events. It allow to have enough statistic for following fit.

For each voxels, we fit the S1 S2 distribution by a two-dimensional gaussian distribution function. This fit function allows to extract the center of S1 and S2 distributions as well as the standard deviation of those distributions.

Then, for each of those four values, we compute their mean for the total volume. Then, for each voxel, we compute the relative variation of those four values to their respective means ($X_{rv} = X - X_{mean}/X_{mean}$).

Finally, we can plot relative variation maps for the whole selected volume for each of those four values. These allows us to spot region where either S1 or S2 or their standard deviation change.

Moreover, in order to only check effect link to the z coordinate, we select some specific regions of each slice and undertake the same method in order to plot relative variation in z.

Results and oulooks

On various relative variation maps and plots made during this work[1], we were able to make various observations. First, near PTFE walls as well as on top and bottom of the TPC we spotted, for some voxels, large variation for S1 and S2 value as for their standard deviation. They're caused by larger variation of the electric field near walls and electrodes. Nonetheless, those variation aren't too significant because such event will be removed by the fiducial volume selection during following studies. Moreover, we saw that perpendicular wires of the gate have an important effect on S2 signal distributions (their centers as well as their standard deviation). Those effects were expected from previous simulations made by the collaboration but remain to be checked as it could be caused by a systematic shifting of the transverse wires too. At last, a variation in z was observed for S1 and S2 distributions with a decrease of S1 and an increase of S2 as z increases. Those variations in z have to be studied by further work in order to better understand their causes and how to correct it for future data taking. Those studies can be new simulation, observations of effects on other value (as signal width or raising time) or on future data taking to see if those effects remain. This can be done either by me or collaboration members.

To conclude, we saw that XENONnT is a low background experiment. It's main goal is to search for WIMP-Xenon interaction but can be used for more physics search. Using the ^{83m}Kr as calibration source allows to check the stability of the detector at the expected energy for WIMP collision. For future data taking, some effect remain to be taken into account or/and corrected as those from perpendicular wires or z variation. Finally, The same method can be used to check the spatial stability of the detector for smaller period of time reducing voxeling, for future data taking and for other energy range using other calibration source. We will thus see if same variations remain in those future data taken and at other energy.

[1] I can't show maps and plots here as it's still a work in progress and not published.

References

[1] Planck collaboration, Planck 2018 results. VI. Cosmological parameters. Astronomy & Astrophysics, 641 :A6, sep 2020.

[2] Leszek Roszkowski, Enrico Maria Sessolo, and Sebastian Trojanowski. WIMP dark matter candidates and searches - current status and future prospects. Reports on Progress in Physics, 81(6) :066201, may 2018

[3] M. Schumann. Direct detection of WIMP dark matter : concepts and status. Journal of Physics G : Nuclear and Particle Physics, 46(10) :103003, aug 2019.

[4] E. Aprile, K. Abe, F. Agostini, and et al. Search for new physics in electronic recoil data from XENONnT. Physical Review Letters, 129(16), oct 2022.

[5] E. Aprile, K. Abe, F. Agostini, and et al. Double-weak decays of 124xe and 136xe in the xenon1t and xenonnt experiments. Physical Review C, 106(2), aug 2022.

[6] Guillaume Plante. The XENON100 Dark Matter Experiment : Design, Construction, Calibration and 2010 Search Results with Improved Measurement of the Scintillation Response of Liquid Xenon to Low-Energy Nuclear Recoils.

[7] E. Aprile, J. Aalbers, F. Agostini, et al. Dark matter search results from a one ton-year exposure of xenon1t. Physical Review Letters, 121(11), Sep 2018

[8] A. Manzur, A. Curioni, L. Kastens, D. N. McKinsey, K. Ni, and T. Wongjirad. Scintillation efficiency and ionization yield of liquid xenon for monoenergetic nuclear recoils down to 4 keV. Physical Review C, 81(2), Feb 2010

[9] E. Aprile, J. Aalbers, F. Agostini, et al. Projected WIMP sensitivity of the XENONnT dark matter experiment. Journal of Cosmology and Astroparticle Physics, 2020(11):031-031, Nov 2020.

[10] E. Aprile, F. Agostini, M. Alfonsi, et al. Lowering the radioactivity of the photomultiplier tubes for the XENON1T dark matter experiment. The European Physical Journal C, 75(11), Nov 2015.

[11] Keiko Fujii, Yuya Endo, Yui Torigoe, et al. High-accuracy measurement of the emission spectrum of liquid xenon in the vacuum ultraviolet region. Nuclear Instruments and Methods in Physics Research Section A: Accelerators, Spectrometers, Detectors and Associated Equipment, 795:293-297, 2015.

[12] E. Aprile, F. Agostini, M. Alfonsi, et al. Conceptual design and simulation of a water Cherenkov muon veto for the XENON1T experiment. Journal of Instrumentation, 9(11):P11006-P11006, Nov 2014.

[13] Ll. Marti, M. Ikeda, Y. Kato, et al. Evaluation of Gadolinium's Action on Water Cherenkov Detector Systems with EGADS, 2020.

[14] E. Aprile, J. Aalbers, F. Agostini, et al. The XENON1T dark matter experiment. The European Physical Journal C,77(12), Dec 2017.

[15] Uwe Oberlack. XENONnT - The next step in XENON Dark Matter Search. IDM 2018, Brown University, Jul 2018.

[16] Masatoshi Kobayashi. XENONnT experiment. darKONline2020, 2020.

[17] E. A. McCutchan. Nuclear Data Sheets for A = 83. Nuclear Data Sheets, 125 :201-394, March 2015.

[18] V. Chepel and H. Araújo. Liquid noble gas detectors for low energy particle physics. Journal of Instrumentation, 8(04):R04001-R04001, Apr 2013.

X-rays constraints on sub-GeV dark matter

Jordan Koechler

Laboratoire de Physique Théorique et Hautes Energies (LPTHE), UMR 7589 CNRS & Sorbonne University, 4 Place Jussieu, F-75252, Paris, France

Abstract — Dark matter (DM) constitutes about 85% of the total matter content in the Universe and yet, we don't know anything about its actual nature. In this proceeding, after a short introduction, I will present my work on DM indirect detection, more especially the computation of X-ray constraints on sub-GeV (or 'light') DM. Photons from the galactic ambient bath see their energy boosted up to X-ray energies when they scatter with electrons or positrons produced by the annihilation or decay of light DM particles. The fluxes of X-rays produced by this process can be predicted and compared with data from X-ray observatories (e.g., INTEGRAL) to obtain competitive constraints on light DM.

Introduction

The Dark Matter (DM) problem is one of the most important problem in modern physics. It was first postulated by Fritz Zwicky in 1933, as he suggested the presence of invisible matter between the galaxies of the Coma cluster [1]. Initially not taken seriously, his work was fully considered by physicists almost 40 years later, mostly thanks to Vera Rubin and Kent Ford's work on the measurement of the Andromeda galaxy rotation curve [2]. Since then, even with the combined, tremendous efforts of (astro-)particle physicists, astrophysicists and cosmologists, this almost a century-old problem is still unresolved. Even though observational evidence for DM exists at all scales, its nature is yet to be understood. All that we know about DM is that: i) it constitutes ∼85% of all matter and ∼25% of the total energy budget of the Universe [3] (which is dominated by an even bigger unknown: Dark Energy), ii) it must be stable or have a mean decay time greater that the age of the Universe ($\tau \gtrsim 4 \times 10^{17}\,\mathrm{s}$), iii) it interacts at least gravitationally with ordinary matter and with itself, and is expected to be electrically neutral and finally iv) it is cold, meaning that it behaves as a non-relativistic fluid in the early Universe.

In order to determine DM's nature, theorists came up (and still are coming up) with a lot of imaginative ways to build models that produce a well-motivated candidate for DM. Many of those models remain unconstrained by experiments and thus the speculated mass range for DM spans more than 90 orders of magnitude.

Particle DM is by far the most studied and motivated category of DM, where WIMPs (with mass between ∼5 GeV and ∼100 TeV) constitute the paradigm. However, since they were first postulated, no such candidates have been detected and therefore the attention is slowly turning to lighter (or heavier) candidates, such as sub-GeV DM. For lower DM masses, indirect detection is a powerful way to constrain candidates, since current direct detection experiments and colliders don't have the right sensitivity to do the same [5]. The principle behind indirect detection is to look for products of destruction (annhiliation or decay) of DM, in the cosmic rays that can be detected by observatories. The goal of these kind of studies is to constraint the DM velocity averaged annhilation cross section $\langle\sigma v\rangle$ and/or decay rate Γ as a function of its mass m_{DM}.

In this proceeding, we present new constraints on DM by predicting fluxes of X-rays from DM destruction and comparing them with data from INTEGRAL. In Sec.2 we explain how we computed such fluxes, in Sec.3 we describe the analysis for constraint computations. Finally, we show and discuss the results in Sec.4.

X-rays from DM destruction

In this proceeding, we use the same formalism as in [6], since we're working in the same regime. We're interested in studying sub-GeV DM indirect signals:

$$1\,\mathrm{MeV} \leq m_{\mathrm{DM}} \leq 5\,\mathrm{GeV}, \tag{1}$$

and on the observational side, we use X-ray data from INTEGRAL. In this DM mass range, we can't use already available numerical tools such as PPPC4DMID [7] to directly compute X-ray fluxes, as these tools generally are relevant for WIMP studies. Therefore, we do all the computations by ourselves.

Given the DM mass, there are only three kinematically open DM destruction channels:

$$\mathrm{DM\ (DM)} \longrightarrow e^+e^-, \tag{2}$$

$$\mathrm{DM\ (DM)} \longrightarrow \mu^+\mu^-, \tag{3}$$

$$\mathrm{DM\ (DM)} \longrightarrow \pi^+\pi^-. \tag{4}$$

We choose to study each channel independently, and not bother choosing a specific particle DM model. DM destruction into neutral pions is not considered, as the energy of the photons from π^0 decays (boosted to the

DM frame) is out of the range of energies covered by INTEGRAL.

When the particles from DM destruction are energetic enough, they can produce X-rays thanks to three processes: *Final State Radiation* (FSR), *Radiative Decays* (Rad) and *Inverse-Compton Scattering* (ICS). The total flux of X-rays from sub-GeV DM destruction is simply the sum of the three contributions. We will explain how to compute each of them in the following.

FSR (as suggested by the name) is simply the emission of an extra photon by one of the particles of the final state:

$$\text{DM (DM)} \longrightarrow e^+e^-\gamma, \tag{5}$$
$$\text{DM (DM)} \longrightarrow \mu^+\mu^-\gamma, \tag{6}$$
$$\text{DM (DM)} \longrightarrow \pi^+\pi^-\gamma. \tag{7}$$

In turn, radiative decays occur when muons and pions undergo a decay with an extra photon emission:

$$\mu^\pm \longrightarrow e^\pm\nu_e\nu_\mu\gamma, \tag{8}$$
$$\pi^\pm \longrightarrow l^\pm\nu_l\gamma, \tag{9}$$

where $l = \{e, \mu\}$.

FSR and radiative decays can somewhat be treated similarly, as they are both prompt (or primary) processes and the flux of photons associated to this kind of processes is computed as follows:

$$\frac{d\Phi_\gamma^f}{dE_\gamma d\Omega} = \frac{1}{4\pi\xi}\frac{dN_\gamma^f}{dE_\gamma}\begin{cases}\frac{\langle\sigma v\rangle}{2}\int_{\text{l.o.s.}} ds \left(\frac{\rho_{\rm DM}(r)}{m_{\rm DM}}\right)^2 & \text{(ann.)}\\ \Gamma \int_{\text{l.o.s.}} ds \left(\frac{\rho_{\rm DM}(r)}{m_{\rm DM}}\right) & \text{(decay)}\end{cases}, \tag{10}$$

where dN_γ^f/dE_γ is the energy spectrum of photons from $f = \{\text{FSR, Rad}\}$. The spherically symmetric DM energy density profile $\rho_{\rm DM}(r)$ (squared for annihilation) is integrated over the variable s that runs along the line of sight (l.o.s.). In this case, s runs from 0 to infinity. r is the distance from the Galactic Center (GC): $r^2 = s^2 + r_\odot^2 - 2sr_\odot\cos\theta$, where $r_\odot = 8.33$ kpc is the distance between the Sun and the GC, and θ is the angle formed by the l.o.s. and the Sun-GC axis. Finally, ξ parameterizes the nature of the DM particle: $\xi = 2$ if DM is its own antiparticle (Majorana fermion or scalar), $\xi = 4$ otherwise (Dirac fermion). In our study we simply chose the case where $\xi = 2$. The FSR and Rad photon energy spectra are directly taken from [6], which treats the annihilation case, and the same expressions can be generalized for the decay case.

Before going into the computation of the last contribution, let's talk about DM energy density profiles. A well-known discrepancy in DM studies is the cusp-core problem [8], where N-body simulations predict cusp profiles ($\rho_{\rm DM} \sim r^{-\gamma}$ for $r \to 0$, $\gamma > 0$) e.g., the Navarro-Frenk-White (NFW) profile [9], while observation of dwarf galaxies suggest more cored profiles ($\rho_{\rm DM} \sim$ const. for $r \to 0$) [10]. This means that the choice of DM profile is a source of uncertainty in our theoretical prediction of the X-ray flux from sub-GeV DM (it actually carries the largest uncertainty among all of the sources). In our study we consider three profiles: The standard NFW profile, a more cuspy NFW profile and the Burkert profile. The two NFW profiles are defined as:

$$\rho_{\text{NFW}\gamma}(r) = \rho_s\left(\frac{r_s}{r}\right)^\gamma\left(1+\frac{r}{r_s}\right)^{\gamma-3}, \tag{11}$$

with $\gamma = 1$ for the standard NFW and $\gamma = 1.26$ for the cuspy one, $\rho_s = 0.184$ GeV/cm^3 and $r_s = 24.42$ kpc in both cases. As of now, the NFW profiles will be denoted $\rho_{\rm NFW}$ and $\rho_{\rm cNFW}$ respectively. On the other hand, the Burkert profile is defined as:

$$\rho_{\rm Bur}(r) = \frac{\rho_s}{(1+r/r_s)(1+(r/r_s)^2)}, \tag{12}$$

with $\rho_s = 0.712$ GeV/cm^3 and $r_s = 12.67$ kpc. The three DM profiles are plotted in Fig.1 for illustration purposes.

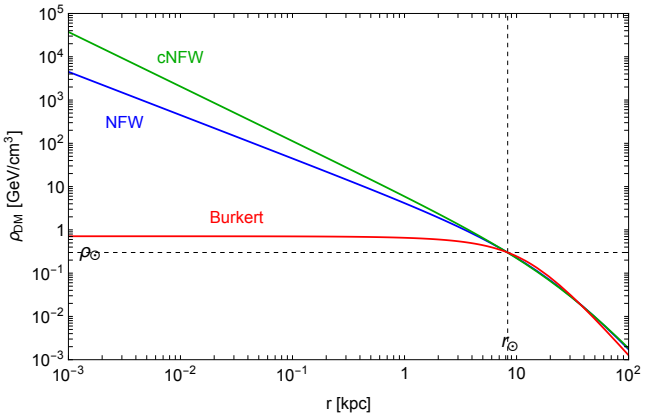

Figure 1: *Plot of the three DM profiles discussed in this section. The dashed lines represent the density of DM at the position of the Sun.*

Now let's tackle the third contribution. The goal is to compute the flux of up-scattered ambient photons by $e^\pm$ produced by DM destruction. This up-scattering process is known as ICS, and if the initial energy of the photon is E_0, the final one is $E \approx 4\gamma_e^2 E_0$, where $\gamma_e = E_e/m_e$ is the Lorentz factor of the incoming $e^\pm$. Given the energy range for these ambient photons is from 0.1 meV and 10 eV and DM mass is sub-GeV, the ambient photons are boosted up to X-ray energies after ICS. The ambient photons come from three sources/processes: the CMB, dust rescattering (IR) and stars (optical, denoted SL for 'starlight' later on). Since the distribution of stars and dust mostly lies in the galactic plane, so do the distribution of the associated photons and therefore, the system is not spherically symmetrical anymore.

The X-ray flux from ICS is given by:

$$\frac{d\Phi_\gamma^{\rm ICS}}{dE_\gamma d\Omega} = \frac{1}{E_\gamma}\int_{\text{l.o.s.}} ds\,\frac{j(E_\gamma,\vec{x})}{4\pi}, \tag{13}$$

where the emissivity j is the convolution of the $e^\pm$

spectral number density $dn_{e^\pm}/dE_e$ and the differential power emitted into photons $\mathcal{P}_{\rm IC}$:

$$j(E_\gamma,\vec{x}) = 2\int_{m_e}^{m_{\rm DM}(/2)} dE_e\,\mathcal{P}_{\rm IC}(E_\gamma,E_e,\vec{x})\,\frac{dn_{e^\pm}}{dE_e}(E_e,\vec{x}), \tag{14}$$

and finally, $\mathcal{P}_{\rm IC}$ is the convolution of the number density of ambient photon n_γ and the Klein-Nishina Inverse Compton cross section $\sigma_{\rm IC}$:

$$\mathcal{P}_{\rm IC}(E_\gamma,E_e,\vec{x}) = E_\gamma\int d\epsilon\,n_\gamma(\epsilon,\vec{x})\,\sigma_{\rm IC}(\epsilon,E_\gamma,E_e). \tag{15}$$

What is also important here is that we assume that the galactic magnetic field keeps the $e^\pm$ confined in a cylinder of radius $R_{\rm gal} = 20$ kpc and height $z_{\rm gal} = 4$ kpc. Consequently the ambient photons are up-scattered in this volume only, and therefore we have to cut appropriately the integration over s in Eq.13.

To compute the X-ray flux from ICS, we need three ingredients: i) the local spectral number density of DM-produced $e^\pm$ $dn_{e^\pm}/dE_e$, ii) the local number density of ambient photons n_γ (more specifically the sum of the three contributions discussed above) and iii) the Klein-Nishina cross section $\sigma_{\rm IC}$.

The CMB contribution of n_γ is computed analytically as it is simply the number density of photons coming out of a black body of temperature $T_{\rm CMB} = 2.725$ K, while the IR and optical contributions are computed using Interstellar Radiation Field (ISRF) maps from GalProp [11]. For the computation of $\sigma_{\rm IC}$ we refer the reader to [7, 12, 13] as it will not be detailed in this proceeding.

The remaining element to compute is $dn_{e^\pm}/dE_e$. To do that, first write the diffusion-loss equation for $e^\pm$ [7]:

$$\frac{\partial f}{\partial t} = \nabla(\mathcal{K}(E_e,\vec{x})\nabla f) + \frac{\partial}{\partial E_e}(b_{\rm tot}(E_e,\vec{x})f) + Q_e(E_e,\vec{x}), \tag{16}$$

where f denotes $dn_{e^\pm}/dE_e$ for simplicity. The first RHS term encodes the diffusion of $e^\pm$, whereas the second RHS term encodes their energy loss during propagation. $\mathcal{K}$ and $b_{\rm tot}$ are respectively the diffusion and energy loss coefficient functions. The third RHS is the simply the source term, which encodes the injection of DM-produced $e^\pm$:

$$Q_e(E_e,\vec{x}) = \frac{dN_{e^\pm}}{dE_e}\begin{cases}\frac{\langle\sigma v\rangle}{2}\left(\frac{\rho_{\rm DM}(\vec{x})}{m_{\rm DM}}\right)^2 & \text{(ann.)}\\ \Gamma\left(\frac{\rho_{\rm DM}(\vec{x})}{m_{\rm DM}}\right) & \text{(decay)}\end{cases}, \tag{17}$$

where $dN_{e^\pm}/dE_e$ is the $e^\pm$ spectrum from DM destruction. Its expression is detailed for each channel in [6].

Eq.16 is solved semi-analytically by assuming that diffusion is negligible, meaning that $e^\pm$ scatter off ambient photons right after their production from DM destruction and in the same location (referred as the 'on the spot' approximation). Although this is a strong assumption, it was verified except for l.o.s. towards high galactic latitudes which don't contribute a lot to the signal anyway.

Removing the LHS (time doesn't affect $dn_{e^\pm}/dE_e$) and the first RHS terms out of the Eq.16, we get in the end:

$$\frac{dn_{e^\pm}}{dE_e}(E_e,\vec{x}) = \frac{1}{b_{\rm tot}(E_e,\vec{x})}\int_{E_e}^{m_{\rm DM}} d\tilde{E}_e\,Q_e(\tilde{E}_e,\vec{x}). \tag{18}$$

Propagating $e^\pm$ may lose their energy due to interactions with the galactic gas, ambient photons and magnetic field: Coulomb interactions, ionization, bremsstrahlung, synchrotron emission and (of course) ICS. With the 'on the spot' approximation, we assume DM-produced $e^\pm$ lose instantaneously their energy through these processes before up-scattering ambient photons. The energy loss coefficient function $b_{\rm tot} = b_{\rm Coul+ioniz} + b_{\rm brem} + b_{\rm syn} + b_{\rm IC}$ is available in a numerical form in PPPC4DMID and we will use this one for our computations. We refer the reader to [7, 12] if they want to learn more on this topic.

Now we have everything we need to compute X-ray fluxes from DM destruction. The only remaining thing to do is to integrate the total differential X-ray flux over the solid angle of observation:

$$\frac{d\Phi_\gamma}{dE_\gamma} = \int_{b_{\rm min}}^{b_{\rm max}}\int_{l_{\rm min}}^{l_{\rm max}} db\,dl\cos b\sum_f \frac{d\Phi_\gamma^f}{dE_\gamma d\Omega}, \tag{19}$$

where $f = \{\rm FSR, Rad, ICS\}$ and (b,l) are respectively the galactic latitude and longitude of observation. (b,l) are also called galactic coordinates and related to θ by $\cos\theta = \cos b\cos l$.

Uncertainties in our theoretical X-ray flux prediction are a major concern as they will propagate up to the constraints we wish to compute. There are four sources of uncertainty, listed in decreasing order of importance: i) as we already mentioned, the choice of DM profile, ii) the normalization of ISRF maps from GalProp, iii) the normalization of gas maps used in the computation of $b_{\rm tot}$ and iv) the choice of galactic magnetic field configuration. We don't want to go into details here, but to summarize we allow both the normalization of gas and ISRF maps to vary by a factor 2, and for the magnetic field, we use three standard configurations named 'MF1', 'MF2' and 'MF3'. We invite the reader to check out [12] for further information.

The theoretical aspect of the study is now complete, in the next section we focus on the Integral data we use and on the analysis for computing the constraints.

Integral data and constraints computation

In this study we used data from the Spi spectrometer built in Integral. This data is reported in [14] and is a compilation of observations from 2003 and 2009 for a total exposure of $\sim 10^8$ s.

We used two datasets from this study, the first one is the spectrum of diffuse emission for $|b| < 15°$ and $|l| < 30°$ (see Fig.7 and 8 of [14]) and we use only for illustration purposes, see Fig.3. The second dataset is the one we use for computing the constraints. As shown

in Fig.5 of [14], it contains latitude profiles divided in five energy bands (27-49 keV, 49-90 keV, 100-200 keV, 200-600 keV and 600-1800 keV) and cover $|l| < 23.1°$ for the first four energy bands and $|l| < 60°$ for the last one. The different areas of observation are summarized in Fig.2.

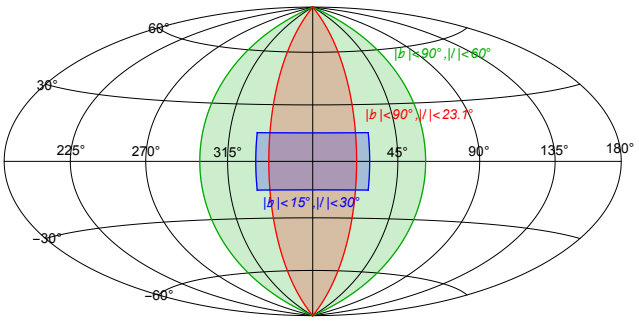

Figure 2: *Map of the Milky Way that shows the observation areas associated to the two datasets. In blue is the area of the first dataset, in red the area for the four first energy bands of the second dataset and in green for the fifth energy band.*

Since the annihilation case has been treated in [6], we focus on decay constraints in this proceeding. Fig.3 illustrates quite well what we want to achieve: for a given decay channel, the decay rate Γ (or the decay half-time $\tau = 1/\Gamma$) and the DM mass $m_{\rm DM}$ are free parameters and we want to impose a bound on them whenever the theory predicts more flux that what is observed. The constraints we obtain from this method are referred as 'conservative' constraints. Another way is to add the

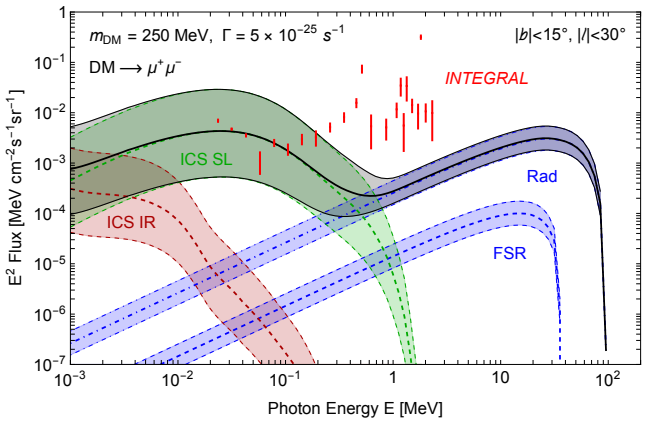

Figure 3: *Example X-ray spectra plotted with the first dataset. The plot shows the different contributions in the total X-ray flux from DM decay into muons, and also includes their respective uncertainty bands.*

astrophysical background to the DM prediction, and do a best-fit to the data. This gives 'optimistic' constraints and they are usually stronger that the conservative ones, though they depend on sometimes strong assumptions on the background.

To compute conservative constraints, we define a simple test statistic based on χ^2:

$$\chi^2_> = \sum_{\text{bands}} \sum_{i \in \{b \text{ bins}\}} \left(\frac{\max(\Phi_{\gamma,i}(\Gamma, m_{\rm DM}) - \phi_i, 0)}{\sigma_i} \right)^2 , \tag{20}$$

where $\Phi_{\gamma,i}$ is the predicted flux for bin i, ϕ_i the observed one and σ_i is the associated error bar. We impose a 2σ bound whenever the values of $(\Gamma, m_{\rm DM})$ solve $\chi^2_> = 4$. A similar test statistic can be used for deriving optimistic constraints, however we don't treat them in this proceeding.

Now we have everything ready for computing the conservative constraints on sub-GeV DM. In the next and final section, we show and discuss the results we obtained.

Results

We plot the conservative constraints we derived with our study, along with two other existing ones for the e^+e^- decay channel, in Fig.4. Our constraints show to

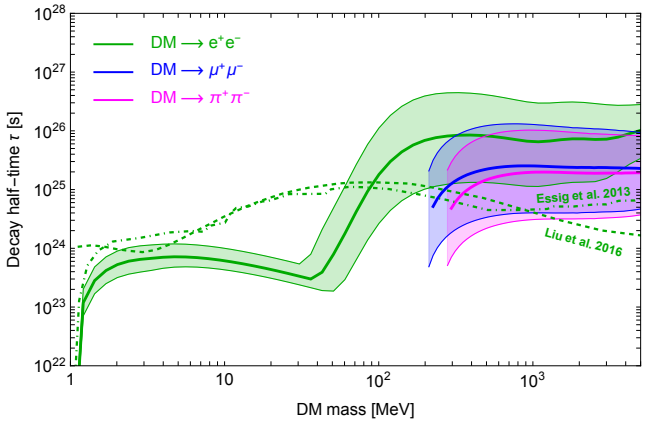

Figure 4: *Our conservative constraints on sub-GeV DM with their uncertainty bands, plotted with other existing constraints for the e^+e^- channel: dot-dashed line for extragalactic photons constraints, from Essig et al. [15] and dashed line for cosmic reionization constraints, from Liu et al. [16].*

be competitive, just like in the annihilation case in [6], especially at $m_{\rm DM} \gtrsim 100$ MeV where the ICS contribution dominates over the FSR and Rad ones. Even though the lower uncertainty band for e^+e^- is around an order of magnitude lower than the central value at higher DM masses, it is still higher than the existing constraints for $m_{\rm DM} \gtrsim 250$ MeV. In this DM mass range, we may have the strongest constraints on DM decay rate yet.

This proceeding shows only a fraction of what has been done on this topic, and we are working on systematizing this study for all relevant X-ray observatories: NuStar, XMM-Newton and Suzaku, in the hope of testing even more deeply a wide region of annihilating/decaying sub-GeV DM.

References

[1] F. Zwicky, Helv. Phys. Acta **6** (1933), 110-127 doi:10.1007/s10714-008-0707-4

[2] V. C. Rubin and W. K. Ford, Jr., Astrophys. J. **159** (1970), 379-403 doi:10.1086/150317

[3] N. Aghanim *et al.* [Planck], Astron. Astrophys. **641** (2020), A6 [erratum: Astron. Astrophys. **652** (2021), C4] doi:10.1051/0004-6361/201833910 [arXiv:1807.06209 [astro-ph.CO]].

[4] M. Cirelli, A. Strumia and J. Zupan (in preparation)

[5] M. Battaglieri, A. Belloni, A. Chou, P. Cushman, B. Echenard, R. Essig, J. Estrada, J. L. Feng, B. Flaugher and P. J. Fox, *et al.* [arXiv:1707.04591 [hep-ph]].

[6] M. Cirelli, N. Fornengo, B. J. Kavanagh and E. Pinetti, Phys. Rev. D **103** (2021) no.6, 063022 doi:10.1103/PhysRevD.103.063022 [arXiv:2007.11493 [hep-ph]].

[7] M. Cirelli, G. Corcella, A. Hektor, G. Hutsi, M. Kadastik, P. Panci, M. Raidal, F. Sala and A. Strumia, JCAP **03** (2011), 051 [erratum: JCAP **10** (2012), E01] doi:10.1088/1475-7516/2012/10/E01 [arXiv:1012.4515 [hep-ph]].

[8] W. J. G. de Blok, Adv. Astron. **2010** (2010), 789293 doi:10.1155/2010/789293 [arXiv:0910.3538 [astro-ph.CO]].

[9] J. F. Navarro, C. S. Frenk and S. D. M. White, Astrophys. J. **462** (1996), 563-575 doi:10.1086/177173 [arXiv:astro-ph/9508025 [astro-ph]].

[10] A. Burkert, Astrophys. J. Lett. **447** (1995), L25 doi:10.1086/309560 [arXiv:astro-ph/9504041 [astro-ph]].

[11] A. E. Vladimirov, S. W. Digel, G. Johannesson, P. F. Michelson, I. V. Moskalenko, P. L. Nolan, E. Orlando, T. A. Porter and A. W. Strong, Comput. Phys. Commun. **182** (2011), 1156-1161 doi:10.1016/j.cpc.2011.01.017 [arXiv:1008.3642 [astro-ph.HE]].

[12] J. Buch, M. Cirelli, G. Giesen and M. Taoso, JCAP **09** (2015), 037 doi:10.1088/1475-7516/2015/9/037 [arXiv:1505.01049 [hep-ph]].

[13] M. Cirelli and P. Panci, Nucl. Phys. B **821** (2009), 399-416 doi:10.1016/j.nuclphysb.2009.06.034 [arXiv:0904.3830 [astro-ph.CO]].

[14] L. Bouchet, A. W. Strong, T. A. Porter, I. V. Moskalenko, E. Jourdain and J. P. Roques, Astrophys. J. **739** (2011), 29 doi:10.1088/0004-637X/739/1/29 [arXiv:1107.0200 [astro-ph.HE]].

[15] R. Essig, E. Kuflik, S. D. McDermott, T. Volansky and K. M. Zurek, JHEP **11** (2013), 193 doi:10.1007/JHEP11(2013)193 [arXiv:1309.4091 [hep-ph]].

[16] H. Liu, T. R. Slatyer and J. Zavala, Phys. Rev. D **94** (2016) no.6, 063507 doi:10.1103/PhysRevD.94.063507 [arXiv:1604.02457 [astro-ph.CO]].

Calibration of the Virgo Gravitational Waves detector using a Newtonian Calibrator for the upcoming O4 observing run

Antoine Syx

IPHC - Strasbourg

Abstract — Since the first direct evidence of gravitational waves (GW) in 2015 the LIGO and Virgo collaboration have provided important results for astrophysics, cosmology or fundamental physics. The upgrades of the detectors through the years has increased the sensitivity and the range of detection, challenging their calibration. This talk reports the latest updates for a calibration method based on the local variation of the gravitational field using Newtonian Calibrators (NCal) on the Virgo detector for the upcoming O4 observing run.

Introduction

Th calibration of the GW detection is done by moving the mirror by a well known quantity using an external device. The NCal system is a system of rotating masses placed close to the end mirrors of the interferometer which induce a variable gravitational force then moves the mirror. The strength of the NCal signal depends mainly on the closeness of the NCal to the mirror, the rotor diameter and its density. Previous versions of the NCal were tested for the last observing run O3 with a calibration error of about 1.4 % [1]. The objective of the O4 NCal is to reduce the calibration error below one percent. This proceeding presents the work done during the first year of my thesis on the NCal system for the upcoming O4 observing run.

NCal principle and O3 results

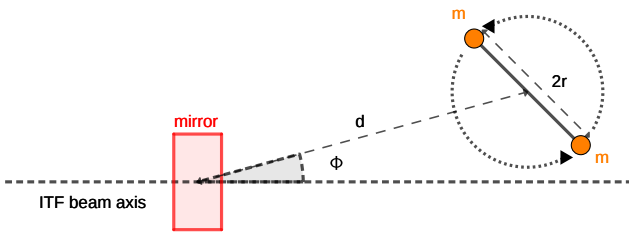

Figure 1: Outline top view of the NCal principle.

Figure 1 shows an outline of the NCal principle. The rotor is made of two sectors with opening angles equal to $\pi/2$. The gravitational strain induced by the NCal on the mirror is measured along the interferometer beam axis and can be expressed at the first order:

$$F_{\text{beam axis}} = \frac{9GmMr^2}{2d^4} \cos(\Phi) \cos(2\theta) \qquad (1)$$

In equation 1 we see that the distance d between the rotor and the mirror is at the fourth power, this parameter is our main source of uncertainties. The angle between the rotor and the beam axis is labelled as Φ, the opening angle of the sectors of the rotor is labelled as θ. When including higher orders, equation 1 (see equation 35 of [1]) must take into account the geometry of the rotor and the mirror such as the thickness, radius and density of the material.

The O3 NCal system uncertainties are shown in table 1. These uncertainties have been determined using table 1 and table 7 of the NCal tests during O3 data taking [1].

Parameter	Uncertainty	Formula	O3 uncertainty (%)
NCal to mirror d	6.4 mm	$4\delta d/d$	1.31
NCal to mirror Φ	3.3 mrad	$\delta\Phi \sin\Phi$	0.19
Rotor geometry	See table 1 of [1]		0.53
Quadratic sum			1.4

Table 1: Uncertainties on the amplitude of the calibration signal at 2f from the O3 NCal.

Using a quadratic sum of the uncertainties considered the estimated accuracy of the NCal system for O3 was about 1.4%.

O4 NCal upgrades and installation

Rotor

To reduce the uncertainties of the NCal system, we improve the design of the rotor, figure 2 shows the O3 rotor design (on the left) and the O4 upgraded design (on the right). Increasing the size of the rotor gives a stronger signal in the interferometer and removing the circular ring on the outside diameter is also important since the signal of the rotor strongly depends on the

alternance between full and empty sectors during the rotation. A total of eight rotors have been machined at the IPHC in Strasbourg using aluminum 7075. I performed the metrology of the rotors to determine their geometry and the associated uncertainties.

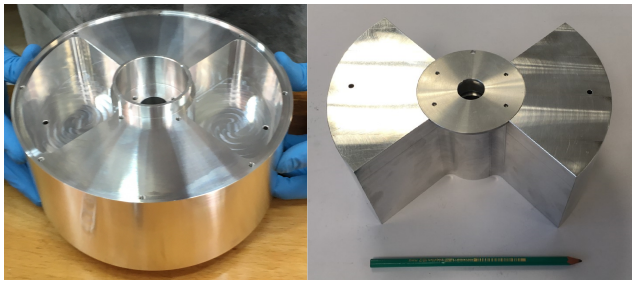

Figure 2: Left: view of the O3 rotor made of two full sectors and two empty sectors with a circular ring on the outside diameter. Right: picture of a O4 rotor with two full sectors and two empty sectors.

The motors and control system have been upgraded for O4. The rotors have been tested and can rotate up to 80 Hz.

Setup

The NCal setup for O4 was also improved. For O3 a pair of NCals were roughly suspended close to the mirror linked by a metal bar. The setups are suspended to reduce the vibrations issued by the rotation and thus to avoid the structure around the mirror to vibrate and induce a gravitational noise in the signal at the rotation frequency. For O4 we designed and installed three improved suspended setups around the mirror (see figure 3). Each setup is composed of a suspended vertical plate with three possible NCal positions. A reference plate is installed below with position sensors to monitor the displacement of the setup over time. The three setups have been installed around the mirror to better estimate the position of the mirror inside of the vacuum chamber which is not well known (maybe a few millimeters). They are located at an angle Φ=34.7 degrees from the beam axis as seen on the right image of figure 3. To achieve a correct precision on the position of the setups we used a two part aluminum template to link the setups while placing them around the mirror, then the template was removed after the setups have been fixed.

Two NCals per setups have been installed for a total of six NCals around the mirror, as represented with color boxes in figure 3. We placed three NCals at 1.7 m from the mirror (green boxes in figure 3), a closer NCal at 1.3 m (red box in figure 3) and two further NCals at 2.1 m and 2.5 m (respectively blue and purple boxes in figure 3). The further NCal on each setup has been rotated by π to measure the altitude of the NCals by comparing their phase.

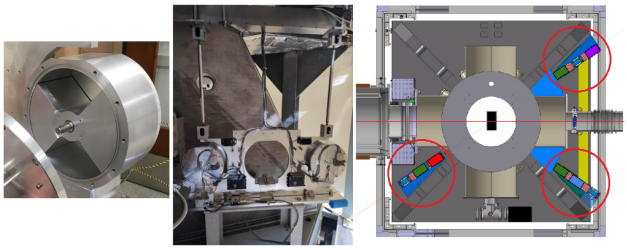

Figure 3: Left: picture of a O4 rotor inside its box. Middle: picture of a suspended setup with two NCal boxes visible. Right: top view of the vacuum chamber and its structure, the mirror is represented in black at the center, the beam axis is represented by the horizontal red line, the NCal setups are circled in red.

Predicting the NCal signal and uncertainties

The calibration accuracy of the interferometer relies on the ability to predict the signal that is injected to compare it with the recovered signal in the interferometer.

Rotor geometry

We use a finite element analysis program named FROMAGE [2] to compute the NCal signal. This program simulates the gravitational force of a rotating object on the mirror. Using my metrology measurements and FROMAGE I compute the expected signal for each rotor. Figure 4 shows the O4 rotor geometry where each sub-sector corresponds to a measurement made on the rotor.

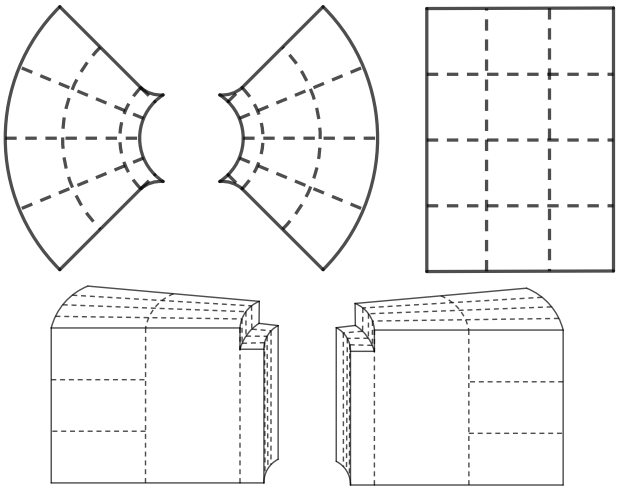

Figure 4: Top, diameter and side view of the O4 rotor geometry. The dashed lines delimit different sections of the rotor simulated in FROMAGE.

Table 2 shows the expected strain signal and the associated uncertainty coming from each rotor geometry determined with the metrology.

As shown in table 2 the overall rotors geometry uncertainty is below 0.1% (we will take this value to remain conservative), a factor 5 better than for O3.

Rotor	strain signal ($d = 1.7$ m)	uncertainty (%)
R4-01	$2.121 \times 10^{-18}/(2f^2)$	0.045
R4-02	$2.118 \times 10^{-18}/(2f^2)$	0.059
R4-03	$2.119 \times 10^{-18}/(2f^2)$	0.061
R4-04	$2.118 \times 10^{-18}/(2f^2)$	0.067
R4-05	$2.119 \times 10^{-18}/(2f^2)$	0.071
R4-06	$2.119 \times 10^{-18}/(2f^2)$	0.063
R4-07	$2.119 \times 10^{-18}/(2f^2)$	0.074
R4-31	$1.154 \times 10^{-19}/(3f^2)$	0.077

Table 2: Uncertainties on the amplitude of the calibration signal. f is the rotor rotation frequency. Rotors 1 to 7 have two sectors and therefore induce a GW signal at $2f$, rotor 31 has three sectors and induces a GW signal at $3f$.

We note that the rotor labelled R4-31 has three sectors with opening angles of $\pi/3$, its signal is therefore weaker than the two sectors rotors. It has been designed to perform high frequency checks during O4.

NCal to mirror distance and angle

To determine the uncertainty on the distance between a NCal to the mirror we take into account the positioning of the reference and suspended plates, their machining precision and the positioning of the rotors in the slots of the suspended plates. With the O4 NCal setup and installation procedure, the mirror to NCal distance uncertainty is below 0.66 mm, a factor 9 better than for O3.

The uncertainty on the angle Φ is 0.3 mrad, a factor 10 better than for O3.

These uncertainties have to be checked during calibration shifts on the working interferometer.

Expected accuracy for O4

The previous measurements made on the setups allow us to compute the expected accuracy of the NCal system for O4. Table 3 shows the uncertainties of the NCal parameters and the estimated signal uncertainty at 2f.

Parameter	Uncertainty	Formula	O4 uncertainty (%)
NCal to mirror d	0.66 mm	$4\delta d/d$	0.1-0.2
NCal to mirror Φ	0.3 mrad	$\delta\Phi \sin\Phi$	0.02
Rotor geometry	See table 2		0.1
Quadratic sum			0.14-0.22

Table 3: Estimated uncertainties on the amplitude of the calibration signal at 2f from the O4 NCal.

The accuracy of the NCal system on O4 is expected to be a factor 6 better than for O3.

NCal frequency range and Virgo sensitivity

The detection potential of the interferometer is determined using a sensitivity curve. Figure 5 shows a sensitivity curve of Virgo during O3 and the projected sensitivity for O4 and O5. This curve shows the noise strain as a function of the frequency. The range of detection quoted in figure 5 is the radius of the sphere equivalent to the volume where binary neutro star (BNS) are detected with a signal to noise ratio (SNR) of 8 (averaged on all sky localizations and BNS orientations). A typical inspiralling BNS signal at a distance of 100 Mpc and the NCal frequency range of the two and three sectors rotors are included in figure 5. The NCal frequency range is expected to be between 0 Hz and 160-240 Hz depending of the rotor (2f and 3f signal). The NCal signal covers the frequency range where most of the BNS signals are collected.

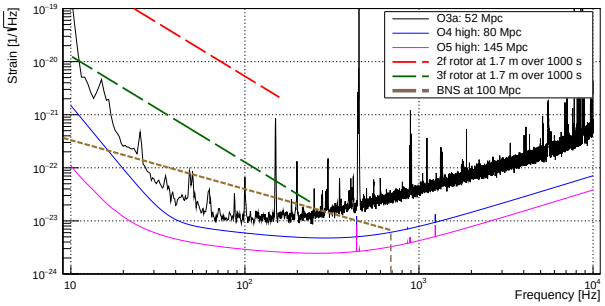

Figure 5: Sensitivity curve of the Virgo interferometer and NCal frequency range. The black curve shows the sensitivity during O3, the blue and purple lines show the expected upper sensitivity for respectively O4 and O5. The red and green dashed line represents the NCal frequency range for respectively the 2f and the 3f for 1000 seconds of integrating time. The dashed brown line represents the signal of an inspiralling BNS at a distance of 100 Mpc as it sweeps across the detector.

Conclusion

During the first year of my thesis I worked on the improvement of the NCal system for the upcoming oberving run O4 of the Virgo interferometer. Through this proceeding I discussed the different improvements made on the system such as a more precise metrology of the rotors and positioning of the NCals around the mirror. The calibration error of the NCal system is expected to be well below one percent for O4.

In the following months we will be able to inject NCal signals in the interferometer to check if the expectations we made were accurate. The NCal system is expected to be used continuously during O4. Improvements of the NCal system are already being discussed and tested at the IPHC for the late part of O4 and the following O5 oberving run.

References

[1] Dimitri Estevez, Benoît Mours and Thierry Pradier. Newtonian calibrator tests during the Virgo O3 data taking, 2020, Class. Quant. Grav. (2021); arXiv:2011.03728. DOI: 10.1088/1361-6382/abe2da.

[2] D. Estevez et al. Numerical simulations for Virgo O3 NCal using FROMAGE, Virgo TDS (2020); **VIR-0759B-20**. https://tds.virgo-gw.eu/ql/?c=15884.

Study of the localization of sources identified by the MBTA pipeline for low latency CBC search and Early Warnings

Christopher Alléné

Laboratoire d'Annecy de Physique des Particules

Abstract — A lot of progress, in many fields [7, 8, 9], has been made thanks to the first multi-messenger detection GW17017 by the LIGO-Virgo Collaboration and by electromagnetic instruments [6]. In order to optimize such detections, Early Warning (EW) strategies are developed for the next observating run. The work presented in this paper investigates the implementation of an EW method in the MBTA low-latency pipeline [1] and its impact on the sky localization processed by the Bayestar software. The consistency of MBTA results with theoretical expectations is shown. The localization accuracy associated to the early cutoff of the template waveform is also shown.

Introduction

The work presented here is supervised by Damir Buskulic in the Virgo group at LAPP. The goal of the thesis is to improve the localization of gravitational waves (GWs) sources with the low latency detection pipeline MBTA (Multi-Band Template Analysis) in the case of EW triggers. In the first section, a brief presentation of the gravitational waves and multi-messenger sources is given. The second section portrays the analysis method and pipeline used to detect and localize the event sources. The third section describes the work around the EWs (with two methods) and the sky localization of the source. The last section will summarize the work done and present its prospects.

Gravitational Waves

The GWs are space-time metric perturbations traveling at the speed of gravity, which is the same as the speed of light ($-3 \times 10^{-15} < \frac{v_{GW}-c}{c} < 7 \times 10^{-16}$ [2]), with two transverse polarizations h_+ and $h_\times$. They were predicted by Einstein in his General Relativity theory in 1916 [3] and were detected for the first time on September 14$^{\text{th}}$, 2015 by Advanced LIGO during the first observation run (O1) [4]. GWs can be emitted by rotating non axis-symmetric objects. The emitted power follows:

$$P \simeq \frac{c^5}{G}\epsilon^2 \left(\frac{R_S}{\Delta}\right)^2 \left(\frac{v}{c}\right)^6 \tag{1}$$

where ϵ is the asymmetric factor, R_S the Schwarzschild radius, Δ the system compactness and v the system speed [5]. In order to detect those systems, they have to be compact and in relativistic motion, that is why Coalescing Binary systems of Compact objects (CBCs) such as Binary Black Hole (BBH), Neutron Star-Black Hole (NSBH), Binary Neutron Star (BNS) are interesting systems. CBCs' evolution can be divided in three stages : the inspiral phase with the two companions rotating and getting closer.At Newtonian order, this phase depends only on the so-called chirp mass :

$$\mathcal{M} = \frac{(m_1 m_2)^{3/5}}{(m_1 + m_2)^{1/5}} \tag{2}$$

Once the two companions get close enough, the plunge and merge phase takes place, during which they collide and merge. The second phase is followed by a ringdown phase, when the final object, usually a black hole, get back to its fundamental state.

In the case of BNS, electromagnetic radiations are expected during the merger phase in addition to the GWs, allowing simultaneous multi-messenger detections, which can bring more informations than mono-messenger ones, like in the case of GW170817 [6]. This event was the first and only (for now) multi-messenger detection (GW and EM), the evolution of the EM spectrum allowed to identify the event as a kilonova in the galaxy NGC4993. Thanks to GW170817, new constraints on the neutron star equation of state have been set [7], a new way to measure the Hubble constant H_0 has been performed [8] and heavy elements production processes have been provided which could explain Earth observed abundances [9]. In order to improve all these models and measurements, more multi-messenger detections are needed. Therefore the question of sending EWs from GW detectors to EM observatories become an important one. The GWs are detected by kilometer size Interferometers (LIGO Hanford and Liv-

ingston in USA, Virgo in Cascina, Italy and KAGRA in Japan) which sensitivities are shown in fig. 1. The detectors signal is sent to low-latency analysis pipelines (MBTA, pyCBC, GstLAL, cWB, SPIIR...) to find astrophysical events. The Multi-Band Template Analysis (MBTA) pipeline is the one used in the work presented.

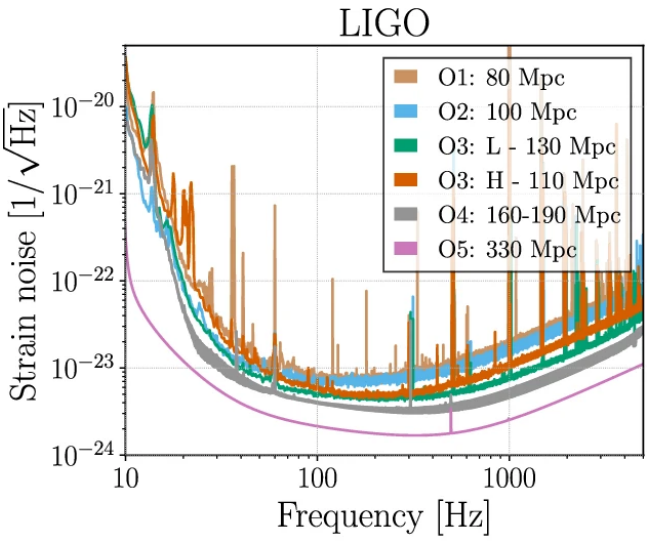

Figure 1: Obtained or expected sensitivities for LIGO and its upgrades from O1 to O5[10]

Analysis

Optimal Filtering

The analysis of the detectors signal performed by MBTA uses the optimal matched filtering method. Filters $\tilde{Q}(f)$ are applied in the frequency domain, on a signal $s(t)$ which is the sum of the noise $n(t)$ and the astrophysical signal $h(t)$: $s(t) = h(t) + n(t)$:

$$S = \int_{-\infty}^{+\infty} \tilde{s}(f)\tilde{Q}^*(f)\mathrm{d}f. \tag{3}$$

This filtered signal S is compared to the filtered noise:

$$N = \int_{-\infty}^{+\infty} \tilde{n}(f)\tilde{Q}^*(f)\mathrm{d}f, \tag{4}$$

building a signal-to-noise ratio (SNR) :

$$SNR = \sqrt{\frac{\langle S \rangle^2}{\langle N^2 \rangle}} \tag{5}$$

The detection occurs when the SNR exceeds a threshold (4.5 for BNS, 4.8 for NSBH and 4.8 for BBH). Since the optimal SNR is obtained when the filter fits an astrophysical event, one needs as many filters as of possible astrophysical events, which would be an infinite amount. To recover the full parameter space, one needs to pave it with a number N_f of filters such that the minimal recovered SNR for any astrophysical signal is 97% of the optimal SNR of the nearest filter. The filters are $\tilde{Q}(f) = \frac{\tilde{h}(f)}{S_n(f)}$ with $h(t)$ the pre-computed waveform (namely template) and $S_n(f)$ the Power Spectral Density (PSD) which is the auto-correlation of the noise:

$$S_n(f) = |\tilde{n}(f)|^2 \tag{6}$$

The specificity of MBTA is to divide the frequency band in several sub-bands, usually in two bands (Low and High Frequency). The separation frequency is defined in order to get an equally distributed SNR between the two bands. Once the filtering is done, MBTA merges the analysis results of the different interferometers.

Coincidences and localization

Since the current worldwide interferometer network is composed of three detectors (the two LIGO and Virgo), coincidences may be build with time coinciding triggers with the same template. One can then use the arrival time in the different detectors to triangulate the sky position of the astrophysical source. In order to localize the events, the Bayestar software is used. Bayestar computes localization probability density using bayesian inference from event parameters [11]. One can then establish an area where the source can be found at a given level of confidence. The area size is reducing when the SNR grows.

Early Warning

In order to detect more multi-messenger sources, one can use shorter templates. It induces a reduction of the SNR and consequently a bigger area size computed by Bayestar. This section is dedicated to the study of those effects caused by the implementation of EW to the analysis process.

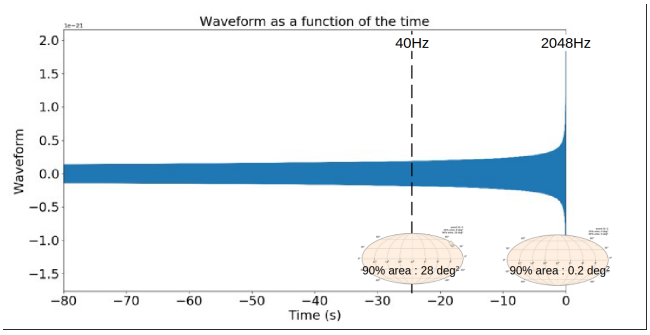

Figure 2: Waveform of a $1.4 - 1.4\,\mathrm{M}_\odot$ BNS at 50 Mpc with the localization skymap corresponding to a full bandwidth detection (until 2048 Hz) and a cutoff around 25 s before the merger phase (until 40 Hz). One can observe an increase of the area at 90% level of confidence when the detection bandwidth is reduced (from $0.2\,\mathrm{deg}^2$ to $28\,\mathrm{deg}^2$).

Implementation in MBTA

To detect a CBC source before the merger, one needs to compute the SNR with shorter templates ending before the merger. A simple solution would be to reduce the sampling frequency of the data. The Nyquist-Shannon sampling theorem [12] constrains the sampling frequency to be twice the maximum detection frequency (also called EW frequency in this proceeding), the latter is then necessarily reduced when a reduction in sampling frequency occurs.

In order to evaluate this solution, the three detectors combined SNR (cSNR) of simulated events found by MBTA has been compared to theoretical ones.

A signal of a standard BNS source ($m_1 = m_2 = 1.4\,\mathrm{M}_\odot$ and spins $s_1 = s_2 = 0$) has been injected in a gaussian noise which PSD is the theoretical expected one for the next observation run (O4). The source has been set at 50 Mpc, which is of the order of the GW170817 distance (in NGC4993 at 40^{+8}_{-14} Mpc [13]). The theoretical cSNR were computed using the PSD and the source parameters. A Newtonian order [14] and a 3.5 Post-Newtonian order waveforms, the latter being computed by Bayestar through LIGO Algorithm Library Suite (LALSuite) function [15], have been compared to the MBTA events on 15 EW cutoff frequencies. One can observe that it produces unconsistent cSNRs which do not reproduce theoretical expectations fig. 3.

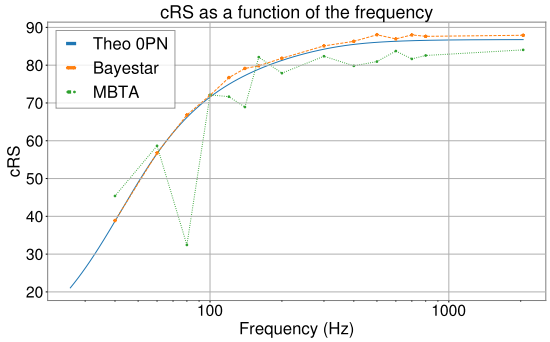

Figure 3: Combined SNR of the three detectors (H, L and V) as a function of the maximum frequency of detection. In blue, the Newtonian order expected SNR. In orange, the 3.5 Post-Newtonian expectation (obtained with LALSuite functions [15] through Bayestar software) for the SNR. In green, the SNR from the simulation computed by MBTA. To reduce te maximum frequency with MBTA, the sampling frequency of the input data is reduced to twice the maximum frequency.

A more elaborated solution is to taper the template in the time-domain with a Tukey window when the frequency is equal to the desired maximum cutoff frequency (at t_{EW}) for a duration of a wave period T_{EW}:

$$w(t)\begin{cases} = 1 & \text{if} \quad t < t_{EW} \\ = \frac{1+cos\left(\pi\frac{(t-t_{EW})}{T_{EW}}\right)}{2} & \text{if} \quad t_{EW} \leq t \leq t_{EW}+T_{EW} \\ = 0 & \text{if} \quad t > t_{EW}+T_{EW} \end{cases} \tag{7}$$

This way, the template is shortened and doing the same test as for the previous method, one can observe that the measured cSNR is consistent 4. This EW method is the one used in the following work developed in this proceeding.

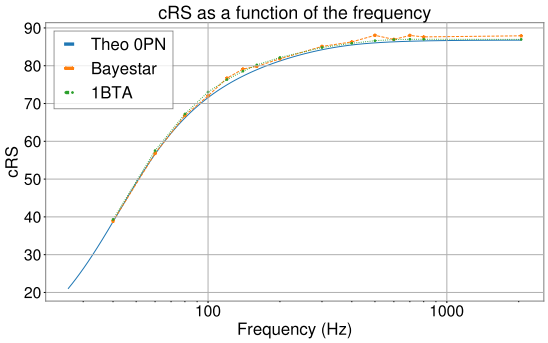

Figure 4: Combined SNR of the three detectors (H, L and V) as a function of the maximum frequency of detection. In blue, the Newtonian order expected SNR. In orange, the 3.5 Post-Newtonian expectation (obtained with LALSuite functions [15] through Bayestar software) for the SNR. In green, the SNR from the simulation computed by MBTA (with only one band). To reduce the maximum frequency with MBTA, the templates are tapered by a Tukey window starting at the desired maximum cutoff frequency. The deviation of the MBTA results with the Bayestar results is less than 1.5 which is compatible for the $1-\sigma$ uncertainty of a SNR.

Effect on Bayestar localization

The events found using the previous technique are localized by Bayestar to compare the size of the area on the skymap. It is observed that the area size of the events found by MBTA have the same increase than the theoretical expectations (fig. 5).

Reducing the frequency of detection (the EW cutoff frequency), the template waveform given to Bayestar and used to infer the localization is shortened which impacts the size of the area thus the precision of the localization. Hence, reducing the frequency to a lower EW frequency induces an increase of the area because of the lower SNR but also because of the shorter waveform. It is then necessary to compare the effect on the area due to SNR only decrease and the one due to the EW frequency cutoff. Hence a simulation with the previous source at the same localization (latitude and longitude) but with different distances from the Earth has been performed. The evolution of the area size as a function of the cSNR is displayed on the fig. 6. One can observe the difference of behavior induced by the cut on the waveform used by Bayestar. This difference shows that the cutoff on the waveforms impacts the accuracy of localization in a non-negligible way.

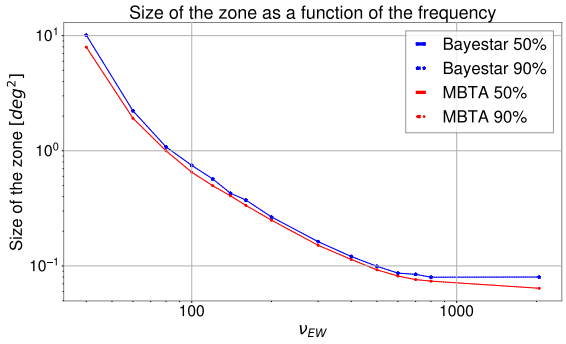

Figure 5: Size of the probability density sky zone computed by Bayestar as a function of the EW frequency cutoff (in Hz) : in blue, the theoretical expectation of Bayestar. In red, the size computed for the event found by MBTA. The bold (dotted) line is the size of the 50% (90%) of confidence zone. The frequency variation of MBTA is obtained by tapering the time-domain template.

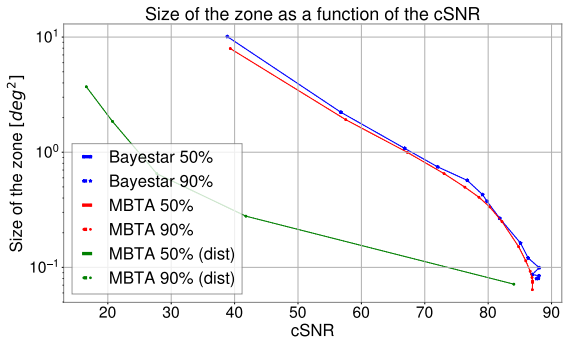

Figure 6: Size of the probability density sky zone computed by Bayestar as a function of the cSNR : In blue, the Theoretical expectation of Bayestar. In red, the size for event found by MBTA. In green, the size for MBTA event for sources at different distances. The bold (dotted) line is the size of the 50% (90%) of confidence zone. The variations of the cSNR on the red and blue curves are obtained by varying the maximum detection frequency.

Prospects and summary

In this proceeding, an MBTA implementation for EW has shown its efficiency, with a gaussian noise, in finding events following theoretical expectations, which allowed to the Bayestar software to compute the localizations. Further studies of the evolution of the measured SNR and the area size as a function of the system chirp mass are in progress. This studies are using a new template bank adapted to the EW frequency and are injecting a simulated signal on a non-gaussian noise obtained by recoloring O3b data to fit with O4 expected PSD. A study of the different cutoffs and rejections (χ^2 cutoff, False Alarm Rate, ...) may also be necessary to adapt them to the EWs. For further prospects, an EW strategy has to be decided with the full MBTA team, which include, for instance, the choice of the EW frequency cutoff.

References

[1] Adams T. et al. Low-latency analysis pipeline for compact binary coalescences in the advanced gravitational wave detector era. Classical and Quantum Gravity, 33(17), 175012, 2016.

[2] B. P. Abbott et al. (Virgo, Fermi-GBM, INTEGRAL, LIGO Scientific), Astrophys. J. 848, 2017.

[3] A. Einstein, Die Grundlage der allgemeinen Relativitätstheorie Annalen der Physik, 49, 1916.

[4] B. P. Abbott et al. (LIGO Scientific Collaboration, Virgo Collaboration), Phys. Rev. Lett. 116, 061102, 2016.

[5] F. Aubin, Recherche à faible latence d'ondes gravitationnelles émises lors de coalescences de binaires compactes durant la troisième période d'observation de Advanced Virgo et Advanced LIGO, Thesis, Université Savoie Mont Blanc, 2020.

[6] B. P. Abbott, R. Abbott, T. D. Abbott, F. Acernese, K. Ackley, C. Adams, T. Adams, P. Addesso, R. X. Adhikari, V. B. Adya, and et al. Multi-messenger Observations of a Binary Neutron Star Merger. The Astrophysical Journal, 848(2) :L12, Oct 2017.

[7] B. P. Abbott, R. Abbott, T. D. Abbott, F. Acernese, K. Ackley, C. Adams, T. Adams, P. Addesso, R. X. Adhikari, V. B. Adya et al. GW170817 : Measurements of Neutron Star Radii and Equation of State. Physical Review Letters, 121(16), Oct 2018.

[8] The LIGO Scientific Collaboration and the Virgo Collaboration et al. A gravitational-wave measurement of the Hubble constant following the second observing run of Advanced LIGO and Virgo. 2019.

[9] M. R. Drout, A. L. Piro, B. J. Shappee, C. D. Kilpatrick, J. D. Simon, C. Contreras, D. A. Coulter, R. J. Foley, M. R. Siebert, N. Morrell, and et al. Light curves of the neutron star merger GW170817/SSS17a : Implications for r-process nucleosynthesis. Science, 358(6370) :1570-1574, Oct 2017.

[10] B. P. Abbott et al. Prospects for observing and localizing gravitational-wave transients with Advanced LIGO, Advanced Virgo and KAGRA. 2013.

[11] Leo P. Singer and Larry R. Price. Rapid Bayesian position reconstruction for gravitational-wave transients. Physical Review D, 93(2), Jan 2016.

[12] Claude E. Shannon. Communication in the presence of noise. Proceedings of the IRE, 37(1) :10-21, 1949.

[13] B. P. Abbott et al. (LIGO Scientific Collaboration and Virgo Collaboration). GW170817: Observation of Gravitational Waves from a Binary Neutron Star Inspiral. Phys. Rev. Lett. 119, 161101, Oct 2017.

[14] Michele Maggiore. Gravitational Waves. Vol. 1 : Theory and Experiments. Oxford Master Series in Physics. Oxford University Press, 2007.

[15] LIGO Scientific Collaboration. LIGO Algorithm Library - LALSuite, 2018.

Part II

Beyond Standard Model

session chaired by Luca CADAMURO

Search for Beyond the Standard Model physics with Emerging Jets and the ATLAS detector during Run-3

Guillaume Albouy

Univ. Grenoble Alpes, CNRS, Grenoble INP, LPSC-IN2P3, 38000 Grenoble, France

Abstract — In the context of the ATLAS Run-3 data taking period, an early-data analysis targeting emerging jets is in preparation. Emerging jets are part of a global Beyond the Standard Model (BSM) theory called Dark QCD. This BSM theory predicts the existence of a new dark sector containing QCD-like particles and interactions, that is separated from the Standard Model (SM), but accessible through a portal producible in proton-proton collisions at the LHC. In addition, emerging jets models predict that dark particles produced at the LHC can decay back to the SM with a long lifetime, leading to displaced objects (tracks, vertices) in the ATLAS detector. This leads to a highly exotic type of signature that until recently was poorly studied. This Run-3 analysis will benefit from a new trigger dedicated to this signature and software upgrades for large radius track reconstruction. An overview of the current state of this analysis will be presented.

Introduction

The LHC and its two general purpose detectors ATLAS and CMS, while being able to make precise measurements of Standard Model (SM) physics, also search thoroughly for Beyond the Standard Model (BSM) physics. One of the main focus is the search for dark matter (DM) by supposing the production of DM during proton-proton collisions. DM then might be detected as missing energy as it does not decay back to SM particles or as exotics signatures if DM is produced in association with other BSM particles which can decay back to SM particles. Dark QCD emerging jets models predict the latter one. This analysis focuses on Emerging Jets in the context of the ATLAS experiment.

The ATLAS experiment

ATLAS is one of the four main detectors of the LHC. It is a general purpose detector like CMS and is dedicated to precision measurements of the SM and the search for BSM physics. It is a cylindrical detector with a multi-layer conception [1]. It is composed of several sub-detectors each one dedicated to specific purposes. From inside to outside, the particles created in the collisions will go through the :

- Inner detector[1] : tracker, measures charged particles trajectories, so their momentum and direction
- Electromagnetic and hadronic calorimeters : stop most of the SM charged and neutral particles (except muons and neutrinos) and measure their energies and directions with some information
- Muon spectrometer[2] : tracker for muons, measures muons trajectories, so their momentum and directions

For this analysis the main physics objects of interest are tracks and jets. A track is the reconstruction of a charged particle trajectory inside the inner detector. As this sub-detector is immersed in a magnetic field, this track is not linear but curved and the measure of this curvature gives access to the transverse momentum of this particle. The main parameters to describe a track are its : direction (η, ϕ), transverse momentum (p_T) and the distances of the point of closest approach to the interaction point[3] $(d0, z0)$. A jet is a more complex object, it is the typical QCD signature of quarks and gluons and is the most common objects in ATLAS. Quarks and gluons, due to colour confinement of the strong force, cannot propagate freely. At LHC any emitted quark or gluon will undergo a parton shower, emitting new quarks and gluons. The partons thereby produced then regroup into hadrons during the hadronisation. All these hadrons are more or less collimated and form a conic object called jet. In ATLAS these jets are reconstructed using both energy deposits in the calorimeters and tracks reconstructed in the inner

[1] Immersed in a magnetic fields for bending charged particles trajectories and measure their transverse momentum p_T

[2] See footnote 1

[3] where the proton-proton collision has taken place

detector and are described by their : direction (η, ϕ), transverse momentum (p_T), energy (E) and mass (m).

Phenomenology of dark QCD and Emerging Jets

As mentioned before, Dark QCD is a BSM theory that proposes an extension of the SM with the addition of a new hidden/dark sector [2]. This new sector would have a content in particles and interactions similar to the SM QCD, meaning there would be dark equivalents to quarks, hadrons (baryons, mesons), gluons and to the strong confining force. But as for dark matter, all these particles would be able to interact only weakly with the SM particles. The dynamics in this sector would then stay in it and be similar to QCD : dark quarks would not propagate freely and form colour-less dark hadrons. These dark hadrons can be either stable and so invisible to any SM detector or unstable and decay to SM particles through a portal. These stable dark hadrons could be dark matter candidates whereas the unstable ones would create signal in a detector. As for the portal, it could be either a new vector or scalar boson but also the Higgs boson as current constraints still allow it to decay in part to BSM particles.

This theory then allows these dark particles to be produced in collider during proton-proton collision using this same portal in the other way : SM → Dark Sector. In the case where these particles are dark quarks it would lead to a parton shower and hadronisation in the dark sector and so the production of a large quantity of dark hadrons, some of which will decay to SM particles. Hence this will produce similar signatures to SM QCD : (dark) jets of collimated particles that are more or less exotics depending on the parameters of the dark sectors (see Figure 1).

Emerging jets models are an application of Dark QCD with special properties giving birth to the most exotics signature of dark jets (top left corner in Figure 1). These models are obtained by having dark particles decay back to the SM with sizeable lifetimes producing objects (tracks and vertices) with visible displacement in the detector. It is highly exotics as most of SM decays are quasi prompt and few particles produce displaced tracks and secondary vertices. For this analysis we are focusing on a two-jets topology with the following production mechanism :

- Production of a new vector boson **Z'** via the annihilation of two SM quarks
- Decay of the **Z'** in two dark quarks
- The dark quarks go through parton showering and hadronisation in the dark sector, leading to the production of many dark hadrons
- All dark hadrons produced are unstable and decay back to SM quarks at different point in the detector

This produces two large jets composed of non-prompt tracks (characterised by large $d0, z0$) and secondary

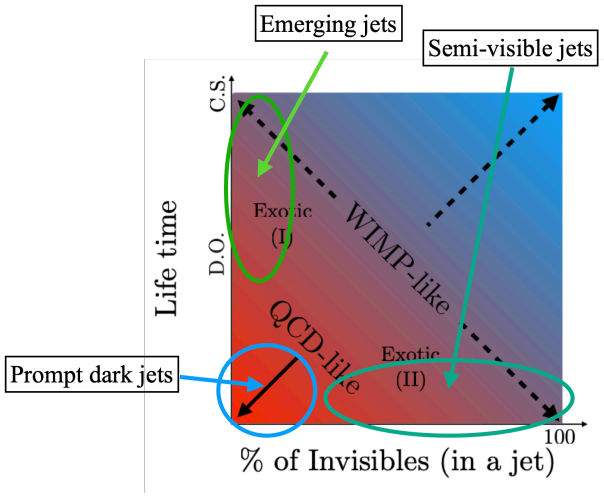

Figure 1: Expected signatures from a dark sector depending on the % of invisible particles in a jet and lifetime of the dark particles decaying to the SM (modified from [3]). Bottom left corner : QCD-like dark jets, fully visible and prompt. Bottom right corner : semi-visible dark jets, in which some dark hardons are stable leading to missing energy. Top left corner : emerging jets, fully visible dark jets but with displaced objects.

vertices (decay point of dark hadrons), called emerging jets. Figure 2 represents what is expected from these models : two jets with no or few tracks coming from the interaction point (centre of the detector, where the protons collides) and the apparition further in the detector of more and more particles coming from the decays of dark hadrons, each decay creating a secondary vertex and leading to deposits in the calorimeters. These jets then tends to 'emerge' in the detector as like they were not produced at the interaction point.

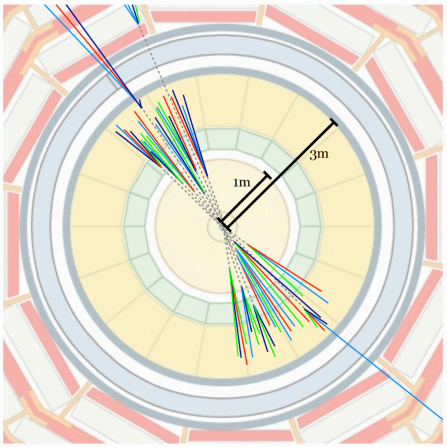

Figure 2: Schematic of an event displaying two emerging jets in the ATLAS detector [4]

Emerging jets are the focus of this analysis, they need to be well understood and characterised to differentiate them from standard model jets (QCD jets).

An ATLAS Run-3 analysis on Emerging Jets

Models and simulation

The models used for the signal studies are generated with Pythia [5] and its Hidden Valley module. This module allows the addition of a simplified dark sector (for simplicity and lack of detailed knowledge of its dynamic) with mass-degenerated dark quarks and only the two lightest dark hadrons, a dark pion and a dark rho (analogous to the SM pion and rho mesons) and with tuneable free parameters [6]. The table 1 resumes the parameters of the two models currently under study.

	Model A	Model E
m_{π_d}	5 GeV	0.8 GeV
$c\tau_{\pi_d}$	1 mm	
$m_{Z'}$	600-800-1000 GeV	
Decay to SM	Dark pions to SM quarks	
Decay in the dark sector	Dark rhos to dark pions	

Table 1: Signal models

These models are then going through the full simulation of the ATLAS detector with Geant4 [7].

Signal discrimination

The main objective of this analysis is to discriminate signal (emerging jets) from SM background. Here the main background is composed of QCD dijets event : events with two standard QCD jets, which most of the times should be composed of prompt tracks and no secondary vertices. However, as said previously some SM QCD processes can lead to displaced objects, as it is the case of bottom-quark initiated jets that produce long-lived B-mesons which decays will produce non-prompt tracks and secondary vertices. It is thus necessary to construct variables that are discriminating between emerging jets and any QCD jets.

Tagging Emerging Jets

We defined three tagging variables, all based on tracks composing a jet :

- fraction of prompt tracks in a jet :

$$PTF = \frac{N_{prompt\ tracks}}{N_{all\ tracks}}$$

- p_T fraction of large radius tracks in a jet :

$$LRTpTF = \frac{\sum_{large\ tracks} p_{T_{track}}}{p_{T_{jet}}}$$

- median of $|d0|$ of all tracks in a jet : $\widetilde{|d0|}$.

To compute and use these variables, selections on tracks are necessary. First to mitigate pile-up (i.e removing tracks coming from others interactions) we apply cuts on the p_T and $z0$ of the tracks, keeping only the ones with sufficient momentum and which are close in with regards to the main Primary Vertex[4]. Indeed, pile-up tracks are mostly at a lower energy and come from other vertices of interactions. Secondly, we need to define quantitatively prompt and large radius tracks. For that, we are using the easiest way to define prompt tracks : a prompt track is a track that is associated to the main Primary Vertex[5] (a large-radius track is then defined as the opposite, i.e tracks that are coming from a secondary vertex and not the main Primary Vertex). This definition of prompt/large radius tracks can lead pile-up tracks to be defined as large radius tracks as they will be associated to other Primary Vertices (noise) without being actually produced at secondary vertices. Pile-up mitigation is then an important step for prompt and large radius tracks definition.

Pile-up mitigation

As said above a selection of the tracks is necessary to remove noise from pile-up interactions. This is to increase the proportion of signal tracks (coming from the interaction of interest, i.e the **Z'** decay) with regards to noise, in order to compute precisely the tagging variables that are dependent of the tracks contained in the jets. Currently we use two selections : $p_{T_{trk}} > p_{T_{min}}$ and $\Delta z = |z0_{trk} - z_{PV}| < z0_{max}$. By varying these threshold we are able to find the best configurations and so obtain the highest signal selection efficiency and the highest noise rejection efficiency. Figure 4 shows the selection/rejection efficiencies of tracks for different value of $z0_{max}$ and $p_{T_{min}}$. Each curve is made using a fixed value of $z0_{max}$ and by varying $p_{T_{min}}$. The optimal point is the one closest to the top right corner corresponding to 100% selection and rejection efficiencies. We then take $p_{T_{min}} = 0.7$GeV and $z0_{max} = 4$mm which gives a selection efficiency of 89.6% and a rejection efficiency of 86.8%.

Preliminary results

Figure 3 is an example of discrimination plot obtained with the PTF and LRTpTF variables. The discrimination with QCD background is extremely good, especially regarding the PTF variable. The last one ($\widetilde{|d0|}$) also performs well in our firsts results. It confirms that emerging jets are highly specific and different from SM QCD jets.

Possible analysis strategy

Knowing that the emerging jets signature is highly specific and exotic, selecting signal events seems direct. This should allow us to run a simple cut and count analysis. First we apply a list of selections to remove

[4] the interaction point, i.e the hard-scatter vertex where the **Z'** was produced and so the dark particles

[5] a track associated to a Primary Vertex means that either it was used to reconstruct the Primary Vertex or it is directly pointing to this Primary Vertex within some distance

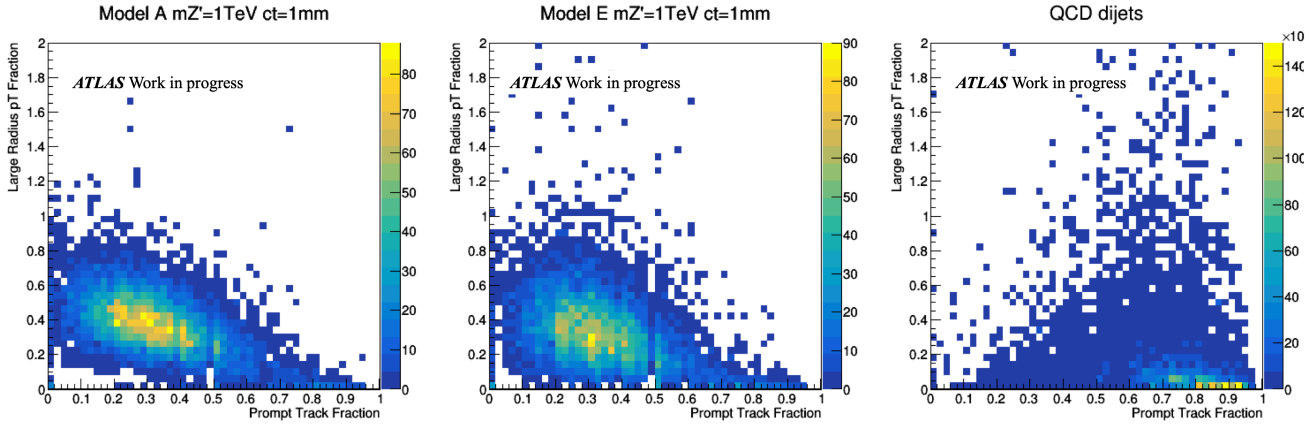

Figure 3: Discrimination plots : Large-radius track p_T fraction versus prompt track fraction for Model A (left), Model E (center) with $m_{Z'} = 1$TeV and $c\tau = 1$mm compared to QCD dijets (right)

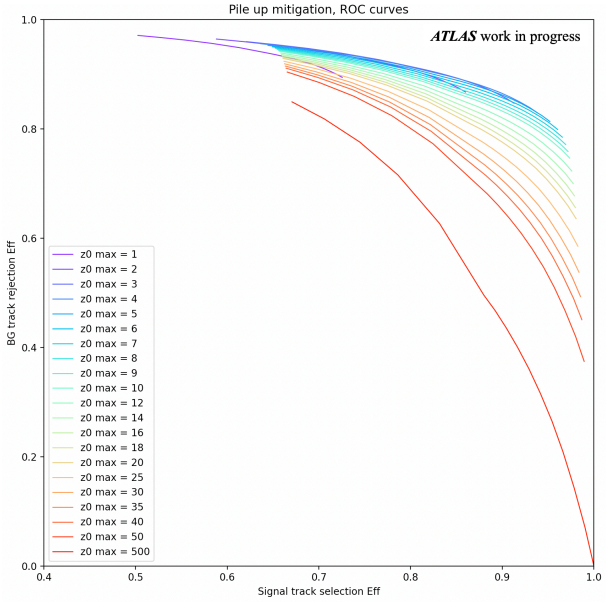

Figure 4: ROC curve for tracks selection

as much background events as possible in order to get the highest signal to background ratio. It will define a signal region where most of the signal is selected and background rejected. But as said before, some SM QCD events can mimic the signal either with actual long-lived signatures or wrongly reconstructed events. It is then necessary to estimate the number of background events that survive the previous selections. A common method used in ATLAS is the ABCD method. It consists in the construction of 4 regions based on two variables $v1$ and $v2$ that are discriminating between the background events and signal :

- region A : $v1 > cut1$, $v2 > cut2$, 'signal region', enriched in signal events,
- regions B,C,D: others combinations[6], control regions, enriched in background events and poor signal contamination.

If $v1$ and $v2$ are uncorrelated enough, background events will be spread uniformly in the $(v1, v2)$ plane and the following relation will be mostly true :

$$\frac{N_C^{bkg}}{N_D^{bkg}} = \frac{N_A^{bkg}}{N_B^{bkg}}$$

From this relation we can easily extract an estimation of the number of background events in region A (signal region) :

$$N_A^{bkg,estimated} = \frac{N_C^{bkg}}{N_D^{bkg}} N_B^{bkg}$$

And so by simply counting the actual number of events in region A, it is possible to assess if there is an excess of event with regards to SM physics only ($\mathbf{N_A^{obs} > N_A^{bkg,estimated}}$), which could point to BSM physics.

The choices of $v1$ and $v2$ variables are very important and combinations of the tagging variables described previously are currently under study.

Conclusion and prospects

The status of this early Run-3 analysis aiming at Emerging Jets produced via a **Z'** mediator with ATLAS was presented. It is the first effort on this signature in the ATLAS collaboration. Our preliminary results on signal discrimination shows promising performances and an analysis strategy is being put in place. However, all these studies were done for signal models with a relatively low lifetime but we aim at being sensible to a broader phase space. Hence more samples from models with higher lifetimes are in preparation and a complete re-investigation of signal discrimination will be necessary to assess the adaptability of the tagging variables to more displaced objects.

[6] B: $v1 > cut1$, $v2 < cut2$; C: $v1 < cut1$, $v2 > cut2$; D: $v1 < cut1$, $v2 < cut2$

The author acknowledges the support of the French Agence Nationale de la Recherche (ANR), under grant ANR-21-CE31-0013 (project DMwithLLPatLHC).

References

[1] The ATLAS Collaboration, "The ATLAS Experiment at the CERN Large Hadron Collider", JINST, vol. 3, p. 437 (2008)

[2] G. Albouy, J. Barron, H. Beauchesne et al, "Theory, phenomenology, and experimental avenues for dark showers: a Snowmass 2021 report", Eur. Phys. J. C 82, 1132 (2022)

[3] M. Park and M. Zhang, "Tagging a jet from a dark sector with Jet-substructures at colliders", Phys. Rev. D, vol. 100, no. 11, p. 115009 (2019)

[4] P. Schwaller, D. Stolarski, A. Weiler, "Emerging jets", J. High Energ. Phys., 59 (2015)

[5] T. Sjostrand et al, "An introduction to PYTHIA 8.2", Computer Physics Communications, vol.191, p. 159-177 (2015)

[6] https://pythia.org/latest-manual/HiddenValleyProcesses.html

[7] The ATLAS Collaboration, "The ATLAS Simulation Infrastructure", The European Physical Journal C, vol.70, issue 3, p. 823-874 (2010)

Search for a Vector Like Quark T' decaying into a quark top and a Higgs boson in the dileptonic same sign final state with the CMS experiment at the LHC

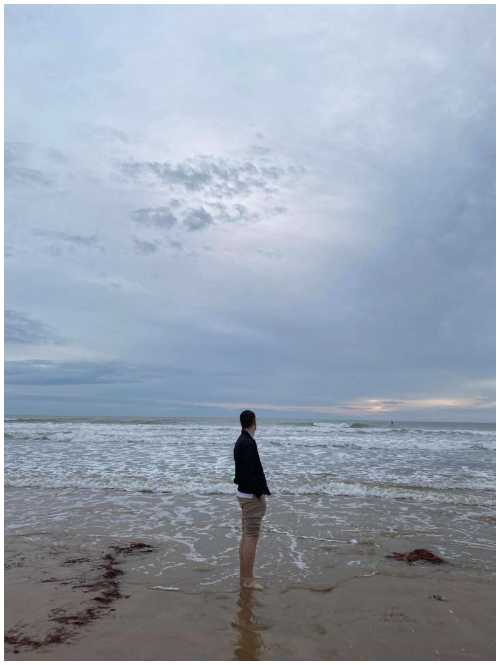

Benjamin Blancon

Université Claude Bernard Lyon 1 / Institut de Physique des Deux Infinis, UMR 5822, IN2P3, CNRS Villeurbanne, France

Abstract — The Standard Model (SM) is complete since 2012 with the discovery of the Higgs boson by both the Compact Muon Solenoid (CMS) and A Toroidal LHC ApparatuS (ATLAS) collaborations. One of the biggest challenges of the SM now is to understand the properties of this new experimental particle and especially what protects the Higgs boson mass from the divergences induced by loop contribution (the mass itself does not diverge since we measure it at 125GeV). The introduction of new particles like Vector-Like Quarks (VLQs) is an interesting explanation as their final decay into SM particles can be well-identified. This extension of the SM in the Beyond Standard Model (BSM) sector is presented here with the decay of the VLQ T' into a quark top and a Higgs boson in the same sign (SS) dileptonic final state. It is a brand new analysis using Run2 data (2016-2018) collected with the CMS detector at the Large Hadron Collider (LHC). The first version of the analysis strategy is made up of a cut-based selection and two Control Regions (CRs) to extract the signal from the background.

Introduction

The Large Hadron Collider (LHC) at CERN near Geneva is the largest particle accelerator in the world [1]. Designed as a proton-proton collider, four main experiments study various particle physics topics: A Large Ion Collider Experiment (ALICE), LHCb, ATLAS and CMS. The CMS apparatus [2] in particular is a multipurpose, nearly hermetic detector designed to trigger on [3, 4] and identify electrons, muons, photons and (charged and neutral) hadrons [5, 6, 7]. A global "particle-flow" (PF) algorithm [8] aims to reconstruct all individual particles in an event combining information provided by the all-silicon inner tracker and by the crystal electromagnetic and brass-scintillator hadron calorimeters, operating inside a 3.8T superconducting solenoid, with data from the gas-ionization muon detectors embedded in the flux-return yoke outside the solenoid. The reconstructed particles are used to build τ leptons, jets and missing transverse momentum [9, 10, 11]. During the Run1 (2010-2012), the CMS and ATLAS collaborations confirmed the experimental existence of the Higgs boson [12] [13] of whose interaction with a particle gives this latter its own mass [14]. This last result is a great success completing the 50 year old SM and making it one of the most precise theory in all physics. However, new SM limitations rise up as long as the energy at the LHC increases. The energy scale of the observed Higgs boson mass cannot be explained as the perturbative corrections make its mass divergent [15]: this is the hierarchy problem. One of the possible solutions to regularize divergences is to add a new particle in the model and the VLQ is an interesting candidate [16]. The VLQ is a coloured fermion which transforms the same way under the SM gauge groups no matter its chirality. Its coupling with the Higgs boson would break the electroweak symmetry and transform the Higgs boson into a pseudo-Goldstone boson, removing the corrections and solving the hierarchy problem. With $m_{\mathrm{H}} = 125$GeV the VLQ mass should be around 1TeV [17] while the energy in the center of mass of LHC for Run2 (2016-2018) is 13TeV: it is enough to observe the presence of the VLQ as a possible extension of the SM. Predicted in many BSM models (composite Higgs models, little Higgs models, supersymmetric nonminimal models...) [18], this would be the first experimental evidence of this hypothetical particle.

The proceedings are divided into three sections. The first section presents the properties of the specific VLQ T' and its decay in the SS dileptonic final state. As

other processes could have a similar final state, we need to reduce them with a dedicated analysis strategy: it is the goal of the second section with the first preliminary results. The CRs will be finally discussed in the last section to extract the signal shape from the background.

Properties of the VLQ T'

We consider the VLQ T' with a weak hypercharge $Y = {}^{7}/_{6}$, an electric charge $Q = {}^{2}/_{3}$ and a weak isospin $I = {}^{-1}/_{2}$ [17]. We assume $m_{T'} = 700$GeV for the rest of this work: additional studies for different VLQ mass values are currently ongoing. It is a single produced VLQ via the interaction of a W or Z boson and a quark q" (see Figure 1). At Primary Vertex (PV) the T' can decay into three modes:

- T' → W boson and quark top t (50% [19]).
- T' → Z boson and quark top t (25% [19]).
- T' → Higgs boson and quark top t (25% [19]). We focus on this decay as we study the interaction between the Higgs boson and the VLQ.

Concerning the final state we focus on the SS dileptonic (electron or muon, we don't consider the tau) channel:

- H → W^+ and W^- bosons (21% [20]) → lepton l and antineutrino $\overline{\nu}$ (11% [20]) and quarks q"' and $\overline{\text{q""}}$(67% [20]).
- t → W^- boson and quark bottom b (100% [20]) → lepton l and antineutrino $\overline{\nu}$ (11% [20]) and quark bottom b.

The final state for the signal is then composed of two SS leptons, three jets coming from the three quarks including one bjet coming from the quark bottom b and two neutrinos which are not considered as we cannot detect them directly in the CMS detector. In the end, the cross-section of the VLQ T' decaying into a Higgs boson and a quark top is 89fb with a global branching ratio of 0.17% for the concerned final state. Three channels are considered depending on the nature of the leptons: the dimuonic channel, the one muon-one electron channel and the dielectronic channel. Let's also note that other analysis with different final states are currently ongoing inside the collaboration.

Unfortunately many processes have the same or a very close final state compared to the signal's one. The background processes can be separated into two parts: the reducible backgrounds have a similar final state because of the misidentification of the characteristics of the particles in the detector. For example the charge misassignment for the electrons vary from 0.1% to 0.3% in the CMS detector depending on the pseudorapidity η (see equation 1 for the definition) [21]. We consider two types of reducible backgrounds: the top processes

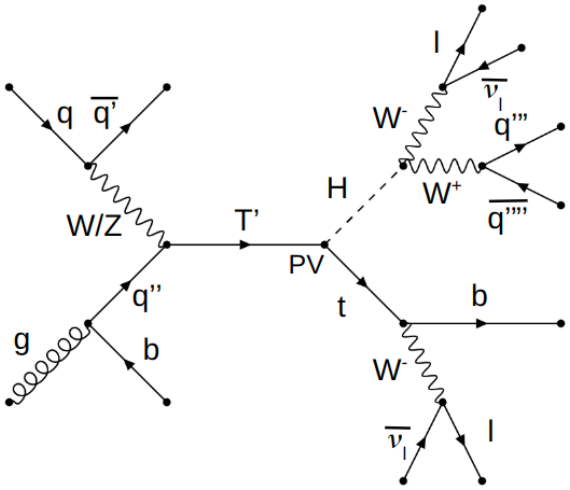

Figure 1: Production of the VLQ T' via a W/Z boson and a quark q". T' decays into a Higgs boson and a quark top t for a SS dileptonic final state. It is made up of two SS leptons, three jets including one bjet and two neutrinos (not considered here).

with opposite sign (OS) leptons and jets including bjets in the final state and the diboson processes with SS leptons and no jets in the final state. The irreducible backgrounds have a similar final state because the decay of the processes themselves is similar making then difficult to separate from the signal. We consider one type of irreducible backgrounds: the ttX processes with SS leptons and jets including bjets in the final state. As all these backgrounds have different characteristics and a much larger cross-section than the signal it is very difficult to discriminate the signal from them: we need to design a unique analysis strategy.

Analysis strategy

The principle of the analysis strategy is to get the background under control to clearly identify the signal. We choose here a cut-based analysis strategy where the background processes are reduced by studying their differences with the signal. We will also determine the background shape thanks to the CRs to extract the signal shape (see next section). The rest of this work is based on simulated events for the 2018 data. Let's see the characteristics of the different background processes to remove them one by one:

- the top processes: they are suppressed by requiring exactly two SS selected leptons. The identification of the leptons is as follows. Concerning the kinematic selection the transverse momentum p_T must be greater than 20GeV for the muons and 25GeV for the electrons and the absolute pseudorapidity $|\eta|$ must be below 2.4 for the muons and 2.5 for the electrons [6].

$$\eta = -\ln\left(\tan\left(\frac{\theta}{2}\right)\right). \quad (1)$$

The identification (ID) of the leptons based on the PF algorithm [8] could take three possible working points WPs (loose, medium or tight) and must be tight for both muons and electrons. The leptons must be close to the PV as well so that the 3D impact parameter must be below 3cm for the muons and 2cm for the electrons. This criterion is very useful to remove the displaced leptons coming from the taus decay. Finally the leptons must be isolated from jets which can decay into leptons so that the isolation variable (see equation 2 for the definition [22]) must be below 0.05 for both electrons and muons.

$$\text{Isolation} = \frac{\sum_{\text{R}_{\text{iso}}} \text{Pt(Particles} - \text{lepton)}}{\text{Pt(lepton)}} \quad \text{with } \text{R}_{\text{iso}} = \frac{10\text{GeV}}{\text{Pt(lepton)}} \text{ the cone size.} \tag{2}$$

- the diboson processes: they are suppressed by requiring jets and bjets in the selected events.
- the ttX processes: they are suppressed by requiring the invariant mass of the combination of three jets to be different than the quark top invariant mass in the selected events. The quark top indeed decays into three jets for ttX processes.

At the end the cut-based selection is as follows:

- Cut 0: asking for exactly two SS selected leptons as mentioned before with the sum of the p_{T} of the two leptons to be greater than 160GeV. The VLQ T' has indeed a large mass so we expect the two leptons to have high p_{T}.
- Cut 1: asking for ΔR between the two leptons (see equation 3 for the definition, ϕ is the azimuthal angle) to be greater than 1.8. The two leptons must indeed be back-to-back.

$$\Delta\text{R} = \sqrt{(\Delta\eta)^2 + (\Delta\phi)^2}. \tag{3}$$

- Cut 2: asking for at least three selected jets with at least one selected bjet with p_{T} greater than 50GeV. A selected jet has p_{T} greater than 30GeV, $|\eta|$ below 4.5 and a tight ID. A selected bjet has p_{T} greater than 30GeV, $|\eta|$ below 2.5, a tight ID and a medium DeepJet value where DeepJet is an algorithm to identify bjets with three possible WPs (loose, medium or tight).
- Cut 3: asking for the minimum invariant mass among all the possible combinations of the selected three jets minus the quark top invariant mass $m_{\text{top}} = 172.9\text{GeV}$ [20] to be greater than 34GeV e.g. the selected three jets invariant mass to be different than the quark top invariant mass $\pm 2\sigma$ (the quark top invariant mass resolution comes from a gaussian fit performed in an internal analysis).

Summing up all the channels the number of expected events for the signal and the background is respectively 9.1 and 269.1 with a S/B = 3.38%. The selection is pretty efficient but the ttX and top processes remain the main backgrounds (respectively 52% and 41%). This is not surprising because the ttX processes are irreducible backgrounds and the top processes have very large cross-sections (364pb and 87pb for the respective semileptonic and dileptonic $t\bar{t}$ processes TT_SL and TT_2L for example). Fortunately it is possible to discriminate the signal over the background if we find a specific variable where the shapes of the signal and the background are different: this is the Variable Of Interest (VOI). We choose here the sum of the p_{T} of the leptons and the jets called St as the VOI. We can see Figure 2 that the signal shape (in red-squared above the stacked histogram) is shifted to a higher p_{T} with a maximum at 600GeV compared to the background (in green for the top processes, orange for the ttX processes and blue for the diboson processes) with a maximum at 500GeV. St is a valid VOI as the behaviour of the signal and the background is different but the background is too large for the signal to be clearly visible on top of the systematic uncertainties. We need to control more specifically the different background processes by determining their own shapes thanks to CRs.

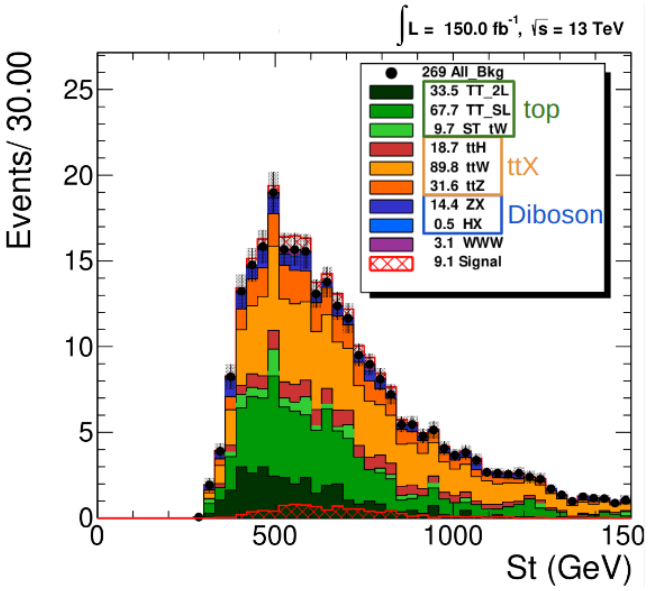

Figure 2: St distribution after the full selection. The signal in red-squared has a maximum at 600GeV and the background (green for the top processes, orange for the ttX processes and blue for the diboson processes) a maximum at 500GeV but the signal is still barely visible.

Control Regions

The goal here is to define the background shape in the CRs where the different background processes are pure and apply it in the Signal Region (SR) to extract the signal shape for the VOI. Let's note that we must verify that the background shape is the same in the SR

and in the CRs for this method to work. We must also check if each background has a different shape in the SR in which case independent CRs for the shape estimation are needed for each background. Considering the Figure 2 we can neglect the diboson processes and the single top process ST_tW in the top processes for the rest of this work. The different ttX processes (ttH, ttW and ttZ) have the same shape in the SR so we only need one global CR for them. The dileptonic and semileptonic $t\bar{t}$ processes in top processes have two different shapes in the SR so we need 3 CRs in total to determine the overall background shape. A simple way to define the CRs is to invert one cut to define a region enriched with a certain background and extract its shape:

- the ttX processes: we will invert the Cut 3 since these backgrounds have a quark top decaying into three jets.
- the dileptonic $t\bar{t}$ process: we will invert the Cut 0 by asking exactly two OS leptons.
- the semileptonic $t\bar{t}$ process: the CR has still not been defined and the studies are ongoing: we will not consider it for the rest of this work.

For the ttX CR, the ttX processes are the main background (63.0%). The semileptonic $t\bar{t}$ process is not negligible (27.6%) but we will not consider it. The dileptonic $t\bar{t}$ process and the signal contamination are negligible so we can confirm this CR for the ttX processes. The Figure 3 shows the normalized distribution of the ttX processes for the VOI St in the SR (in black) and the ttX CR (in purple). The two shapes are compatible uncertainties included: the background estimation method with a CR is valid for the ttX processes.

For the dileptonic $t\bar{t}$ CR, the dileptonic $t\bar{t}$ process is the main background (92.1%). The semileptonic $t\bar{t}$ and ttX processes and the signal contamination are negligible so we can confirm this CR for the dileptonic $t\bar{t}$ process. The Figure 4 shows the normalized distribution of the dileptonic $t\bar{t}$ process for the VOI St in the SR (in black) and the dileptonic $t\bar{t}$ CR (in red). The two shapes are not compatible but we lack statistics in the SR to confirm it: the full (2016-2018) Run2 statistics must be added up to have a definitive answer.

Summary

VLQs searches are crucial as they appear in many BSM models and can explain the hierarchy problem. We presented here the search for a VLQ T' decaying into a Higgs boson and a quark top in the dileptonic SS final state. The analysis strategy made up of a cut-based selection and the use of CRs for the background estimation is efficient but needs improvement to reduce and/or control the semileptonic $t\bar{t}$ background process. This is the last step before validating the analysis strategy and comparing the MC simulation with the full Run2 data.

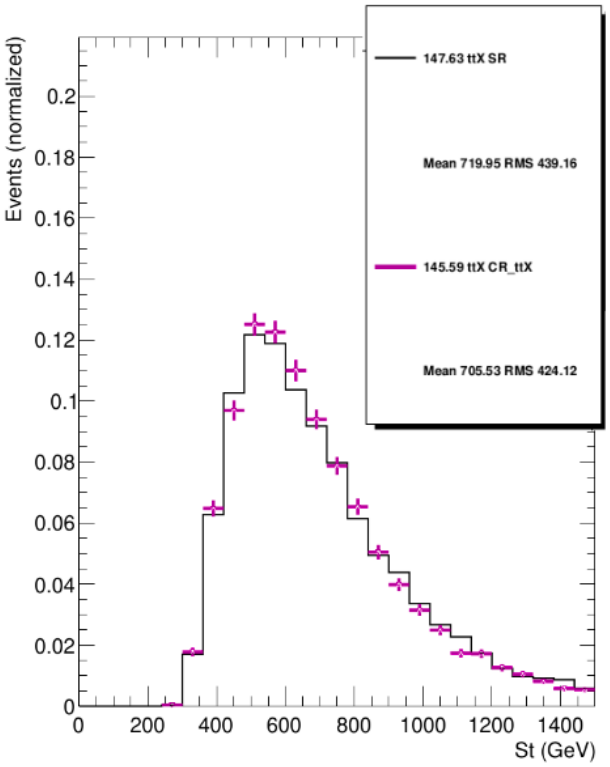

Figure 3: Normalized St distribution of the ttX processes in the SR (in black) and the ttX CR (in purple). The two shapes are compatible uncertainties included.

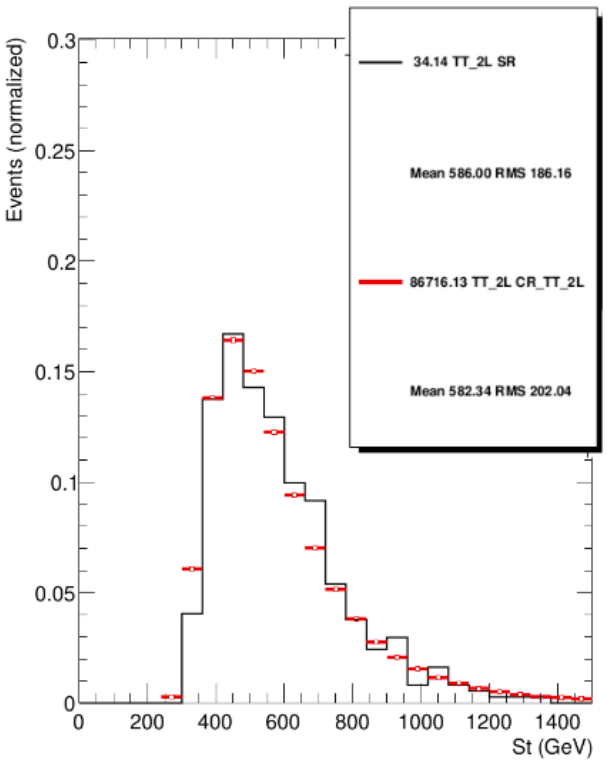

Figure 4: Normalized St distribution of the dileptonic $t\bar{t}$ process in the SR (in black) and the dileptonic $t\bar{t}$ CR (in red). The two shapes are not compatible but we need more statistics in the SR to have a definitive answer.

References

[1] Evans Lyndon, and Philip Bryant. "LHC machine." Journal of instrumentation 3.08 (2008): S08001.

[2] CMS Collaboration "The CMS experiment at the CERN LHC." Journal of instrumentation 3.08 (2008): S08004.

[3] CMS Collaboration "Performance of the CMS Level-1 trigger in proton-proton collisions at $\sqrt{s} =$ 13 TeV." Journal of Instrumentation 15.10 (2017): P10017.

[4] CMS Collaboration "The CMS trigger system." Journal of Instrumentation 12.01 (2017): P01020.

[5] CMS Collaboration "Particle-flow reconstruction and global event description with the CMS detector." Journal of Instrumentation 12.10 (2017): P10003.

[6] CMS Collaboration "Performance of the CMS muon detector and muon reconstruction with proton-proton collisions at $\sqrt{s} = 13$ TeV." Journal of Instrumentation 13.06 (2018): P06015.

[7] CMS Collaboration "Description and performance of track and primary-vertex reconstruction with the CMS tracker." Journal of Instrumentation 9.10 (2014): P10009.

[8] CMS Collaboration "Particle-flow reconstruction and global event description with the CMS detector." Journal of Instrumentation 12.10 (2017): P10003.

[9] CMS Collaboration "Performance of reconstruction and identification of τ leptons decaying to hadrons and ν_τ in pp collisions at $\sqrt{s} = 13$ TeV." Journal of Instrumentation 13.10 (2018): P10005.

[10] CMS Collaboration "Jet energy scale and resolution in the CMS experiment in pp collisions at 8 TeV." Journal of Instrumentation 12.02 (2017): P02014.

[11] CMS Collaboration "Performance of missing transverse momentum reconstruction in proton-proton collisions at $\sqrt{s}=$ 13 TeV using the CMS detector." Journal of Instrumentation 14.07 (2019): P07004.

[12] CMS Collaboration "Observation of a new boson at a mass of 125 GeV with the CMS experiment at the LHC." Physics Letters B 716.1 (2012): 30-61.

[13] ATLAS Collaboration "Observation of a new particle in the search for the Standard Model Higgs boson with the ATLAS detector at the LHC." Physics Letters B 716.1 (2012): 1-29.

[14] Higgs Peter W. "Broken symmetries and the masses of gauge bosons." Physical Review Letters 13.16 (1964): 508.

[15] Chaichian Masud, Ricardo Gonzalez Felipe, and Katri Huitu. "On quadratic divergences and the Higgs mass." Physics Letters B 363.1-2 (1995): 101-105.

[16] Cacciapaglia Giacomo, et al. "Heavy vector-like top partners at the LHC and flavour constraints." Journal of High Energy Physics 2012.3 (2012): 1-45.

[17] Buchkremer Mathieu, et al. "Model-independent framework for searches of top partners." Nuclear Physics B 876.2 (2013): 376-417.

[18] Okada, Yasuhiro, and Luca Panizzi. "LHC signatures of vector-like quarks." Advances in High Energy Physics 2013 (2013).

[19] Beauceron Stéphanie, et al. "Fully hadronic decays of a singly produced vectorlike top partner at the LHC." Physical Review D 90.11 (2014): 115008.

[20] https://pdg.lbl.gov/2022/tables/contents_tables.html

[21] CMS Collaboration "Electron and photon reconstruction and identification with the CMS experiment at the CERN LHC." Journal of Instrumentation 16.05 (2021): P05014.

[22] Heller Ryan Edward "A search for supersymmetry with the CMS detector in the single-lepton final state using the sum of masses of large-radius jets." University of California, Santa Barbara, 2018.

Jet Calibration and Search for Vector-Like Quarks decaying into top+Higgs in hadronic final states using Run2 CMS data with Neural Networks

Jieun Choi

Institut de Physique des Deux Infinis, UMR 5822, IN2P3, CNRS Villeurbanne, France

Abstract — The discovery of the Higgs boson completes the standard model. However, There are remaining questions that cannot be explained in the standard model, and that could be solved by extending it with the presence of Vector-Like quarks. A dedicated analysis for the search of Vector-Like T' was performed with the 2016 dataset collected by the CMS experiment, and found an excess over the background-only hypothesis in the full hadronic final state. In this article, we investigate the ongoing analysis on search for single produced Vector-Like T' increasing the sensitivity using neural network. Jets are a fundamental object in this analysis, and we detail how their calibration are derived in the CMS experiment.

Introduction

The Large Hadron Collider (LHC) is producing numerous particle physics phenomena by colliding proton bunches. The two general purpose detectors in LHC, Compact Muon Solenoid (CMS) and A Toroidal LHC Apparatus (ATLAS) experiments have contributed to complete the standard model from the discovery of Higgs in 2012 [1, 2]. But there are still various phenomena that cannot be explained by the current standard model such as hierarchy problem between weak force and gravity. The Vector-Like Quark (VLQ) [3] is introduced as one of the candidates for new physics extending our physics horizon beyond the standard model explaining the hierarchy problem. Search for VLQ will provide valuable input for evaluating many underlying models that explain the stabilization of the Higgs boson mass, offering a potential solution to the hierarchy problem, and so on.
In this article, the search for single produced vector-like T' decaying into top quark and Higgs boson in the full hadronic final state is covered explaining how the jet object is reconstructed and calibrated in the CMS experiment. A previous search for T' decaying into the top quark and Higgs boson in the hadronic final state was presented using the 2016 dataset. In this study, we compare the performance between the cut-based method which was used in the previous analysis, and neural network (NN), showing the benchmark for the study using full Run 2 (2016-2018) and Run 3 (2022-) datasets.

Jet in the CMS experiment

Compact Muon Solenoid

The CMS apparatus [4] is a multipurpose, nearly hermetic detector, designed to trigger on [5, 6] and identify electrons, muons, photons, and (charged and neutral) hadrons [7, 8, 9]. A global "particle-flow" (PF) algorithm [10] aims to reconstruct all individual particles in an event, combining information provided by the all-silicon inner tracker and by the crystal electromagnetic and brass-scintillator hadron calorimeters, operating inside a 3.8T superconducting solenoid, with data from the gas-ionization muon detectors embedded in the flux-return yoke outside the solenoid. The reconstructed particles are used to build leptons, jets, and missing transverse momentum (MET) [11, 12, 13].

Definition of Jet

When bunches of protons collide with each other, quarks and gluons are produced as a result of the proton interaction. But these cannot exist freely due to color confinement. While trying to keep forming color-neutral hadrons, they are making a shower structure from hadronization. This particle physics object is called a Jet. While simulations can reproduce the physical behaviour of individual particles in jet, their experimental measurement is limited by the spatial and energy resolution of the detectors which must be corrected for with a dedicated calibration procedure.

Jet Calibration in CMS

The CMS collaboration has several procedures to reconstruct Jets. First of all, it starts with detector clustering by grouping the energy deposit in a ECAL and a HCAL. The next step is building particle objects using the PF consists is linking all sub-detectors and subtracting additional energy from low-energy proton-proton collisions. From these PF objects, Jet and MET objects are reconstructed with a given cone size, and subsequently calibrated and tagged. Jet property such as Jet energy scale, resolution, and flavor is determined in this step. Eventually, the final object resulting from these procedures can be used in physics analysis. This article covers a shallow detail about the Jet Calibration part, which is dealing with Jet Energy Correction (JEC) and Jet Energy Resolution (JER). Especially JERC are established in factorized approach in CMS, as described in Figure 1[14].

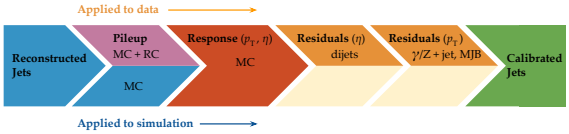

Figure 1: Jet Calibration procedure in CMS

The approach for determining JERC in the CMS consists of three main steps. In the first step, additional energy subtraction from collisions happening simultaneously is placed. Secondly, the non-linear response of the calorimeter from angular differences is compensated. In the last place, residual corrections from comparing data and MC are applied. The residual corrections are targeting a photon or Z boson + jet event to calibrate the jet clearly while reconstructing the object on the other side of a jet thanks to better precision in the other detectors for reconstructing photons in ECAL and muon in the muon chamber. After following the Jet calibration procedure, the uncertainty of the energy scale is known to the percent level. A better understanding of these scale uncertainties will allow us the most precise measurements as possible.

Jet response in the γ + jet channel in Run 3

In this section, the p_T balance method is covered which is one of the methods for determining the JEC for explaining ongoing work. In this study, we are using the p_T balance method in the photon + jet channel. The p_T balance method considers events with one photon emitted back-to-back with respect to one jet, so that the two objects are expected to have the same transverse momentum. The excellent precision on the photon energy determination can be used to precisely calibrate the jet energy. The p_T balance method uses mainly using two variables: response and alpha. The response is defined as transverse momentum (p_T) divided by photon p_T, and alpha is defined as sub-leading jet p_T divided by photon p_T. As we are expecting a photon-jet back-to-back event, in the ideal case, when the response is close to 1, alpha is going to be 0 as there is one leading jet and one photon expecting without any other jet. The distribution of the response observed in a sample of data collected in 2022 with photon triggers is shown in Figure 2.

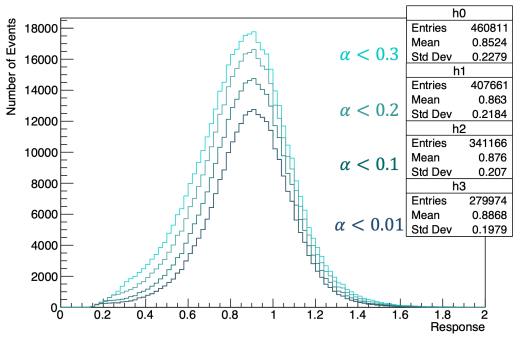

Figure 2: Jet Response distribution from p_T balancing method in Run 3 in CMS

The distributions in Figure 2 are shown with a different alpha variation where darker color refers to a lower alpha value. As a rough description for this distribution, the mean value of the distribution is moving to 1 with a lower alpha value, but not 1. An issue discovered subsequently with the HCAL caused a miscalibration of the jets and, consequently, a reconstructed energy about 70% lower than expected. This study still has much room for improvement with the MPF (Missing Transverse Energy Projection Faction) method which uses information of MET as the MPF method dominates precision in Run 2 data [15]. By doing this study we can understand data better in early stage so that when an anomaly is observed we can distinguish if the effect is coming from the detector problem or possibly new physics.

Search for Vector-Like Quarks in hadronic final states

Motivation

In particle physics, spin is one of the fundamental properties of particles, and it is used to define their handedness or helicity. If the direction of spin and motion are opposite, the particle is called "left-handed". The chirality of a particle is similar to the helicity, but it is determined by whether the particle transforms in a right or left-handed representation of the Poincare group. Chirality is Lorentz invariant but is not a constant of motion property, totally opposite to helicity. In the standard model, only a left-handed chiral quark can interact with the weak interaction. But "vector-like" quarks are not chiral, which means they can interact identically with the weak interaction as left-handed and right-handed versions. This search for VLQ will evalu-

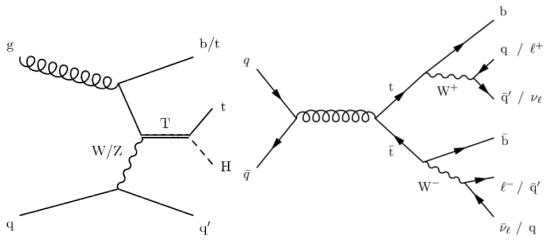

Figure 3: Feynman diagram of the signal process (T' decaying into top and Higgs, top) and background process ($t\bar{t}$ hadronic decay, bottom)

ate various underlying models such as composite Higgs models, extra dimensions, gauging of the flavor group, little Higgs models, and supersymmetric nonminimal extensions of the standard model [3]. This study is targeting single-produced vector-like T' particle decaying into the top quark and Higgs boson, where the top quark decays into 2 jets and 1 b-jet, Higgs boson decays into 2 b-jets. In the previous study presented with 2016 data from CMS, there was an excess at a T' mass of around 700 GeV [16]. This study will be performed to gain more significance by using NN techniques in Run 2 and Run 3 data for further study.

Analysis Strategy

The previous analysis was performed with the cut-based method. The cut-based method is categorizing events with a certain selection criterion on data. This study uses information from the cut-based method which was optimized based on kinematic observable for maximizing significance into NN. Two of the major background process of this study were $t\bar{t}$ decaying hadronically and QCD (multi-jet) as the final state contains many jets. This NN is trained for signal and background classification using MC sample provided by CMS. Since there are few events selected in the QCD sample, $t\bar{t}$ is chosen as one background against the signal process for evaluating the performance from the comparison between the cut-based method and NN. A signal with an invariant mass of 700 GeV is used as benchmark 3.

The structure of NN used for this study is a simple deep neural network (DNN). The hyperparameter used for building the DNN structure is the following: 3 layers with 100 nodes each with 100 epochs having 2048 batch size. For the optimizer, Adam is used and since we are dealing with signal and background binary classification, sigmoid and binary cross-entropy is used for activation and loss function respectively. NN structure is built with Keras with Tensorflow, an open-source library created by Google for machine learning. To maximize the number of training data but to have the same phase space with background, events selected for NN training must contain at least 6 jets, and at least 2 of these must be b-tagged. The 33 input features were selected based on the cut-based method. The details of input features are the following:

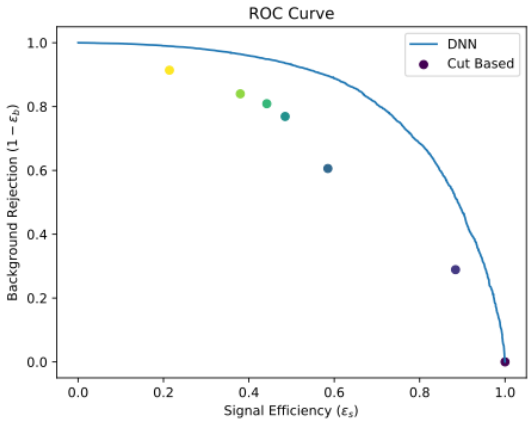

Figure 4: Receiver Operating Characteristic curve on the cut-based method (dots, lighter color with tighter selection) and NN method (line)

- number of (b-tagged) jet (2)
- angular positions of (b-tagged) jets in detector: η of 5 leading (b-tagged) jets (7)
- energy of (b-tagged) jets (7)
- Discriminant value from probability that a (b-tagged) jet is from b-quark (7)
- Variables from finding jet candidates from top and Higgs coming from T' using χ^2 method (selecting candidates from reconstruction of top quark, W boson and Higgs boson mass)
  - minimum (maximum) χ^2 value from reconstruction candidates (3)
  - angle between candidates (3)
  - invariant mass of candidates (2)
  - (relative value of) Scalar energy sum of candidates (2)

A NN should not learn specific statistical features of a data set as this would limit its actual performance on similar, statistically independent data sets. This overtraining was checked by comparing loss curves and output distribution from the training and validation set which was divided into 80% and 20% respectively from the input dataset. The result of the training is compared with the cut-based in Figure. 4

The Receiver Operating Characteristic (ROC) curve is showing the performance in terms of signal efficiency and background rejection. The performance was presented in the evaluation set which was not used for training. Starting from the baseline selection in the bottom right to top left in Figure. 4, DNN has better signal efficiency having the same background rejection. This study has much room for improvement as this trial was performed without hyperparameter optimization, and the number of the signal data was constrained to the MC sample of T' having 700 GeV of invariant mass. If we study optimization in structure with more signal samples, we can expect there will be more gain than this result.

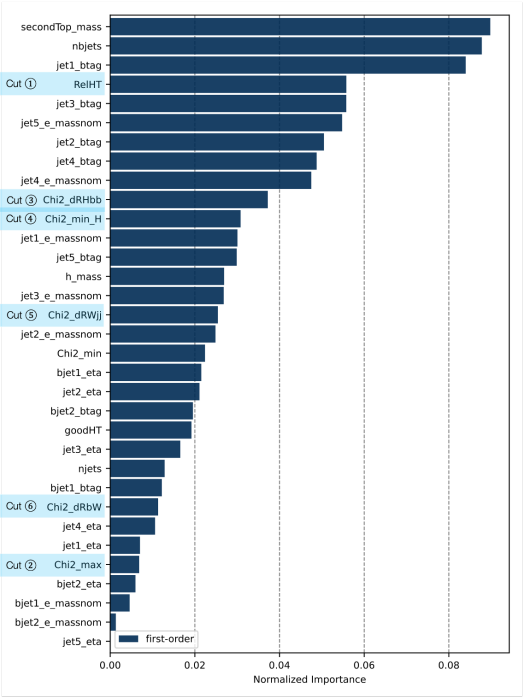

Figure 5: 1st order feature importance from taylor expansion method

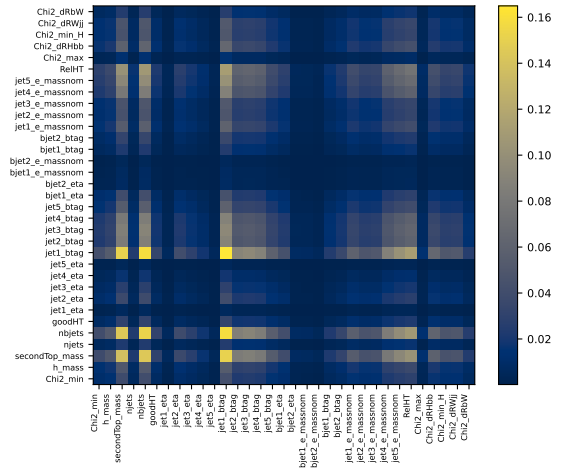

Figure 6: 2nd order feature importance from Taylor expansion method

Feature importance

While NN is a powerful tool to distinguish signals from the background, we do not know what is happening inside the procedure. To use NN wisely, one of the questions to be answered corresponds to the usage of the input features. Feeding information on various physics observables might confuse training. So we need to determine which physics observable is more meaningful or important than others, in the other words, we need to understand which input feature has the largest impact on the NN output node. This study uses the Taylor expansion to extract the feature importance. The Taylor expansion method for extracting feature importance is introduced to see the impact of each input feature on a model [17]. This method calculates gradients of output for each input feature. A function in TensorFlow `tf.GradientTape` allows us to track down the gradient per each training step by recording operations for automatic differentiation. Then we can extract the average gradient for each input feature in the output node. By following procedures, we can see how much each variable affects the training model.

The first and second order of feature importance is shown in Figure 5 and 6. The importance is calculated on the evaluation set and it is normalized by the sum of importance to be 1, to compare importance among input features. The first-order gradient refers to the physical location of the feature in the output function, i.e. weight w_i for x_i. In Figure 5 for instance the input feature "`nbjets`" - number of b-tagged jets are in the second place, which means that it has more effect on a model in training than "`njets`" - number of jets, which is placed in 24th among 33 input features. 6 selections that were used for the cut-based method were marked with captions in blue color. Some selections are having even lower influence than the other lower level features such as "`jet5_e_massnom`" - the energy of the 5th jet normalized by the T' mass.

The second order gradient refers to a gradient of each element of the source to the target, i.e. weight w_{ij} for feature $x_i \times x_j$. It is shown as hessian matrices. Unlike the correlation matrices, when the importance value of a feature is larger in this matrix, it means it is more important than others. This shows how much the combination of two input features influences the training model. In Figure 6, the feature "`nbjets`" is affecting the other features as well. From this information, better performance and fewer resource requirements are expected by getting rid of some input features which might make confusion.

Conclusion

In this article, the brief methodology on how the jet calibration is performed and how important it is in CMS is covered. If we can manage the precise calibration, it will be propagated into more precise measurements in various studies. This will enable a more precise study so that we can approach analysis beyond the standard model searches such as VLQ. Vector-like T' have been analyzed to evaluate various physics models and found an excess in result with the 2016 dataset. In the further study, we are going to use the NN technique to increase sensitivity while we demonstrated a better signal efficiency in the same background rejection in comparison to the cut-based method and NN without any optimization. With a better understanding of the jet object and NN technique with more statistics in Run 2 and 3 data, we expect to have better gain in the search for VLQ in the future.

References

[1] The CMS Collaboration, "Observation of a new boson at a mass of 125 GeV with the CMS experiment at the LHC". Physics Letters B 716.1 (2012): 30-61.

[2] The ATLAS Collaboration, "Observation of a new particle in the search for the Standard Model Higgs boson with the ATLAS detector at the LHC". Physics Letters B 716.1 (2012): 1-29.

[3] Y. Okada, L. Panizzi, "LHC signatures of vector-like quarks", Adv. High Energy Phys. 2013 (2013) 364936.

[4] The CMS Collaboration, "The CMS experiment at the CERN LHC". *JINST*, 3:S08004, 2008.

[5] The CMS Collaboration, "Performance of the CMS Level-1 trigger in proton-proton collisions at $\sqrt{s} = 13\,\text{TeV}$". *JINST*, 15:P10017, 2022.

[6] The CMS Collaboration, "The CMS trigger system" *JINST*, 12:P01020, 2017.

[7] The CMS Collaboration, "Electron and photon reconstruction and identification with the CMS experiment at the CERN LHC" *JINST*, 16:P05014, 2021.

[8] The CMS Collaboration, "Performance of the CMS muon detector and muon reconstruction with proton-proton collisions at $\sqrt{s} = 13$ TeV " *JINST*, 13:P06016, 2018.

[9] The CMS Collaboration, "Description and performance of track and primary-vertex reconstruction with the CMS tracker"*JINST*, 9:P10009, 2014.

[10] The CMS Collaboration, "Particle-flow reconstruction and global event description with the CMS detector" *JINST*, 12:P10003, 2017.

[11] The CMS Collaboration, "Performance of reconstruction and identification of τ leptons decaying to hadrons and ν_τ in pp collisions at $\sqrt{s} = 13$ TeV" *JINST*, 13:P10005, 2018.

[12] The CMS Collaboration, "Jet energy scale and resolution in the CMS experiment in pp collisions at 8 TeV" *JINST*, 12:P02014, 2017.

[13] The CMS Collaboration, "Performance of missing transverse momentum reconstruction in proton-proton collisions at $\sqrt{s} = 13\,\text{TeV}$ using the CMS detector" *JINST*, 14:P07004, 2019.

[14] The CMS Collaboration, "Jet energy scale and resolution measurement with Run 2 Legacy Data Collected by CMS at 13 TeV" 2021. [Online]. Available: http://cds.cern.ch/record/2792322

[15] The CMS Collaboration, "Jet energy scale and resolution performance with 13 TeV data collected by CMS in 2016-2018" 2020. [Online]. Available: https://cds.cern.ch/record/2715872

[16] The CMS Collaboration, Search for electroweak production of a vector-like T quark using fully hadronic final states. *J. High Energ. Phys.* **2020**, 36 (2020).

[17] Wunsch, S., Friese, R., Wolf, R. et al., "Identifying the Relevant Dependencies of the Neural Network Response on Characteristics of the Input Space". *Comput Softw Big Sci* **2**, 5 (2018).

Searches for CP symmetry violation in the top quark sector with CMS at the LHC, and the tracker Endcap upgrade for the High Luminosity LHC

Christopher Greenberg

Univ. Lyon, Univ. Claude Bernard Lyon 1, CNRS/IN2P3, IP2I Lyon, F-69622, Villeurbanne, France.

Abstract — The Standard Model (SM) is unable to explain the predominance of matter over antimatter in our present universe. Matter and antimatter are linked by a CP-symmetry transformation, and most scenarios for baryogenesis require a new source of CP symmetry breaking. An effective field theory (EFT) will be used to describe CP-symmetry violation, which will be searched for by analyzing the production and decay of single top quark in the t-channel with CMS at the LHC. A phenomelogy study is conducted to assess the impact of the EFT on the production and decay of the single top quark. The CMS tracker Endcap will be upgraded to sustain the high radiation environment of the High Luminosity LHC (HL-LHC), a project called TEDD (Tracker Endcap Double-Discs). The TEDD is composed of several Dees, which are the mechanical structures that holds the detection modules. In this work, we analyze metrological properties of the Dees and prepare for the future Dee production.

Introduction

The Standard Model (SM) does not explain the predominance of matter over antimatter in the observable universe. New sources of CP symmetry violation beyond the Standard Model (BSM) are required. Currently, the energy scale involved in new physics could possibly be unattainable in accelerator experiments, nevertheless, by searching for deviations from the SM in data precision measurements we could be able to probe it, with the help of the effective field theory (EFT). EFT studies require a lot of data because they require high precision. An improvement on the current LHC is needed for these studies. The High-Luminosity Large Hadron Collider (HL-LHC) project aims to increase the integrated luminosity by ten beyond the LHC design value. An upgrade of the CMS tracker detector is necessary to sustain higher radiation levels and the ability to trigger data acquisition on events with high momentum tracks. The remainder of this report is organized as follows. In section II we present a phenomenological study of the impacts of EFT operators in production and decay of the single-top quark process through the usage of Monte Carlo simulations. In part III, we present results on metrology measurements of the main structure of the CMS Tracker Endcap Double-Discs (TEDD), called a Dee.

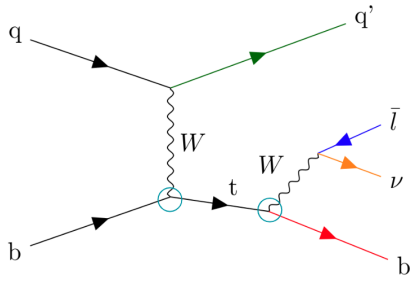

Figure 1: Example of single top quark t-channel Feynman diagram. Here, q represents an up or antidown quark, q' being the spectator quark represents a down or antiup quark. b and t are bottom and top quarks, and the lepton from the W decay can be an electron e or a muon μ. The presence of a lepton in the W decay implies the creation of a neutrino ν.

CP violation with top quark

Single Top Quark process

The heaviest known elementary particle is the top quark, which is about as heavy as a gold atom. The top quark is a third generation fermion within the SM. The enormous mass will have several implications regarding the dynamics of the top quark production and decay:

- Coupling with the Higgs boson is close to the unit.
- Its lifetime $\mathcal{O}(10^{-25}s)$ is smaller than its hadroni-

sation time-scale $\mathcal{O}(10^{-24}s)$ and its depolarisation timescale $\mathcal{O}(10^{-21}s)$ [1]

The production of single top quarks at the LHC takes place via electroweak interaction and has, for this reason, a smaller cross section compared to top quark pair production ($t\bar{t}$) at the LHC. We are interested in single-top quark process rather than $t\bar{t}$ production because single-top is more sensitive to CP violation. The study of the single-top process has the added benefit of holding the same vertex (**Wtb** vertex) at production and decay, as circled in blue in Fig. 1. The **Wtb** vertex is sensitive to CP violation effects. We will use the LHC as a top quark production machine.

Effective Field Theory

EFT is a tool to describe new interactions arising at a given energy scale in a model independent way without explicitly giving the underlying theory beyond the SM. The EFT Lagrangian density writes:

$$\mathcal{L}_{eff} = \mathcal{L}_{SM} + \sum_i \frac{C_i}{\Lambda_i^2} O_i + h.c. \quad (1)$$

Each term of the effective Lagrangian represent different contribution to the dynamics of the physical system. Contributions are encoded by dimensionless coupling parameters C_i called Wilson coefficients (for the remainder of this report, we will refer to them as EFT coefficients). O_i are EFT operators with a higher mass dimension than the SM ones. EFT can be interpreted as an expansion on energy scales Λ_i of the SM Lagrangian. The main goal of our study is to constrain 6 EFT coefficients, 3 of them violating CP, and impacting to the **Wtb** vertex in single top quark production and decay. The EFT operators linked to the 6 EFT coefficients of interest are:

$$O_{tW} = (\bar{q}\sigma^{\mu\nu}\tau^I t)\tilde{\varphi}W^I_{\mu\nu} \quad (2)$$

$$O_{bW} = (\bar{q}\sigma^{\mu\nu}\tau^I b)\tilde{\varphi}W^I_{\mu\nu} \quad (3)$$

$$O_{\varphi tb} = (\tilde{\varphi}^\dagger iD_\mu\varphi)(\bar{u}_i\gamma^\mu u_j) \quad (4)$$

The notation and normalization were chosen in accordance to reference [2]. We have 6 parameters to constrain since EFT coefficients are complex numbers. CP violation is interpreted as a non zero value of the imaginary parts of these EFT coefficients.
We begin by performing a phenomenological study to assess the sensitivity of kinematic variables to the 6 EFT coefficients.

Kinematic variables

A coordinate system (Fig. 2) is defined in the top quark rest frame for the remaining of the phenomenological analysis. The $\hat{z}$ axis is chosen in the direction of the $W^\pm$ boson, $\hat{W} = \hat{z}$. To define the $\hat{y}$ axis we use the spectator quark direction $\hat{p_s}$ as follows: $\hat{y} = \hat{p_s} \times \hat{W}$. The lepton momentum $\hat{p_l^*}$ is characterized by the polar

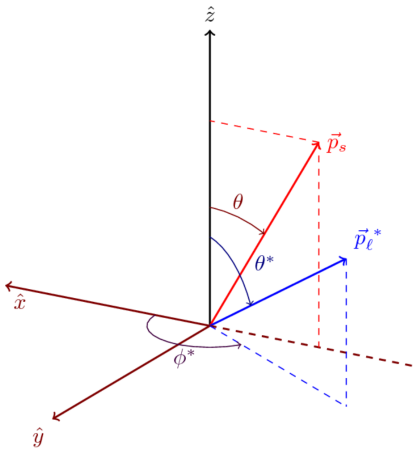

Figure 2: Definition of the right-handed coordinate system with $\hat{x}$, $\hat{y}$ and $\hat{z}$

angle θ^* and the azimuthal angle ϕ^*. The angle θ indicates the direction of the spectator quark momentum. The coordinate system is the same as in reference [3] and motivated by the sensitivity of the defined angular distributions to the effects of the EFT operators O_{tW}, O_{bW}, and $O_{\varphi tb}$. To measure CP violation we must measure the differential cross section as a function of ϕ^*, θ and θ^* and interprete the results within this EFT context.

Sample generation and Reweighting

We generate single top quark t-channel Monte Carlo (MC) samples at leading order (LO) with MadGraph5_aMC@NLO (MG5) [4]. The hadronization is performed using PYTHIA8 to obtain samples at generator level. We have a 6 dimension parameter space. The 6 axes of such space represent all the possible values that we allow the EFT coefficients to take. We include EFT effects at production and decay of single top quark t-channel. In order to fill as much of the relevant parameter space we use the reweighting method. Reweighting allows different regions of the parameter space to be probed with a single Monte Carlo sample. It is important to note that during reweighting the initial point (i.e. the starting point) and the alternative points (i.e. the reweight points) have some overlap. The SM cannot be taken as starting point, since the EFT operators lead to new vertices that are not part of the SM. Therefore, it is important to validate the reweighted samples. We compare reweighted samples to dedicated MG5 samples. As seen in Fig. 3 the reweighting procedure is validated for the set of parameter values chosen for the reweighting in this particular case. Both distributions overlap with each other within statistical uncertainties from the simulation. For this study, we generated 729 reweighting points in the parameter space (including the SM).

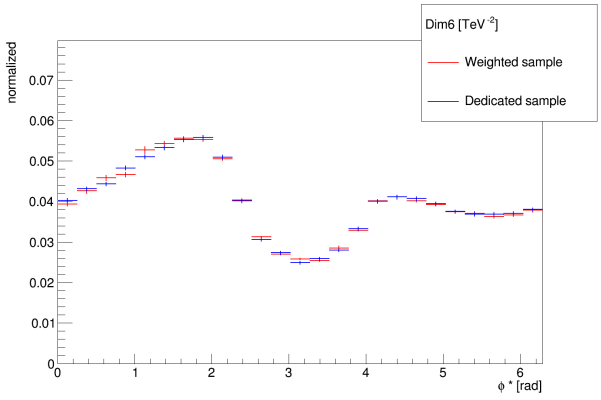

Figure 3: Example of ϕ^* distribution comparing weighted sample against dedicated sample at a non SM point in the parameter space

Results: EFT effects on kinematic variables

Parton level

Physical objects contributing to the hard interaction before hadronization are referred to as parton level. Using the samples including EFT weights we plot the ϕ^* distribution after event selection and compare several points in the parameter space at parton level with non zero imaginary EFT coefficients values. The distribution shape changes with the value of the EFT coefficients. In Fig. 4 the SM distribution is symmetric at $\phi^* = \pi$, it describes the behavior of the lepton's direction on the XY plane from Fig. 2 as the same on $[0, \pi]$ and $[\pi, 2\pi]$. The distribution is asymmetric on non SM points. CP-violation can be measured on this reference frame using such angles.

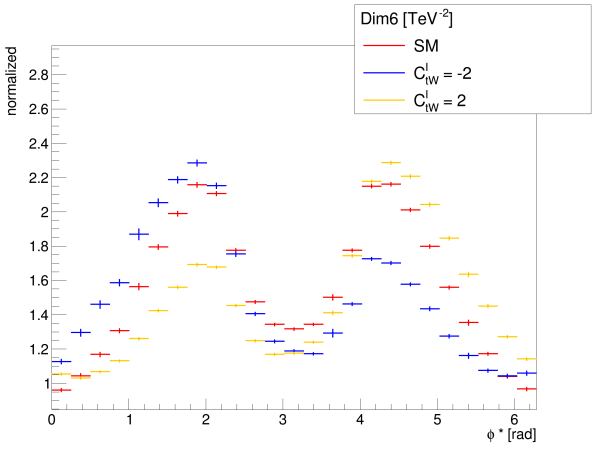

Figure 4: Example of ϕ^* distribution at parton level

Generator level

Parton showering and hadronization for the samples is performed with the PYTHIA8 generator. We reconstruct the top quark 4-momentum, ignoring the neutrino p_z such as to mimic the particles which would be reconstructed in the detector. In order to validate the sample, we test it against the CMS official single top quark t-channel sample generated with POWHEG+PYTHIA. We will use the SM point as the control point. As seen in Fig. 5, the distributions do not overlap. This may be due to the fact that the samples generated for this study are at Leading Order (LO) precision; as for the official CMS samples are at Next to Leading Order (NLO) precision. This discrepancy is, at the moment, under investigation. The proposed solution is to add an additional jet at Matrix Element level (parton level) to reproduce the NLO.

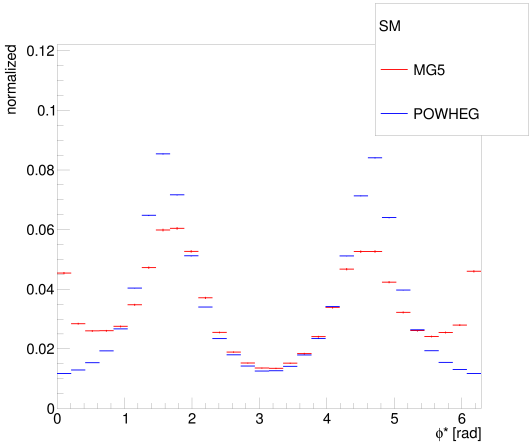

Figure 5: Example of ϕ^* distribution at generator level

Conclusion

Current theories are unable to explain the asymmetry between matter and anti matter in the observable universe. In order to provide an explanation to this phenomena, a phenomenological study is conducted to assess CP violation impact on single top quark t-channel process in an EFT context. The future analysis will use the full LHC Run2 datasets. Current investigation is ongoing regarding the discrepancy observed at generator level. The analysis using data taken at LHC Run2 is under work.

CMS tracker upgrade

Future CMS tracker

The future CMS tracker will consist of a little over 13000 silicon detector modules. The tracker has a cylindrical shape, the inner radii (500mm around the beam axis) will be instrumented with Pixel strip (PS) detection modules. The outer radii will be occupied by two strip (2S) detection modules. The modules will be mounted on mechanical structures called 'Dees'. Modules are installed at specific points given by the insert positions on the Dee. A disk is made of two Dees, and five double-disks are arranged togheter to compose the

Tracker Endcap Double-Disks (TEDD). The design requires a cooling system at $-35°C$ using CO_2 at phase transition for optimal cooling of the detection modules. A schematic of the new tracker can be seen in Fig. 6

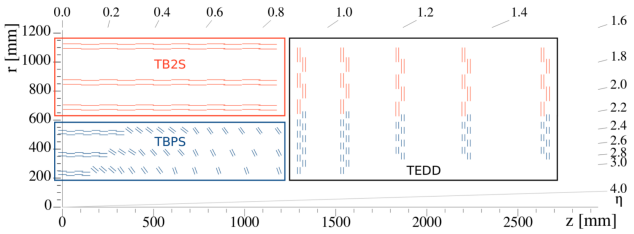

Figure 6: Layout of the future tracker of the CMS experiment. In red: 2S detection modules. In blue: PS detection modules

Metrology Measurements

The metology measurements presented in this report were taken from a Dee prototype produced by the end of 2019, at IP2I, Lyon.

Measuring Dee planarity

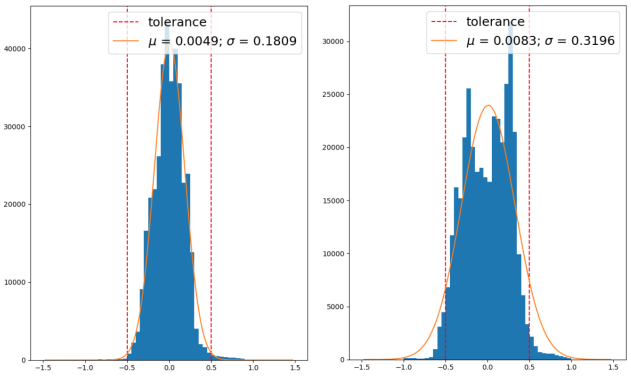

Figure 7: **Left**: Distribution of the distance between measured points and fitted plane in [mm]. **Right**: Distribution of the distance between measured points to nominal plane in [mm]. The Y-axis represents the number of points taken with the laser scan.

A laser scan of the surface was performed to verify the flatness of the Dee. We performed a plane fit from the data using a reduced chi-square method. Fig. 7 shows the distance between the measured point and the fitted plane against the distance between the measured points and the nominal plane. We can see an improvement on the width of the distribution using a fitted plane rather than the nominal plane. With these results we have a better perspective on the true flatness of the Dee, since there can be a displacement angle between the nominal plane and the Dee's surface. The red line in Fig. 7 indicates the tolerance on the Dee's surface. We can see that measurements respect the tolerance and the Dee is sufficiently flat to support detection modules at the integration step.

Ability to mount modules

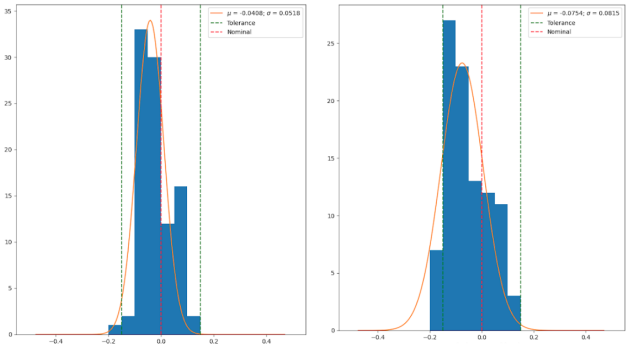

Figure 8: Distributions of the insert positions to mount 2S modules on the XY plane (i.e. the Dee's surface plane). **Left**: Nominal Y - Measured Y [mm]. **Right**: Nominal X - Measured X [mm]. The tolerance line (in green) indicates the limiting values between which measurements must lie in to be acceptable.

Fig. 8 and 9 allows us to assess the ability to mount the detection modules on the Dee. The distributions show the difference between the nominal x and y values against the measured x and y values of the inserts. As we can see, almost every value is inside the tolerance. The 2S and PS modules can be mounted on the Dee.

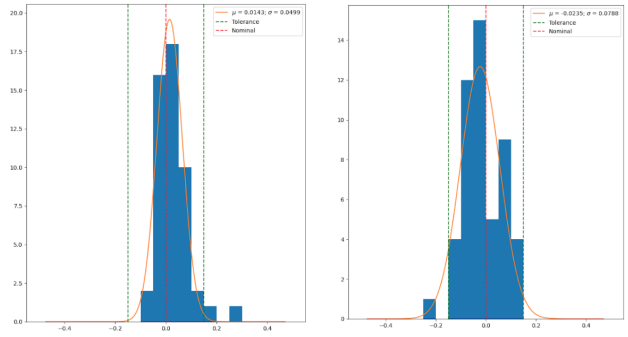

Figure 9: Distributions of the insert positions to mount PS modules on the XY plane (i.e. the Dee's surface plane). **Left**: Nominal Y - Measured Y [mm]. **Right**: Nominal X - Measured X [mm]. The tolerance line (in green) indicates the limiting values between which measurements must lie in to be acceptable.

Conclusion

In conclusion, the metrology tests serve as preliminary study to verify how the mechanical structure behaves. An analysis framework was designed to be applied to future Dee's. The main goal of this study is to test if the Dees are capable of holding the detection modules and if the Dees can be mounted together into double-disks while respecting the volume allowed to the TEDD. Production of 24 Dees will start at the end of 2023. The metrology analysis framework will be used to analyse all future Dees.

References

[1] I. Bigi et al. 'Production and decay properties of ultra-heavy quarks'. In: Physics Letters B 181.1 (1986), pp. 157-163. issn: 0370-2693.

[2] Cen Zhang. 'Single Top Production at Next-to-Leading Order in the Standard Model Effective Field Theory'. In: Physical Review Letters 116.16 (Apr. 2016). issn: 1079-7114.

[3] M. Aaboud et al. 'Analysis of the Wtb vertex from the measurement of triple-differential angular at 8 TeV with the ATLAS detector'. In: Journal of High Energy Physics 2017.12 (Dec. 2017)

[4] J. Alwall et al. The automated computation of tree-level and next-to-leading order differential cross sections, and their matching to parton shower simulations. In: Journal of High Energy Physics 2014.7 (July 2014). issn: 1029-8479.

Search for new heavy stable charged particles with the CMS experiment

Raphael Haeberle

Institut Pluridisciplinaire Hubert Curien

Abstract — The search for new physics beyond the Standard Model is a central focus of modern particle physics research, with the direct search for heavy stable charged particles (HSCP) being one of its many components. In this paper, we review the current state of the search for HSCP, including the use of particle detector to search for the telltale signs of these particles, such as high ionization, or low velocities. We discuss our ongoing studies and results, as well as the importance of continued efforts in this field in order to further our knowledge of physics beyond the Standard Model

Introduction

The CMS [1] experiment at the Large Hadron Collider (LHC) is one of the main detectors used to study the properties of the subatomic world. Multiple important discoveries, including the Higgs boson, have been made by the CMS experiment, which remains at the forefront of the search for new physics. In this paper, we present an overview of the ongoing efforts to search for heavy stable charged particles using data collected by CMS during run II of the LHC (2^{nd} data taking period, 2015-2018). These particles, also referred as long-lived particles (LLP), are of great interest in the field of physics beyond the Standard Model, yet their search is challenging due to their long lifetime and unusual signatures, and also due to their low production rates. With the first data from run 3 already being analyzed and published, the focus of this study is on the analysis of data from run 2, highlighting the latest results and ongoing efforts to identify these elusive particles. We present a review of the current experimental constraints on heavy stable charged particles and the various techniques employed to search for these particles, with a specific emphasis on the direct search method. The analysis presented in this review is ongoing, with the final results set to be published in the upcoming months.

Scientifical context

The discovery of the Higgs boson in 2012 [2, 3] marked a major milestone in the field of particle physics, providing strong evidence for the validity of the EWSB mechanism embedded in the Standard Model. However, despite its success in explaining a wide range of phenomena, the Standard Model has several unresolved issues, such as the nature of dark matter, the imbalance between matter and antimatter in the universe, or the so-called hierarchy problem [4]. In light of these limitations, there is a pressing need to explore new physics beyond the Standard Model. One promising approach for doing so is the search for long-lived particles, whose existence have been postulated by several theories beyond the Standard Model, including supersymmetry, extra dimensions, and composite models [5, 6]. These theories offer potential solutions to some of the above mentioned issues.

After several years of unsuccessful research, the design of the analyses was shifted towards a focus on experimental signatures, rather than theoretical hypotheses. This approach allows for a more comprehensive search for long-lived particles, as it is not limited to a specific theoretical framework or model. One example of signature based search is the search for heavy stable charged particles. In the context of supersymmetry, the gluino particle can have an HSCP signature if it is long-lived. This prediction is of particular interest in the split supersymmetry scenario, due to the gluino's mass spectrum [7]. By utilizing various experimental signatures, this search is able to be more sensitive to a wider range of HSCP models. Additionally, this method allows for the discovery of HSCP that may not fit within the current theoretical frameworks and may lead to new discoveries in the field of physics beyond the Standard Model.

Long-lived particles discovery

There are various methodologies that scientists employ in their search for new physics, including the search for long-lived particles. Some examples include:

1. Direct searches : they involve looking for their direct production in high-energy proton-proton collisions. While direct search provide unambiguous

particle detection, they are limited to the energies reached by LHC. There are multiples categories within the direct search for particles : prompt searches, meaning the particle will decay within the detector, or long-lived, meaning that its decay products will either be displaced with respect to the primary vertex, or the decay happens outside the fiducial volume of the detector. Within the long-lived searches, there is again several different searches : direct detection, or displaced tracks, vertices and objects in general.

2. Indirect searches involve looking for the effects of these particles on other observed phenomena. These searches are based on the idea that long-lived particles could interact with the Standard Model particles in ways that would affect the production or decay rates of other particles, even if those particles are not produced directly in the collision. For instance in flavor physics, standard model deviations in processes involving b quarks could be signs of new physics, with charged higgs signatures. Some lower energy scale processes might involve the production of these particles within loops.

Overall, the search for new physics is a multifaceted endeavor that involves a combination of experimental searches, precision measurements, and theoretical predictions. By using a range of different approaches, scientists can work to uncover the fundamental mysteries of the universe and advance our understanding of the laws of nature.

A previous HSCP study has been performed [9], and limits on the masses of gluinos and staus have been determined.

Silicon tracker

The CMS experiment utilizes a silicon tracker, composed of several layers of detectors to measure the trajectories of charged particles produced in proton-proton collisions. These detectors are used to measure the precise position and momentum of charged particles, allowing for the reconstruction of the trajectories of these particles, and their vertices. The first layer, known as the pixel detector, is closest to the interaction point and has the highest resolution. It is composed of over 66 million pixels, each measuring 100x150 μm^2. The pixel detector is used to precisely measure the impact point of particles produced in the collision and to identify the primary vertex.

The following layers, known as the strip detector, are composed of micro-strips silicon sensors. These layers have a lower resolution than the pixel detector but cover a larger area, allowing for a more complete measurement of the trajectories of particles. The strip detector is used to measure the momentum of particles produced in the collision, as well as to identify the type of particle based on the specific patterns of energy deposition in the detector.

This information is used to reconstruct the properties of the particles and to identify them in the collision. The tracker also measures the deposited charge per hit, which is of most importance in the search for HSCP.

Experimental signatures

In the context of the search for HSCP, we consider two benchmark scenarios: stable gluinos and stable scalar sleptons. Gluinos are hypothetical particles that are predicted to exist by supersymmetry. They are bosons, meaning that they have integer-valued spin, and they are believed to be carrying the strong nuclear force. If they are stable, they could potentially be candidates for HSCP. The second type of signal consists of HSCP that behave like leptons. The minimal gauge mediated supersymmetry breaking (mGMSB) model is selected as a benchmark for lepton-like HSCP. Production of supersymmetric quasi-stable leptons $\widetilde{\tau}$ at the LHC can occur either directly or via the production of heavier supersymmetric particles (mainly squarks and gluino pairs) that decay and lead to one or more $\widetilde{\tau}$ particles at the end of the decay chain. If they are stable, they could also potentially be candidates for HSCP. Particles that exhibit such properties would have specific experimental signatures, as for instance :

1. Stable (long-lived) : Stable means that they will not decay within the detector.

2. Heavy : Such high masses will induce a ratio $\frac{p}{m} = \beta\gamma < 1$, therefore they live in a non ultra-relativistic regime, and are delayed compared to muons.

3. Charged : those particles will interact electromagnetically within the tracker, and deposit energy : $-\frac{dE}{dx} \approx \frac{1}{\beta^2}$ in the non ultra-relativistic regime. The higher the mass, the higher the $\frac{dE}{dx}$ as described above.

Signal selection

Trigger and event selection

The trigger system of the CMS experiment is a two-level system that performs real-time data selection and event saving. The first level (L1) trigger is a hardware-based system that quickly analyzes detector data and identifies events that meet predefined criteria, such as the presence of certain particles or patterns indicative of new physics. The process is carried out very rapidly, within 4 microseconds, to ensure minimal data loss from the high collision rate at the LHC. The second level, called high level trigger (HLT) is a software-based system that further refines the event selection using more detailed analysis, taking on average 150 ms to make the decision. This process is essential in the CMS experiment, enabling efficient identification and preservation of data from interesting events while disregarding non-relevant collisions.

The expected yield of gluinos produced during run II of the LHC can be estimated (upper bound) from the limits on their cross-sections determined in prior studies, to be around 150. This represents around $10^{-14}\%$ of events selected. By optimizing trigger performance (uncorrelated trigger combinations, new trigger development etc..), we can increase the sensitivity of our detection method. A previous study allowed an absolute gain of 10% in signal detection efficiency, by utilizing a combination of three orthogonal triggers (triggers based on non-correlated experimental signatures such as isolated tracks or missing transverse energy).

In addition to the real-time selection by the trigger system, offline preselection criteria are applied to further filter the data and retain only events of interest for our analysis : these criteria include the requirement for high-quality, isolated tracks.

Ionization variables in our analysis

The CMS tracker is capable of measuring ionization due to heavy charged particles passing through the entire detector, as they are expected to deposit more energy than minimum ionizing particles (MIPs) [8]. In practical cases, most relativistic particles (e.g., cosmic-ray muons) have mean energy loss rates close to the minimum, and are said to be MIPs.

We determine a dE/dx discriminator, G_i used to distinguish SM particles from HSCP candidates. G_i can take any value between 0 and 1, 0 being for a SM particle, and 1 an HSCP candidate :

$$G_i = \frac{3}{N} * \left(\frac{1}{12N} + \sum_{i=1}^{N} [P_i * (P_i - \frac{2i-1}{2N})^2] \right) \quad (1)$$

where N is the number of measurements in the silicontacker detectors, P_i is the probability for a minimum-ionizing particle to produce a charge higher or equal to that of the i-th measurement for the observed path length in the detector, and the sum is over the tracks measurements ordered in terms of increasing P_i. Figure 1 shows the distributions of the G_i discriminator on data, and on two Monte-Carlo simulations of HSCP.

The G_i discriminator is very robust against detector effects provided that those are also encoded in the templates used to extract the P_i probabilities. To account as much as possible for all detector effects we use separate templates as a function of sensor topology and path-length, for each data taking era. There were 14 different topologies for the strip detectors. In order to avoid signal contamination, the templates are derived in an orthogonal momentum region.

In addition, the dE/dx of a track is estimated using a harmonic-2 estimator I_h as following :

$$I_h = \left(\frac{1}{N_{85\%}} \sum_{i}^{N_{85\%}} c_i^{-2} \right)^{-\frac{1}{2}} \quad (2)$$

where c_i is the charge per unit path length in the

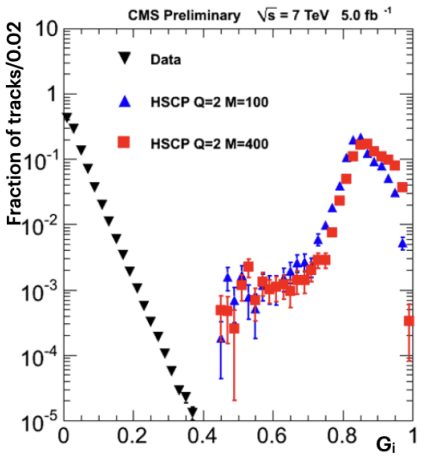

Figure 1: Distribution of G_i discriminator on data and on double-charged HSCP (Q=2e) for masses of 100 GeV and 400 GeV

sensitive part of the silicon detector of the i-th track measurement. The harmonic-2 estimator has units MeV/cm and the summation is over the 85% pixel and strip silicon detector measurements with the highest charge. Ignoring the 15% measurements with the lowest charge increases the resilience of the estimator against instrumental biases. This procedure is not necessary for G_i which is, by construction, robust against that type of bias.

Secondary collisions dependency

One way that pile-up (secondary collisions within an event) can influence the energy deposit estimator and discriminator is by causing an overestimation of the energy deposited in a given cluster. This can happen if the energy deposits from multiple clusters caused by multiple particles are not properly separated, and instead summed together as if they were from the same particle, thus leaving a single hit in the tracker, with in average twice the standard energy deposit. That can lead to highly ionizing particle signature, when it is in fact only due to a sum of effects. To mitigate the effects of pile-up, we added a third dependence to our G_i templates : the number of primary vertices which is an indicator of the overall multiplicity of the event. Figure 2 shows the overall shape of the discriminator as a function of the number of primary vertices, with and without the third dependence.

The mass spectrum method

Normalization with an ABCD method

The goal of the mass spectrum method is to derive the mass spectra of all the backgrounds in our analysis as well as the event yields. To perform that, we define three control regions and one signal region based on cuts on the uncorrelated variables G_i, the dE/dx discriminator, and p_T the transverse momentum. The signal region D corresponds to HSCP candidate with high

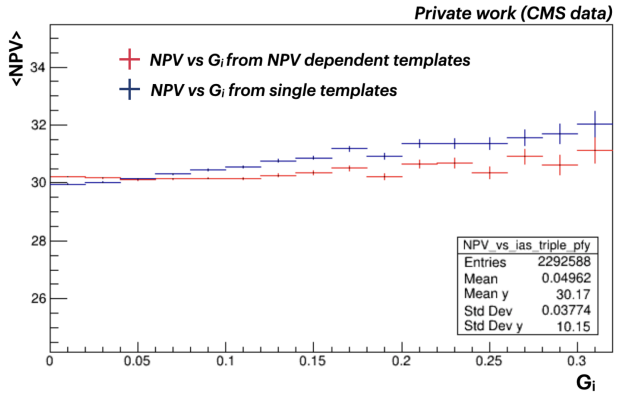

Figure 2: Effect of the mean number of primary vertices per event on the G_i discriminator

p_T and high G_i, and the control regions A,B and C respectively to candidates with low p_T and low G_i, to candidates with low p_T and high G_i, and to candidates with high p_T and low G_i values, as shown on figure 3.

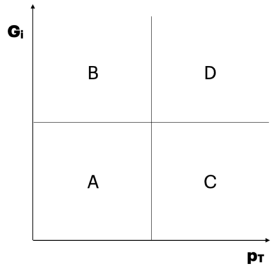

Figure 3: Definition of the control regions A,B and C, and of the signal region D

Event yields

The method predicts the normalisation (the number of events N) in the signal region D, based on the number of events of the control regions A, B and C, such as

$$N_D = N_B \times N_C / N_A \tag{3}$$

Shape of the mass distribution

The method predicts the shape of the mass distribution in the signal region D, based on information coming from control regions B and C. In order to do this shape prediction, templates are extracted from both regions B and C. The dE/dx estimator I_h is taken from region B, whereas the momentum p distribution from region C, allowing to compute the mass of the HSCP such as shown in figure 4. For Q = 1e particles, the mass can be determined using :

$$m = p \times \sqrt{\frac{I_h - C_{MIP}}{K}} \tag{4}$$

where K and C_{MIP} are empirical parameters extracted from data. The fit is performed in two steps, first we fit the C parameter on the pion line in the region of minimum ionization ($p \subset [3-5]$ GeV), then we fit the K parameter on the proton line, the region of low momentum and high ionization, with C fixed from the previous step. We then perform a cut-and-count analysis after applying a given mass cut in the signal region.

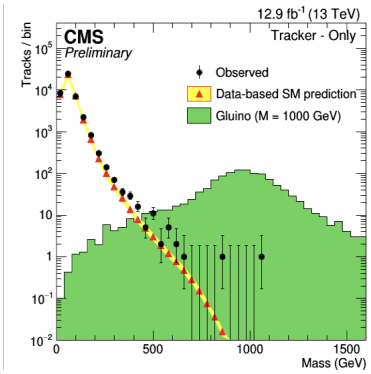

Figure 4: Predicted (red triangles) and observed (black dots) masses for HSCP candidates, obtained with a luminosity of 12.9 fb^{-1}. A Monte-Carlo Gluino signal (1000 GeV)

Results and interpretation

The analysis paper has not yet been made public as there is still ongoing work regarding the optimisation of the definition of the signal region D. We present the limit computation plot from the previous analysis [9]. A lot of changes have been implemented between 2016 and today, the change with the highest potential impact being the amount of data that is analyzed, which has an integrated luminosity two times bigger as compared to the previous publication.

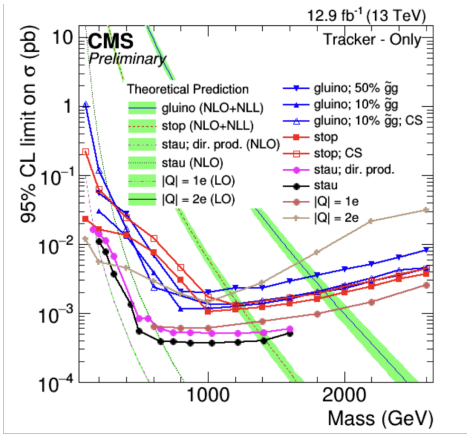

Figure 5: Cross section upper limits at 95% CL on various signal models for the tracker-only analysis at $\sqrt{s} = 13$ TeV

References

[1] CMS Collaboration, et al. The CMS experiment at the CERN LHC. Jinst, 2008, vol. 803, p. S08004. doi: 0.1088/1748-0221/3/08/S08004

[2] CMS Collaboration, et al. "Observation of a new boson at a mass of 125 GeV with the CMS experiment at the LHC", Phys. Lett. B 716 (2012) 30, doi:10.1016/j.physletb.2012.08.021

[3] ATLAS Collaboration, et al. "Observation of a new particle in the search for the Standard Model Higgs boson with the ATLAS detector at the LHC", Phys. Lett. B 716 (2012) 1, doi:10.1016/j.physletb.2012.08.020

[4] BHATTACHARYYA, Gautam. Hierarchy problem and BSM physics. Pramana, 2017, vol. 89, no 4, p. 1-3. doi:10.1007/s12043-017-1448-2

[5] CHEUNG, Kingman et KEUNG, Wai-Yee. Split supersymmetry, stable gluino, and gluinonium. Physical Review D, 2005, vol. 71, no 1, p. 015015. doi:10.1103/PhysRevD.71.015015

[6] CMS Collaboration, et al. Search for long-lived charged particles in proton-proton collisions at $\sqrt{s}$ = 13 TeV. Physical Review D, 2016, vol. 94, no 11, p. 112004. doi:10.1103/PhysRevD.94.112004

[7] ARKANI-HAMED, Nima, DIMOPOULOS, S., GIUDICE, G. F., et al. Aspects of split supersymmetry. Nuclear Physics B, 2005, vol. 709, no 1-2, p. 3-46. doi:10.1016/j.nuclphysb.2004.12.026

[8] QUERTENMONT, Loic. Particle identification with ionization energy loss in the CMS silicon strip tracker. Nuclear Physics B-Proceedings Supplements, 2011, vol. 215, no 1, p. 95-97. doi:10.1016/j.nuclphysbps.2011.03.145

[9] CMS Collaboration, et al. Search for heavy stable charged particles with 12.9 fb^{-1} of 2016 data. CMS-PAS-EXO-16-036, 2016.

[10] ATLAS Collaboration, et al. Search for heavy, long-lived, charged particles with large ionisation energy loss in pp collisions at $\sqrt{s} = 13$ TeV using the ATLAS experiment and the full Run 2 dataset. JHEP, 2022.doi:10.48550/ARXIV.2205.06013

Part III

Cosmology

session chaired by Julien MASBOU

Supernova cosmology with the Zwicky Transient Facility

Leander Lacroix

Laboratoire de Physique Nucleaire et des Hautes Energies de Paris (LPNHE), 75005 Paris, France

Abstract — Constraining the luminosity distance-versus-redshift relation using type Ia supernovae is one of the most sensitive probes of the nature of Dark Energy, through the measurement of its equation of state. Over the last 15 years, large surveys have produced high-quality type Ia supernovae samples in the redshift range $0.05 < z < 0.8$ and published the best constrains on w. The Hubble diagram is still notoriously under-constrained at high and low redshift, precisely where the sensitivity to w is the highest. This project is about populating the low-z part of the Hubble diagram with a sample of about 8000 nearby, cosmology-grade, supernovae discovered and followed-up by the Zwicky Transient Facility.

Introduction

At the end of the 20th century, two independent teams, using type Ia supernovae (SNe Ia) as luminosity distance indicators, announced that the Universe expansion is accelerating [1, 3], in contradiction with what would be expected if the Universe only contained matter. This result is commonly interpreted as the existence of some mysterious fluid, dubbed Dark Energy (DE), filling the Universe and pulling the structures apart. Since this discovery, observational evidences for DE using independent probes (study of the large scale structure, cosmic microwave background, ...) keep adding up [10]. This discovery led to ΛCDM, which with 6 parameters only is able to describe all cosmological observations. According to this model, the Universe is made up of 68% DE, 27% cold dark matter and only 5% of ordinary matter (baryons). DE is thought to drive the expansion acceleration and is modeled by the addition of the cosmological constant Λ in the Einstein equation of general relativity. The evolution of DE can be described through its equation of state $P = w\rho$ with P the pressure, ρ the density and w a dimensionless number characterizing the fluid. Determining constraints on this equation is a very active field of study within observational cosmology, and the ultimate goal of this work.

SNe Ia are one of the most sensitive and direct probe of cosmic acceleration [15]. By estimating their distances and redshifts, it is possible to map the Universe expansion history in what is called a Hubble diagram. By comparing it with predictions given by universe models of given constituents, it is possible to place constraints on the densities and equations of states of the constituents of the Univers. SNe Ia are called standard candles, that is, objects of at least uniform brightness, making it possible to precisely measure their distance. Furthermore, SNe Ia can be standardized bringing the dispersion in SN luminosities down to $\sim 15\%$. Given a large number of these objects, this dispersion can be reduced further by statistical power.

Currently, the Hubble diagram is well constrained in the medium redshift range [2], the low ($z \leq 0.15$) and high ($z \geq 0.8$) being notoriously difficult to map. However, it is at low and high redshift that probing for dark energy is the more sensible. The low redshift part is difficult to probe due to the low volume of nearby Universe available, which limits the number of SNe to discover. High redshift is difficult due to the faintness of the SNe, needing very large and costly earth or space telescope.

The Zwicky Transient Facility (ZTF) is a robotic survey of the northern sky employing a 48" ($\sim$ 1.2m) wide-field telescope at the Palomar Observatory in California, USA [7]. Its wide field of view, coupled with a fast acquisition cadence makes it ideal to study the nearby dynamic Universe. It is able to image the whole sky once every 3 nights. On-site field spectrographs ensure object classification of all discovered transients down to a luminosity threshold (corresponding to the peak luminosity of SNe Ia at a redshift of 0.1). All this makes ZTF ideal to detect and follow supernovae, which is one of its primary goal [11]. Until now, approximately 4000 SNe Ia have been spectroscopicaly identified, with a well sampled lightcurve in most cases. This sample is complete up to a redshift of $z = 0.06$, that is, most if not all SNe Ia have been detected and its amount is only limited by the low volume of available universe. This makes this sample as free as possible from selection biases and other sources of systematic error.

This SNe Ia dataset gives the possibility to fill in the low redshift part of the Hubble diagram and, combined with high redshift SNe (such as given by the 8m Subaru telescode [16]), can give strong constraints on the dark energy equation of state.

Precision SN Ia cosmology requires accurate photo-

metric flux measurements. As with every physical experimental measurements, photometry comes with its share of statistical and systematics uncertainties. The goal of this work is to develop a modern photometry pipeline to calibrate the ZTF SNe Ia lightcurves at the 0.2% level.

Given the large size of the ZTF dataset (6 PB of images, 250 TB only for SNe Ia), this work also prepare the advent of next generation large scale surveys such as the Large Survey of Space and Time (LSST) which will be performed at the future Vera Rubin observatory.

Calibrating SNe Ia lightcurves: a scene modeling approach

Since 2018, the ZTF survey is ongoing. Half of its expected statistics has been collected until the end of its phase II program.

Forced photometry

The survey pipeline routinely produce lightcurves for all ZTF transients. These lightcurves are computed using forced photometry [6]: this involves subtracting images in order to create a difference image. All exposures taken before the SN explosions and after the SN has faded are stacked into a reference image (also called OFF exposure). It is then subtracked from the images where the SN is happening (ON exposures). As the SN flux evolves with time, these changes appear in the difference image, on which flux measurement is performed.

Forced photometry is simple, robust and computationally efficient. However, one main caveat limit its use for precision cosmology. Since difference images does not contain any stars, calibrating the supernova flux on the surrounding stars (called tertiary stars) is impossible. This is incompatible with our 0.1% precision goal, as it increase the systematics and dispersion budget. Ideally, flux measurement of the SN and its surrounding tertiary stars should use the the same estimator. This is the main motivation for developing a new algorithm for lightcurve estimation.

Scene Modeling Photometry

Scene Modeling Photometry (SMP) involves constructing a detailed mathematical model of the supernova and the host galaxy that surrounds it. The model is then fit to the observed data to determine the best-fit parameters that describe the scene.

A SMP pipeline has been developed to process the complete ZTF spectroscopic SN Ia sample. It relies on the algorithm developed for SNLS [5] which has been extensively described and tested [4]. In this implementation, the parameters of the model are:

- SN position
- SN flux at each image
- Empirical galaxy profile (pixel matrix)

From the followup images of a given supernova, a reference image is defined from which computed measurements will be relative to. The reference is chosen as the image with the best seeing (measure of the blurring caused by the Earth atmosphere).

The model is defined as a maximum likelihood estimator. The flux model $M_{i,p}$ expected for image i at pixel p (located at x_p) is

$$M_{i,p} = R_i \left[f_i \, \phi(x_p - T_i(x_{\rm obj}) + G(T_i^{-1}(x_p)) \otimes K_i + S_i \right], \quad (1)$$

where f_i is the SN flux in image i, G the galaxy model (pixel map, assumed to be non-variable in time) and $x_{\rm obj}$ the SN position. Several other functions are determined before the fit: T_i defines a mapping in pixel coordinates from the reference image to image i and R_i the flux scale from reference image to image i, equivalent to a relative zero point (ZP) from the reference. S_i is the sky level of image i and ϕ_i its Point Spread Function (PSF) model (that is, the response of the instrument to a point like source such as a star). Finally, K_i is a convolution kernel to match the reference image PSF $\phi_{\rm ref}$, computed on the fly by the algorithm.

This model is compared to data using a least-square procedure

$$\chi^2 = \sum_i \sum_p w_{i,p} (M_{i,p} - I_{i,p})^2, \quad (2)$$

where $I_{i,p}$ is the image data and $M_{i,p}$ the model. As the Hessian can be analytically computed, Newton descent method is used as the fitting scheme, which guarantees quick convergence given good initial conditions.

The empirical galaxy model is trained on OFF images. The number of OFF images is defined as roughly 3 times the ON images before the SN and 3 times after, thus giving an accurate empirical galaxy model. The galaxy model G, the SN position $x_{\rm obj}$ and SN fluxes f_i (i.e, the lightcurve) are fitted at the same time.

This model is optimal from a statistical point of view by reaching the minimum variance bound set by the Cramer-Rao inequality.

Ingredients for SMP: preprocessing

Before fitting the SMP model, the functions T_i, ϕ_i and constants S_i, R_i need to be determined in preprocessing steps.

First, from ZTF science images, a sky level is computed (i.e, S_i) using SExtractor [12] and sources are extracted and identified (stars, galaxies, cosmics) using the moment method (stars clumps in a small area on the second order centered moments plane). Isolated stars then get used to train a PSF model (i.e, ϕ_i).

The PSF model has an analytical part (based on a Moffat distribution) complemented with an empirical part, at the same sampling than the image, to account for asymmetry and guiding errors. The PSF model linearly allows for spatial variations at the quadrant level.

Two quality cuts are applied to cleanup the data:

- Images with a seeing superior than 4 arcseconds
- Images with less than 150 isolated stars (leading to a bad PSF estimation)

The main SMP algorithm and several of the preprocessing steps are already implemented and used for the SNLS survey. However, the pipeline assembling and several key algorithms still need to be implemented.

Relative astrometry

Images need to be aligned to the reference image, that is, to determine a geometrical transformation T_i mapping pixels from the reference to a given image i. For simplicity and since this transformation is quasi linear, the mapping can be defined as a 2D polynomial of predetermined degree.

A robust approach is to project all the stars on the tangent plane centered on the host galaxy, and map polynomials t_i on the stars from image to the tangent plane 1. The final mapping from the reference image to an other image i can then be composed by

$$T_i = t_i \circ t_{\text{ref}}^{-1}, \tag{3}$$

which is efficient computationally wise as we are only dealing with polynomials. Thus, only t_i needs to be fitted and t_{ref} needs to be inverted (by doing an inverse fit from a grid on the tangent plane to pixels).

Tangent plane projection is done by matching identified isolated stars to the Gaia catalog [9, 8] which gives precise sky coordinates, then projected on the tangent plane defined by the Gnomonic projection G centered on the host galaxy. We find that 100% of the identified isolated stars are in the Gaia catalog, which is no surprise given the shallow depth of the ZTF survey.

Using order 5 polynomials, the algorithm is able to reach a 30 milliarcseconds (mas) floor precision i.e. transformed bright stars from image i are not further away than 30 mas in the reference image.

One could directly map from the pixel to sky space, however as this transformation is non linear, a big part of the polynomial higher order parts gets absorbed in this transformation, leading to imprecision.

Relative photometry

As the images in the SN sequence are acquired in different observing conditions (airmass, humidity, Moon phase, ...), their flux and sky level varies, thus giving different fluxes values at different times for a given non variable star. This effect is corrected by applying a Zero Point (ZP) on the object magnitudes to homogenize the luminosity level across the whole SN sequence. The ZTF pipeline provides an absolute ZP per image, however at an insufficient precision level to perform precision cosmology.

A robust approach, as for relative astrometry, is to anchor fluxes to the Gaia catalog. This can be done by fitting this linear model

$$m^{s,i} - m^{s,i}_{\text{Gaia}} = P(B^s_p - R^s_p) + ZP^i, \tag{4}$$

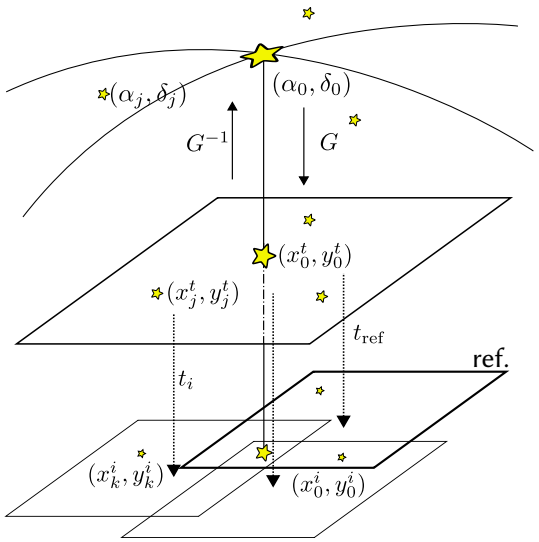

Figure 1: Illustration of the relative astrometry method. Bottom squares represent quadrants in pixel space. The middle layer the tangent plane centered on the SN and the top arcs, the skydome.

with s the star index and P the polynomial to account for star color $B_p - R_p$ non-linearity. Fitted parameters are thus one ZP per image and coefficients of the P polynomials. Given this absolute ZP anchored to the Gaia catalog, it is easy to get back a multiplicative constant used by SMP. Indeed, it can be shown that

$$R_i = 10^{-0.4(ZP_i - ZP_{\text{ref}})}. \tag{5}$$

One drawback of this method is the noise induced by filter conversion (Gaia and ZTF having widely different band pass filters), that is, the additional dispersion contribution given by the polynomial P. By using a catalog having closer matching filters or even a catalog built on ZTF should be less noisier.

Calibrating lightcurves: SMP of tertiary stars

One can assume observing conditions are similar between the SN and its surrounding stars.

Scene modeling is performed on the tertiary stars (with no host galaxy component) to get their lightcurves. After identification of variable stars (by looking at their χ^2), these stars can be compared to an external calibrated star catalog. By doing so, it is possible to express SN flux into standard stars flux units, homogenizing the whole SN survey.

Results

The pipeline described above has been assembled during my thesis and deployed at the CC-IN2P3 Computing Center (Lyon). I am currently using it to analyze the full ZTF SN Ia sample. Resulting lightcurves can then be compared to forced photometry 2. It is able to

process the whole 3700 SNe Ia sample, including tertiary stars lightcurve, in $\sim$ 3 days using 1500 CPUs.

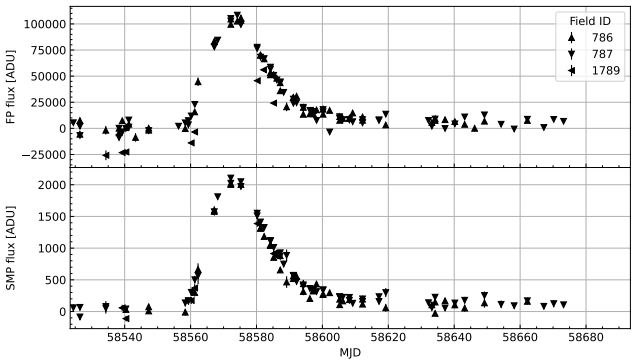

(a) ZTF19aanbojt - g band

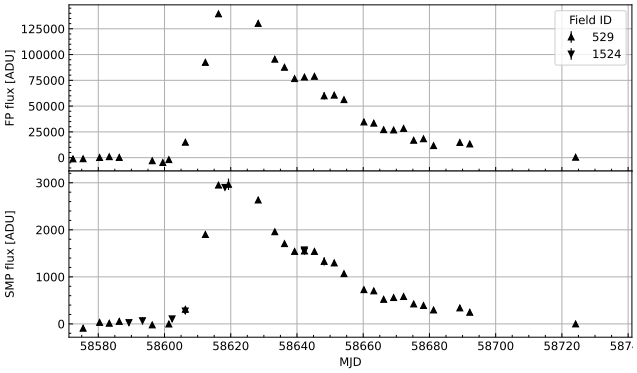

(b) ZTF19aaujiwc - r band

Figure 2: Lightcurve examples for several SNe Ia, comparing FP and SMP methods.

Future work

Calibration at the survey level

Currently, generated lightcurves flux are expressed as relative to the reference image. In order to be able to compare SNe within the sample or with other samples, flux need to be converted into a common magnitude system. This is done by comparing tertiary stars around the SN to a calibrated star catalog, as described previously. Such catalogs exists e.g, Pan-STARRS [13, 17, 14]. This induce color transformation noise due to band pass filter differences.

The ultimate solution is to use a precisely calibrated catalog acquired with ZTF, thus nullifying color transformation noise. Such a catalog is currently being designed. Until the release of the purely ZTF calibration catalog, I am using the Pan-STARRS full northern sky survey as my calibration anchor.

Mapping instrument non-uniformities

A substantial amount of engineering work is done to get a telescope optical system and its imager response as linear as possible. However, at the set precision goal, residual non-linearity impact lightcurve calibration, leading to a higher dispersion. These instrumental imperfections can be characterized by doing what is called a "starflat", that is, acquiring many images from a given field with a given dithering pattern so that a given star (with a given constant magnitude) ends up in different parts on the focal plane. By doing so, flux transmission variation across the focal plane, at the CCD level and and then a the pixel level can be characterized and accounted for when doing PSF photometry. These starflats show up to 2% level peak-to-peak non-uniformity.

Unexpected magnitude-asymmetry relationship

An unexpected effect was observed in which the asymmetry of the stamps collected for each isolated star was found to positively correlate with the star's magnitude. That is, fainter stars tends to be more skewed. This is problematic as it indicates that the PSF varies with magnitude, which goes against the expected linear relationship between the PSF and the star's flux. The effect is currently being analyzed in order to determine its cause. Fixes will be applied to the CCD readout chain and to the preprocessing stage of the analysis pipeline to correct at pixel-level images affected by this problem.

Conclusion

The next cosmological grade ZTF SNe Ia sample is bound to be released in the first quarter of 2023, containing 3700 SNe Ia. At the end of the survey, the final release will contain of the order of 6000 SNe Ia with an exquisite sampling. This is currently the largest SNe Ia sample ever. Combined with current samples and with high redshift ones from the Subaru telescope, the next generation Hubble diagram can be produced and give strong constraints on the DE equation of state, which should remain undefeated up to the LSST era.

References

[1] RIESS, Adam G., FILIPPENKO, Alexei V., CHALLIS, Peter, et al. Observational evidence from supernovae for an accelerating universe and a cosmological constant. The Astronomical Journal, 1998, vol. 116, no 3, p. 1009.

[2] BETOULE, M. E. A., KESSLER, R., GUY, J., et al. Improved cosmological constraints from a joint analysis of the SDSS-II and SNLS supernova samples. Astronomy & Astrophysics, 2014, vol. 568, p. A22.

[3] PERLMUTTER, Saul, ALDERING, Goldhaber, GOLDHABER, Gerson, et al. Measurements of Ω and Λ from 42 high-redshift supernovae. The Astrophysical Journal, 1999, vol. 517, no 2, p. 565.

[4] ASTIER, P., EL HAGE, P., GUY, J., et al. Photometry of supernovae in an image series: methods and application to the SuperNova Legacy Survey (SNLS). Astronomy & Astrophysics, 2013, vol. 557, p. A55.

[5] PRITCHET, C. J., SNLS COLLABORATION, et al. SNLS–The Supernova Legacy Survey. In : Observing Dark Energy. 2005. p. 60.

[6] ZACKAY, Barak, OFEK, Eran O., et GAL-YAM, Avishay. Proper image subtraction-optimal transient detection, photometry, and hypothesis testing. The Astrophysical Journal, 2016, vol. 830, no 1, p. 27.

[7] BELLM, Eric C., KULKARNI, Shrinivas R., GRAHAM, Matthew J., et al. The zwicky transient facility: system overview, performance, and first results. Publications of the Astronomical Society of the Pacific, 2018, vol. 131, no 995, p. 018002.

[8] VALLENARI, A., BROWN, A. G. A., et PRUSTI, T. Gaia data release 3. summary of the content and survey properties. Astronomy & Astrophysics, 2022.

[9] COLLABORATION, Gaia, et al. Description of the Gaia mission (spacecraft, instruments, survey and measurement principles, and operations). Gaia Collaboration et al.(2016a): Summary description of Gaia DR1, 2016.

[10] ASTIER, Pierre et PAIN, Reynald. Observational evidence of the accelerated expansion of the universe. Comptes Rendus Physique, 2012, vol. 13, no 6-7, p. 521-538.

[11] DHAWAN, Suhail, GOOBAR, Ariel, SMITH, M., et al. The Zwicky Transient Facility Type Ia supernova survey: first data release and results. Monthly Notices of the Royal Astronomical Society, 2022, vol. 510, no 2, p. 2228-2241.

[12] BERTIN, Emmanuel et ARNOUTS, Stephane. SExtractor: Software for source extraction. Astronomy and astrophysics supplement series, 1996, vol. 117, no 2, p. 393-404.

[13] KAISER, Nick, BURGETT, William, CHAMBERS, Ken, et al. The Pan-STARRS wide-field optical/NIR imaging survey. In : Ground-based and airborne telescopes III. SPIE, 2010. p. 159-172.

[14] CHAMBERS, Kenneth C., MAGNIER, E. A., METCALFE, N., et al. The pan-starrs1 surveys. arXiv preprint arXiv:1612.05560, 2016.

[15] ASTIER, Pierre. The expansion of the universe observed with supernovae. Reports on Progress in Physics, 2012, vol. 75, no 11, p. 116901.

[16] YASUDA, Naoki, TANAKA, Masaomi, TOMINAGA, Nozomu, et al. The hyper suprime-cam SSP transient survey in COSMOS: overview. Publications of the Astronomical Society of Japan, 2019, vol. 71, no 4, p. 74.

[17] SCOLNIC, D., CASERTANO, S., RIESS, A., et al. SUPERCAL: Cross-calibration of multiple photometric systems to improve cosmological measurements with type Ia supernovae. The Astrophysical Journal, 2015, vol. 815, no 2, p. 117.

Gravitational Wave Cosmology: Constraints on the Hubble Constant using Dark-Sirens and Binary Black-hole Spins

Gregoire Pierra

Universite Lyon, Universite Claude Bernard Lyon 1, CNRS, IP2I Lyon / IN2P3, UMR 5822, F-69622 Villeurbanne, France

Abstract — The LIGO-Virgo-Kagra (LVK) collaboration has detected 90 gravitational-wave (GW) events since September 2015 [7], over three observing runs. These GW events can be used to infer the cosmological parameters of our Universe and peculiarly the Hubble constant H_0 [1]. The Hubble constant is constrained using the luminosity distance estimated from each GW signals of compact binary coalescence, combined with an estimation of their corresponding redshift. The redshift is obtained via two approaches : The first method uses galaxy catalog information and the second one investigates the mass-redshift degeneracy. By breaking this degeneracy, the cosmological parameters are inferred jointly along with the population of BBH systems. When combined with the binary neutron star event GW170817, the Hubble constant was estimated at $H_0 = 68^{+12}_{-8}\mathrm{km.s^{-1}Mpc^{-1}}$ (68%CL) [1] [2]. This work presents the inclusion of binary black-hole spin information and its impact on the inference of cosmological parameters. Two models are explored, the Default model and the Gaussian spin model, with respectively 4 and 2 free parameters. So far, using 42 highly confident binary black hole events from the O3 run with an inverse false alarm rate (IFAR)>4, we find $H_0 = 91.39^{+50}_{-37}\mathrm{km.s^{-1}Mpc^{-1}}$ (68%CL) and no clear sign of correlation between the spin of black-holes and the cosmological parameters.

Introduction

The LVK network is composed of four grand interferometers : LIGO Livingston and Hanford, situated in the United States of America, with 4km long arms, Virgo in Cascina Italy with 3km arms, and KAGRA the last one located in Japan, with 3km arms. After three observing runs (O1, O2, and O3) that lasted approximately one year each , the LVK collaboration has detected 90 confident gravitational wave signals. During O1 (2015-2016), the collaboration made the first direct detection of gravitational waves produced by the merger of two black-holes of 36 and 31 solar masses (GW150914) [5]. In August 2017 (O2), an extraordinary GW signal from a binary neutron stars (BNS) merger is seen by LIGO-Virgo (GW170817) [3], as well as a gamma-ray burst (GRB 170817A) produced by the same source a few seconds later. This joint detection opened the door to cosmological measurements of the Hubble constant with GWs, providing the first GW based value of $H_0 = 70^{+12}_{-8}\mathrm{km.s^{-1}Mpc^{-1}}$ (68%CL) [4].

The dominant source of detectable gravitational waves in our Universe are compact binary coalescence, during which two incredibly dense astrophysical objects such as neutron-stars or black-holes merge together. The gravitational merger can be decomposed into three phases : During the inspiral phase, the distance between the two compact objects decreases as the gravitationally bounded system looses angular momentum, under of the form of gravitational waves. The merger phase starts as soon as the least massive object reaches the last stable circular orbit (ISCO). This time period is associated to maximum amplitude of emitted gravitational waves. Finally, the system relaxes into a stable state of a newly formed compact object. The detected GW signal directly gives a measure of several important properties about the sources. The most important ones are the luminosity distance of the source $\mathrm{d_L}$, obtained independently of any distance ladder, the primary masses $\mathrm{m_1}$ and $\mathrm{m_2}$ in the detector frame and the spins of each black-holes. Although, if GWs signals are able to tell us about the luminosity distance of the source, the estimation of cosmological parameters such as the Hubble constant requires an other measurement : the redshift of the source. The GRB of GW170817 allowed optical telescope to locate the host galaxy of the merger, hence giving an accurate measurement of the redshift of the source z. Unfortunately, GW170817 is the only event seen by the LVK with an associated electromagnetic counterpart so far. Alternative approaches to estimate the redshift of the sources are under development, for instance Mastrogiovanni et al. in [2] compare the spectrum of the detected mass distribution of binary black-holes (BBH) with astrophysical models of

the true source frame mass distribution of BBH, aiming to break the mass-redshift degeneracy. An other method proposed in [9], [8], statistically infers the redshift of the host galaxy, making use of galaxy catalog and superimposing them with the sky localization of GWs sources.

The proceeding is organized as follows. In the next section, GW Cosmology with Dark-Sirens, I present in detail the population method and to what extent GWs can help break the mass-redshift degeneracy. The third section discusses the inclusion of BBH spin parameters in the hierarchical bayesian analysis to infer cosmological and population parameters. In the last section, I present the preliminary results of spin parameters and cosmological parameters estimated using a chosen subset of GW events from the third observing run of LVK.

GW Cosmology with Dark-Sirens

Dark-Sirens are GW mergers with no electromagnetic counterpart associated, usually, in that type of compact binary coalescence (CBC), at least one of the two objects is a black-hole, which prevents any GRB to be emitted. Dark-Sirens events are uninformative about the cosmology on their own, since the redshift of the source stays unknown. The so-called Pure Population method presented in [2] introduces a new way to access the redshift information of the sources using the intrinsic degeneracy between the detected masses (detector frame) of the merging black-holes and the true masses (source frame). The fundamental principle of the method relies on the cosmological expansion of the universe [11], [10]. GWs emitted by a CBC are redshifted due to the expansion of the universe, as they propagate towards the Earth there waveforms are modulated in frequency, amplitude and phase. Hence, parameters inferred from GW signals in the LVK interferometers are biased since they are estimated from redshifted signals. In particular, the relation between the detected masses and the true masses can be expressed as

$$m_i^{\rm source} = \frac{m_i^{\rm det}}{1 + z(H_0, \Omega_m, w_0)}. \tag{1}$$

The key idea highlighted in Eq. 1 shows that, if the source frame masses are somehow known, and the detected masses $m_1^{\rm det}, m_2^{\rm det}$ measured with the GWs, the redshift of the binary system is accessible easily. Moreover, as explained in the previous section, GWs detections provide direct measurement of the distance luminosity $\rm d_L$ of the source, independently of the distance ladder. The Hubble constant H_0 can then be determined through the Hubble-Lemaitre [12] law

$$\rm d_L(z) = \frac{1+z}{H_0} c \int_0^z \frac{dz}{(\Omega_m(1+z)^3 + \Omega_\Lambda)}, \tag{2}$$

injecting the measured value of the luminosity distance and the redshift of the source.

The global idea is rather simple, but the actual use of this method is highly non trivial since the cosmology as well as the source mass distribution of BBHs are unknown, and may vary w.r.t the redshift. In other words, by fixing the cosmology (H_0, Ω_m, w_0) in Eq. 1, one could determine the true masses in source frame of the merging black-holes. On the other hand, by fixing the source mass distribution of black-holes, one could measure with accuracy the underlying values of the cosmological parameters with Eq. 1, as previously done in the O3 LVK collaboration paper [13]. BBH population properties and cosmological parameters have to be jointly fitted in order to break the mass-redshift degeneracy in Eq. 1.

Inferring Cosmology and Astrophysics with Observations of Gravitational Waves (ICAROGW) [2] is a python code developed within the LIGO-Virgo-KAGRA scientific collaboration that infers jointly the underlying properties of the BBH population and the cosmology, using real GW signals and injections (to compensate for the selection effects). The joint inference relies on a hierarchical bayesian analysis evaluating a likelihood function via nested-sampling method [14],[15]. The IcaroGW complete likelihood function for $N_{\rm EXP}$ GW events over a time $T_{\rm OBS}$ according to the population parameters θ and the cosmological parameters Λ is given by :

$$\mathcal{L}(x|\Lambda, N) \propto e^{-N_{\rm exp}(\Lambda)} (N_{\rm exp}(\Lambda))^{N_{\rm obs}} \prod_i^{N_{\rm obs}} \frac{\int \mathcal{L}(x_i|\theta, \Lambda)}{\pi(\theta|\Lambda) d\theta} \frac{N_{\rm exp}(\Lambda)}{N}, \tag{3}$$

where

- $\mathcal{L}(x|\Lambda, N)$: Likelihood from which IcaroGW samples, where x are the GW data, and N is the total number of black-hole mergers in the universe.
- $N_{exp}(\Lambda)$: The number of GW events we expect to detect over the total observation time T_{obs}.
- N_{obs} : Number of detected events.
- $\mathcal{L}(x_i|\theta, \Lambda)$: Likelihood of individual GW events.
- $\frac{N_{exp}}{N_{tot}}$: Fraction of detectable events (accounts for selection effects).
- $\pi(\theta, \Lambda)$: Priors on population parameters (masses, redshift, and now spins).
- x_i : The gravitational waves data for the $i^{\rm th}$ event.

IcaroGW is written to be modular and flexible, several parametrized models for the mass distribution, the redshift distribution and spins are available, it allows us to perform comparisons and determine not only the best values for the parameters, but also the leading population models. Finally, the presence of sharp features such as bumps, cut-off, long tail in the source mass distributions are crucial to overall convergence of IcaroGW [1].

The inclusion of BBH spins

Since the first observing run of LVK, the estimation of spins from GWs detections has made a lot of progress, alongside with the global understanding of black-hole properties [16], [17]. The aim of this work is to generalize IcaroGW inference by implementing BBH spin models into the analysis, incorporating two physically motivated models : the Default and Gaussian spin models [13]. Doing so, we investigate the impact of BBH spins on the inference of population and cosmological parameters, especially its effects on the posterior of H_0. The major motivation to look at spins in GW cosmology is that spins could correlate with other inferred parameters, either cosmological, population related, or both. If a correlation exists with one or more parameters and are not taken into account properly, it would introduced a bias in the other estimated distributions, H_0 included. According to [18],[19],[27], the alignment of the spin w.r.t the angular orbital momentum is crucial and plays an important role in the total energy radiated by the BBH. This increase of energy radiated (under the form of GWs) is related to the duration of the coalescence. The number of orbits that the two black-holes undergo increases as the spin of each black-hole are aligned with the angular orbital momentum $\vec{L}$ and decreases when the spins tends to be anti-aligned w.r.t $\vec{L}$. The amount of GW radiated energy depends on the duration of the BBH inspiral phase, which in turn depends on the spin configuration. So BBH systems with similar total masses but different spin configurations could be detected at different luminosity distance. An other motivation supports a direct correlation with the masses and/or the redshift of the system. In the chapter 1 of [20] , M. Mapelli discusses the effects of BBH formation channels on the masses, redshift and spins. Spins of black-holes and especially binary black-holes are not randomly drawn. The origin of these spins can be understood via their formation channels. A system formed in a very dense environment, where large quantity of angular momentum can be gained or lost is not expected to have the same spin distribution as a system formed in a isolated field. The same argument supports the idea of various mass distributions and redshift of formation distributions. As a consequence, spins could correlate with some of the cosmological parameters due to the way BBH systems form, and have an impact on the constraints GWs put on the cosmology, or introduce a bias.

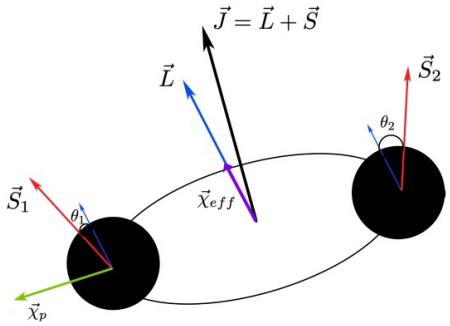

Figure 1: Scheme of a binary black hole system with all spin parameters. $\vec{S}_{1,2}$ are the dimensionless spin magnitudes, $\theta_{1,2}$ are the tilt angles (angles between the spin orientation and the angular momentum of the binary system) and $\chi_{\rm eff}$, $\chi_{\rm p}$ are respectively the effective inspiral spin parameter and the effective precessing spin parameter.

The origin of BBH spins results from complex interactions in their formation processes [20],[21],[22]. The two chosen spin models implemented in IcaroGW are built in a way to test the hypothesis mentioned above. The Default model was first introduced in [13], with four free parameters : $\chi_{1,2}$ are the dimensionless spin magnitudes describe by a Beta distribution and $\theta_{1,2}$ are the tilt angles, built as a mixed distribution between a truncated gaussian G_t and an isotropic distribution $\mathcal{F}$ (c.f. Eq. 4-5). This model allows us to explore the proportion of BBH merger coming from the isolated or the dynamical channel, especially through the tilt angle parametrization. Dynamically formed BBH tend to have more isotropic alignment of their spins w.r.t the angular momentum of the system, and on the contrary spins for isolated BBH favor aligned or anti aligned spins w.r.t $\vec{L}$.

$$\pi(\chi_{1,2}|\alpha_\chi, \beta_\chi) = \text{Beta}(\alpha_\chi, \beta_\chi) \tag{4}$$

$$\pi(cos\theta_{1,2}|\xi, \sigma_t) = \xi G_t(cos\theta|\sigma_t) + (1-\xi)\mathcal{F}(cos\theta) \tag{5}$$

The Gaussian spin model firstly presented by Roulet. J in [23], is defined as shown below in the Eq. 6-8.

$$\pi(\chi_{eff}, \chi_p|\mu_{eff,p}, \sigma_{eff,p}) = G^{2D}_{[-1,1],[0,1]}(\chi_{eff}, \chi_p|\mu, \Sigma) \tag{6}$$

$$\vec{\mu} = (\mu_{eff}, \mu_p) \tag{7}$$

$$\Sigma = \begin{pmatrix} \sigma^2_{eff} & \rho\sigma_{eff}\sigma_p \\ \rho\sigma_{eff}\sigma_p & \sigma^2_p \end{pmatrix} \tag{8}$$

The Gaussian spin model does not use the same parameters than the Default spin model, but rather a dimensional reduction with only two parameters : χ_{eff} and χ_p. χ_{eff} is the effective inspiral spin parameter bounded between $(-1, 1)$, it accounts for the amount of spin aligned with the orbital angular momentum $\vec{L}$. χ_p is the effective precession spin parameter that quantify the amount of spin perpendicular to the total angular momentum [23], bounded between $(0, 1)$. This model investigates the global spin asymmetries and precession effect that are induced in the BBH population via their formation channels.

Preliminary Results

The inclusion of binary black-hole spins inside IcaroGW's inference is now complete. The official re-

view by the LVK scientific collaboration will start in January 2023, as IcaroGW will be one of the two pipelines used for the analysis of the next observing run O4. In this section, I present some of the preliminary results employed to test the new version of the pipeline, inferring spins alongside cosmological and masses parameters using real GW events produced by LVK. The aim is to check to overall inference using both models and try to recover similar values as the one found in [24], where they fixed all non population related parameters. The results are obtained using 42 BBH GW events from O3 with an IFAR > 4. The figure 2 and 3 display posterior distributions of the inferred values of each parameter used in both spin models (the posteriors for the masses and the redshift are not shown here). Using the Default spin model, we see no spin

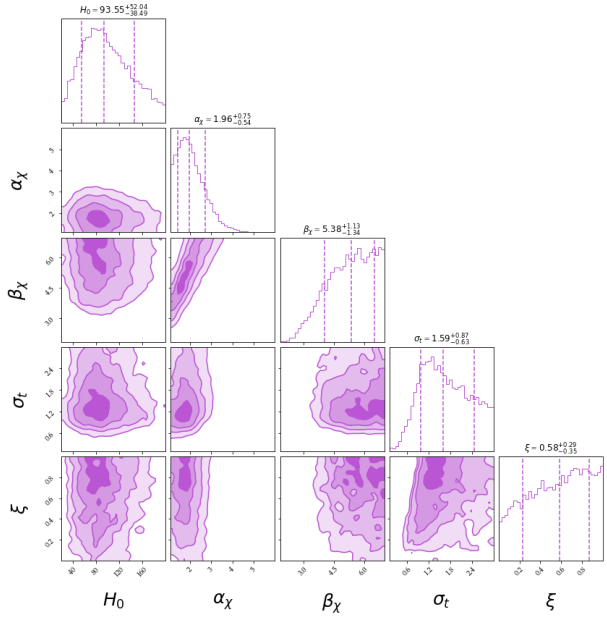

Figure 2: Default spin model corner plot. The upper plots show the final posterior distributions with the associated value for each spin parameters. The 2D plots are the bi-dimensional distributions, highlighting potential correlation effects.

correlation with the cosmological parameters. The estimated value of $\xi = 0.58^{+0.29}_{-0.35}$ is in agreement with a mixed population of binary black hole systems, formed in isolated and dynamical fields, with a slight penchant for aligned spins with the angular momentum. Finally, a clear preference for slowly spinning black-hole is supported by the recovered values of α_χ and β_χ.

The inference with the Gaussian spin model fig. 2 does not show any correlation between the spin parameters and the Hubble constant H_0 so far. Moreover, BBH systems with aligned spins and slow spin magnitudes are favoured ($\mu_{\chi_{eff}} > 0$), in agreement with the inferred population using the Default spin model, and the results of the O3 Rate and Population paper [24]. The value of μ_{χ_p} centered on 0 is compatible with non-precessing binaries, consistent with other works [6],[7].

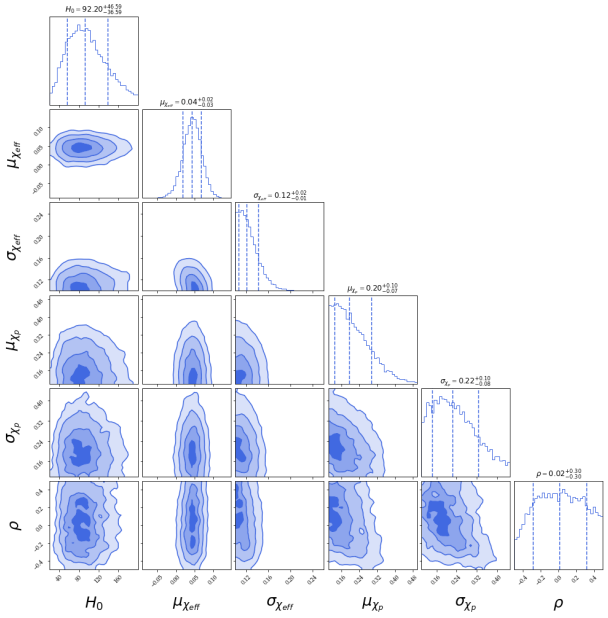

Figure 3: Gaussian spin model corner plot. The upper plots show the final posterior distributions with the associated value for each spin parameters. The 2D plots are the bi-dimensional distributions, highlighting potential correlation effects.

Discussion

This analysis is the first joint estimation of cosmological parameters along with the spin parameters of BBHs using real GWs data. The results with both the Default and Gaussian spin model are mainly compatible with the O3 Rate & Population paper, favouring a slowly spinning BBH population with a preference for aligned spins. On the other side, as shown in 2 and 3, some posteriors stay poorly informative due to non-explored areas in the parameter space, induced by a lack of available GW events. On the cosmological side, we do not find any correlation between the spins parameters and any cosmological parameters. These results are not excluding spin-mass or spin-redshift correlation since BBH spins are not well measured. Since IcaroGW's method is statistical, we expect to see large improvements in the inference of spins in the future, with the next observing runs and the increased sensitivity of the interferometers. Moreover, the two models implemented do not contain any direct dependency with the mass and/or the redshift, future astrophysically motivated models will incorporate such dependencies. At last, the inferred values of the Hubble constant $H_0 = 93.55^{+52}_{-38}\text{km.s}^{-1}\text{Mpc}^{-1}$ (68%CL) with the Default model, and $H_0 = 92.20^{+46}_{-36}\text{km.s}^{-1}\text{Mpc}^{-1}$ (68%CL) with the Gaussian model, remain compatible with the Planck18 [25] and the SH0ES [26] values.

References

[1] Constraints on the cosmic expansion history from GWTC-3, Abbott et .al, 2021

[2] On the importance of source population models for gravitational-wave cosmology, Mastrogiovanni et .al, 2021

[3] Troja, Elenora, et al. "The X-ray counterpart to the gravitational-wave event GW170817." Nature 551.7678 (2017): 71-74.

[4] DLT40 Collaboration. "A gravitational-wave standard siren measurement of the Hubble constant." Nature 551.7678 (2017): 85-88.

[5] Abbott, Benjamin P., et al. "Observation of gravitational waves from a binary black hole merger." Physical review letters 116.6 (2016): 061102.

[6] Abbott, R., et al. "Gwtc-2.1: Deep extended catalog of compact binary coalescences observed by ligo and virgo during the first half of the third observing run." arXiv preprint arXiv:2108.01045 (2021).

[7] Abbott, R., et al. "GWTC-3: compact binary coalescences observed by LIGO and Virgo during the second part of the third observing run." arXiv preprint arXiv:2111.03606 (2021).

[8] Gray, Rachel, et al. "Cosmological inference using gravitational wave standard sirens: A mock data analysis." Physical Review D 101.12 (2020): 122001.

[9] Gair, J. R., Ghosh, A., Gray, R., Holz, D. E., Mastrogiovanni, S., Mukherjee, S., ..., Pierra, G., & Vallejo-Pena, S. A. (2022). "The Hitchhiker's guide to the galaxy catalog approach for gravitational wave cosmology". arXiv preprint arXiv:2212.08694.

[10] Linder, Eric V. "Exploring the expansion history of the universe." Physical Review Letters 90.9 (2003): 091301.

[11] Freedman, Wendy L., et al. "Final results from the Hubble Space Telescope key project to measure the Hubble constant." The Astrophysical Journal 553.1 (2001): 47.

[12] Hubble, Edwin. "A relation between distance and radial velocity among extra-galactic nebulae." Proceedings of the national academy of sciences 15.3 (1929): 168-173.

[13] Abbott, Rich, et al. "Population properties of compact objects from the second LIGO-Virgo gravitational-wave transient catalog." The Astrophysical journal letters 913.1 (2021): L7.

[14] Speagle, Joshua S. "A conceptual introduction to markov chain monte carlo methods." arXiv preprint arXiv:1909.12313 (2019).

[15] Vitale, Salvatore, et al. "Inferring the properties of a population of compact binaries in presence of selection effects." Handbook of Gravitational Wave Astronomy. Singapore: Springer Singapore, 2022. 1-60.

[16] Ng, Ken KY, et al. "Gravitational-wave astrophysics with effective-spin measurements: asymmetries and selection biases." Physical Review D 98.8 (2018): 083007.

[17] Bavera, Simone S., et al. "The origin of spin in binary black holes-Predicting the distributions of the main observables of Advanced LIGO." Astronomy & Astrophysics 635 (2020): A97.

[18] Maggiore, Michele. Gravitational Waves: Volume 2: Astrophysics and Cosmology. Oxford University Press, 2018.

[19] Campanelli, Manuela, Carlos O. Lousto, and Yosef Zlochower. "Spin-orbit interactions in black-hole binaries." Physical Review D 74.8 (2006): 084023.

[20] Mapelli, Michela. "Formation channels of single and binary stellar-mass black holes." Handbook of gravitational wave astronomy (2022): 705-769.

[21] Mapelli, Michela, et al. "The cosmic evolution of binary black holes in young, globular, and nuclear star clusters: rates, masses, spins, and mixing fractions." Monthly Notices of the Royal Astronomical Society 511.4 (2022): 5797-5816.

[22] Mapelli, Michela, et al. "Hierarchical black hole mergers in young, globular and nuclear star clusters: the effect of metallicity, spin and cluster properties." Monthly Notices of the Royal Astronomical Society 505.1 (2021): 339-358.

[23] Roulet, Javier, et al. "Distribution of effective spins and masses of binary black holes from the LIGO and Virgo O1-O3a observing runs." Physical Review D 104.8 (2021): 083010.

[24] Abbott, R., et al. "The population of merging compact binaries inferred using gravitational waves through GWTC-3." arXiv preprint arXiv:2111.03634 (2022).

[25] Collaboration, Planck, et al. "Planck 2018 results. VI. Cosmological parameters." (2020).

[26] Riess, Adam G., et al. "A Comprehensive Measurement of the Local Value of the Hubble Constant with 1 km/s." Mpc Uncertainty from the Hubble Space Telescope and the SH0ES Team. arXiv e-prints (2021).

[27] Campanelli, Manuela, Carlos O. Lousto, and Yosef Zlochower. "Spinning-black-hole binaries: The orbital hang-up." Physical Review D 74.4 (2006): 041501.

Detection of Baryon Acoustic Oscillations using Lyman-α Forests in eBOSS/DESI

Ting Tan

Sorbonne Université, CNRS/IN2P3, Laboratoire de Physique Nucléaire et des Hautes Energies, LPNHE, 4 Place Jussieu, F-75252 Paris, France

Abstract — The Baryon Acoustic Oscillations (BAO) is a powerful large-scale structure probe that is used to constrain dark energy models, by measuring the expansion history of the universe. It can be detected by measuring the correlation function of galaxies, quasars, and Lyman-α absorption systems, i.e. the so-called Lyman-α forests. In our study, we focus on the measurement of BAO using Lyman-α forests and the modeling of the Lyman-α correlation function, especially the High Column Density Systems, seen as strong absorptions in the forests.

Introduction

The Lyman-α forests

The accelerated expansion of the universe was first observed by the measurement of luminosity distances of type Ia supernovae (SNe Ia) [1, 2]. The SNe Ia probe provides desirable measurements at low redshifts, and constraints on dark energy models. Alternatively, a "comoving standard ruler", i.e. the comoving scale for the peak of the baryonic acoustic oscillations (BAO), can be used to measure the expansion rate of the universe at higher redshifts $z > 0.2$. The BAO signal reveals the primordial fluctuations of the matter fields in the early stages of the universe when it was still a plasma, where their imprints can be seen as a peak at the sound horizon scale. This BAO scale demonstrates how a sound wave traveled through the universe between the Big Bang and the epoch of recombination. The BAO scale can be measured at different redshifts using $D_M(z)/r_d$ and $D_H(z)/r_d$ ($D_M(z)$ is the comoving angular-diameter distance at a certain redshift z, $D_H(z) = \frac{c}{H(z)}$ is the Hubble distance relevant to the expansion rate of the universe $H(z)$, $r_d = 147.3 \pm 0.5$Mpc is the comoving scale for the BAO peak [3]). The BAO peak can be constrained in the two-point correlation function of discrete matter tracers of the quasi-linear matter density field, e.g. galaxies [4, 5] and quasars [6]. It can also be detected using continuous matter tracers [8], such as Lyman-α forests, seen as the series of absorption lines in the high-redshift quasar ($z > 2.1$) spectra. They are caused by the Lyman-alpha transitions of neutral hydrogen in the low-density, high-redshift intergalactic medium (IGM). Figure 1 gives an example of a quasar spectrum from the eBOSS DR16 Lyman-α catalog, at the redshift $z_{\rm QSO} = 3.058$. Lyman-α forests are present as the absorption lines in between the Lyman-α peak and the overlapping Lyman-β+OVI emission lines. The auto (cross) correlation function of the Lyman-α forests (with quasars) has been used to detect BAO at the redshift $z \sim 2.3$ [7, 8, 9]. High Column Density Systems (HCDs) are seen as strong absorbers in the Lyman-α forests. In this work, we focus on the theoretical modeling of HCDs on the Lyman-α correlation function, which is one of the most important systematics in the Lyman-α analysis. We provide a new model, the `Voigt` model, that gives a physical measurement of the HCD bias.

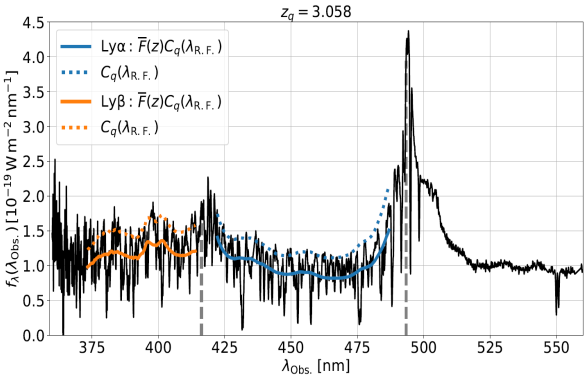

Figure 1: A quasar spectrum from the eBOSS DR16 data [8], with $z_{\rm QSO} = 3.058$. The Lyman-α peak and the overlapping Lyman-β+OVI emission lines are marked with grey lines.

Cosmological Surveys

The high precision statistical constraints on BAO using Lyman-α forests are facilitated with the development of large cosmology surveys, e.g. the extended Baryon

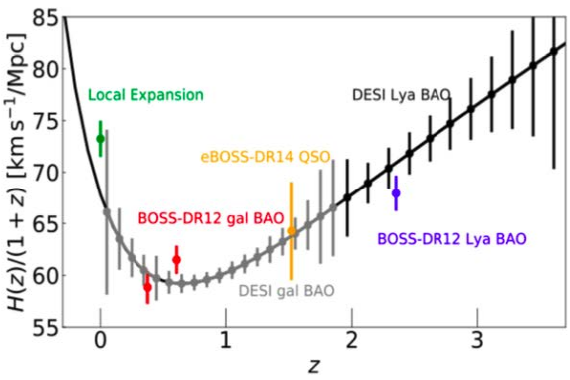

Figure 2: Constraints of the Hubble parameter with a ΛCDM model [3], using galaxies and Lyman-α forests from BOSS, eBOSS, and the forecast of DESI [22].

Oscillation Spectroscopic Survey (eBOSS [1][23]) and the on-going Dark Energy Spectroscopic Instrument (DESI [2]). The eBOSS survey was part of the fourth generation of the Sloan Digital Sky Survey (SDSS-IV [20] [21]), which used a 2.5m Ritchey-Chrétien telescope installed at Apache Point Observatory (APO) in New Mexico, USA. It covered over $\sim 10000\text{deg}^2$ of the sky and collected a large catalog of $\sim 200,000$ Ly-α quasars with $z > 2.1$ in the sixteenth data release (DR16 [10]), that were used in the BAO detection [8]. Since May, 2021, the DESI survey started its 5-year commission, which was designed to obtain spectra of about a million Lyman-α quasars covering over 14000deg^2 of the sky, using the 4-meter Mayall telescope at Kitt Peak National Observatory in Arizona, USA. Figure 2 shows the constraints on the Hubble parameter with a ΛCDM model [3], using different tracers from BOSS, eBOSS, and the expected one from DESI [22].

The Lyman-α correlation function

The Ly-α correlation functions are computed following the pipeline detailed in [8] using the Package for Igm Cosmological-Correlations Analyses (Picca[3]). For each collected Lyman-α quasar spectrum, the fluctuation of the flux-transmission field $F(\lambda)$ is defined as:

$$\delta_q(\lambda) = \frac{f_q(\lambda)}{C_q(\lambda)\bar{F}(\lambda)} - 1, \quad (1)$$

with $f_q(\lambda)$ the observed flux in each line-of-sight q at wavelength λ, $C_q(\lambda)$ the quasar continuum without adsorptions and $\bar{F}(\lambda)$ the mean transmission. The 3D Lyman-α auto-correlation function is computed as

$$\xi_A = \frac{\sum\limits_{(i,j)\in A} w_i w_j \delta_i \delta_j}{\sum\limits_{(i,j)\in A} w_i w_j}, \quad (2)$$

where A refers to the ensemble of spectra pixels in separation bins of $4h^{-1}$Mpc in ($r_\perp \in [0, 200]h^{-1}$Mpc, $r_{||} \in [-200, 200]h^{-1}$Mpc), where $r_{||}$ refers to the direction along the line-of-sight, and $r_\perp$ refers to the transverse direction. w_i shows the weight for each separation grid. The Lyman-α-quasar cross-correlation function is then computed by considering quasars as point-like objects. Figure 3 shows the auto-correlation and cross-correlation of Lyman-α forests computed using eBOSS DR16 data [8], along the direction $0.8 < |\mu| < 0.95$, where $|\mu| = |\frac{r_{||}}{r}|$ ($\mu = 1$ is along the line-of-sight). The BAO peak is measured at $\sim 100h^{-1}$Mpc.

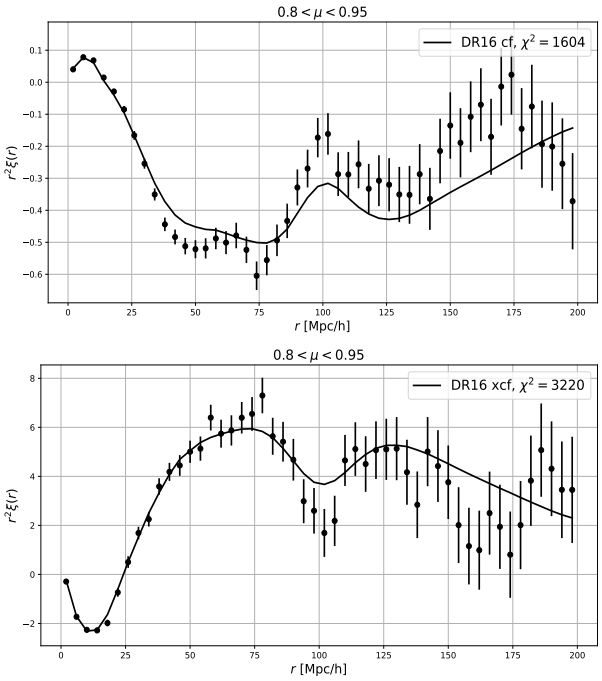

Figure 3: The auto-correlation and cross-correlation of Lyman-α forests computed using eBOSS DR16 data, along the direction $0.8 < |\mu| < 0.95$. The correlations are multiplied by r^2, and the black curves show the fits over the range $10 < r < 180h^{-1}$Mpc.

The High Column Density Systems

The High Column Density Systems are categorized as HCDs or Damped Lyman-α Systems (DLAs) by the high NHI column density of the neutral hydrogen gas concentration along the line of sight: HCDs: $log(\text{NHI}/\text{cm}^{-2}) \geq 17$; DLAs: $log(\text{NHI}/\text{cm}^{-2}) \geq 20$. DLAs are seen as strong absorption regions with damping wings in the Lyman-α forests, and usually parameterized using a Voigt profile, which is a convolution of a Gaussian profile and a Lorentzian profile, due to the thermal Doppler broadening and cross-section of the Neutral Hydrogen respectively. DLAs are detectable using Voigt profile fitting [11, 12] and machine learning algorithms [14]. We can smooth the Lyman-α flux-fluctuation fields by masking out the detected DLAs, shown in Figure 4. However, the smaller HCDs that are undetectable still have significant impact on the mod-

[1] https://www.sdss4.org/surveys/eboss/
[2] https://www.desi.lbl.gov/
[3] https://github.com/igmhub/picca

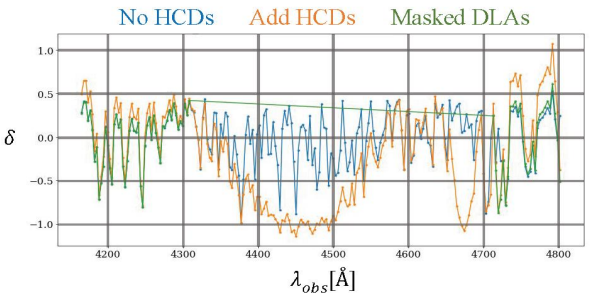

Figure 4: An example of the fluctuation of the flux-transmission field of a Lyman-α forest (Defined in Equation 1) from the Lyman-α Saclay mocks [17]. The blue curve shows the field without any HCDs, and the orange curve shows the case with an HCD present in the absorptions. We can smooth the field by masking out these large detectable DLAs, with the result shown as the green curve.

eling of Lyman-α correlation function. The modeling of the Lyman-α correlation function is realized at the power spectrum level, which is the Fourier transform of the correlation function. It is defined as:

$$P_{\mathrm{Ly}\alpha}(\mathbf{k}) = P_{\mathrm{QL}}(\mathbf{k}) D_{\mathrm{NL}}(\mathbf{k}) b^2_{\mathrm{Ly}\alpha}(1+\beta_{\mathrm{Ly}\alpha}\mu^2)^2. \quad (3)$$

Here P_{QL} is the quasi-linear power spectrum, D_{NL} [15] is the non-linear correction for small scales, $b_{\mathrm{Ly}\alpha}$ and $\beta_{\mathrm{Ly}\alpha}$ are two parameters referring to the amplitude of the power spectrum and the redshift space distortion effect (RSD) respectively.

The Fourier Transformation of the absorption profiles of those HCDs will induce a cut-off for the Lyman-α power spectrum at high $k_{||}$ ($\mathbf{k}$ along the line-of-sight), and it affects the bias and redshift distortion parameters of Lyman-$*alpha* tracers.

The impact of HCDs is modeled as a correction for the Lyman-α parameters with two additional HCD parameters b_{HCD} and β_{HCD} [16]. A $F_{\mathrm{HCD}}(k_{||})$ function is proposed to characterize the damping wings of HCDs (the wings of the absorptions). The effective k-dependent bias and RSD parameters are

$$\begin{aligned} b'_{\mathrm{Ly}\alpha} &= b_{\mathrm{Ly}\alpha} + b_{\mathrm{HCD}} F_{\mathrm{HCD}}(k_{||}), \\ b'_{\mathrm{Ly}\alpha}\beta'_{\mathrm{Ly}\alpha} &= b_{\mathrm{Ly}\alpha}\beta_{\mathrm{Ly}\alpha} + b_{\mathrm{HCD}}\beta_{\mathrm{HCD}} F_{\mathrm{HCD}}(k_{||}). \end{aligned} \quad (4)$$

In the eBOSS DR16 analysis [8], the F_{HCD} function is modeled using a empirical `Exp` model:

$$F^{\mathrm{exp}}_{\mathrm{HCD}}(k_{||}) = \exp\left(-L_{\mathrm{HCD}} * k_{||}\right). \quad (5)$$

In this case, L_{HCD} is a free parameter characterizing the scale of HCDs effect, which is fixed to $10h^{-1}$Mpc in the DR16 analysis.

In our study, we model the F_{HCD} function theoretically from the distribution of HCDs [18], assuming HCDs are parameterized with a Voigt profile [19]:

$$F^{\mathrm{Voigt}}_{\mathrm{HCD}}(k_{||}) = \int \widetilde{(V-1)}(k_{||}, n) f(n) \mathrm{d}n, \quad (6)$$

where V is a Voigt profile, n refers to the NHI and $f(n)$ represents the NHI distribution of HCDs.

Results

We compare these two models on the fits of eBOSS DR16 data. The `Exp` fitting function gives a comparable fitting and a good agreement with the `Voigt` model, as shown in Figure 5. However, the `Voigt` model provides a physical measurement of the bias parameter of HCDs, b_{HCD}, that can not be obtained using the `Exp` model. Moreover, none of these models give a good fitting for the region $25 < r < 80$, where HCDs play the most important role. This motivates us to search for a better understanding of the physics in this regime.

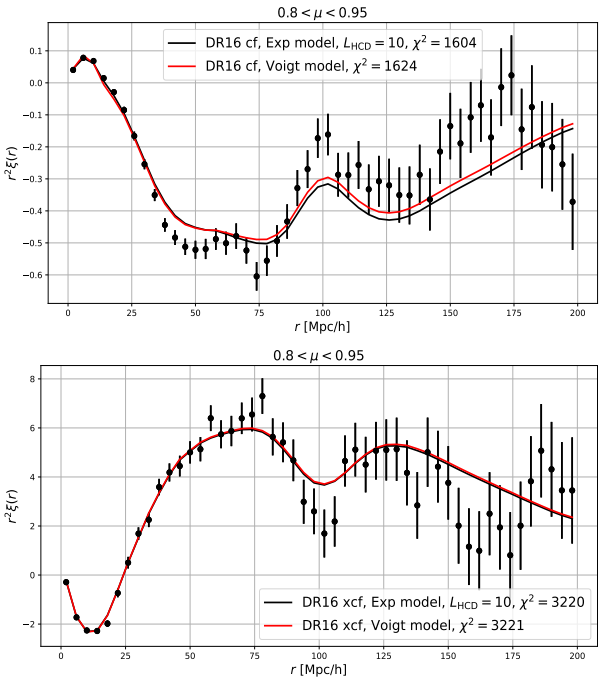

Figure 5: The auto-correlation and cross-correlation of Lyman-α forests computed using eBOSS DR16 data, along the direction $0.8 < |\mu| < 0.95$, fitted with the exp fitting function (Black) and the `Voigt` model (Red). These two models show comparable fitting results for both the auto- and cross-correlation function.

References

[1] Adam G Riess, et al. Observational evidence from supernovae for an accelerating universe and a cosmological constant. *The Astronomical Journal*, 116(3):1009, 1998.

[2] Saul Perlmutter, et al. Measurements of ω and λ from 42 high-redshift supernovae. *The Astrophysical Journal*, 517(2):565, 1999.

[3] Peter AR Ade, et al. Planck 2015 results-xiii. cosmological parameters. *Astronomy & Astrophysics*, 594:A13, 2016.

[4] Will J Percival, Shaun Cole, Daniel J Eisenstein, Robert C Nichol, John A Peacock, Adrian C Pope, and Alexander S Szalay. Measuring the baryon acoustic oscillation scale using the sloan digital sky survey and 2df galaxy redshift survey. *Monthly Notices of the Royal Astronomical Society*, 381(3):1053–1066, 2007.

[5] Will J Percival, et al. Baryon acoustic oscillations in the sloan digital sky survey data release 7 galaxy sample. *Monthly Notices of the Royal Astronomical Society*, 401(4):2148–2168, 2010.

[6] Metin Ata, et al. The clustering of the sdss-iv extended baryon oscillation spectroscopic survey dr14 quasar sample: first measurement of baryon acoustic oscillations between redshift 0.8 and 2.2. *Monthly Notices of the Royal Astronomical Society*, 473(4):4773–4794, 2018.

[7] Timothee Delubac, et al. Baryon acoustic oscillations in the lyα forest of boss quasars. *Astronomy & Astrophysics*, 552:A96, 2013.

[8] Helion Du Mas Des Bourboux, et al. The completed sdss-iv extended baryon oscillation spectroscopic survey: baryon acoustic oscillations with lyα forests. *The Astrophysical Journal*, 901(2):153, 2020.

[9] Andreu Font-Ribera, et al. Quasar-lyman α forest cross-correlation from boss dr11: Baryon acoustic oscillations. *Journal of Cosmology and Astroparticle Physics*, 2014(05):027, 2014.

[10] Romina Ahumada, et al. The 16th data release of the sloan digital sky surveys: first release from the apogee-2 southern survey and full release of eboss spectra. *The Astrophysical Journal Supplement Series*, 249(1):3, 2020.

[11] P Noterdaeme, P Petitjean, C Ledoux, and R Srianand. Evolution of the cosmological mass density of neutral gas from sloan digital sky survey ii–data release 7. *Astronomy & Astrophysics*, 505(3):1087–1098, 2009.

[12] P Noterdaeme, et al. Column density distribution and cosmological mass density of neutral gas: Sloan digital sky survey-iii data release 9. *Astronomy & Astrophysics*, 547:L1, 2012.

[13] Jason X Prochaska, Stéphane Herbert-Fort, and Arthur M Wolfe. The sdss damped lyα survey: data release 3. *The Astrophysical Journal*, 635(1):123, 2005.

[14] David Parks, J Xavier Prochaska, Shawfeng Dong, and Zheng Cai. Deep learning of quasar spectra to discover and characterize damped lyα systems. *Monthly Notices of the Royal Astronomical Society*, 476(1):1151–1168, 2018.

[15] Andreu Arinyo-i Prats, Jordi Miralda-Escudé, Matteo Viel, and Renyue Cen. The non-linear power spectrum of the lyman alpha forest. *Journal of Cosmology and Astroparticle Physics*, 2015(12):017, 2015.

[16] Andreu Font-Ribera and Jordi Miralda-Escudé. The effect of high column density systems on the measurement of the lyman-α forest correlation function. *Journal of Cosmology and Astroparticle Physics*, 2012(07):028, 2012.

[17] Thomas Etourneau, Jean-Marc Le Goff, Ting Tan, James Rich, and Julianna Vittoria Stermer. *in prep*, 2022.

[18] Keir K Rogers, Simeon Bird, Hiranya V Peiris, Andrew Pontzen, Andreu Font-Ribera, and Boris Leistedt. Correlations in the three-dimensional lyman-alpha forest contaminated by high column density absorbers. *Monthly Notices of the Royal Astronomical Society*, 476(3):3716–3728, 2018.

[19] Héctor Oscar Di Rocco and Alicia Cruzado. The voigt profile as a sum of a gaussian and a lorentzian functions, when the weight coefficient depends only on the widths ratio. *Acta Physica Polonica A*, 122, 2012.

[20] Donald G York, et al. The sloan digital sky survey: Technical summary. *The Astronomical Journal*, 120(3):1579, 2000.

[21] Michael R Blanton, et al. Sloan digital sky survey iv: Mapping the milky way, nearby galaxies, and the distant universe. *The Astronomical Journal*, 154(1):28, 2017.

[22] Amir Aghamousa, et al. The desi experiment part i: science, targeting, and survey design. *arXiv preprint arXiv:1611.00036*, 2016.

[23] Kyle S Dawson, et al. The sdss-iv extended baryon oscillation spectroscopic survey: overview and early data. *The Astronomical Journal*, 151(2):44, 2016.

Part IV

Hadronic Physics

session chaired by Guillaume TAILLEPIED

e^+e^- emission in pp at 4.5 GeV with HADES

Rayane Abou Yassine

IJCLab, Orsay

Abstract — p+p collisions provide reference spectra for the hot and dense (heavy-ion collisions A+A) and cold nuclear matter (p+A collisions) studies with HADES. At 4.5 GeV beam kinetic energy (at SIS18 accelerator), the investigations of dielectron production above the ϕ meson mass will be enabled. The different steps of the e^+e^- pair reconstruction are presented. Preliminary simulations with the PLUTO event generator, that will help in the data interpretation, are also discussed.

Introduction

The High Acceptance Di-Electron Spectrometer (HADES) at GSI, Darmstadt, Germany is an experimental setup dedicated to study the hadronic matter in the region of large net baryon densities and moderate temperatures as shown in Fig 1, using heavy-ion collisions in the incident energy range of few GeV/nucleon. These studies are complementary to those performed with the LHC, SPS, RHIC experiments that are interested in the region of low baryochemical potential and high temperatures. The analyses made with HADES are used to understand the microscopic structure of baryon rich matter where the baryonic resonances play an important role.

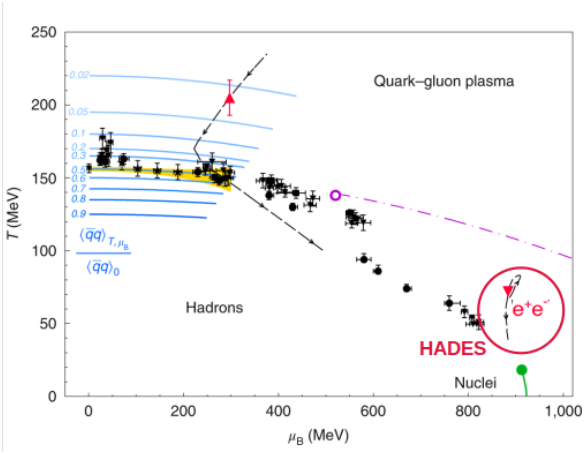

Figure 1: The QCD phase diagram representing the strongly interacting matter as a function of temperature and baryochemical potential [1].

HADES experimental setup

HADES is a fixed target experiment located at the GSI Helmholtz Center for Heavy-Ion Research in Darmstadt, Germany [2]. It is divided into six identical sectors covering full azimuthal angles and polar range between 18° and 85° with respect to the beam axis as shown in Figure 2. The tracking system, formed by 4

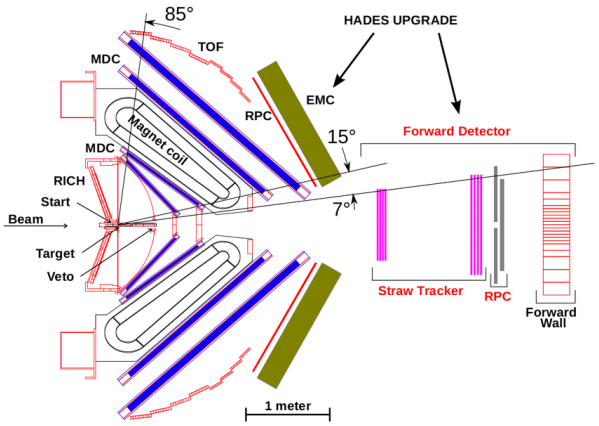

Figure 2: Schematic layout of the HADES detector.

planes of Mini-Drift Chambers (MDC) located in front and behind a toroidal magnetic field, allow the track reconstruction of charged particles and their momentum determination. To identify e^+ and e^- candidates, the Ring Imaging CHerenkov (RICH) detector and Electromagnetic Calorimeter (ECAL) are used in addition to the time of flight detectors (RPC for $\theta < 45°$ and TOF for $\theta > 45°$). The Forward detector is a new setup that allows the measurement of particles at small polar angles ($0.5° < \theta < 7°$).

Dileptons in heavy ion collisions

The study of dielectrons in heavy ion collisions is an ideal probe to understand the phase of dense and hot matter, as they don't interact strongly at the final state, that means they have a free mean path larger than the system size and therefore can reflect the whole history of the collision and give information on the matter properties (lifetime of the fireball, possible chiral symmetry restoration, temperature, etc ...). On the other hand, e^+e^- are used to study the in-medium properties of vector mesons (ρ, ω, ϕ), which have the same photon quantum numbers ($J^P = 1^-$) and can decay into e^+e^-

pair [3].

meson	mass (MeV/c^2)	Γ (MeV/c^2)	$c\tau$ (fm)	Main decay	BR to e^+e^-
ρ	768	152	1.3	$\pi^+\pi^-$	4.4×10^{-5}
ω	782	8.43	23.4	$\pi^+\pi^-\pi^0$	7.2×10^{-5}
ϕ	1019	4.43	44.4	K^+K^-	3.1×10^{-4}

Table 1: Vector mesons main characteristics

Dileptons in elementary reactions

In the HADES program, the studies of elementary reactions (pp and np) are also important: such reactions produce a medium with no impact on hadron structure via density or/and temperature effects.

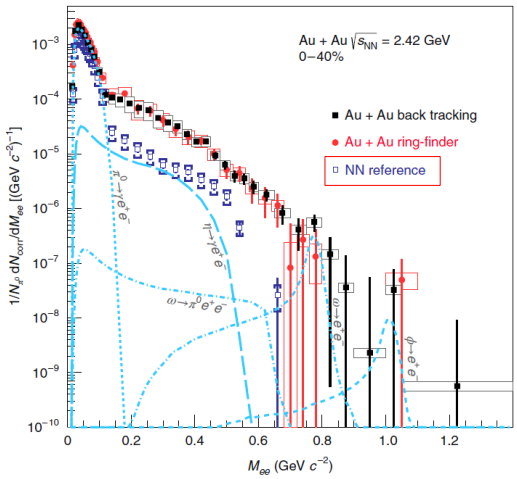

Figure 3: Di-electron invariant mass spectrum in Au-Au collisions at $\sqrt{s} = 2.42$ GeV (black dots) and the NN reference measurements at the same energy (blue dots)[1].

The study of the inclusive spectrum will provide reference spectra to the heavy ion collisions studies, as shown in Figures 3 and 4, while exclusive channels allow for a selective study of production mechanisms.
Dielectrons are mainly produced by the following sources in the GSI energy range:

- Meson Dalitz decay: ($\pi^0/\eta/\eta' \rightarrow \gamma e^+e^-$, $\omega \rightarrow \pi^0 e^+e^-$).
- Vector meson direct decay ($\rho/\omega/\phi \rightarrow e^+e^-$).
- Baryonic resonances Dalitz decay ($\Delta/N^* \rightarrow Ne^+e^-$).

The study of e^+e^- invariant mass distributions allows to determine cross sections for the meson production. In addition, the spectral function of the broad ρ meson, which is sensitive to the coupling to baryon resonances, can be investigated. This process is therefore strongly connected to the baryon resonance Dalitz decay. Finally, the yield above the ϕ mass ($M > 1\ GeV/c^2$) is interesting as a reference to search for chiral symmetry restoration signals[9].

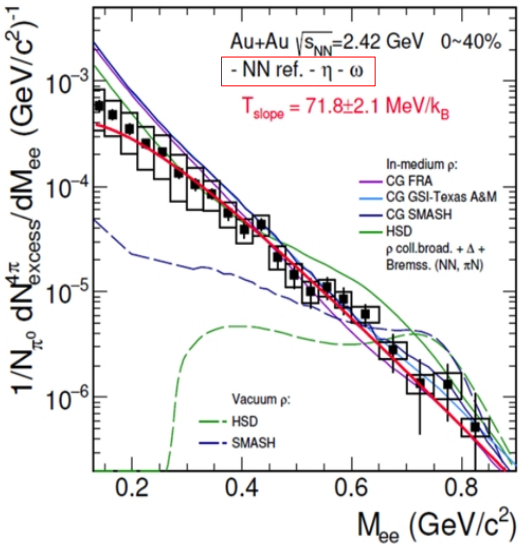

Figure 4: Di-electron invariant mass spectrum after subtraction of NN reference: strong broadening of in-medium ρ spectral function due to its coupling to baryonic resonances [1].

e^+/e^- candidates selection in pp at 4.5 GeV

The experiment took place in February 2022, using a proton beam with a kinetic energy of 4.5 GeV/nucleon on a liquid hydrogen target. In order to identify e^+ and e^- candidates in the data sample, RICH and ECAL information is used to increase the purity of the selection as will be discussed in the following sections. At this stage of analysis, time of flight detectors are not YET used due to some calibration problems.

RICH detector

The Ring Imaging Cherenkov detector (RICH) is the most important detector for electron identification. It is based on the Cherenkov effect: a charged particle with velocity larger than the speed of light in the RICH material (C_4F_{10}) creates a Cherenkov light in a cone. The photons are then reflected by the RICH mirror and form a ring on the photon detector.
Only particles with a velocity β greater than 0.9985 can produce light, which corresponds to 0.009 GeV/c for an electron, 2.5 GeV/c for a pion and 17 GeV/c for a proton. This threshold will clearly be reached only by electrons. Thus a signal in the RICH means the presence of an electron/positron candidate.
The parameters used to select lepton tracks are the difference $\Delta\theta(\Delta\phi)$ between the polar(azimuthal) angle of the track and the ones of the ring. The correlation between $\Delta\theta$ and $\Delta\phi$ is shown in the left part of Figure 5. The strategy is to keep events in a $\pm 2\sigma$ region around the peak.

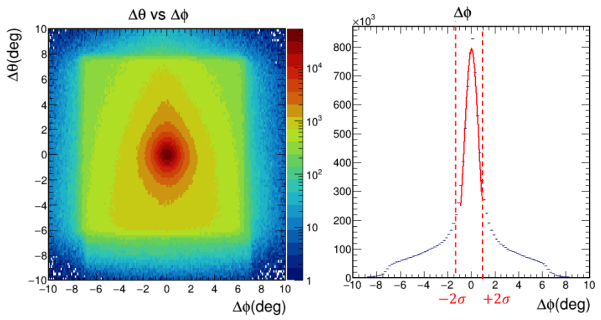

Figure 5: Angular correlation between track and ring. Left: Polar $\Delta\theta$ as a function of azimuthal angle $\Delta\phi$ difference. Right: $\Delta\phi$ distribution. The red curve is a gaussian fit and the dashed lines show the $\pm 2\sigma$ selection.

ECAL detector

In order to improve the purity of the candidate selection, the ECAL information matched with the track is also checked. The value of the quantity $E-P$ indicates

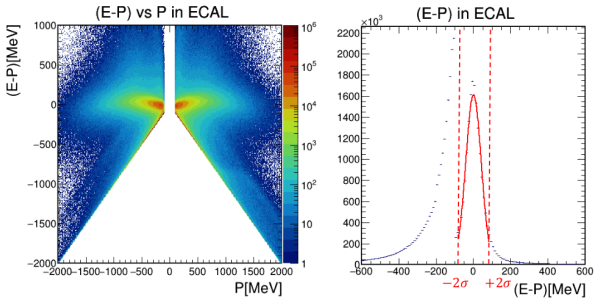

Figure 6: Left: difference between the energy deposited in the ECAL and the momentum. Right:$(E-P)$ projection, showing the lepton peak around $(E-P=0)$ a gaussian fit (red curve) and the $\pm 2\sigma$ selection.

the type of measured particles, it is around 0 for electrons and positrons, as they leave all their energies in the material, while it is expected to be negative for the hadrons that leave much less energy passing through the detector. This is illustrated in Figure 6. The peak around $(E-P=0)$ is fitted with a gaussian and leptons are selected using a $\pm 2\sigma$ cut. In this way, the purity of the lepton selection can be improved at the highest momenta.

Invariant mass spectra

After the selection of e^+ and e^- candidates, they should be grouped into pairs. Two kinds of background, which are in fact connected, must be reduced: the production of e^+e^- pairs via conversion of real photons in the target and detector material, and the combinatorial background due to the combination of leptons produced by different real or virtual photons. As the conversion is a strong source of combinatorial background, it is important to try to reduce it. The combinatorial background (CB), due to the combination of leptons produced by different real or virtual photons must be subtracted. There are two categories of combinatorial background: correlated and un-correlated CB as shown in Figure 7. The CB is estimated by the geometrical mean of like-sign $e^+e^+(N_{++})$ and $e^-e^-(N_{--})$ pairs [4]:

$$CB_{+-} = 2\sqrt{N_{++}N_{--}}.$$

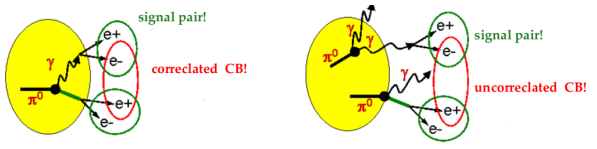

Figure 7: Left: Correlated CB where e^+ and e^- come from the same mother particle but from different intermediate photons. Right: Uncorrelated CB where e^+ and e^- come from different mother particles.

A strong contribution to the CB arises from the conversion of real photons in the target and detector material, it is therefore important to suppress it as much as possible. As these pairs are characterized by a small opening angle, a partner of a conversion pair is identified in the analysis code if the ring has a high number of hits in the photon detector (overlapping rings) or if a nearby track segment, in a cone of 4° is found in the inner detectors. Such tracks are removed from the sample and hence do not contribute to the CB. Finally, after CB subtraction, only pairs with opening angle larger than 9° are kept, to fully suppress the conversion contamination.
A preliminary result of e^+e^- invariant mass spectrum (obtained from 7 days of data taking, out of the 28 available) is shown in the Figure 8.

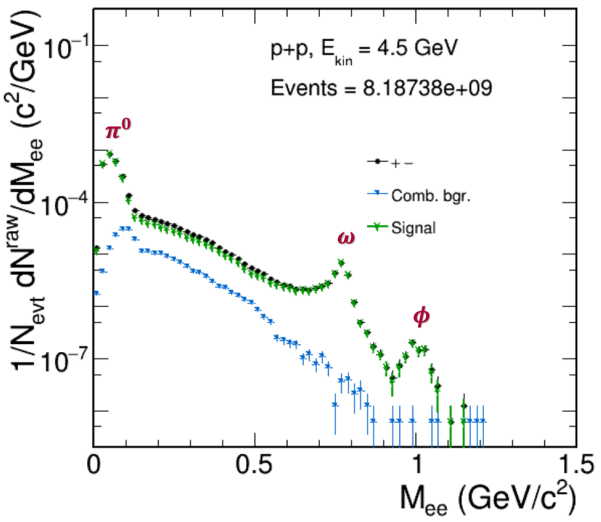

Figure 8: e^+e^- invariant mass spectrum in pp collisions at 4.5 GeV with HADES (preliminary): the distribution features clear peaks around π^0, ω and ϕ masses.

PLUTO simulations

PLUTO is an event generator developped by the HADES collaboration [5], and it is based on the ROOT framework. It allows to describe particle production and their hadronic and leptonic decays in elementary and heavy-ion reactions. For example, in pp collisions at 4.5 GeV, it is used to build the "inclusive" cocktail with defined cross sections for each source of e^+e^-. The events are first generated in PLUTO, then passed through GEANT where the detector geometry and instrumental effects are taken into account, and finally reconstructed similarly to data analysis. The cross sections of π^0, η, Δ, ρ and ω are extrapolated from HADES measurements at 3.5 GeV[6], the η' cross section is estimated based on the η'/η ratio measured by DISTO [7] ($\sigma_{\eta'} = \sigma_\eta \times 0.83 \times 10^{-2}$) and ϕ on the ϕ/ω ratio measured by ANKE [8]($\sigma_\phi = \sigma_\omega \times 8 \times 10^{-3}$). We also introduced the double Δ production, using cross section from SMASH and calculating the isospin factors for the different isospin states as shown in Figure 9, as in pp we can have two Δ production in the following way:

$$pp \rightarrow \Delta^+(pe^+e^-)\Delta^+(p\pi^0 or\ n\pi^+).$$

and

$$pp \rightarrow \Delta^0(ne^+e^-)\Delta^{++}(p\pi^+).$$

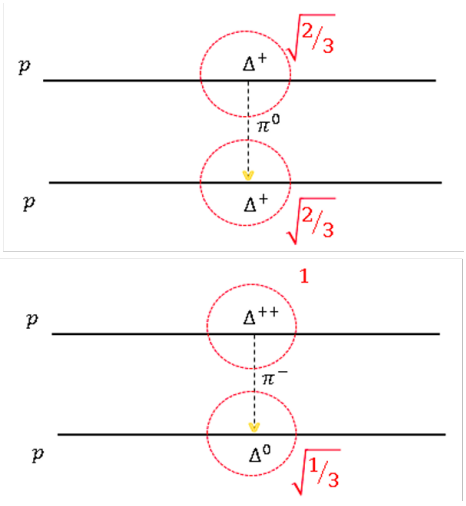

Figure 9: Schematic representation of isospin factor determination for double Δ production in pp collisions.

For the Δ Daliz decay ($\Delta \rightarrow Ne^+e^-$), we use the branching ratio 4.2×10^{-5}, as measured by the HADES collaboration[10]. The table 2 summarizes the cross sections and branching ratios for all contributions to the cocktail.

The cocktail for pp at 4.5 GeV using PLUTO is shown in Figure 10, once the efficiency of the simulations will be checked to be realistic, the result will be compared to the data.

Source	cross section [mb]	Branching Ratio [%]
Mesons Dalitz decay		
π^0	22.2	1.2
$\pi\pi$	11	1.8
η	1.5	0.6
η'	1.2×10^{-2}	4.7×10^{-4}
ω	0.35	7.7×10^{-4}
Mesons direct decay		
ω	0.35	7×10^{-5}
ρ	0.35	4×10^{-5}
ϕ	2.8×10^{-3}	3×10^{-4}
Baryon Dalitz decay		
$N(1520)$	5	2.3×10^{-5}
$\Delta(1232)$	11.5	4.2×10^{-5}
$\Delta(1232)\Delta(1232)$	8.3	6.6×10^{-5}

Table 2: Cross sections used as inputs for PLUTO simulations.

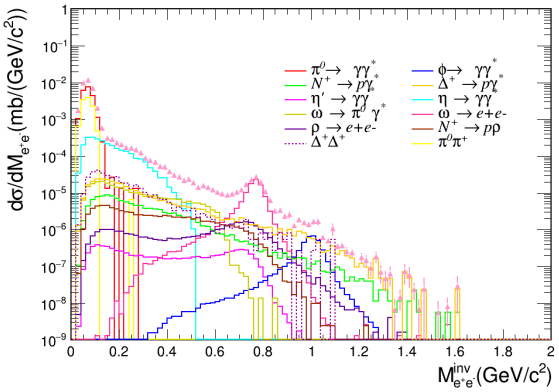

Figure 10: PLUTO simulations (preliminary) for pp at 4.5 GeV

Conclusions and Outlook

The study of e^+e^- emission in pp collisions at 4.5 GeV will be a reference for future measurements in heavy-ion collisions with HADES. It will help to understand the in-medium effect in the hot and dense phase. The purity of the e^+e^- selection will improve when all calibration procedures will be completed, and then it will be possible to extract ω and ϕ production cross sections. More detailed simulations are needed to verify the efficiency of data reconstruction.
Not only the inclusive channels are important, but also the exclusive ones (where one proton is detected in addition to the e^+e^- pair) that allow for a selective study of baryon resonance Dalitz decay and ρ/ω decay, via the $pp \rightarrow ppe^+e^-$ reaction.

References

[1] J. Adamczewski-Musch et al. (HADES collaboration), Probing dense baryon-rich matter with virtual photons, Nature Phys. 15 (2019) 1040-1045.

[2] G. Agakishiev et al. (HADES collaboration), Eur.Phys. J. A41, 243-277 (2009).

[3] G. E. Brown and M. Rho, Phys. Rev. Lett. 66, 2720 (1991), Scaling effective Lagrangians in a dense medium.

[4] M. Gázdzicki and M.I. Gorenstein, Background subtraction from the dilepton spectra in nuclear collisions, (2000).

[5] I. Frohlich et al. (HADES collaboration), Pluto : A Monte Carlo Simulation Tool for Hadronic Physics. PoS ACAT, 2007.

[6] G. Agakishiev et al. (HADES collaboration), Inclusive dielectron spectra in p+p collisions at 3.5 GeV kinetic beam energy. Eur. Phys. J. A (2012).

[7] F. Balestra et al. (DISTO), Phys. Lett. B 491 (2000)29.

[8] M. Hartmann et al.(ANKE), Phys. Rev. Lett. 96 (2006) 242301.

[9] U. Mosel, Fields, Symetries and Quarks (Springer, Berlin, 1999).

[10] J. Adamczewski-Musch et al. (HADES collaboration), Phys.Rev.C 95 (2017) 6, 065205.

Charged-particle pseudorapidity density in proton-proton collisions at $\sqrt{s} = 900$ GeV with the ALICE MFT and ITS2

Sarah Herrmann

IP2I Lyon

Abstract — Charged-particle pseudorapidity density measurements help to understand the particle production mechanisms in high-energy hadronic collisions, from proton-proton to heavy-ion systems. Performing such measurements at forward rapidity, in particular, allows one to access the details of the phenomena associated with particle production close to the fragmentation region of the colliding nuclei. In ALICE, these measurement are performed in the LHC Run 3 exploiting the Muon Forward Tracker (MFT), a newly installed detector extending the inner tracking pseudorapidity coverage of ALICE in the range $-3.6 < \eta < -2.5$. The performance of the ALICE MFT will be presented for the pilot beam data taking of October 2021 for proton-proton collisions at $\sqrt{s} = 900$ GeV, together with a preliminary result for the charged-particle pseudorapidity density at midrapidity.

Introduction

The MFT is a high-precision tracking detector designed to provide prompt/non-prompt quarkonium separation by adding vertexing capabilities to the ALICE muon spectrometer. This new detector also allows ALICE to extend its multiplicity measurements via particle tracking to the forward rapidity region.

Charged-particle pseudorapidity density is defined as the number of primary charged particles per collision and unit of pseudorapidity: in other terms, it is a multiplicity measurement as a function of the pseudorapidity. Thanks to the addition of the MFT, the charged-particle pseudorapidity density can now be studied in ALICE in two pseudorapidity regions: the central one $-1.2 < \eta < 1.2$ and the forward one $-3.6 < \eta < -2.5$.

In the following, the detectors used to estimate the charged-particle pseudorapidity density will be presented, and their performance during the pilot proton-proton (pp) run at $\sqrt{s} = 0.9$ TeV will be shown.

Description of the detectors

The three ALICE sub-detectors used to perform the measurement are the upgraded Inner Tracking System (ITS2), the Time Projection Chamber (TPC) and the Muon Forward Tracker (MFT).

The MFT and the ITS2 detectors are both used for tracking and vertexing purposes, and are equipped with ALPIDE chips developed by the ALICE collaboration, implementing the Complementary Metal-Oxide-Semiconductor (CMOS) Monolithic Active Pixels Sensors (MAPS) technology. The specificity of this technology is the integration of the sensitive volume and the read-out electronics in the same silicon layer [5], resulting in a significant reduction of the material budget with respect to the hybrid silicon pixel detectors. The pixel pitch of the ALPIDE chip allows for a space resolution of 5 μm and the time resolution is lower than 4 μs. Their usage in the ITS2 and MFT constitute the first large-scale application of this technology in an LHC experiment.

The ITS2 is an upgraded version of the ITS exploited during Run 1 and Run 2, and is made of seven cylindrical detector layers (from $R = 22$ mm to $R = 400$ mm). Its pseudorapidity coverage is $|\eta| < 0.9$. The ITS and TPC tracks can be matched with each other, extending the coverage to $|\eta| < 1.2$.

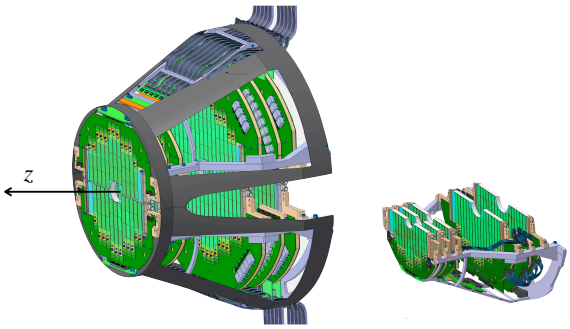

Figure 1: The MFT detector layout, and its bottom half cone

The MFT is one of the main improvement of ALICE in view of Run 3. It was installed at the end of 2020, and enables the tracking of charged particles at forward pseudorapidity, a feature which was not possible during Run 1 and Run 2. This detector is made of two half cones composed of five detection disks perpendicular to the beam axis, as one can see in the Figure 1, located between $z = -460$ mm and $z = -768$ mm (the nominal

interaction point being located in $z = 0$). Each disk consists of a front and back detection planes [6] and the ensemble covers the pseudorapidity region $-3.6 < \eta < -2.5$.

MFT performance

In order to test the behavior of the ALICE detector,data were collected in October 2021 from proton-proton collisions at a centre-of-mass energy of $\sqrt{s} = 0.9$ TeV, exploiting the first pilot beams circulating in the LHC after the Long Shutdown 2.

Long Shutdown 2 was a time period in which the LHC stopped taking data, it was scheduled to start in July 2018 and ended in September 2021. During this time, maintenance and consolidation of both the LHC and the detectors took place, along with detector upgrades.

In this section we will show performance studies conducted using both pilot beam data and Monte Carlo simulations, such as the (x, y) distribution of the transverse position of clusters in the farthest disk from the interaction point (in Figure 2) and the product of the MFT geometrical acceptance and reconstruction efficiency (Acc × Eff in Figure 3). As one can see in Figure 2, there are very few and limited inefficient (dead) zones, which are visible in white. In Figure 3 one can appreciate the η-z_{vtx}dependence of the combined geometrical acceptance and reconstruction efficiency, and the correlation between the two variables due to the geometrical configuration of the detector. As expected, the product of acceptance times efficiency is larger than 90% in a significant part of the distribution, defining the region corresponding to the nominal acceptance of the detector.

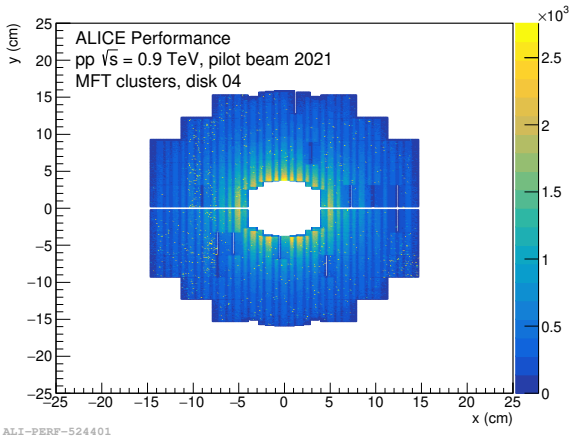

Figure 2: (x, y) position of MFT clusters in the farthest disk from the interaction point

These two figures confirm the excellent performances of the MFT in terms of geometrical acceptance and reconstruction efficiency, and the limited amount of inefficient detecting regions.

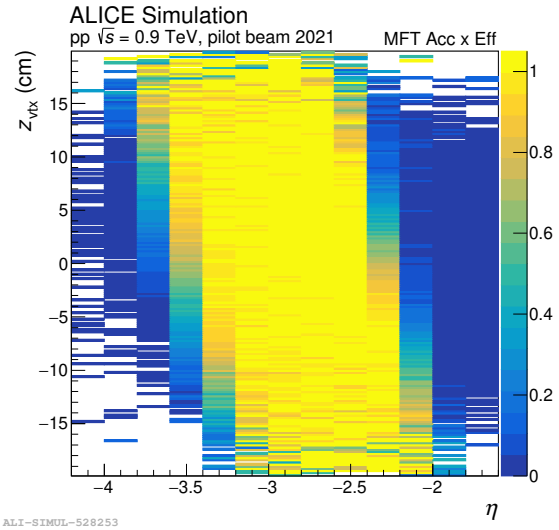

Figure 3: MFT Acceptance times efficiency as a function of z_{vtx} and η

Analysis strategy

In this section the general analysis strategy is described. The corresponding analysis task was implemented in the new analysis framework of ALICE [7]. At the time of the conference, the results for the charged-particle pseudorapidity density with the MFT were not yet finalized, and are therefore not shown here.

For the analysis at midrapidity, we considered tracks reconstructed with the ITS2 and the TPC detectors. For the measurement at forward rapidity, we used only tracks reconstructed with the MFT (imposing the condition that they have a hit in at least 4 out of the 5 MFT disks). The kinematics of the reconstructed tracks and their number are corrected by the combined effect of geometrical acceptance and reconstruction efficiency. The acceptance times efficiency is estimated exploiting simulations implementing PYTHIA8 [8] for the particle generation and GEANT3 [9] for the transport through the experimental setup. The corresponding distributions for the MFT and ITS2+TPC are shown in Figure 3 and 4, respectively.

The correction procedure is composed of two different types of correction: the track-to-particle correction, corresponding to the acceptance times efficiency profile, and the triggering efficiency correction, representing the fraction of triggered events over all generated events[2].

On top of these two corrections, an additional one is necessary to account for the underestimated cross-section of diffraction events in PYTHIA8: the single and double diffractive events, representing respectively 20% and 10% of the total inelastic cross-section [4], are underestimated by PYTHIA8. Consequently, the total number of inelastic events is also underestimated and the charged-particle pseudorapidity density is overestimated. Including this correction is the next foreseen step, with a detailed study of systematic uncertainties based on different models.

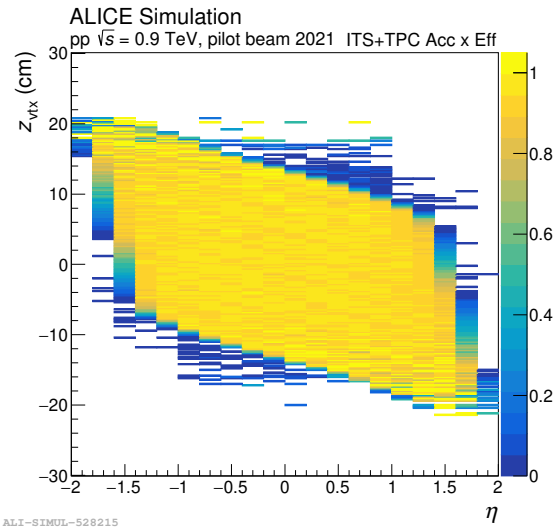

Figure 4: ITS2+TPC Acceptance times efficiency as a function of z_{vtx} and η

Results

The charged-particle pseudorapidity density is measured from all inelastic events of the pilot beam data and is shown in Figure 5 for the pseudorapidity interval $|\eta| < 1.2$. The projected systematic uncertainties are represented by the red band and have been estimated using the systematic uncertainty computed in [3]. This result is also compared with the ALICE measurements of charged-particle pseudorapidity density performed during the LHC Run 1 [3], and with Monte Carlo simulations based on PYTHIA8. The overall shift between the pilot beam and Run 1 results is due to the lack of diffraction tuning of the pilot beam MC simulation used, as mentioned above.

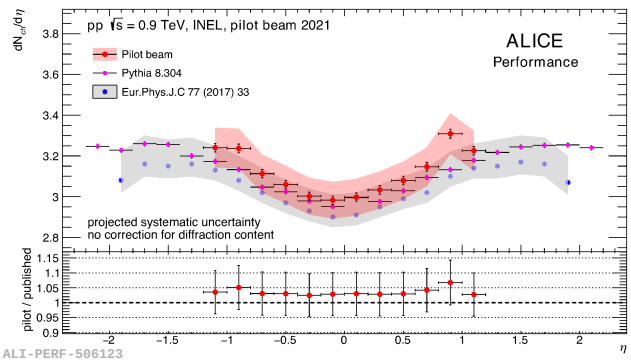

Figure 5: $\mathrm{d}N_{\mathrm{ch}}/\mathrm{d}\eta$ result in pilot beam October 2021 at midrapidity

The Run 1 and Run 3 data are compatible within uncertainties, which provides a reliability check on the performances of the ITS2 and of the new analysis framework.

This work will be completed by the addition of the forward rapidity measurement performed with the MFT, extending the results in the region $-3.6 < \eta < -2.5$ and fully characterizing the charged-particle pseudorapidity density in ALICE Run 3.

References

[1] Wolschin, G. Aspects of Relativistic Heavy-Ion Collisions. Universe 2020, 6, 61. https://doi.org/10.3390/universe6050061

[2] A. Alkin and B. Kim, Analysis note: Charged-particle multiplicity and pseudorapidity density measurements in pp collisions from $\sqrt{s} = 0.9$ to 8 TeV, using improved track counting algorithms, tech. rep. (ALICE-ANA-2015-2432, 2017).

[3] Adam, J., Adamova, D., Aggarwal, M.M. et al. *Charged-particle multiplicities in proton-proton collisions at $\sqrt{s}$=0.9 to 8 TeV*. Eur. Phys. J. C 77, 33 (2017)

[4] ALICE Collaboration, *Measurement of inelastic, single- and double-diffraction cross sections in proton-proton collisions at the LHC with ALICE* Eur.Phys.J. C73 no. 6, (2013)

[5] The ALICE Collaboration, *Technical Design Report for the Upgrade of the ALICE Inner Tracking System* (2014) J. Phys. G: Nucl. Part. Phys. 41 087002

[6] The ALICE collaboration, *Technical Design Report for the Muon Forward Tracker*, CERN-LHCC-2015-001, ALICE-TDR-018 (2015), https://cds.cern.ch/record/1981898

[7] Buncic, P and Krzewicki, M and Vande Vyvre, P, *Technical Design Report for the Upgrade of the Online-Offline Computing System*, 2015

[8] C. Bierlich et al, SciPost Phys. Codebases 8-r8.3 (2022) [arXiv:2203.11601 [hep-ph]], *A comprehensive guide to the physics and usage of PYTHIA 8.3*

[9] Brun, R and Bruyant, F and Maire, M and McPherson, A C and Zanarini, P, (1987) *GEANT 3: user's guide Geant 3.10, Geant 3.11; rev. version*, `https://cds.cern.ch/record/1119728`

Dynamics of the conserved charge fluctuations in an expanding medium

Gregoire Pihan

SUBATECH UMR 6457 (IMT Atlantique, Université de Nantes, IN2P3/CNRS), 4 rue Alfred Kastler, 44307 Nantes, France

Abstract — A non-monotonic net-proton kurtosis as a function of the collision energy for very central collisions has been suggested and may be confirmed by recent BES-II program results advocating for the existence of the QCD critical point. Fluctuations at the origin of this peculiar behavior are produced in the highly dynamic environment of ultra-relativistic collisions. The violent longitudinal expansion and the associated temperature cooling in the hadronic medium in the last stage of the collision may have a non-trivial impact on how we interpret the experimental data. The in- or out-of-equilibrium nature of the fluctuations during this stage is a crucial question in discriminating between critical contributions and purely dynamical features. Here, we inspect the diffusive dynamics of the conserved-charges net-densities fluctuations in a Bjorken-type 1+1D expanding system in the hadronic medium. We suppose fluctuations to be at thermal equilibrium right after the chemical freeze-out. We observe the impact of their dynamical evolution until the kinetic freeze-out. The thermodynamics is determined by the hadron resonance gas of the 19 lightest species at first order in the chemical potentials. The non-trivial interplay between the diffusive properties of the constituents given by the diffusion matrix and the longitudinal expansion of the medium allows us to study the survival of the initial fluctuations in the hadronic phase until kinetic freeze-out. We observe that the diffusion in the hadronic medium has a huge impact on the amplitude of the critical fluctuations. We conclude that the signal is largely affected by the evolution in the hadronic medium.

Introduction

The fluctuations of conserved-charges are a relevant probe for the study of the QCD criticality in heavy-ion collisions [1, 2]. Then, having a clear understanding of their dynamical evolution in a collision is a crucial step before interpreting any experimental measurement. Due to the violent longitudinal expansion and the rapid temperature cooling of the medium, they may not survive long enough to be detected experimentally. During a heavy-ion collision, the dynamics of the three conserved charges, the baryon number (B), the electric charge (Q), and the strangeness (S), is coupled. At the microscopic level, particles generally carry several conserved-charges simultaneously. The diffusion of particles thus implies a coupled diffusion of the conserved charges. Due to the Fluctuation-Dissipation Theorem (FDT) [3] relating the diffusion and the fluctuations one expects to have a coupling between *the fluctuations* of the conserved charges.

In the hadronic phase, the equilibrium properties of the QCD matter are described by the Hadron Resonance Gas (HRG) model. From this model, one can evaluate the transport properties via a microscopic theory. The diffusion matrix $\boldsymbol{\kappa}$ as a function of the temperature and baryo-chemical potential μ_B has been calculated in [4]. In this work, we use the FDT to compute the correlation between the fluctuations of B, Q, and S based on the $\boldsymbol{\kappa}$ matrix. Starting from that, we build a set of coupled stochastic diffusion equations (SDE) which reflects the dynamical evolution of the conserved charge fluctuations in the hadronic medium. We then perform simulations based on a realistic collision model in the LHC conditions and evaluate the impact of the dynamical evolution on the conserved-charges covariances amplitudes.

Model for the dynamics of conserved-charges fluctuations

Coupled stochastic diffusion equations

Considering the global charge conservation for multiple conserved charges

$$\partial_{;\mu} N_i^\mu = 0, \tag{1}$$

where $i = B, Q, S$ and ";" stands for covariant derivative, we decompose the net-charge number current four-vector in the basis $(u^\mu, \Delta^{\mu\nu})$ as $N_i^\mu = n_i u^\mu + j_i^\mu$, n_i and j_i being respectively the net-density and current of conserved charge i [6]. Here, u^μ is the four-velocity of flow and $\Delta^{\mu\nu}$ is the projection operator orthogonal to u^μ. Now, we generalize the expression for the current in Ref [5] for multiple conserved-charges as

$$j_i^\mu = \kappa_{ij} \Delta^{\mu\nu} \partial_{;\nu} \left\{ \frac{\mu_j}{T} \right\} + \xi_i. \tag{2}$$

where μ_j the chemical potential associated to conserved charge i, k_{ij} the $\boldsymbol{\kappa}$ matrix element between charges i and j, T the temperature and ξ_i the random noise associated to charge i. Note that the Einstein convention is used on repeated Latin indices. We then obtain the equation of motion for the conserved charge densities as

$$\partial_\tau n_i = \partial_y \Big\{ \frac{\kappa_{ij}}{\tau} \partial_y \Big\{ \frac{\mu_j}{T} \Big\} \Big\} - \partial_y \xi_i \tag{3}$$

The dynamical variables τ and y are respectively the proper time and the spatial rapidity. They are used here to account for the Bjorken longitudinal expansion of the medium, particularly adapted to LHC conditions. The noise associated to conserved charge i, ξ_i is determined by its correlation function

$$\langle \xi_i(\tau, y) \xi_j(\tau', y') \rangle = \frac{2}{\tau} \kappa_{ij}(T, \mu_j) \delta(\tau - \tau') \delta(y - y') \,. \tag{4}$$

The coefficient before the Dirac-δ functions is given by the FDT. Relation (4) imposes that

$$\xi_i = \sqrt{\frac{2}{\tau}} C_{ij} Z_j \tag{5}$$

where Z_j is a centered Gaussian variable with unit variance and $\boldsymbol{C}$ is the Cholesky decomposition of the matrix $\boldsymbol{\kappa}$ defined as

$$\boldsymbol{\kappa} = \boldsymbol{C}\boldsymbol{C}^T \tag{6}$$

The matrix $\boldsymbol{C}$ exists if $\boldsymbol{\kappa}$ is a positive or semi-positive definite matrix. This is guaranteed by the second law of thermodynamics. In Fig. 1 we show $\boldsymbol{\kappa}$ (upper pannel) and $\boldsymbol{C}$ (lower panel) as a function of the temperature for LHC conditions, $\mu_B = \mu_Q = \mu_S = 0$ MeV. We observe that the dominant element matrix is in the strangeness sector. We thus expect the strangeness fluctuations to be close to equilibrium during the evolution. We also note that in all sectors both $\boldsymbol{\kappa}/T^2$ and $\boldsymbol{C}/T$ stay constant or decreases in amplitude toward zero except for the electric charge. Consequently, as the temperature decreases, the amplitude of the fluctuation and their distance to equilibrium will respectively diminish and increase. The electric charge behaves in the opposite manner.

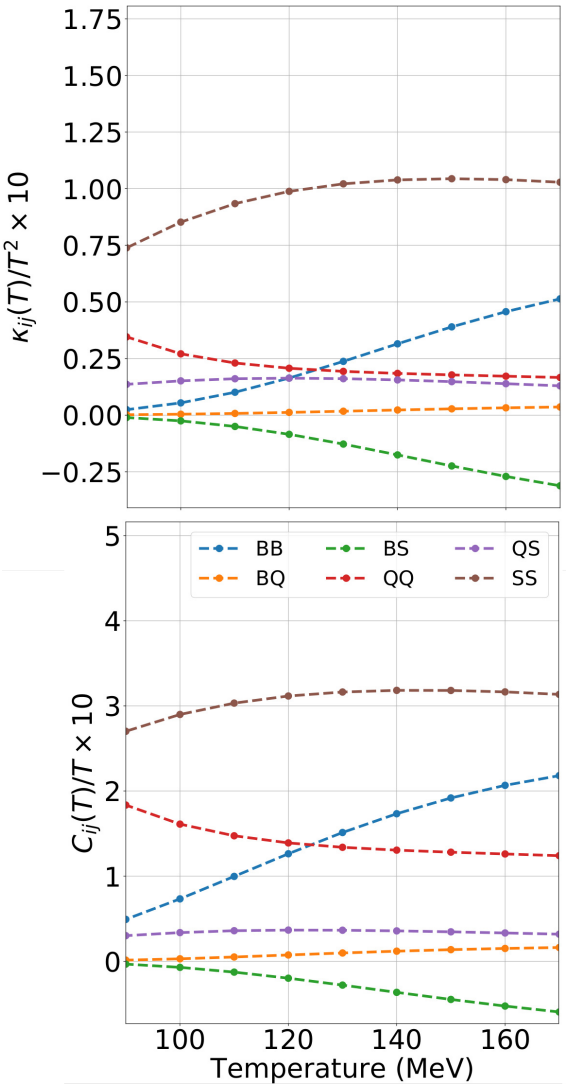

Figure 1: (color online) Upper panel: The scaled diffusion matrix element $i, j = B, Q, S$ for LHC conditions $\mu_B = \mu_Q = \mu_S = 0$ MeV as a function of the temperature. The diffusion matrix coefficients are taken from from Ref [4] and are shown here for understanding purposes. Lower panel: The scaled matrix element of the Cholesky decomposition of the diffusion $i, j = B, Q, S$ for LHC conditions $\mu_B = \mu_Q = \mu_S = 0$ MeV as a function of the temperature.

The Linear approximation in the HRG model

We use the HRG model to describe the thermodynamics in the latter stages of the collision ($T \sim 150 - 100$ MeV). In particular, we express the relation between the chemical potentials and the densities at first order as

$$n_i = \chi_{ij} \mu_j \tag{7}$$

where $\chi_{ij} = \partial n_i / \partial \mu_j$ are the cross-susceptibilities of the HRG model (see Figure 2). The relation 7 is still not linear as χ_{ij} is a function of the chemical potential. Moreover, the amplitude of the noise is given by the matrix elements of the Cholesky decomposition of the $\boldsymbol{\kappa}$ matrix, which depends on the chemical potential and

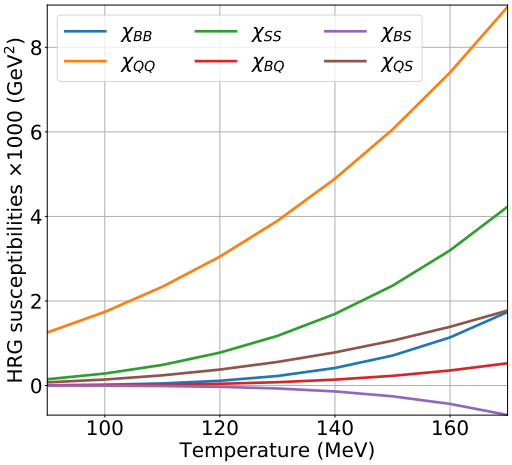

Figure 2: The cross-susceptibilities of the HRG model in LHC conditions as a function of the temperature.

thus on the density fields. The noise is multiplicative and difficult to interpret. As a first approach, we circumvent these two issues. We consider that $\boldsymbol{\kappa}$ and $\boldsymbol{\chi}$ do not depend on the local values of the chemical potentials but only on their spatial average $\boldsymbol{\mu}_0$. Relation 7 is now linear and the model only contains additive noise. It allows to rewrite equations 3 as

$$\partial_\tau n_i(\tau, y) = \frac{D_{ij}(T, \boldsymbol{\mu}_0)}{\tau} \partial_y^2 n_j(\tau, y) - \sqrt{\frac{2}{\tau}} C_{ij}(T, \boldsymbol{\mu}_0) \partial_y Z_j \quad (8)$$

where

$$D_{ij}(T, \mu_j) = \frac{1}{T} \kappa_{il}(T, \mu_j) (\boldsymbol{\chi}^{-1})_{lj}(T, \mu_j) \quad (9)$$

Equations 8 are now a set of coupled stochastic heat equation with diffusion matrix $\boldsymbol{D}$.

Dynamics of the coupled conserved-charges fluctuations

Model for the collision

In equations 8, T and $\boldsymbol{\mu}_0$ are used to determine the model for the late stage of the collision. Consistently with the longitudinal Bjorken expansion, the temperature is connected to the proper-time as

$$T(\tau) = T_i \left(\frac{\tau_0}{\tau} \right)^\alpha \quad (10)$$

with $T_i = 500$ MeV, the initial temperature, $\tau_0 = 1$ fm/c, the initial proper-time. Following the argument in Ref [7] we take $\alpha = 1$. In all generality, $\boldsymbol{\mu}_0 = \boldsymbol{\mu}_0(T)$, however, as a first approach we take $\boldsymbol{\mu}_0 = (0, 0, 0)$ MeV. It corresponds to the LHC conditions where the net densities of the conserved baryon number, electric charge and strangeness are close to 0. We split the collision into two steps, first an equilibration step to mimic a signal coming earlier in the collision. We consider the fluid in a fixed-sized box at constant temperature for a long enough duration. At the end of this stage, the density fluctuations are equilibrated at $T = 160$ MeV. Then we start the expansion and the temperature cooling from $T = 160$ MeV to $T = 100$ MeV for a total duration of 1.9 fm/c.

Equilibration of the net-baryon density fluctuations

In a first attempt, we study the evolution of the net-baryon density only, which means that $\kappa_{ij} = \kappa_{BB} \delta_{iB} \delta_{jB}$. In Fig. 3, we show the dynamical evolution of the net-baryon density variance in the equilibration procedure. The variance of the net-baryon

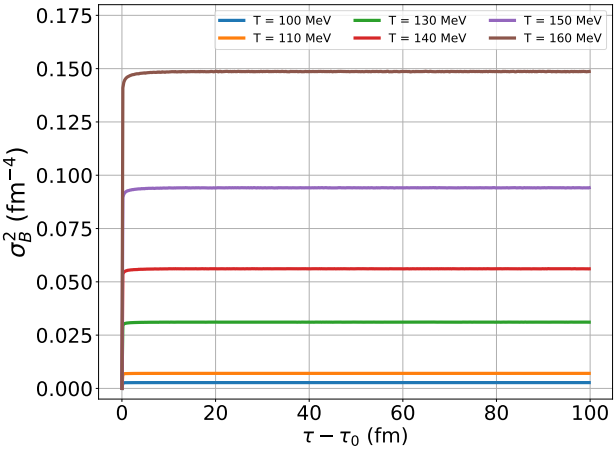

Figure 3: The dynamical evolution of the net-baryon density variance during the equilibration process for different temperatures.

density reaches a constant value for each temperature. It demonstrates that the fluctuations are at equilibrium after less than 100 fm/c. Note that the equilibration time has no physical significance here. We also see that the variance at equilibrium decreases with the temperature consistent with the variation of the susceptibility as a function of temperature in the baryon sector (blue curve in Fig. 2).

Evolution of the net-baryon density fluctuations during the expansion

Starting from the equilibrated situation obtained in the equilibration procedure at $T = 160$ MeV (brown curve in Fig. 3) we let the system expand. In Fig. 4, we show the dynamical evolution of the net-baryon density variance during the expansion as a function of the proper time (red dotted line). We compare it to the equilibrium values (black line) obtained via the equilibration procedure described above for the different temperatures. We also compare it to the net-baryon variance evolution for a fluid where the diffusion coefficient κ_{BB}

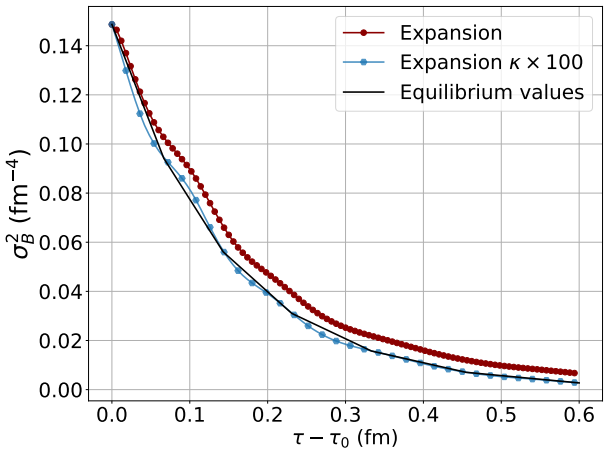

Figure 4: The dynamical evolution of the net-baryon density variance during the expansion (red dotted line) and the same evolution with artificially enhanced κ_{BB} value (blue dotted line) compared to the equilibrium values (black line) obtained via the equilibrium procedure shown in Fig. 3.

has been artificially multiplied by 100.
We observe that the variance of the net-baryon density is slightly off-equilibrium during the whole evolution. When the diffusion coefficient is artificially multiplied by 100, the variance is closer to the equilibrium values as expected from the inverse relation between the diffusion coefficient and the relaxation time [8].
We clearly see that the dynamics largely impact the evolution of the net-baryon density fluctuations in the hadronic medium. In other words, the diffusion of the fluctuations is large enough so they do not survive in the expanding hadronic medium.

Conclusion

In this work, we studied the dynamical evolution of the net-baryon density fluctuations in an expanding medium. We showed that the net-baryon density variance is largely affected by the latter stage of the collision. A signal coming from the critical point after chemical freeze-out have thus a short life-time in the LHC conditions. As it is now known from lattice QCD calculations that the critical point is not at vanishing μ_B. This result needs to be tested at finite baryo-chemical potential before claiming any major limitations on the search for criticality in the QCD phase diagram via heavy-ion collisions.
This study is preliminary and has to be understood more as proof of feasibility than a proper study. Indeed, crude approximations have been performed to obtain this result and the full model may reveal unexpected behavior due to its high non-linearity.

Acknowledgement

G. Pihan acknowledges the support of M. Bluhm, M. Nahrgang and the program "Etoiles montantes en Pays de la Loire 2017". The authors acknowledge the support of the TY-FJPPL program of IN2P3-CNRS.

References

[1] M. Asakawa, U. Heinz, and B. Müller, "Fluctuation probes of quark deconfinement," *Phys. Rev. Lett.*, vol. 85, pp. 2072–2075, Sep 2000.

[2] S. Jeon and V. Koch, "Charged particle ratio fluctuation as a signal for quark-gluon plasma," *Phys. Rev. Lett.*, vol. 85, pp. 2076–2079, Sep 2000.

[3] R. Kubo, "The fluctuation-dissipation theorem," *Reports on Progress in Physics*, vol. 29, p. 255, jan 1966.

[4] J. A. Fotakis, M. Greif, C. Greiner, G. S. Denicol, and H. Niemi, "Diffusion processes involving multiple conserved charges: A study from kinetic theory and implications to the fluid-dynamical modeling of heavy ion collisions," *Phys. Rev. D*, vol. 101, p. 076007, Apr 2020.

[5] G. Pihan, M. Bluhm, M. Kitazawa, T. Sami, and M. Nahrgang, "Critical net-baryon fluctuations in an expanding system," 2022.

[6] T. Hirano, N. van der Kolk, and A. Bilandzic, "Hydrodynamics and Flow," *Lect. Notes Phys.*, vol. 785, pp. 139–178, 2010.

[7] S. Mukherjee, R. Venugopalan, and Y. Yin, "Real-time evolution of non-gaussian cumulants in the qcd critical regime," *Phys. Rev. C*, vol. 92, p. 034912, Sep 2015.

[8] M. Nahrgang, M. Bluhm, T. Schäfer, and S. A. Bass, "Diffusive dynamics of critical fluctuations near the qcd critical point," *Phys. Rev. D*, vol. 99, p. 116015, Jun 2019.

Testing CPT symmetry via the mass difference between anti-hyperons and hyperons in pp collisions with ALICE

Romain Schotter

Institut Pluridisciplinaire Hubert Curien, UMR7178, CNRS – Strasbourg, France

Abstract — Measurements of the Ξ^-, $\overline{\Xi}^+$, Ω^-, $\overline{\Omega}^+$ masses and mass differences between particle and anti-particle, using data collected by the ALICE collaboration during the LHC Run 2 in pp collisions at a centre-of-mass energy of 13 TeV, are presented. The $\Xi^\pm$ and $\Omega^\pm$ hyperons are analysed in the decay channel $\Xi^\pm \to \pi^\pm\Lambda \to \pi^\pm\pi^\pm p^\mp$ and $\Omega^\pm \to K^\pm\Lambda \to K^\pm\pi^\pm p^\mp$. The results provide, so far, the most precise measurements of mass and mass difference of multi-strange baryons.

Introduction

Symmetries certainly stand as one of the most fruitful concepts in Physics. They are of two kinds: continuous — such as the global translations in both space and time, or the Lorentz transformations — and discrete — for example, the space- (P) and time- (T) inversions, the charge conjugation (C), and their combined transformation given by CPT. In particular, the Lorentz and CPT symmetries are connected by the so-called CPT theorem which states that any local Lorentz-invariant quantum field theory must also (under some extra requirements) be CPT invariant [1]. Consequently, the CPT violation implies the breaking of the Lorentz symmetry, and vice versa[1] [6]. Another implication involves the relation between the properties of matter and antimatter: due to the charge conjugation linking particles to antiparticles, the CPT symmetry imposes that they share the same invariant mass, energy spectra, lifetime, coupling constants, etc [5]. Most of the experimental checks of CPT invariance stem from these physical consequences.

The Particle Data Group (PDG) [7] compiles a large variety of CPT tests from many experiments and with a high degree of precision; so far, no CPT violation have been observed. However, for a certain number of them, there is some room for improvements. For example, we can mention the measurements of the mass difference between particle and anti-particle in the multi-strange baryon sector. The only test of this nature dates back to 2006 [8] for the Ξ^- and $\overline{\Xi}^+$, and from 1998 [9] for the Ω^- and $\overline{\Omega}^+$ mass differences. Both studies suffer from low statistics: ∼2500(2300) reconstructed Ξ^- ($\overline{\Xi}^+$) and ∼6323(2607) reconstructed Ω^- ($\overline{\Omega}^+$) were used.

In these proceedings, we present a measurement of the mass difference of the Ξ^- and $\overline{\Xi}^+$, and of the Ω^- and $\overline{\Omega}^+$ baryons. The data samples are much larger than those exploited previously: ∼2 400 000 ($\Xi^- + \overline{\Xi}^+$) and ∼129 000 ($\Omega^- + \overline{\Omega}^+$) with little background. These direct measurements of the mass difference offer a test of the CPT invariance to an unprecedented precision in the multi-strange baryon sector. The absolute masses are updated as well, with a precision substantially better than the current values listed in the PDG and presented in the Tab. 18.

In the following, the mass difference will always refer to the normalized one, namely $(M_{\overline{\text{part}}} - M_{\text{part}})/M_{\text{part}}$.

Parameter	Ξ^- ($\overline{\Xi}^+$)	Ω^- ($\overline{\Omega}^+$)
Quark content	dss ($\bar{d}\bar{s}\bar{s}$)	sss ($\bar{s}\bar{s}\bar{s}$)
Mass (MeV/c^2)	1321.71 ± 0.07	1672.45 ± 0.29
Mass difference ($\times 10^{-5}$)	-2.5 ± 8.7	-1.44 ± 7.98

Table 1: Particle properties as of 2022, listed into [7].

Detector setup and data sample

All the aforementioned particles are reconstructed at mid-rapidity ($|y| < 0.5$), using the central detectors of the ALICE experiment [10] at the LHC: the primary

[1] In fact, there is another option; to allow for CPT to be violated, either the Lorentz symmetry must be broken – as in the string theory [2] or the Standard-Model Extension [3] – or some of the other extra assumptions of the CPT theorem must be dropped, namely the energy positivity, local interactions, finite spin, etc [4][5].

and secondary vertices are built using the Inner Tracking System (ITS), composed of six concentric layers of silicon detectors. The main tracking device is the Time Projection Chamber (TPC), that also provides particle identification of pions, kaons and protons based on their energy loss in the detector. The central part of the experiment is embedded in a large solenoid magnet (also called the L3 magnet), which offers three magnetic field configurations: +0.5, -0.5 and -0.2 T.

The mass of the particles of interest is measured in pp collisions at a centre-of-mass energy $\sqrt{s} = 13$ TeV, using approximately 2.6×10^9 minimum bias events collected in 2016, 2017 and 2018. Only data taken with the L3 magnet set to a magnetic field value of ± 0.5 T are considered.

The data analysis

In this analysis, the charged Ξ and Ω baryons are studied in their cascade decay channel: $\Xi^{\pm} \rightarrow \pi^{\pm}\Lambda \rightarrow \pi^{\pm}\pi^{\pm}p^{\mp}$ (with a branching ratio BR = 63.9 %) and $\Omega^{\pm} \rightarrow K^{\pm}\Lambda \rightarrow K^{\pm}\pi^{\pm}p^{\mp}$ (BR = 43.4 %). The reconstruction of these decay topologies is achieved by, first, reconstructing the Λ candidates, which are then matched with a pion or kaon track. To reduce the induced combinatorial background, various topological and kinematic cuts are being used (similar to what is done in [11]).

The masses of the multi-strange baryons are measured from their invariant mass distributions, as shown on the figure 1. One can see that the signal for each species sits on top of a small residual background. It is isolated from the background through a fit of the invariant mass distribution, using the sum of two functions: one for the peak, the other for the background. For the first, several functions can be considered: a simple, double or modified Gaussian [12] or a Bukin distribution [13]. For the background shape, it consists either in a constant or linear function.

The fitting procedure provides the mass measurement: it corresponds to the center of the invariant mass peak, given by the position of the maximum of the Gaussian or Bukin function – denoted as μ. The width – the parameter σ – provides an estimation of the mass resolution. The uncertainties on both quantities come from the errors returned by the fit procedure. Based on these parameters, two regions are delimited: the peak region, containing all the signal and some residual background, is defined in $[\mu - 5\sigma; \mu + 5\sigma]$; the sidebands region, exclusively constituted of background, consists in two bands surrounding the peak region, that is $[\mu - 12\sigma; \mu - 7\sigma] \bigcup [\mu + 7\sigma; \mu + 12\sigma]$. The peak and background populations are estimated by counting the number of candidates in their respective regions; the signal in the peak region is obtained by subtracting the background from the peak population.

Figure 1 presents the invariant mass distributions of the Ξ^-, $\overline{\Xi}^+$, Ω^-, $\overline{\Omega}^+$ where the peak is represented by a Bukin function and the background by a linear function. Considering the reduced χ^2 values, all display a reasonably good fit. The mass peak sits on a small background ; 1 237 666 ±1162 Ξ^- (1 168 882 ±1128 $\overline{\Xi}^+$) and 65 232 ±277 Ω^- (63 842 ±274 $\overline{\Omega}^+$) baryons were reconstructed.

Study of systematic uncertainties

The dominant source of systematic uncertainty comes from the momentum scale calibration. This can originate from the uncertainty on the value of the magnetic field or imperfect energy loss corrections.

Momentum scale calibration

Since the data sample comes from two opposite magnetic field polarities, it has been first checked that the mass and mass difference measurements are compatible between both field configurations. Moreover, the magnetic field, B, inside the L3 magnet is known with a precision of 2 Gauss [14]. An uncertainty on B translates into a scaling of the transverse momentum of the decay daughters, and propagates to the reconstructed mass of the mother particle. This systematic uncertainty is assessed by varying the nominal value of the L3 magnetic field by ± 2 Gauss. The effect in the mass difference is small and can be neglected; on the mass value though, a variation of at most 0.028 MeV/c^2 is observed.

The errors on the energy loss corrections can arise at two different levels: there is the misknowledge on the material budget in the detectors; on top of that, the application of these corrections during the event reconstruction can also be erroneous.

A hint of the latter is found when the reconstructed mass has been observed to increase up to 0.8 MeV/c^2 with the transverse momentum and the radial position of the decay vertex. It turns out that, on one hand, too much energy[2] was added during the track reconstruction, leading to a shift in the invariant mass. On the other hand, the energy losses are calculated using the Bethe-Bloch formula [7], which depends on the mass of the tracked particle; sometimes, a wrong mass hypothesis may be applied resulting in miscalculated energy loss corrections. Both issues have been fixed directly in the reconstruction code.

If there is a discrepancy between the amount of *known* crossed material and the actual one, the estimation of the energy loss – and therefore the reconstructed mass – will be directly impacted. The material budget in the central part of the ALICE detector is known with an error of about 4.5% [15][16]. By varying the material budget in simulations by 30% and assuming linearity, the systematic effect due to an error of 4.5% on the material budget is estimated. It amounts to 0.005 and 0.004 MeV/c^2 for the Ξ^- and $\overline{\Xi}^+$, and 0.49 $\times 10^{-5}$ for their mass difference. The evaluation of the corresponding systematic uncertainties on $\Omega^{\pm}$ is ongoing.

[2] The excess of energy builds up with the decay point position.

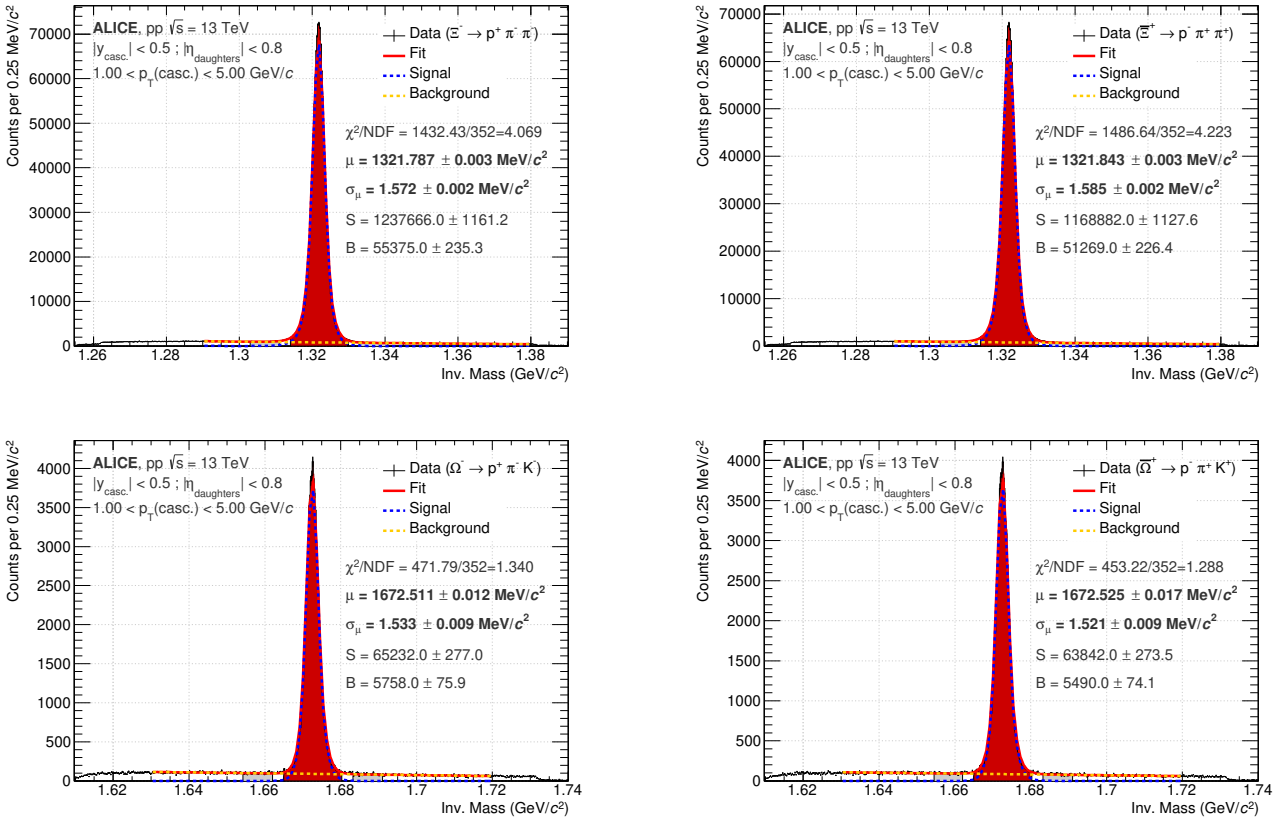

Figure 1: Invariant mass distributions of the Ξ^- (top left), $\overline{\Xi}^+$ (top right), Ω^- (bottom left) and $\overline{\Omega}^+$ (bottom right). The peak is modelled by a Bukin function, and the background by a first order polynomial. The measured mass and mass resolution, with their associated statistical uncertainties, are displayed in bold font. The red area represents the peak region; the grey ones correspond to the side-bands region.

Other systematic effects

The bias due to the candidate selections is determined by varying the topological and kinematic cuts. To go over the correlations between each selection variable, the analysis is repeated with 20 000 randomly generated sets of cuts. The masses and mass differences are averaged over all the sets: these averages will correspond to the final values. Similarly, the statistical uncertainty is given by the mean statistical error over all the sets of cuts. The standard deviation of the mass (mass difference) provides the systematic uncertainty due to the selection criteria, which varies from 0.014 to 0.019 MeV/c^2 (0.39 to 0.77 $\times 10^{-5}$ respectively) for both $\Xi^{\pm}$ and $\Omega^{\pm}$.

The effect of the shape of the mass peak or the background has been estimated, as well as the choice of the fitting range. All combinations of the peak and background functions mentioned above have been tried; the fluctuations of the mass and mass difference do not exceed 0.013 MeV/c^2 and 0.12 $\times 10^{-5}$ respectively. About 20 000 randomized fitting ranges were tested; no statistically significant variation has been observed.

The stability of the fit with respect to the bin width has been investigated by increasing it by a factor two, three and four. This led to variations in the mass value of $\pm$ 0.002 and $\pm$ 0.003 MeV/c^2, and mass difference of $\pm$ 0.03 and $\pm$ 0.13 $\times 10^{-5}$ for $\Xi^{\pm}$ and $\Omega^{\pm}$ respectively.

The mass of the $\Xi^{\pm}$ ($\Omega^{\pm}$) candidates also depends on the value of $\pi^{\pm}$ ($K^{\pm}$ respectively) and Λ masses. The influence of the uncertainties on the decay daughters mass is estimated by generating random masses according to a Gaussian distribution centred on their nominal mass with their associated uncertainties as standard deviation, and looking at the induced mass and mass difference deviations. The corresponding uncertainties on the $\Xi^{\pm}$ and $\Omega^{\pm}$ masses amount to 0.007 and 0.017 MeV/c^2 respectively; they are negligible for the mass differences.

The contribution of the pile-up is evaluated by varying the requirements on the pile-up rejection. The effect has been found to be small: 0.004 and 0.003 MeV/c^2 on the $\Xi^{\pm}$ and $\Omega^{\pm}$ masses; it is negligible on their mass differences.

Finally, in order to correct for any remaining bias due to the data processing, the analysis or the fit procedure, the mass measured in real data are corrected for the mass offset observed in MC with respect to the injected mass. Such a correction assumes a good agreement between the data and MC. To that end, the simulation has been re-weighted to match the p_{T} spectra from the data. Tables 2 and 3 show these corrections, the corrected mass and mass difference values, as well as the systematic uncertainty attached to these correc-

Particle	Ξ^-	$\overline{\Xi}^+$	Ω^-	$\overline{\Omega}^+$
Mass offset in data (MeV/c^2)	0.004 ± 0.004	0.055 ± 0.004	0.090 ± 0.014	0.066 ± 0.014
Mass offset in MC (MeV/c^2)	-0.127 ± 0.003	-0.125 ± 0.003	-0.023 ± 0.004	-0.005 ± 0.004
Corrected mass (MeV/c^2)	1321.841 ± 0.005	1321.890 ± 0.005	1672.517 ± 0.015	1672.511 ± 0.015
Systematic uncertainty (MeV/c^2)	0.003	0.003	0.004	0.004

Table 2: Measurements of the mass offsets from the PDG value (which coincides with the injected mass in MC), and the final corrected masses as well as the systematic uncertainty on that correction for Ξ^-, $\overline{\Xi}^+$, Ω^-, $\overline{\Omega}^+$. The uncertainties on the masses correspond to the statistical one; the systematic uncertainty due to the offset correction has been propagated into the error on the corrected mass.

Particle	$\Xi^\pm$	$\Omega^\pm$
Mass difference in data ($\times 10^{-5}$)	3.85 ± 0.37	-1.41 ± 1.13
Mass difference in MC ($\times 10^{-5}$)	0.16 ± 0.33	-1.08 ± 0.34
Corrected mass difference ($\times 10^{-5}$)	3.69 ± 0.50	-0.33 ± 1.19
Systematic uncertainty ($\times 10^{-5}$)	0.33	0.34

Table 3: Measurements of the mass differences, and the final corrected mass differences as well as the systematic uncertainty on that correction for $\Xi^\pm$ and $\Omega^\pm$. The uncertainties on the mass differences correspond to the statistical one; the systematic uncertainty due to the offset correction has been propagated into the error on the corrected mass difference.

tions. The latter corresponds to the statistical error in the MC simulation.

Results

All the aforementioned biases are *a priori* independent, and therefore the total systematic uncertainties can be taken as the quadratic sum of all the contributions. The final values of the $\Xi^\pm$ and $\Omega^\pm$ masses are:

$$M(\Xi^-) = 1321.841 \pm 0.004(\text{stat.}) \pm 0.033(\text{syst.})\ \text{MeV}/c^2,$$
$$M(\overline{\Xi}^+) = 1321.890 \pm 0.004(\text{stat.}) \pm 0.034(\text{syst.})\ \text{MeV}/c^2,$$
$$M(\Omega^-) = 1672.517 \pm 0.014(\text{stat.}) \pm 0.035(\text{syst.})\ \text{MeV}/c^2,$$
$$M(\overline{\Omega}^+) = 1672.511 \pm 0.014(\text{stat.}) \pm 0.037(\text{syst.})\ \text{MeV}/c^2.$$

The final (normalized) mass difference between particle and anti-particle are:

$$\frac{M(\overline{\Xi}^+) - M(\Xi^-)}{M(\Xi^-)} = [3.69 \pm 0.81(\text{tot.})] \times 10^{-5},$$

$$\frac{M(\overline{\Omega}^+) - M(\Omega^-)}{M(\Omega^-)} = [-0.33 \pm 1.43(\text{tot.})] \times 10^{-5},$$

where the total uncertainty is calculated by summing the statistical and systematic uncertainties in quadrature.

Our measurements can be compared to the current values given by the PDG [7] reproduced in Tab. 18. The uncertainty on the mass values has been reduced by approximately a factor of 2 for the $\Xi^\pm$ and 7.2 for the $\Omega^\pm$ particles. On the mass difference, the precision has been improved by a factor of ~ 10 and ~ 5.5, for Ξ and Ω baryons respectively. These are so far the most precise measurements of the $\Xi^\pm$ and $\Omega^\pm$ masses, and mass differences between these particle and anti-particle.

Conclusion

Based on a sample of approximately 2 400 000 ($\Xi^- + \Xi^+$) and 129 000 ($\Omega^- + \Omega^+$) collected by the ALICE experiment, measurements of their masses, as well as their mass differences between particle and anti-particle have been performed. The presented results are based on a statistics of strange baryons that is much larger than that cited by the PDG and thus are dominated by the statistical uncertainties anymore.

Through this paper, it also has been shown that a good understanding of the momentum scale is essential to perform such measurements, and that requires a fine comprehension of the data reconstruction. In the end, this stands as the dominant source of systematic effects.

Considering our precision, it should be mentioned that the $\Omega^\pm$ masses are both compatible with the value tabulated by the PDG. However, the Ξ^- and $\overline{\Xi}^+$ results are off by almost 2 and 3 σ_{PDG} respectively. Moreover, the $\Xi^\pm$ masses are separated by 0.049 MeV/c^2, leading the measured mass difference to be incompatible with 0 and thus suggesting a violation of the CPT symmetry. Conversely, the mass difference between Ω^- and $\overline{\Omega}^+$ validates the CPT invariance. This difference between the Ξ and Ω results requires further investigation.

References

[1] Kostelecky, arXiv:hep-ph/9810365 (1998)

[2] Kostelecký and Samuel, Phys. Rev. D **39**, 683 (1989)

[3] Colladay and Kostelecký, Phys. Rev. D **58**, 116002 (1998)

[4] Greenberg, Phys. Rev. Lett. **89**, 231602 (2002)

[5] Lehnert, Symmetry **2016**, 8(11), 114 (2016)

[6] Sozzi, J. Phys. G: Nucl. Part. Phys. **47** 013001 (2020)

[7] Particle Data Group, Prog. Theor. Exp. Phys. **2022**, 083C01 (2022)

[8] DELPHI Collaboration, Phys. Lett. B 639, 179-191 (2006)

[9] E756 Collaboration, Phys. Rev. D **58**, 072002 (1998)

[10] ALICE Collaboration, J. Inst. **3**, S08002 (2008)

[11] ALICE Collaboration, Eur. Phys. J. C **80**, 167 (2020)

[12] ATLAS Collaboration, Phys. Rev. D **85**, 012001 (2012)

[13] Bukin, arXiv:0711.4449 (2007)

[14] Shahoyan, ALICE-INT-2007-012 (2007)

[15] ALICE Collaboration, Int. J. Mod. Phys. A, 29(24) **47** 1430044 (2014)

[16] ALICE Collaboration, Nat. Phys. (2022)

Rapidity-differential J/ψ photoproduction in Pb−Pb collisions with nuclear overlap measured in ALICE at the LHC

Afnan Shatat

Université Paris-Saclay, Laboratoire de Physique des 2 Infinis, Irène Joliot-Curie, Orsay, France

Abstract — An unexpected significant excess of low $p_{\rm T}$ J/ψ meson over the expected hadronic J/ψ production was recently observed in peripheral Pb−Pb collisions at $\sqrt{s_{\rm NN}} = 5.02$ TeV with ALICE at the LHC. Measurements were performed in the dimuon decay channel at forward rapidity ($2.5 < y < 4$) and in the dielectron decay channel at midrapidity ($y < |0.9|$). A significant increase in the J/ψ nuclear modification factor was observed in peripheral Pb−Pb collisions at low $p_{\rm T}$, below 0.3 GeV/c. Most of the excess is believed to originate from a coherent photoproduction mechanism, which was unexpected in peripheral collisions with nuclear overlap and is well known in ultraperipheral Pb−Pb collisions. Coherent photoproduction implies that the photon emitted by the first nucleus interacts with the second nucleus as a whole, which stays intact after the interaction. Many theoretical models developed for ultraperipheral collisions have been extended in order to provide as well a description of the coherent photoproduction mechanism in Pb−Pb collisions with nuclear overlap.

Introduction

Quantum Chromodynamics (QCD) predicts the formation of a state of matter called the Quark-Gluon Plasma (QGP), where the quarks and gluons are deconfined. This state of matter is assumed to have existed a few microseconds after the Big Bang. In order to form a QGP medium, a very high temperature and/or energy density need to be reached. Experimentally, ultrarelativistic heavy-ion collisions recreate the required conditions to form a QGP medium. This medium is studied, among others, in the ALICE experiment at the Large Hadron Collider LHC of CERN.

One important probe of heavy-ion collisions is heavy quarkonium, e.g., the charmonium, which is a bound state of a charm and an anti-charm quark ($c\bar{c}$). Since heavy quarks are created in the early stage of the collision, they thus experience the whole medium evolution. The charmonium will interact with the hot-colored QGP medium, and the bound state is expected to be dissociated due to color screening [[1], [2]], resulting in a suppression in the number of measured charmonium with respect to scaled proton-proton collisions used as reference. In addition, in relativistic heavy-ion collisions, the high energy provided for the collision results in producing a high number of charm quark pairs. Those uncorrelated ($c\bar{c}$) pairs can recombine either in medium [3] or at the phase boundary [4] to form charmonium. The ground state of the charmonium vector mesons is the J/ψ. Higher state mesons can decay (i.e., $\psi(2S)$, χ_c) to a J/ψ. This contribution is called a feed-down contribution. Moreover, in AA collisions, Cold Nuclear Matter effects (CNM) take place along with hot nuclear matter effects. The CNM effects are not related to the formation of the hot QGP medium. The CNM effects include, e.g., shadowing, which is a modification of the initial state quark and gluon structure function of a nucleon inside a nucleus. It plays an important role in heavy-ion collisions [5], as shown by the study of pA collisions that are used as a reference for AA collisions. The nuclear matter effects on the J/ψ are usually quantified by the observable $R_{\rm AA}$, the nuclear modification factor, which is the ratio between the yield of J/ψ, in heavy-ion collision with respect to its production yield in pp collisions scaled by the number of binary nucleon-nucleon collisions in the heavy-ion collision. The $R_{\rm AA}$ is expected to be different from unity if hot or cold nuclear matter effects are at play.

The production of the J/ψ meson in Pb-Pb collisions has been extensively studied by ALICE, e.g., [[6]-[8]]. At the LHC, J/ψ can be either hadroproduced or photoproduced. Hadronic production can take place whenever there is a nuclear overlap between the colliding nuclei. Photoproduction mechanism is well known when the interacting nuclei are separated by a transverse distance between the center of the two nuclei (i.e. the impact parameter) larger than the sum of their radii. Such interactions are called Ultra Peripheral Collisions (UPC).

In relativistic heavy-ion collisions, the heavy nucleus is a strong electromagnetic field emitter, providing a flux of quasi-real photons. A photon can fluctuate into a color dipole made of a quark and an anti-quark, exchange a pomeron [1] with a target nucleus, and re-

[1] A pomeron exchange is equivalent to two gluon exchange in

combine into a vector meson (VM), e.g., a J/ψ [9]. If the dipole couples coherently with the whole target nucleus, the photoproduction is called coherent, the nucleus stays intact, and the produced VM has a low $p_{\rm T}$ (1/nucleus radius $\approx$ 60 MeV/c). Whereas if the dipole couples with a single nucleon in the target nucleus, the VM production is called incoherent, the target nucleus usually breaks, and the VM has a larger $p_{\rm T}$ ($\approx$ 500 MeV/c). Using UPC, the low $p_{\rm T}$ VM allows one to probe the poorly known gluon content in the target nucleus in the low Bjorken-x range $\sim 10^{-5}$ to 10^{-2}, which can be derived from the simplified relation between the Bjorken-x, the VM mass $m_{J/\psi}$ and its rapidity y: $x_B = (m_{J/\psi}/\sqrt{s_{\rm NN}}) \times \exp(\pm y)$, where $\sqrt{s_{\rm NN}}$ is the center of mass energy per nucleon-nucleon collision [[10], [11]].

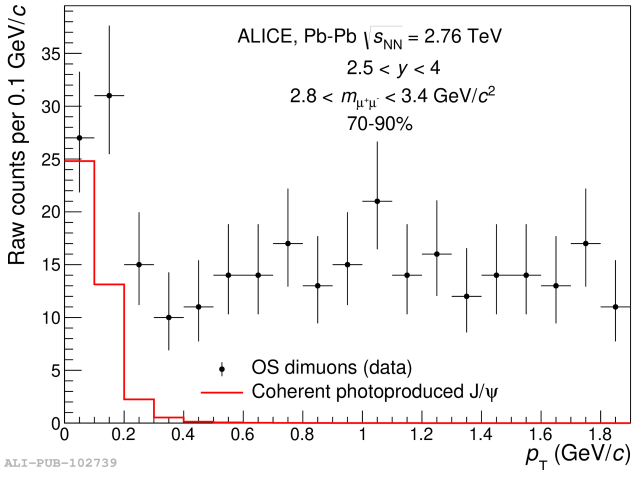

Figure 1: p_T distribution of raw opposite sign dimuons, measured with ALICE, in the invariant mass window $2.8 < m_{\mu^+\mu^-} < 3.4$ GeV/c^2 and the centrality class $(70-90)\%$. The red line represents the p_T distribution predicted by the STARLIGHT MC generator [12] for coherent J/ψ photoproduction in Pb-Pb UPC, convoluted with the response function of the muon spectrometer. The normalization of the red line is given by the measured excess number of J/ψ after correction for the coherently photoproduced $\psi(2S)$ feed-down and photoproduced J/ψ incoherent contributions [13].

For the first time in nuclear collisions in the presence of a nuclear overlap, ALICE has reported an excess in the yield of low $p_{\rm T}$ J/ψ for $2.5 < y < 4$ in most peripheral Pb-Pb collisions (centrality class (70-90) %), at $\sqrt{s_{\rm NN}} = 2.76$ TeV. The excess has been studied via the leptonic decay channel J/ψ to $\mu^+\mu^-$ [13]. The $p_{\rm T}$ shape of that excess is similar to the coherent photoproduced J/ψ $p_{\rm T}$ shape predicted by STARLIGHT MC generator [12] for UPC, as shown in figure 1. This excess observation was further quantified by measuring an unexpectedly large J/ψ $R_{\rm AA}$ for $p_{\rm T} < 0.3$ GeV/c, which couldn't be explained by any combination of hot and/or cold nuclear matter effects [14]. The coherent J/ψ photoproduction mechanism was suggested to explain these measurements.

perturbative QCD.

ALICE experiment

The ALICE apparatus is described in details in Ref [15]. It had two main parts. The central barrel and the muon arm. The detectors relevant to this analysis will be described below. The J/ψ analysis is performed via the dimuon decay channel at forward rapidity $2.5 < y < 4$. The ALICE forward muon arm allows for inclusive quarkonium measurements down to $p_{\rm T} = 0$. It consists of 5 tracking stations and two triggering stations. A dipole magnet surrounds the third tracking station for charge and momentum determination. The Silicon Pixel Detector (SPD) in the central barrel provides the reconstruction of the primary vertex. The V0 detectors on both sides of the interaction point provide the triggering, the centrality determination and are used for beam-gas background rejection. The Zero Degree Calorimeters (ZDC) are located at small angles, far from the interaction point on both sides. By combining the time information from the V0 and ZDC, and by requiring a minimum energy deposition in the neutron ZDCs, the background from electromagnetic dissociation processes can be reduced.

Data analysis

The coherent J/ψ photoproduction cross section measurement requires quantifying the coherent J/ψ yield from the yield excess after subtracting the incoherent J/ψ photoproduction fraction (f_I) and the higher state $\psi(2S)$ coherent photoproduction feed-down fraction (f_D) contributions. The fractions (f_I) and (f_D) are obtained from a previous UPC analysis [8].

In the $p_{\rm T}$ interval of interest, $0 < p_{\rm T} < 0.3$ GeV/c, in order to obtain the J/ψ yield excess in Pb-Pb collisions $N_{AA}^{excess\ J/\psi}$, the expected J/ψ hadronic yield is subtracted from the raw J/ψ yield measurement, $N_{AA}^{J/\psi\ raw}$. The hadronic J/ψ contribution , $N_{AA}^{h\ J/\psi}$, is estimated in Pb-Pb collisions from the J/ψ hadronic cross section in pp collision, $\sigma_{pp}^{h\ J/\psi}$, and using the nuclear modification factor $R_{\rm AA}$, as follows:

$$\frac{{\rm d}N_{AA}^{h\ J/\psi}}{{\rm d}p_{\rm T}} = \mathcal{N} \times \frac{{\rm d}\sigma_{pp}^{h\ J/\psi}}{{\rm d}p_{\rm T}} \times R_{AA}^{h\ J/\psi} \times (\mathcal{A} \times \varepsilon)_{AA}^{h\ J/\psi} \quad (1)$$

where

$$R_{AA}^{h\ J/\psi} = \frac{N_{AA}^{J/\psi\ raw}}{< T_{AA} > .\sigma_{pp}^{h\ J/\psi} \times B.R. \times (\mathcal{A} \times \varepsilon)_{AA}^{h\ J/\psi} \times N_{ev.}} \quad (2)$$

where $B.R.$ is the J/ψ decay channel $J/\psi \to \mu^+\mu^-$ branching ratio which amounts for $(5.961 \pm 0.033)\%$ [16]. The $(\mathcal{A} \times \varepsilon)_{AA}^{h\ J/\psi}$ is the hadronic J/ψ acceptance times efficiency of the muon spectrometer. $N_{ev.}$ is the number of equivalent minimum bias analyzed events. The $< T_{AA} >$ is the average nuclear overlap function which can be derived from the number

of binary nucleon-nucleon collisions, $<N_{\rm coll}>$, using Glauber MonteCarlo simulations [17]. The normalization factor $\mathcal{N}$ in Equation 1. is made such that the integral of the model function in the $p_{\rm T}$ interval $1 < p_{\rm T} < 8$ GeV/c is equal to the measured J/ψ raw yield in the same interval.

The coherent J/ψ photoproduction cross section $\sigma_{AA}^{coh\ J/\psi}$ in $0 < p_{\rm T} < 0.3$ GeV/c in each rapidity interval Δy is computed as follows:

$$\frac{d\sigma_{AA}^{coh\ J/\psi}}{dy} = \frac{N_{AA}^{coh\ J/\psi}}{(\mathcal{A}\times\varepsilon)^{coh\ J/\psi}\times B.R.\times\mathcal{L}\times\Delta y} \qquad (3)$$

where $N_{AA}^{coh\ J/\psi}$ is the coherent J/ψ yield calculated from the excess yield using

$$N_{AA}^{coh\ J/\psi} = \frac{N_{AA}^{excess\ J/\psi}}{1+f_I+f_D}$$

The $(\mathcal{A}\times\varepsilon)^{coh\ J/\psi}$ is the acceptance times efficiency of the muon spectrometer for the coherent J/ψ process, and $\mathcal{L}$ is the luminosity of the used data sample and is equal to $756.3 \pm 18.9\ \mu{\rm b}^{-1}$.

The main sources of systematic uncertainties on the coherent J/ψ photoproduction cross section measurement come from the J/ψ signal extraction, the triggering and tracking efficiencies, and the centrality limits.

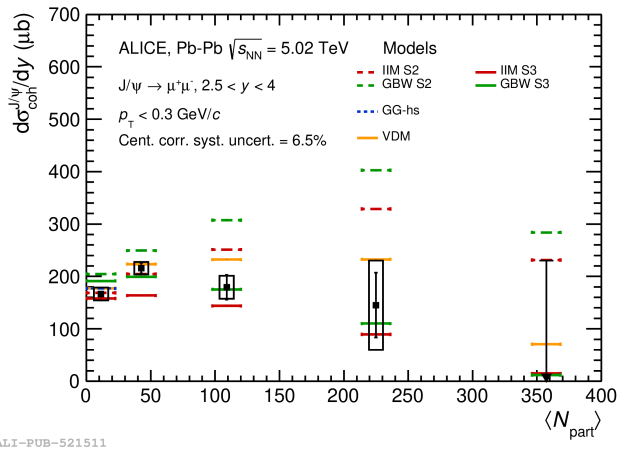

Figure 2: J/ψ coherent photoproduction cross section as a function of $<N_{\rm part}>$ at forward rapidity in Pb-Pb collisions at $\sqrt{s_{\rm NN}} = 5.02$ TeV. The vertical bars are the statistical uncertainties, and the uncorrelated systematic uncertainties are represented as boxes. The centrality correlated systematic uncertainties are quoted in the legend. Note that the most central bin, where only an upper limit is given, is half the size of the other intervals. Therefore, to evaluate the centrality dependence of the J/ψ coherent photoproduction cross section, both data and theory have to be multiplied by a factor of two in the most central bin [21].

Results

Figure 2 shows the coherent J/ψ photoproduction cross section measured recently by ALICE in $2.5 < y < 4$ as a function of the average number of nucleons that participate in the nucleus-nucleus collisions $<N_{\rm part}>$. The latter quantifies the centrality of the collision. The larger the number of participating nucleons, the more central the event is. The cross section measurement doesn't show a significant centrality dependence. The measurement is compared with many theoretical models that use J/ψ photoproduction in UPC as a baseline computation for J/ψ photoproduction in collisions with nuclear overlap. These models either modify only the photon flux to account for the nuclear overlap (VDM [18], GG-hs [19], GBW/IIM(S2) [20]) or both the photon flux and photonuclear cross sections (GBW/IIM(S3) [20]).

The order of magnitude of the cross section in peripheral collisions $(70-90)\%$ is qualitatively reproduced by all models. In semicentral and central collisions, the cross section is better reproduced by the IIM/GBW(S3) models and the VDM model. The theoretical models that are able to reproduce the measurement have at least a modified photon flux or, in addition, a modified photonuclear cross section.

Perspectives

The theoretical models GBW and IIM(S3) are able to describe the coherent J/ψ photoproduction cross section in $2.5 < y < 4$ as a function of centrality within the uncertainties. The GBW/IIM model predicts a strong rapidity dependence, especially in the forward rapidity region, as shown in figure 3 for the S2 scenario case. A rapidity-differential study of the cross section would therefore constrain more the theoretical description.

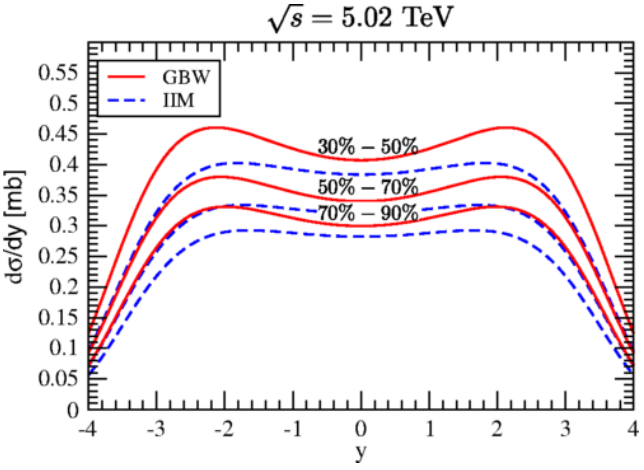

Figure 3: Rapidity distribution for photoproduced J/ψ in Pb-Pb collisions, at $\sqrt{s_{\rm NN}} = 5.02$ TeV and for different centrality classes using the GBW (S2) and IIM (S2) dipole models from [20].

The analysis method described in the data analysis section is the same as the one applied in y intervals in order to perform the $y-$differential cross section mea-

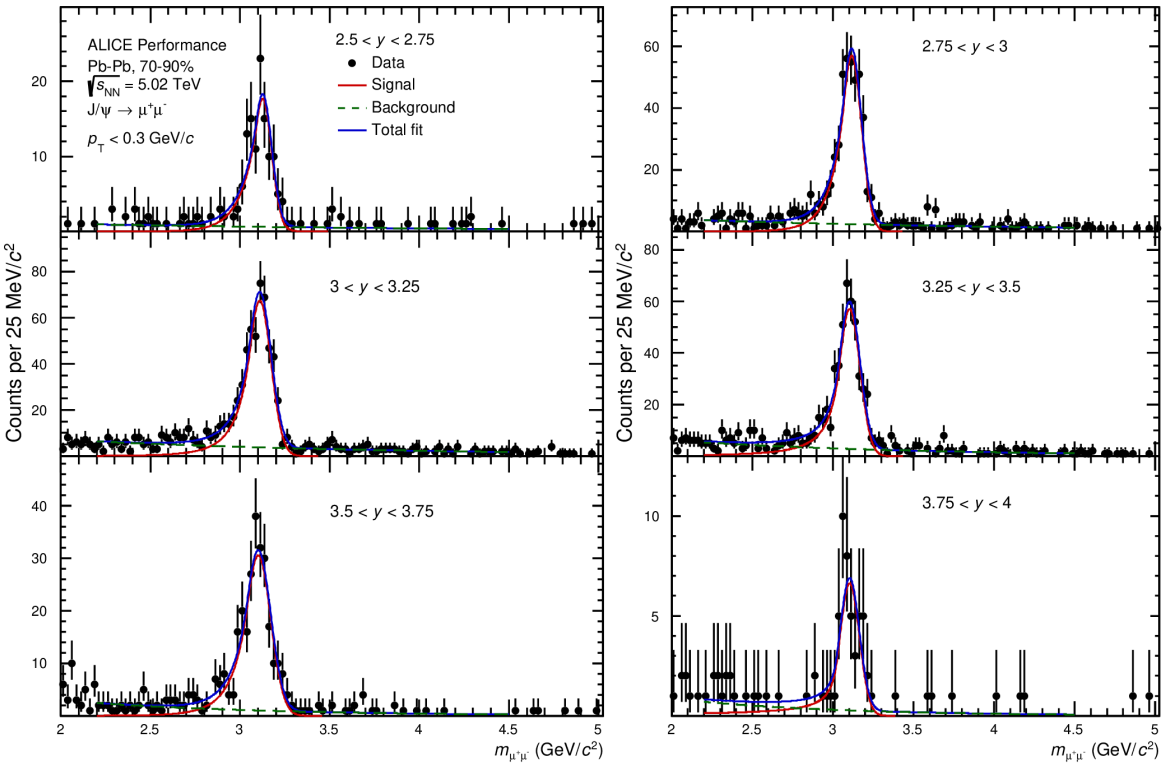

Figure 4: Raw invariant mass distribution of opposite sign dimuons, measured with ALICE in Pb-Pb collisions in the centrality class $(70-90)\%$ in six rapidity intervals in the range $2.5 < y < 4$ for $p_{\rm T} < 0.3$ GeV/c.

surement. In this analysis, six rapidity intervals are studied in the range $2.5 < y < 4$. The raw J/ψ yield is extracted in six rapidity intervals and as a function of $p_{\rm T}$, both in pp and Pb-Pb collisions together with its systematic uncertainties. The work is ongoing to determine the acceptance times efficiency corrections on the extracted yield. The $R_{\rm AA}$ will then be calculated, as well as the coherent J/ψ photoproduction cross section in each y interval of study.

Figure 4 shows the potential for raw J/ψ yield extraction in six rapidity intervals in the range $2.5 < y < 4$ for $p_{\rm T} < 0.3$ GeV/c from the invariant mass distribution of opposite sign dimuons in Pb-Pb collisions in the centrality class $(70-90)\%$.

References

[1] H. Satz, J. Phys. G: Nucl. Part. Phys. 32 R25, 2006.

[2] A. Rothkopf, T. Hatsuda and S. Sasaki, arXiv:1108.1579v2 [hep-lat], 2012.

[3] R. L. Thews, M. Schroedter, and J. Rafelski, Phys. Rev. C 63, 054905, 2001.

[4] P. Braun-Munzinger and J. Stachel, Phys.Lett. B 490 (2000) 196-202.

[5] ALICE Collaboration, JHEP, 07 (2018) 160.

[6] ALICE collaboration, Physics Letters B 734 (2014) 314.

[7] ALICE collaboration, Physics Letters B 766 (2017) 212.

[8] ALICE collaboration, Phys. Lett. B 798 (2019) 134926.

[9] S. R. Klein and H. Mantysaari, Nature Rev.Phys. 1 (2019) 11, 662-674.

[10] V. Rebyakova, M. Strikman, and M. Zhalov, Phys. Lett. B710 (2012) 647.

[11] J. G. Contreras, Phys. Rev. C 96, 015203 (2017).

[12] STARLIGHT MC website, `http://starlight.hepforge.org/`.

[13] ALICE collaboration, Phys. Rev. Lett. 116, 222301.

[14] W. Shi, W. Zha and B. Chen, Phys.Lett. B777 (2018) 399-405.

[15] ALICE Collaboration, K. Aamodt et al., J. Instrum. 3 (2008), Article S08002.

[16] R.L. Workman et al.(Particle Data Group), Prog.Theor.Exp.Phys.2022, 083C01 (2022).

[17] ALICE Collaboration, Phys. Rev. C 88 (2013) 044909.

[18] M. Klusek-Gawenda and A. Szczurek, Phys. Rev. C 93 no. 4, (2016) 044912, arXiv:1509.03173 [nucl-th].

[19] Cepila, J. G. Contreras, and M. Krelina, Phys. Rev. C 97 no. 2, (2018) 024901, arXiv:1711.01855 [hep-ph].

[20] M. Gay Ducati and S. Martins, Phys. Rev. D 97 no. 11, (2018) 116013, arXiv:1804.09836 [hep-ph].

[21] ALICE collaboration, arXiv:2204.10684 [nucl-ex].

Part V

Instrumentation

session chaired by Christina AGAPOPOULOU

Tests and calibration of multi-channel photodetectors for balloon and space-based EUSO missions

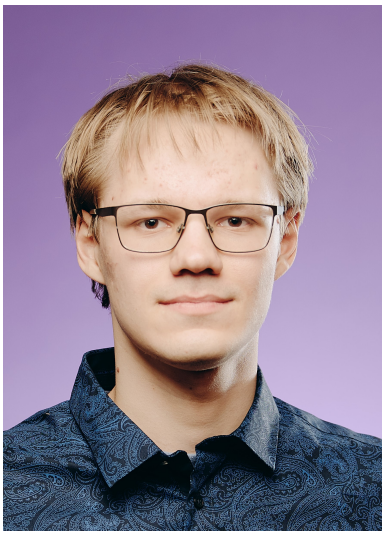

Daniil Trofimov[1,2,3], ***with Etienne Parizot***[1], ***Pavel Klimov***[2] ***on behalf of JEM-EUSO collaboration***

[1] *CNRS, Astroparticule et Cosmologie, Universite Paris Cite, F-75013 Paris, France;* [2] *Skobeltsyn Institute of Nuclear Physics, Lomonosov Moscow State University, Moscow 119991, Russia;* [3] *Faculty of Physics, Lomonosov Moscow State University, Moscow 119991, Russia*

Abstract — The JEM-EUSO collaboration develops a series of balloon and orbital telescopes to detect transient UV emission from the Earth atmosphere, with the primary goal to study ultra-high-energy cosmic rays from space. These detectors are wide field-of-view telescopes with high temporal resolution (1-2.5 μs) and sensitivity provided by a large aperture. One of these detectors is currently operating onboard the ISS (MINI-EUSO), one is planned to be launched in 2023 (EUSO-SPB2) and one is in preparation stage (K-EUSO). These projects use the same photo-detection modules (PDMs) composed of 36 multi-anode photomultiplier tubes with 2304 channels in total, used in single photon counting mode. The absolute calibration of the photodetection units of the EUSO-SPB2 mission is presented, also revealing sub-pixel structures, associated with spatial variations in the photoelectron collection efficiency. The calibration of the three PDMs of EUSO-SPB2 was performed in a so-called "black box", using light sources with controlled intensity. The method uses an integrating sphere illuminated by light-emitting diodes (LEDs) with a wavelength of either 375 or 405 nm, with a known fraction of the light flux directed towards the photodetectors and another fraction directed towards an absolutely-calibrated photodiode, read by a power-meter to monitor permanently the light intensity. The detection efficiency of all pixels was then obtained, after determining the optimal level of the discriminator threshold used in the front-end electronics, pixel by pixel, providing the highest efficiency while ensuring negligible contribution of fake photoelectron counts from electronic noise.

Introduction

Cosmic rays are high-energy protons and atomic nuclei accelerated in Galactic astrophysical sources, which are still not fully understood. Their energy distribution extends over a very wide spectrum, from subrelativistic energies up to 10^{20} eV and beyond, i.e. macroscopic energies (several tens of Joules!). The most energetic of them, so-called Ultra-High-Energy Cosmic Rays (UHECRs), cannot be confined by the Galactic magnetic field and actually have an extragalactic origin. Their sources remain one of the most challenging mysteries in high-energy astrophysics.

When a primary cosmic ray with high energy enters the atmosphere, a cascade of secondary energetic particles and electromagnetic radiation develops, creating a so-called extensive air shower (EAS), by which the UHECRs can be detected. However, the flux of the highest energy particles is extremely low, down to $\sim$ 1 particle per m^2 per billion years, so their study requires extremely large observatories, covering thousands of km^2, like the Pierre Auger Observatory [1] and the Telescope Array [2]. Yet, only around two dozen of events with energies exceeding 10^{20} eV were detected so far [3], with very non uniform exposure of the sky in the northern and southern hemispheres. This proved to be insufficient to identify their sources and acceleration mechanism. A significant increase in exposure, as well as near-uniform full-sky coverage, will be needed to increase the statistics, better characterise the UHECR anisotropies, and understand the origin of these nuclei, which are the most energetic particles known in the Universe.

The JEM-EUSO (Joint Experiment Missions for Extreme Universe Space Observatory) [4] international collaboration has endeavoured to extend the study of UHECRs by operating for the first time an observatory from space, which offers the possibility to observe a huge volume of atmosphere at once, with one sin-

gle instrument. It thus started a program to develop the appropriate technology allowing to detect UHECRs and neutrinos by the fluorescence and Cherenkov light of EAS from a low Earth orbit. The first attempt to measure UHECR from orbit was carried out in the TUS experiment [5]. The SPB2 (Super Pressure Balloon) experiment [6] is a stratospheric pathfinder for the K-EUSO [7] and POEMMA [8] orbital missions. It was made in order to verify the method of recording cosmic rays of ultra-high and extremely high energies (E $>$ 1 EeV) by measuring the fluorescence of extensive air showers (EASs), as well as high-energy neutrinos (E $>$ 10 PeV) from Cherenkov radiation of EASs. To solve these problems, the scientific equipment of the project includes two telescopes: a fluorescence telescope, directed to nadir and a Cherenkov telescope directed towards the limb of the Earth. The telescopes complement each other because they operate in different energy ranges. The Cherenkov telescope will also confirm the methods of neutrino detection in the atmosphere. High energy neurtinos will copmlement the UHECR measurements and allow us to detect sources of UHECR.

The planned launch time of the stratospheric observatory is spring 2023. Measurements will be made from an altitude of 33 km, for up to 100 days, when the balloon will be moving in the circumpolar vortex. The vortex will provide the stable and long flight at a certain altitude.

Scientific objectives of the EUSO-SPB2 experiment

The EUSO-SPB2 experiment has a lot of scientific objectives for the flight:

- The first observations of extensive air showers (EAS) using a fluorescence telescope from suborbital space.
- Detection of the Cherenkov light of EAS induced by high-energy cosmic rays.
- Measurement of the background for the detection of neutrino-induced ascending EAS.
- Search for neutrinos as a result of transient astrophysical events (for example, during the merger of binary neutron stars).

To solve these problems, the mission includes two instruments: fluorescence and Cherenkov telescopes.

The Fluorescence telescope of the EUSO-SPB2 project will provide first measurements of EASs via the fluorescence technique from suborbital space. Expected number of EAS events: 0.12 ± 0.01 events/hour, or $\sim$0.6 events per night (Figure 1). This estimations were obtained in [6].

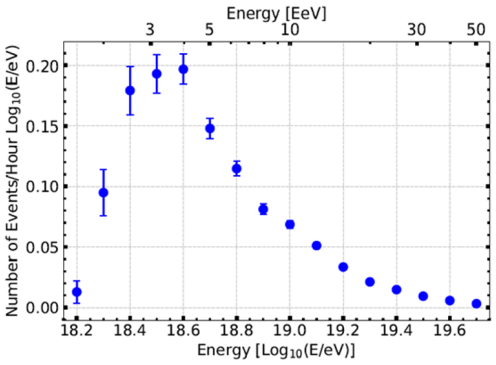

Figure 1: Expected number of events from the Fluorescence telescope [6]

Characteristics of the EUSO-SPB2 fluorescence telescope

The fluorescent telescope is being built according to the Schmidt camera scheme and has a mirror with a radius of curvature of 1659.8 mm and an effective focal length of 860 mm [9]. Other characteristics are:

- Altitude: 33 km
- Field of view: $37.4° \times 11.4°$
- Aperture: 1 m
- Time resolution: 1 μs
- Number of modules/channels: 3/ 6,912

The photodetection surface contains 3 PDMs, (Figure 2). Each PDM consists of 9 elementary cells (ECs). Each EC-unit contains a SPACIROC-3 chip [10], the basis of which is a discriminator of single-photoelectronic pulses. Each EC-unit consists of 4 HAMAMATSU R11265-103-M64 multi-anode photomultiplier tubes (MAPMTs), each has 64 channels (pixels). Each PDM has 2304 channels of registration.

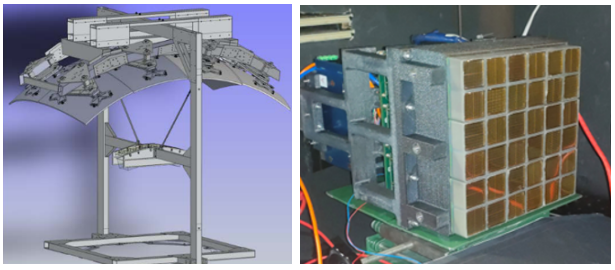

Figure 2: The scheme of the fluorescence telescope (left) and a photodetection module (PDM, right)

The electronics of the EUSO-SPB2 PDMs contain ananalog-to-digital convertor, which counts photoelectrons using the SPACIROC-3, a digital data processing unit based on XILINX's Zynq system (xilinx.com), and a high-voltage module (HVPS) [11]. SPACIROC-3

is a specialized chip designed to count photoelectronic pulses for a certain time. The basis of the chip is an amplitude discriminator, which provides the selection of single-photoelectronic pulses in accordance with the threshold. There are 2 types of thresholds: 10-bit DAC, which is set for each MAPMT and 7-bit DAC, individual for each registration channel. Setting individual thresholds allows to optimize the efficiency of registration of each channel separately.

Calibration of EUSO-SPB2 modules

Calibration is carried out in a special non-transparent box (Blackbox) with a photodetector inside, a light source in the integrating sphere (creating uniform illumination of the photodetector and performing the function of a luminous flux divider), a power meter with two calibrated photodiodes (one is located inside the sphere, the other is next to photodetector), as well as a precision positioning system, which allows to direct accurately the collimated luminous flux to one pixel.

Measurements are carried out either in the mode of full illumination (all pixels are illuminated at the same time) or in the mode of illumination of one pixel (with a collimator on the integrating sphere, Figure 3). The first type of measurement allows to determine the efficiency of all pixels at the same time and find the optimal values of the discriminator thresholds. The second type of measurement is used for a scanning procedure that allows to determine the actual borders of each pixel and their internal structure.

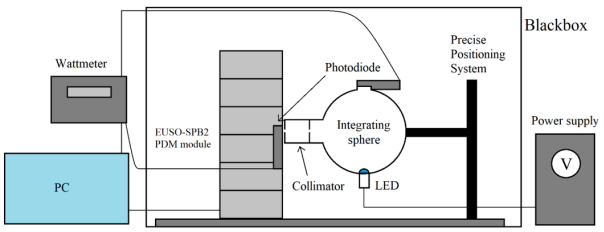

Figure 3: Scheme of the calibration process, with a collimator attached to the integrating sphere for single pixel illumination

Firstly, the measurements of S-curve in the full-illumination mode were made. S-curve is the dependence of the number of photoelectrons (or detection efficiency) on the threshold of the DAC (7-bit or 10-bit) discriminator.

The S-curve is measured to set the optimal thresholds on each pixel and to verify their performance. The threshold cuts off noise and counts pulses corresponding to the signal of 1 photoelectron.

A 10-bit DAC allows to set the threshold at the level of each PMT, while a 7-bit DAC allows to shift the 10-bit DAC scale individually for each pixel. In our case, we use a single 10-bit DAC threshold at 800, after adjusting all pedestals with the use of the 7-bit DAC pixel by pixel. After setting the optimal individual thresholds, the pedestals of all pixels begin almost simultaneously in 10-bit DAC mode (see Figure 4). Optimal thresholds also give us maximum of efficiency for each pixel.

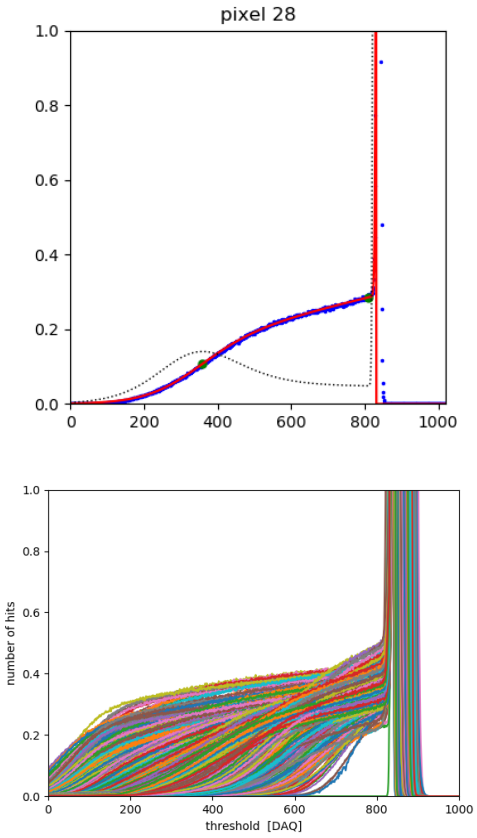

Figure 4: S-curve for one pixel (left) and for all pixels of 1 PDM (right)

The second stage is to scan all PDMs using the collimator and precision positioning system (the second type of scanning procedure). For each PDM full scan with 200×200 measurements per PDM area were made. It provides a uniform coverage of the PDM surface. Example of one PDM scan in the Figure 5.

Partial PDM scan allows us to see the internal structure of each pixel. The structure of the pixels depends on the direction of scanning (vertically or horizontally) In the center of each pixel, the efficiency is less due to the internal structure of the PMTs (Figure 6).

At high light intensity, the effect of overlapping impulses (pile-up) makes a big contribution (Figure 7). Pile-up occurs when the time interval between consecutive photoelectrons is smaller than the time resolution of the ASIC (a few ns). The number of counts thus saturates and eventually decreases as the photon rate increases (more and more photons being missed). The expected counting rate is $\varepsilon N \times \exp(-\varepsilon N \delta t)$, where N is the incoming photon rate, ε is the detection efficiency and δt is the double pulse resolution (dead time). The average dead time is approximately 10 to 12 nanoseconds.

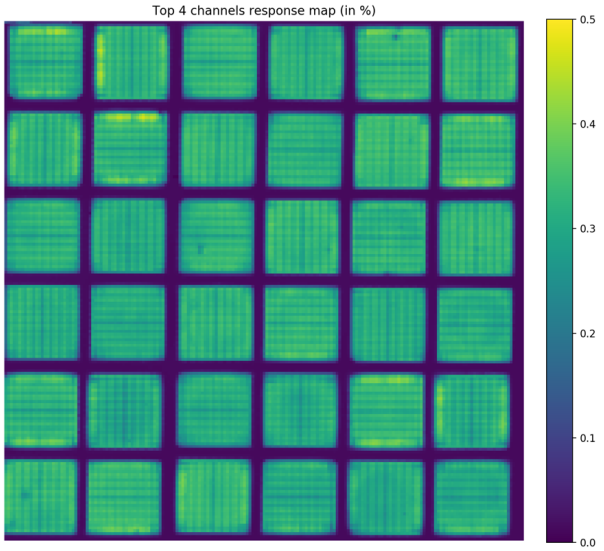

Figure 5: The result of PDM3 scanning. The color shows the efficiency of each pixel. Dark areas are the boundaries between the MAPMTs. Scanning resolution is 200×200 points, the wavelength of the LED is 375 nm

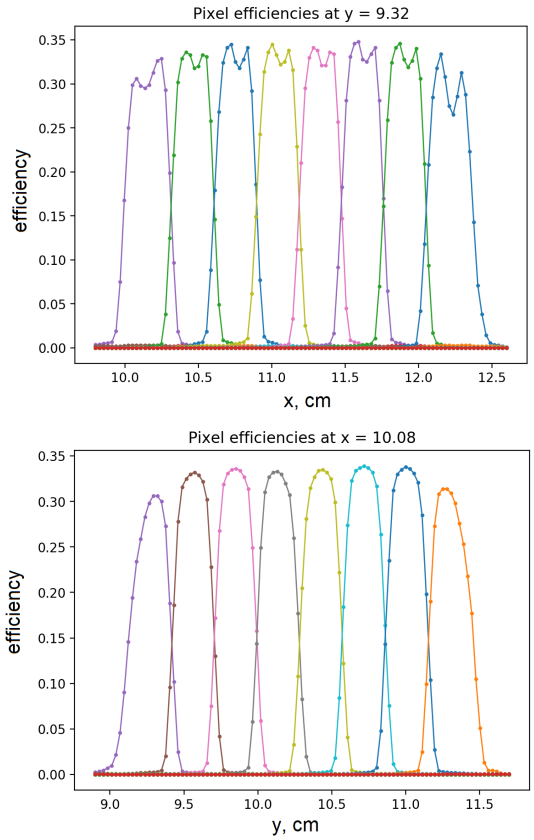

Figure 6: Linear scans of multianode photomultiplier tubes (MAPMTs). Vertical axis is an efficiency, horizontal axis is a coordinate (cm). Different colors correspond to different channels of registration (pixels) PMT22 of PDM2, wavelength $\lambda = 405$nm

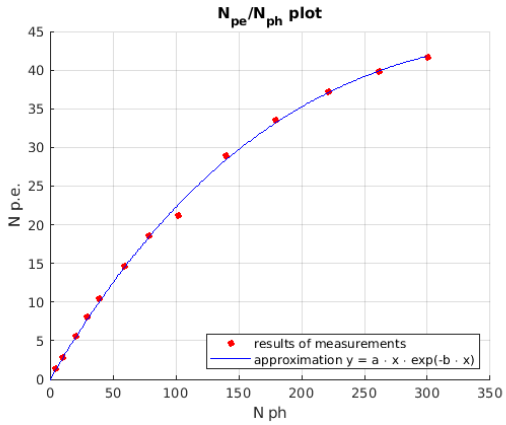

Figure 7: Example of a pile-up curve, measured for one pixel and fitted with $\delta t = 8.3$ ns (LED wavelength $\lambda = 405$ nm). N_{ph} - number of photons per GTU, $N_{p.e.}$ - number of photoelectrons per GTU

Results

The EUSO-SPB2 photodetection modules have been calibrated with high precision in different modes. Detailed information about the size and efficiency of each pixel will allow to analyse of extensive air showers and other events detected during the mission, which is expected to be launched in spring 2023 from Wanaka in New Zealand. The calibration will help us reconstruct with higher precision the luminosity of EAS, and thus the energy of the incoming particle.

The first observation of EAS via the fluorescence technique from suborbital space will confirm this method and open the way to orbital projects K-EUSO and POEMMA. The fluorescence detection from space is expected to produce a huge statistics and reveal the mystery of UHECR.

References

[1] R. Caruso on behalf of The Pierre Auger Collaboration, Operations of the Pierre Auger Observatory, 7th International Cosmic Ray Conference (ICRC 2021). doi: 10.22323/1.395.0238

[2] G.I. Rubtsov on behalf of the Telescope Array Collaboration, Highlights from the Telescope Array experiment, 37th International Cosmic Ray Conference (ICRC 2021). doi: 10.22323/1.395.0012

[3] The Pierre Auger Collaboration, Arrival Directions of Cosmic Rays above 32 EeV from Phase One of the Pierre Auger Observatory, 2022. doi: 10.48550/arXiv.2206.134927

[4] M. Bertaina on behalf of the JEM-EUSO Collaboration, An overview of the JEM-EUSO program and results, 37th International Cosmic Ray Conference (ICRC 2021). doi: 10.48550/arXiv.2112.09954

[5] D. Barghini, M. Bertaina, A. Cellino, et al., UV telescope TUS on board Lomonosov satellite: Selected results of the mission. Advances in Space Research, 2022, 70(9), 2734-2749, doi: 10.1016/j.asr.2021.11.044

[6] J.Eser, A. V. Olinto, L. Wiencke, Science and mission status of EUSO-SPB2, 37th International Cosmic Ray Conference (ICRC 2021). doi: 10.48550/arXiv.2112.08509

[7] P. Klimov, M. Battisti, A. Belov et al., Status of the K-EUSO Orbital Detector of Ultra-High Energy Cosmic Rays. Universe 2022, 8, 88, doi: 10.3390/universe8020088

[8] A.V. Olinto, J. Krizmanic, J.H. Adams et al., The POEMMA (Probe of Extreme Multi-Messenger Astrophysics) observatory, Journal of Cosmology and Astroparticle Physics 2021, V. 2021, 06, doi: 10.1088/1475-7516/2021/06/007

[9] G. Osteria, J. Adams, M.Battisti et al., The Fluorescence Telescope on board EUSO-SPB2 for the detection of Ultra High Energy Cosmic Rays, Proceeding of Science (ICRC2021) 206, doi: 10.22323/1.395.0206

[10] S. Blin et al. (JEM-EUSO Coll.), SPACIROC3: 100 MHz photon counting ASIC for EUSO-SPB, Nuclear Instruments and Methods in Physics Research, 2018 ,Volume 912, 363-367, doi: 10.1016/j.nima.2017.12.060

[11] Z. Plebaniak et al. (JEM-EUSO Coll.), HVPS system for * - EUSO detectors, Proceeding of Science (ICRC2017) 301, doi: 10.22323/1.301.0378

In vitro dosimetry for assessment of targeted alpha therapy

Alexis Doudard

Grand Accélérateur National d'Ions Lourds (GANIL)

Abstract — Targeted alpha therapy is an internal and vectorized radiotherapy using radiopharmaceuticals, highly biologically lethal sources of irradiation which are useful in applications such as the treatment of disseminated brain metastases. Part of the development of new radiopharmaceuticals consists of *in vitro* assays, where the small range of α-particles in water (a few dozen micrometers) leads to a more challenging dosimetry. The dose delivered to the cells depends significantly on the spatial distribution of the radionuclides inside the culture medium, and is critical to construct reliable dose-effect relationships needed to compare the assessed treatment to other existing methods. To probe the spatial distribution of the radionuclides during *in vitro* assays, a system was developed, based on the use of silicon semiconductor detectors placed below custom-made culture wells which record energy spectra of the α-particles passing through the culture medium and cell layer. A detector chamber was also conceived to hold and protect the electronics mainly from the saturated humidity of the culture chambers. A spectral deconvolution method was developed to extrapolate the radionuclide time and spatial distribution from the energy spectra acquired during an experiment, which allows to compute the dose delivered to the cells. Reliability of the methodology has been assessed and it has been demonstrated that the dose computation errors are limited to 3% when applied to simulated ^{212}Pb or ^{223}Ra irradiations. The methodology was then applied to spectra acquired during preliminary experiments for both nuclides and revealed that the different radionuclides of complex decay chains, like the one of ^{223}Ra, may be characterized by different distributions, which has further consequences on dose computation and highlights the necessity of such new experimental *in vitro* dosimetry methods.

Introduction

Targeted alpha therapy (TAT) is a cancer treatment method based on the injection of radiopharmaceuticals to the patient. TAT radiopharmaceuticals consist of a coupling between a biological vector, that specifically targets tissues of interest because of their unique properties (either cancer cells or tissues nearby), and an α-emitting radionuclide for irradiation of the nearby tissues. TAT is actually a sub-branch of targeted radionuclide therapy that is currently being heavily researched thanks to developments in radionuclide production [1, 2]. Interest of using α-emitters instead of more conventional β-emitters is due to their higher linear energy transfer (LET) values, leading to a shorter range in matter and thus a more localized action sparing healthy tissues, but also to their larger propensity to generate direct biological effects, thus making the therapy less dependent on oxygen levels in the targeted tissues [4].

During the development of a new radiopharmaceutical, *in vitro* assays are carried and aim at determining its relative biological effectiveness (RBE), a quantity comparing the amount of dose to be delivered to a target to produce a given effect with respect to the one necessary for other reference treating methods. However, since TAT employs high-LET emissions, the delivered dose to cells significantly depends on the spatial distribution of the radionuclides inside the culture well during the irradiation, leading to potentially large dosimetric errors if a hypothesis of homogeneous distribution is used [3]. A dosimetry system based on α-spectroscopy of the culture wells during the assays was thus conceived, along with a spectral deconvolution method allowing to reconstruct the spatial and time distributions of the radionuclides diluted in the culture medium, along the vertical axis. These distributions may then be converted to a delivered dose to the cells with the use of pre-computed Monte-Carlo simulations.

Experimental setup for dosimetry of *in vitro* assays

Spectroscopy of α-particles emitted from the culture medium is carried with a dedicated setup described in **Figure 1**. Silicon semi-conductor detectors (a) are placed directly below the culture wells (b), and are linked to a FASTER (LPC Caen) acquisition system [5]. With appropriate tuning of the acquisition system with the help of a vacuum chamber and of a ^{241}Am source, the energy resolutions for α-particles of the different detectors used range between 22 keV and 32 keV FWHM at 5.486 MeV. To allow transmission of the

α-particles from the culture medium (c) towards the detector, the culture wells are built as hollow cylinders carved out of a plexiglass plate, and the bottom of the well consists of a 2.5 μm-thick mylar foil (d). All the electronics are placed inside a humidity-proof chamber (e, shown in the picture below) that allows the use of the setup inside humidity-saturated culture chambers, necessary to keep the cells in optimal conditions during the assays.

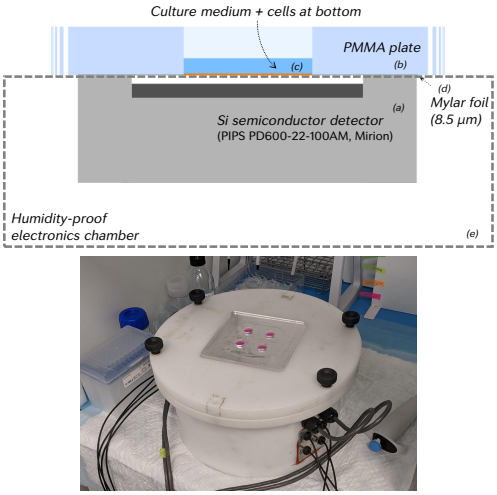

Figure 1: On the top side, description of the setup for α-energy spectroscopy of *in vitro* assays. On the bottom side, a picture of the electronics chamber.

Since this project is a part of a larger study for the development of a new radiopharmaceutical based on ^{212}Pb, ^{212}Pb-αVCAM-1, this radioisotope was considered in this work. The decay chain of ^{212}Pb, presented in **Figure 2a**, consists of a single α-decay. ^{223}Ra was also considered here, since this radionuclide (clinically available as *Xofigo*, $Cl_2{}^{223}Ra$) is characterized by a longer decay chain composed of four successive α-decays, as shown in **Figure 2b**.

Development of a new spectral deconvolution method

While the α-emissions energy probability distribution corresponding to a given radionuclide is a discrete spectrum, the α-energy spectra measured with the setup of **Figure 1** are continuous due to the α-particles crossing different paths in culture medium, cells, air and mylar before reaching the detector, leading to an energy straggling. The acquired spectra are thus described as a sum of elementary spectra that would be obtained in the detector for emissions homogeneously distributed inside different elementary volumes spanning different locations of the culture medium. As such, as described in **Figure 3**, a vertical discretization of the culture wells (z axis) was proposed to describe any acquired spectrum, this dimension providing the largest variations in detection energy probability distribution due

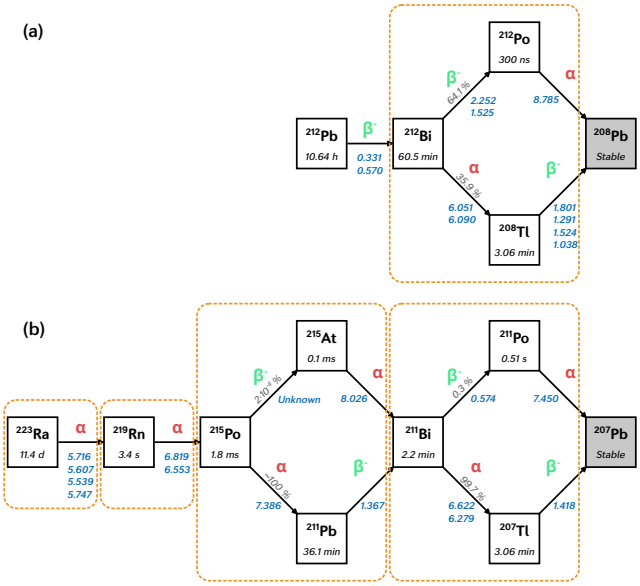

Figure 2: (a) ^{212}Pb and (b) ^{223}Ra decay chains. The main emission energies are indicated in MeV. Each dotted-line box corresponds to a group of radionuclides that are assumed to share the same spatial distribution.

to the detection geometry.

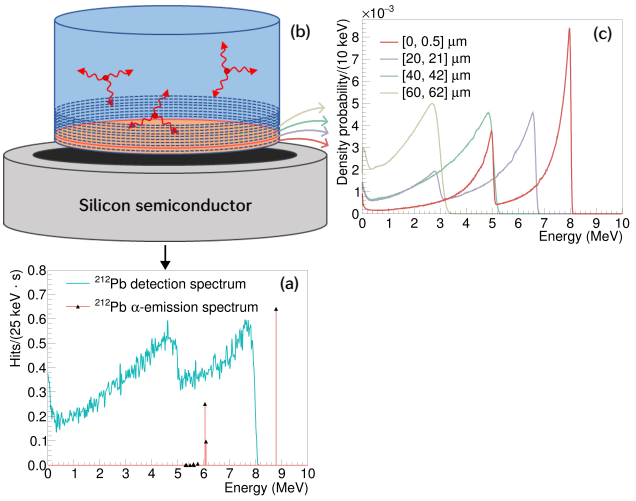

Figure 3: Principle behind the proposed spectroscopy analysis. A measured α-energy spectrum (a) is continuous and smeared compared to the emission spectrum. To describe the measurement, the culture well is divided in cylindrical slices along the vertical dimension z (b). For each slice, an average spectrum per disintegration is computed, whose shape varies with the height z of the slice (c).

Dividing the culture medium in elementary cylinders located at different heights inside the culture well, Monte-Carlo simulations using Geant4 were done to compute the different detection probability distributions associated to the different emission heights. Those distributions, corresponding to average spectra produced per disintegration at a given location, were stored as vectors joined together inside a matrix $\mathbf{X}$, called the deconvolution basis. To reconstruct a mea-

surement, that can similarly be rewritten as a vector $\mathbf{y}$, all elementary spectra should be given weights, corresponding to local activity concentrations, that can be summarized in a vector $\mathbf{a}$. As such, the deconvolution procedure consists of finding an optimal solution for $\mathbf{a}$ to the equation:

$$\mathbf{X}\mathbf{a} = \mathbf{y} \tag{1}$$

The classical least-square solving of this problem was first tested but provided too sparse and partially negative results that are unmistakably non-physical. The solving of the equation was thus changed to adjust a few constraints that improve the physical credibility of the solution computed but also act as regularizers to the solving. First of all, a non-negativity constraint was imposed following the Non-Negative-Least-Squares solving method of Lawson and Hanson [6], meaning all concentration coefficients of a given solution are ensured to be positive. Moreover, the probabilistic nature of the number of hits for a given energy was considered. Thus, the solving algorithm was changed to follow a maximum likelihood criterion, all energy counts being assumed to follow Poisson distributions. The solution was also constrained to exhibit a continuous gradient by enforcing the first ten numerical derivatives of the solution to be strictly monotonous. Finally, the total activity associated to a computed solution was enforced to be close to the known total activity present inside the culture well. All these physical considerations were implemented into a single minimisation procedure, iterative due to the nature of likelihood optimizations :

$$\mathbf{a}^{(10)}_{(n+1)} = \min_{\mathbf{a}^{(10)}>\mathbf{0}} \frac{1}{\mathbf{\Lambda}_{(n)}} \left\| \begin{pmatrix} \mathbf{X} \\ p \cdot \mathbf{h}^T \end{pmatrix} \mathbf{D}_{10}^{-1} \mathbf{a}^{(10)} - \begin{pmatrix} \mathbf{y} \\ p \cdot A_r \end{pmatrix} \right\|_2^2 \tag{2}$$

This dedicated optimization was named as the Constrained Non-Negative Maximum Likelihood (C-NNML) method. In this method, $\mathbf{a}^{(10)}$ is the tenth order numerical derivative of the activity distribution, $\mathbf{\Lambda}_{(n)} = \mathbf{X}\mathbf{a}_{(n)}$ corresponds to the fit obtained at the n-th estimation, $\mathbf{h}$ is the vector containing the heights of the elementary cylinder volumes, $\mathbf{D}_{10}$ is the tenth order numerical derivation matrix, A_r is the real total activity inside the culture well, and p is an adjusted scalar weight. Starting from an homogeneous distribution solution, ten iterative computations of **Equation 2** proved sufficient to reach convergence. Solving this problem for a spectrum acquired at time t and for a duration Δt provides the corresponding cumulated activity distribution, which then may be used to compute the delivered dose to the cells. Using the same well discretization scheme employed to construct the matrix $\mathbf{X}$, average doses to the cells per disintegration $D_1(z_i)$ are also computed through Geant4 simulations. Following the Medical Internal Radiation Dosimetry formalism[7], the dose delivered in the time interval $[t, t + \Delta t]$ is given by:

$$D_{t,t+\Delta_t} = \sum_i a\,(t, z_i) \cdot D_1(z_i) \cdot \Delta t \tag{3}$$

Validation of the new deconvolution method

The newly developed deconvolution method was assessed to quantify its ability to accurately reconstruct the spatial distribution of the radionuclides in the culture medium, and to evaluate the potential impact on dosimetry accuracy. To that end, *in vitro* irradiations using ^{212}Pb or ^{223}Ra as the radioisotope were simulated using Geant4. These irradiations were simulated using predefined, realistic activity distributions with different gradient shapes. Five different spatial distribution models, plausible in the light of the previous observations, were elected to reproduce different types of concentration at the bottom of the well, and for different total activity values that are representative of total activities at the beginning or at the end of *in vitro* experiments. Reproducing ten times the simulation for each pair of activity distribution model and of total activity, a database of 150 spectra was constructed for ^{212}Pb, each of them corresponding to a 600 s integration time. For each simulation, the measured spectrum on the detector and the dose delivered to the cells were recorded. The simulated spectra were then analyzed and the computed spatial distributions and doses to the cells were compared to their simulated, ground-truth, counterparts. A similar assessment was done with ^{223}Ra, with the specificity that the possibility for the different α-emitting groups identified in **Figure 2b** to have different activity distributions was accounted for. Given the very fast decay of ^{215}Po following the decay of ^{219}Rn, these two sources of α-emissions were constrained to share the same spatial distribution, which in light of experimental data (see **Figure 5**) is a reasonable hypothesis. Again, realistic gradient shapes were attributed to each of the α-emitting group activity distributions, and a data base of 60 simulated spectra and their corresponding doses to the cells was constructed, each of them corresponding to 300 s irradiations.

As illustrated in **Figure 4**, the analysis of spectra corresponding to ^{212}Pb irradiations showed a very good fitting ability of the method, with no noticeable deviations between simulated and deconvoluted distributions. When converted into doses with the use of **Equation 3**, the relative difference between computed and ground truth doses was systematically below 3%, and normally distributed.

On the other hand, the analysis of the spectra obtained through simulation of ^{223}Ra irradiations exhibited larger deviations between the simulated and deconvoluted distributions, exceeding occasionally three estimated standard deviations on the activity values. However, when translated into dose computations, compensation phenomena between the different α-emitting groups activities seem to be taking place as the relative error was systematically below 2% for all 60 simulated spectra, hiding that the errors on the dose delivered by a specific group of emitters widely varied from -45.4% to 27.7%.

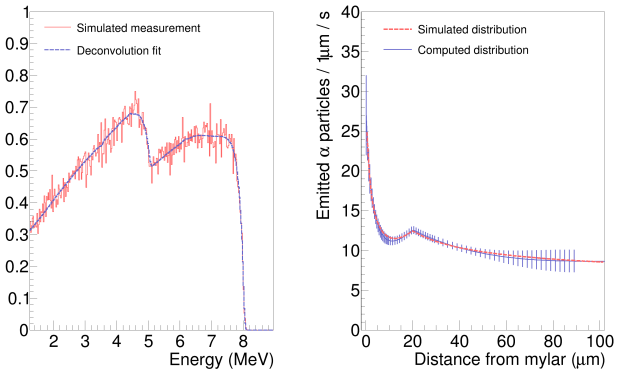

Figure 4: Example of a deconvolution carried on a simulated inverse-power gradient of ^{212}Pb. The left-hand side plot compares the simulated and reconstructed spectra. The right-hand side plot shows the corresponding simulated and deconvoluted spatial distributions. The error bars on the deconvoluted spatial distributions correspond to three estimated standard deviations (from a Monte-Carlo uncertainty estimation method).

Analysis of measurements in *in vitro* conditions with ^{212}Pb and ^{223}Ra

The new C-NNML method was applied to experimental spectra acquired using a similar setup to the one showed in **Figure 1**. For both nuclides, the wells were simply filled with tap water in which 15 kBq of ^{212}Pb or 9.3 kBq of ^{223}Ra was diluted. The experiments with ^{212}Pb were carried before the conception of the C-NNML algorithm, and were already analyzed with a different algorithm, based on parametric fitting [3]. A re-analysis was done using the newly developed C-NNML algorithm. It lead to similar results in terms of computed time and spatial distributions, albeit the larger flexibility of the method allowed for slightly different gradient shapes being retrieved. However, a first look at potential dosimetry results showed compatibility of the two algorithms. The most noticeable difference between the two algorithms concerned computational performance, since the analysis of one spectrum was done in less than 0.1 s with the C-NNML minimisation method while the previous algorithm was computationally expensive and took more than one minute per spectrum. This is especially relevant because this gain in performance enables the use of the methodology as an online dosimetric tool.

The C-NNML algorithm was also applied to experiments where the culture medium was composed of water with diluted ^{223}Ra. The shape of the spectra, presented in the top part of **Figure 5**, is characterized by the presence of peaks corresponding to each of the α-emitting groups. However, it also clearly appears that the amplitude of these peaks differ widely, with most noticeably the peak attributed to ^{211}Bi being way more intense than the others. This indicates that the the different emitter groups are characterized by different spatial and temporal distributions, as showcased in the bottom part of **Figure 5**.

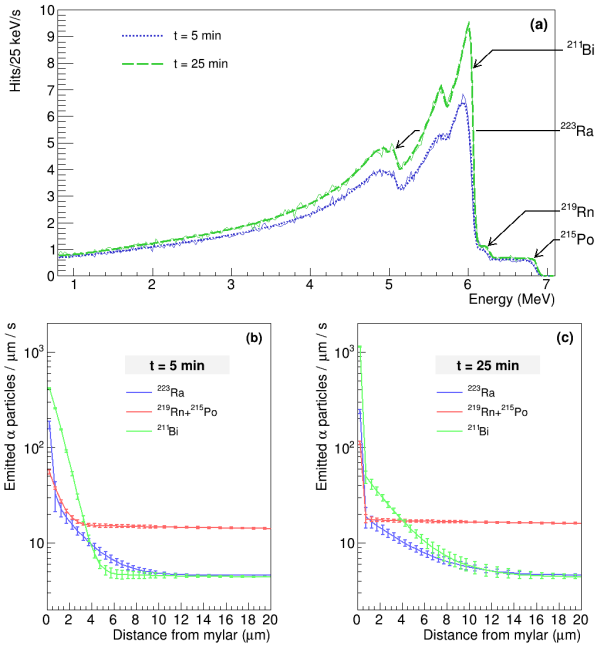

Figure 5: (a) Superposition of energy spectra measured by the detectors 5 min and 25 min after ^{223}Ra deposition in a well and fits obtained from C-NNML deconvolution. (b,c) Spatial distributions computed in the first 20 μm at the bottom of the well. Uncertainty bars are given as three estimated standard deviations.

Conclusion

A new algorithm, faster and more flexible, was developed to deconvolute the vertical and time distribution of α-emitting radionuclides being tested during *in vitro* assays. The reliability of the method was also assessed, and showed over 210 spectra corresponding to simulated irradiations that the relative error on dose was systematically below 3%. Moreover, analysis of assays carried with ^{223}Ra highlighted that radionuclides with more complex decay chains must be treated carefully, as each of the successive α-emitters may be characterized by different spatial and time distributions. This in turn leads to larger risks of over-fitting of the acquired spectra, rendering the individual spatial distributions estimated less reliable. However, as shown during the validation using simulated assays with different spatial distributions for ^{223}Ra and its daughter nuclides, it should ultimately have no significant impact on the global dosimetry.

Acknowledgements

This project was funded by the Centre National de la Recherche Scientifique (CNRS) through the MITI interdisciplinary program ISOTOP2020.

References

[1] V. Radchenko et al., J Nucl Med. 62, 1495-1503 (2021).

[2] F. Bruchertseifer, A. Kellerbauer, R. Malmbeck, A. Morgenstern, J Label Compd Radiopharm. 62, 794-802 (2019).

[3] A. Frelin-Labalme et al., Med. Phys. 47, 1317-1326 (2020).

[4] J. Dahle, N. Abbas, O. S. Bruland, R. H. Larsen, CRP. 4, 321-328 (2011).

[5] FASTER, http://faster.in2p3.fr/

[6] C. L. Lawson, R. J. Hanson, Solving Least Squares Problems (Society for Industrial and Applied Mathematics, 1995).

[7] W. E. Bolch, K. F. Eckerman, G. Sgouros, S. R. Thomas, J Nucl Med. 50, 477-484 (2009).

Nuclear data for particle therapy and spatial radioprotection

Levana Gesson

Under the supervision of M.Vanstalle IPHC Strasbourg, and U.Weber GSI Darmstadt

Abstract — In the past years, advanced techniques were developed for particle therapy to deliver a more conformal dose to the tumor while sparing healthy tissues [1]. However, the ion beam fragmentation and the interaction between the beam and the target produce secondary particles which need to be characterized by their atomic number and their effects inside the patient body. The work presented here is focused on the characterization of these secondary particles, through two different projects. The first one aims at measuring the physical properties of the secondary particles together with their impact on biomolecules, in order to improve simulation tools used in treatment planning system. In regards to the physical properties measurement, ΔE-E method and a TOF (Time Of Flight) method are proposed. The second one intends to use the secondary particles to monitor the treatment of moving tumors, which is still a challenging problem for ion beam therapy. In the case of lung cancer, the respiratory motion of the patient can induce strong doses inhomogeneities and range shifts during the treatment due to high density gradients between the lung, the tumor tissue and the bones in the case the beam misses the tumor volume [2].Therefore, several range monitoring techniques were investigated, by using the secondary particles production during the treatment (e.g., PET). In this work, another approach is proposed by detecting the strong density gradients between lung, tumor tissue and bones, by using a CMOS-based tracker system, which can detect the secondary charged particles produced by the primary carbon ions. To verify if the treatment is delivered as planned, the vertex distribution [3] will be computed after reconstruction of the secondary charged particle trajectories, and compared to the predicted one.

Introduction

In particle therapy, advanced techniques were developed to deliver a more conformal dose to tumor volumes while sparing the surrounding healthy tissues. Compared to conventional therapy, such as X-rays, the depth dose profile and the biological effectiveness of ions are favorable to deliver precise doses (Figure 1).

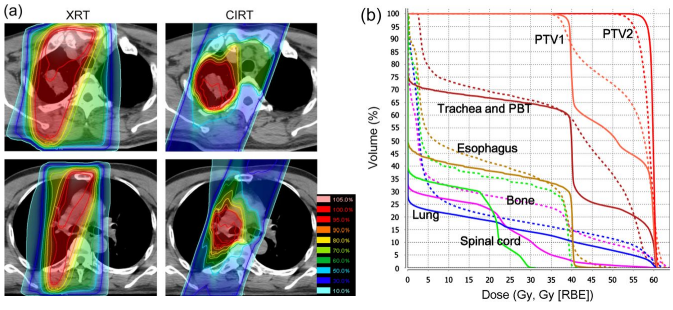

Figure 1: Comparison between X-ray (XRT) and carbon ion (CIRT) radiotherapy for a lung cancer. A dose of 40 Gy/Gy (RBE) was delivered to PTV1. A total dose of 60 Gy/Gy (RBE) was administered to PTV2. (a) Dose distributions for XRT (left) and CIRT (right). (b) DVHs for the XRT (dashed lines) and CIRT (solid lines). [4]

However, the beam fragmentation and the interaction between the beam and the target produce secondary particles (Figure 2), which is an important concern in the use of carbon ions for treating pediatric cancers, one of the main indications of CPT (Charged-Particle Therapy)[12].

Those secondary particles can be used for online control (in general prompt-γ or proton) but their production and interaction processes are not accurately known due to a lack of experimental data. The simulation codes of those processes exhibit important discrepancies with data (Figure 3), therefore improvement of Monte Carlo codes, such as Geant4 and Geant4-DNA, which are commonly used in CPT, are needed to improve treatment planning.

Measurement of secondary particles in particle therapy with CLINM setup

The first project presented (CLINM - Cross-sections of Light Ion and Neutron Measurement) is a combine measurement of the physical properties of the secondary particles together with their impact on biomolecules, in order to improve simulation tools used in treatment planning system. The secondary particle characterization is achieved through two different experimental setups, typically used in nuclear physics measurements.

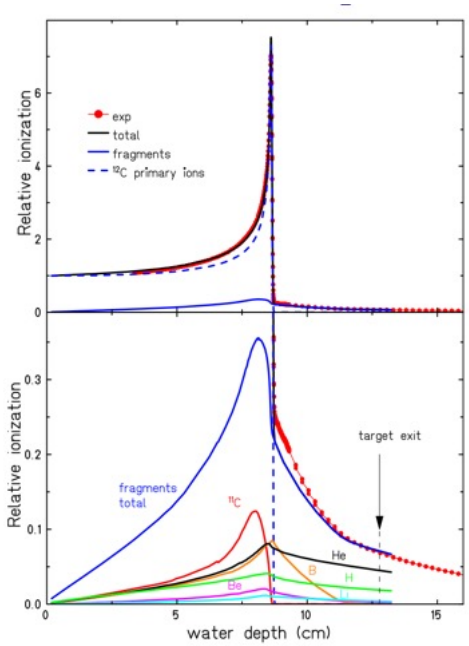

Figure 2: Secondary beam fragments produced by 200 MeV/u 12C ions in water and their dose contribution in carbon ion therapy. [5]

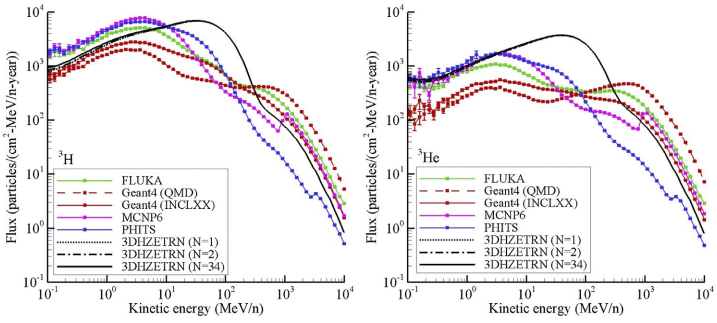

Figure 3: Comparaison between simulation codes for helium projectile fragmentation. [6]

The first one is based on a ΔE-E telescope. This setup consists in a thin plastic scintillator (2mm thickness) placed in front of a CeBr3 crystal scintillator. When the primary beam interacts with a PMMA target (which emulates the atomic composition of human body), it produces secondary particles which will deposit a small amount of energy in the plastic ΔE and then will stop in the CeBr3 where they deposit all the rest of their energy E (Figure 4).

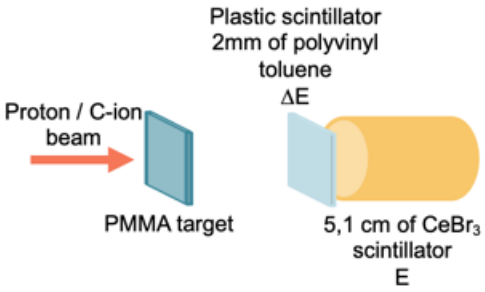

Figure 4: Experimental setup for the ΔE-E measurement method.

With this measurement method, we can build a ΔE-E diagram (Figure 5) where we can identify each Z of the secondary particles and reconstruct their kinetic en

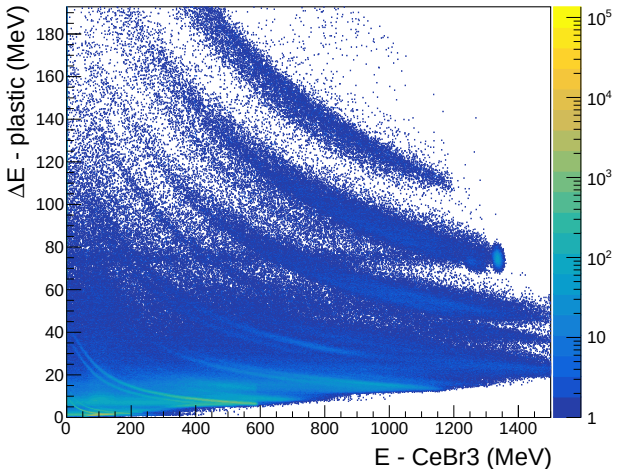

Figure 5: ΔE-E results from simulation with a carbon-ion beam of 200MeV/u, the detectors at 5° from the beam axis, and a PMMA target of 4 cm.

Limitations of this technique appears at high energy, because the secondary particles will cross the CeBr3 and thus it will no longer possible to reconstruct the total energy. To overcome this problem, a second measurement method is proposed.

This second methos consists of measuring the TOF (Time Of Flight) of the secondary particles. The setup is composed of the CeBr3 crystal scintillator added to a plastic scintillator placed in front of the target. This first scintillator plastic is the START signal for a primary particle passing through it. The secondary particles produced in the PMMA target interacts with the

CeBr3 scintillator that will provide the STOP signal for the time-of-flight measurement (Figure 6).

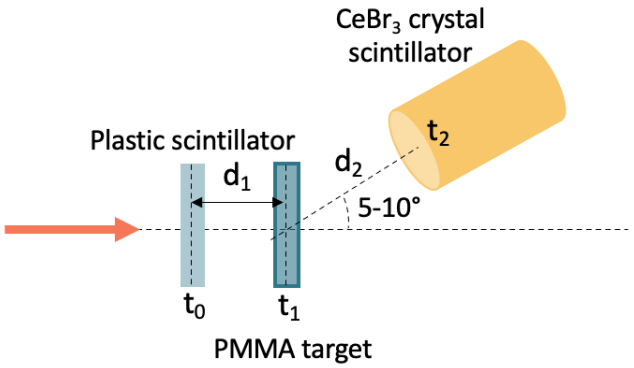

Figure 6: Experimental setup for the TOF measurement method.

Thus, we can deduce the time of flight of each secondary particle and identify its Z through deltaE-ToF map, as presented on Figure 7.(Figure 7).

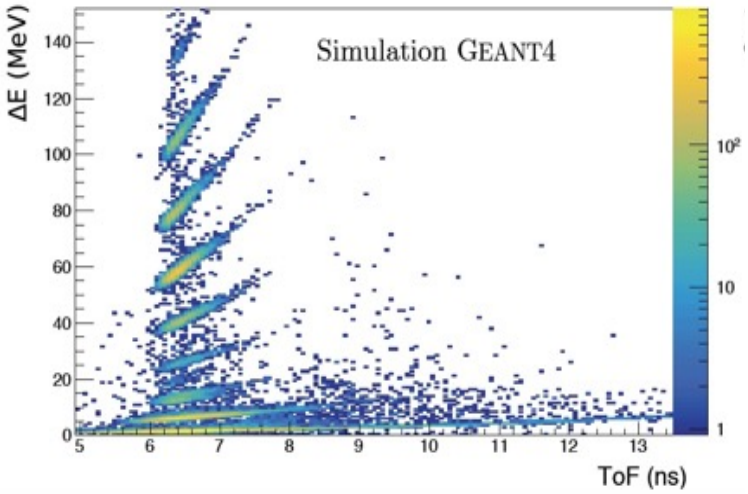

Figure 7: TOF results from simulation with a carbon-ion beam of 200MeV, the detectors at 5° from the beam axis, and a PMMA target of 4 cm. Work done by A.Secher, PhD thesis

The first part of this project was to performed a calibration of our detectors to typical clinic ion beam energies (Figure 8). The calibration experiments were carried out at Cyrce cyclotron (IPHC, Strasbourg, France), with a proton beam of an energy between 25-6 MeV/u, and at CAL protontherapy center (Centre Antoine Lacassagne, Nice, France), with a proton beam of 60 MeV/u.

Another CeBr3 calibration was done for carbon ion beam between 120-180 Mev/u and thus allows in the coming months to start taking data with the two methods experiments, with carbon ion or proton beams at clinic energies.

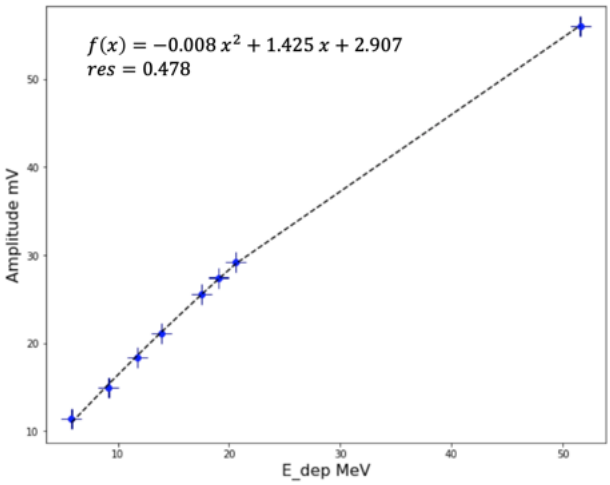

Figure 8: Calibration in energy for protons for the CeBr3 scintillator with a polynomial of second order fitl.

Real time monitoring of density gradients for 4D treatment in ion-beam therapy

Secondary particles produced in CPT can be used for monitoring purposes, in order to improve accuracy of treatment delivery. The second projects presented intends to use the secondary particles to monitor the treatment of moving tumors, which is still a challenging problem for ion beam therapy.

In the case of lung cancer, because of the respiratory motion of the patient and the strong density gradient between the lung, the tumor tissue and the bones, treatment with ion beams needs to be very precise to avoid over- and underdosage in the patient body.

In this work, the goal is to measure density gradients between the lung, tumor tissue and bones, in order to verify if the treatment was delivered as planned. For this, a beamtime campaign was done, where several CMOS-based tracker systems were used to detect the emitted secondary charged particles, due to the nuclear fragmentation of the primary carbon ion beam with the target material.

These measurements intend to verify if the tumor was properly irradiated by the carbon ion beam, after computing and comparing the vertices (production point) of secondary protons, obtained from the reconstructed trajectories of the secondary fragments, to the predicted ones. Since the density gradients between the different tissues are important, the measured vertex distributions will also show significant discrepancies according to the irradiated area.

A preliminary study was performed at the Ion-beam Therapy Center in Marburg (MIT) in March 2022, before the main experiment, which was planned in June 2022 at the same facility. The phantom was composed of a thin PMMA aquarium of 25×25×25 cm^3, where

a foam cube of 0.3 g/cm^3 density, comparable to the one of lung tissue, was inserted. A hole in the center of the foam cube allowed to insert a PMMA cylinder of 5 cm diameter with a spherical shape at one end (representing the tumor volume). The target was placed on a moving table, representing the respiratory motion of a patient body in real time. In addition, the measurements were performed for a planned spherical volume of 5 cm diameter, using the raster scanning system. The beam position information were given by the two Multi Wire Proportional Chambers (MWPC) of the beam nozzle.

The secondary fragments were detected by four tracker systems, composed of three MIMOSA-28 pixel sensors [7] each, which were placed at several angles behind the target. MIMOSA-28 is a high spatial resolution detector consisting of 928 rows x 960 columns with a pitch of 20.7 μm, a sensitive area of 2×2 cm^2 and a readout time of 186.5 μs. This sensor has a spatial track resolution better than 10 μm [8].

The four tracker systems were placed at ±10.5° and ±21° behind the target with respect to the beam axis, and at a distance of 24.8 cm compared to the target center. These values were chosen after Monte Carlo simulations with Geant4 [9][10][11] to determine the best compromise between the number of vertices reconstructed and their resolution. The experimental setup is shown in Figure 9.

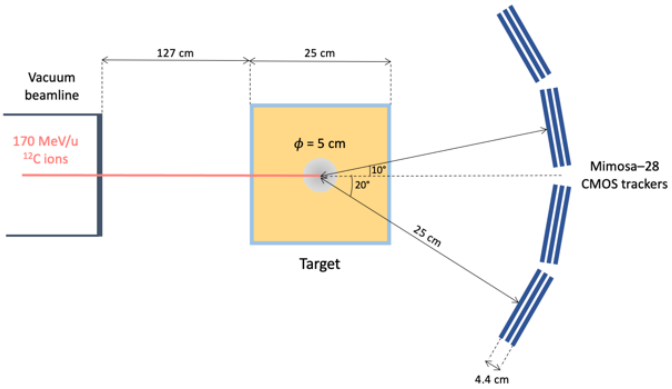

Figure 9: MIT experimental setup (march 2022) for the measurement of the high density gradients with four CMOS tracker system placed at several angles behind the target.

In Figure 10, the fragment production point (vertex) distributions are shown along the beam axis for the same planning treatment (sphere of 44 mm diameter with optimized plan of 2 Gy), in the case of the target (PMMA cylinder) is exactly where the beam is scanning (in blue) and in the case of the beam is only touching foam (in green).

Significant differences between the two distributions are measured due to the high density gradients between the foam and the PMMA. For the case where the PMMA cylinder is centered as planned, the amount of vertices increases until dropping down around the zero position, as expected since the carbon ions fully stop in the PMMA cylinder. In the case where the beam is

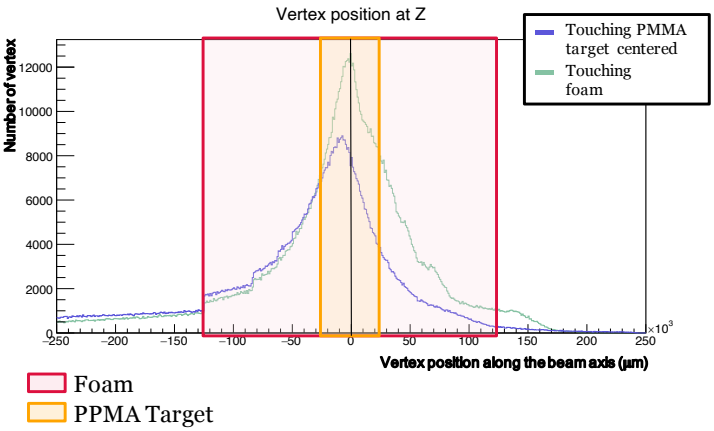

Figure 10: Vertex distributions along the beam axis reconstructed with the CMOS-tracker placed at 10° with respect to the beam axis. The zero position represents the center of the target.

touching the foam only, the decrease of vertices number is less pronounced around zero because the carbon ions have a longer range when not passing through the PMMA cylinder, and thus continue to produce a bigger amount of secondary particles until the end of the target.

For the future of this project, the goal is to provide a concept that can be used for online monitoring for 4D treatments of lung cancer on a real human phantom, and which can provide a fast information on the beam delivery during a patient treatment, in order to be used in clinic in the future.

References

[1] D. Schardt, T. Elsasser, and D. Schulz-Ertner. Heavy-ion tumor therapy; Physical and radiobological benefits. Rev, Mod. Phys., 82(1):383, 2010. doi: 10.1103/RevModPhys82.383.

[2] M. E. Wolf. Robust optimization in 4D treatment planning for carbon ion therapy of lung tumors. PhD thesis, Technische Universitat, Darmstadt, November 2018. URL http://tuprints.ulb.tu-darmstadt.de/8354/.

[3] C. Finck. et al. Study for online range monitoring with the interaction vertex imaging method. Phys. Med. Biol., 62(24):9220, 2017. doi: 10.1088/1361-6560/1195-4e.

[4] Kubo, Nobuteru et al. (2016). Dosimetric comparison of carbon ion and X-ray radiotherapy for Stage IIIA non-small cell lung cancer. Journal of Radiation Research. 57. doi: 10.1093/jrr/rrw041.

[5] Gunzert-Marx and al. New J. Phys. (2008)

[6] Norbury JW, et al. (2020) Are Further Cross Section Measurements Necessary for Space Radiation Protection or Ion Therapy Applications?

Helium Projectiles. Front. Phys. 8:565954. doi: 10.3389/fphy.2020.565954

[7] I. Valin, et al. A reticle size CMOS pixel sensor dedicated to the STAIR HFT. J.Instrum., 7(01):C01102, 2012. doi: 10.1088/1748-0221/7/01/C01102.

[8] R. Rescigno, et al. Performance of the reconstruction algorithms of the FIRST experiment pixel sensors vertex detector. Nucl. Instrum. Meth. A., 767:34-40, 2014. doi: 10.1016/j.nima.2014.08/024

[9] S. Agostinelli, et al. Geant4-a simulation toolkit. Nucl. Instrum. Meth. A, 506(3):250 - 303, 2003. ISSN 0168-9002. doi: 10.1016/S0168-9002(03)01368-8.

[10] J.Allison, et al. Geant4 developments and applications. IEEE Trans. Nucl. Sci., 53(1):270-278, Feb 2006. ISSN 1558-1578. doi: 10.1109/TNS.2006.869826

[11] J. Allison et al. Recent developments in Geant4. Nucl. Instrum. Meth. A, 835:186 - 225, 2016. ISSN 0168-9002. doi: 10.1016/j.nima.2016.06.125

[12] Mizumoto et al. 2017, DOI: 10.2176/nmc.ra.2017-0003

Studies of Frisch grid performance and calibration of light measurement in liquid xenon detector for small animal medical imaging

Dingbang Cai

SUBATECH, IMT Atlantique, CNRS/IN2P3, Université de Nantes, 44307 Nantes, France.

Abstract — In the past decades, an advanced medical imaging technology, called 3-gamma medical imaging, was proposed and has been continuously developed. However, it is always of great interest to search for a new medical imaging technology that functions at lower activity level compared to the existing ones. Therefore, our team has developed a prototype of single-phase liquid xenon Compton telescope for small animals, named as XEMIS2, by using 3-gamma medical imaging technology. The objective is to realize low-activity medical imaging by reducing the operating time or the dose of injected radio-pharmaceuticals while always maintaining high imaging performance. This paper reports and discusses some preparatory work for XEMIS2 including Frisch grid performance investigation, light measurement calibration as well as optimization. Results indicate that the modified grid of gas electron multiplier (GEM-modified) can potentially replace the MicroMegas grid which has been installed in XEMIS1. Moreover, the present work uses a new calibration protocol to prove that the acquisition chain of scintillation light is ready for the following experiments.

Introduction

As an important and powerful tool for both diagnosis, treatment and research, medical imaging has flourished in recent decades. The development of medical imaging always revolves around three aspects: i) improving the quality of imaging, ii) reducing injected dose to patients and iii) shortening the examination time. Based on these three objectives, a variety of theories and technologies have been proposed and studied, such as xSPECT technology[1] (which combines single photon emission computed tomography (SPECT) with X-rays computed tomography (CT)), total-body positron emission tomography (PET) technology[2], Time-of-flight PET technology[3], Depth-of-interaction PET technology [4, 5] and 3-gamma imaging technology[6, 7].

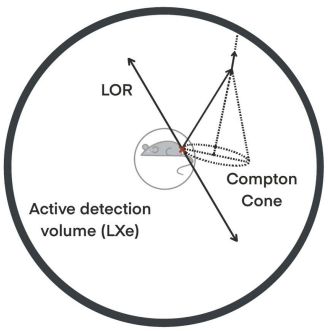

Figure 1: Schematic diagram of 3-gamma medical imaging technology

As one of the most innovative medical imaging technologies, the 3-gamma imaging technology, which is developed at SUBATECH laboratory, aims at reconstructing the radiotracer distribution[6, 8]. The radiotracer that is labeled with a (β+,γ) emitter such as scandium-44 emits a photon and a positron quasi-simultaneously. The positron annihilates with an electron, producing two back-to-back photons with an energy of 511 keV and creating a line-of-response (LOR). The third gamma that is directly emitted by (β+,γ) emitter can be detected by a Compton camera and will form a Compton cone, shown in Fig.1. The intersection of the formed Compton cone with the LOR indicates the localization of the (β+,γ) emitter. XEMIS2 is designed based on the concept mentioned above and is being installed in Centre hospitalier universitaire de Nantes (CHU).

Figure 2: Overview of XEMIS2 facility in CHU

XEMIS1, the first prototype of the XEMIS project, has proven that the single-phase liquid xenon time projection chamber (LXeTPC) designed by our research team is feasible and has many promising features: large

field-of-view, high sensitivity, satisfying energy and space resolution. LXeTPC has an energy resolution of about 5% and a spatial resolution at sub-millimeter level for the incident photons with the energy of 511 keV under an electric field of 1 kV/cm[6, 8]. Furthermore, simulation results reveal that the energy resolution of XEMIS2 can even reach to 4% under a higher electric field of 2 kV/cm[9, 10].

XEMIS2 Camera

The XEMIS2 facility consists of three functional subsystems: i) a purification and circulation system which maintains the circulation of liquid xenon and sustains its impurity level below 1 ppb O2 equivalent, ii) a high-pressure resistant recover-storage system of xenon (ReStoX) which stores the 200 kg liquid xenon and maintains the working condition (172 K at 1.5 bar abs) for XEMIS2 camera and iii) a LXeTPC container which performs scintillation light and charge measurement. The complete facility is illustrated in Fig.2 and the longitudinal section design of XEMIS2 is shown in Fig.3.

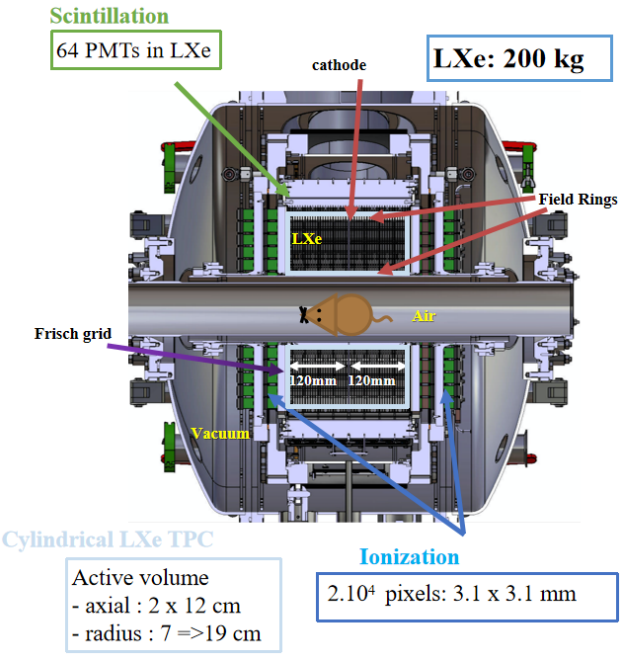

Figure 3: Longitudinal section design of XEMIS2

The XEMIS2 camera consists of two identical LXeTPCs sharing a common cathode. Each TPC has a segmented anode on the end side. The active region of each TPC passes through a void cylinder with a drift length of 12 cm, an inner radius of 7 cm and an outer radius of 19 cm, which is surrounded by a set of field rings to ensure the uniform distribution of the drift electric field[8]. 64 VUV-sensitive Hamamatsu R7600-06 MOD-ASSY PMTs are evenly distributed around the TPC to detect scintillation light. Each segmented anode consists of more than 10,000 pixels of 3.1mm × 3.1mm to detect ionization signals. A Frisch grid, supported by 130 μm micro-pillars, is installed to enable

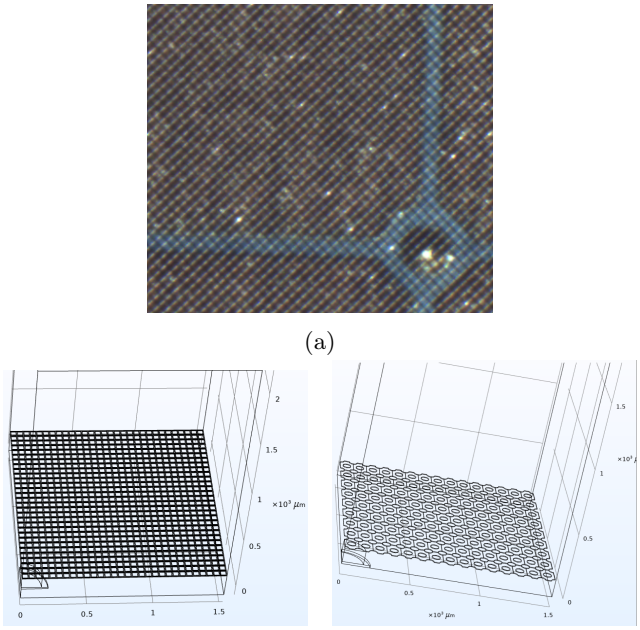

(a) (b) (c)

Figure 4: (a) MIMELI grid geometry in reality (b) MIMELI grid geometry simulated by COMSOL Multiphysics[14] and (c) GEM-modified grid geometry simulated by COMSOL Multiphysics

detection of readable ionization signals whose amplitude is i) proportional to the number of collected electrons and ii) is independent of the interaction position along the drift direction[10]. The scintillation signals in XEMIS2 mainly provide the information of gamma-ray interaction time while ionization signals provide information on the deposited energy as well as the position of each interaction vertex[11, 12].

Frisch grid simulation

Several studies[10, 13] have been conducted to demonstrate the promising performance of micro-mesh for dense liquid ionization chambers (MIMELI) which has already been installed in XEMIS1. Made of copper, the MIMELI grid has a thickness of 5 microns with a micro-mesh of 500 lines per inch (LPI) and contains 12 micron bars, making it a good candidate for XEMIS2. However, the surface of the XEMIS2 anode is much larger than that of XEMIS1, making MIMELI grid mechanically unfavorable for XEMIS2. Consequently, a more solid or a thicker grid is required.
By using the finite element method, simulations were performed in this work to investigate the electronic transparency of the MIMELI grid and also of the GEM-modified grid at different electric field ratios, which is a key factor in predicting the grid performance. The electronic transparency of the grid is defined as the ratio of the number of electrons collected by the anode pixels to the initial number of electrons released by the virtual plane close to the cathode.
In this work, the simulation delimits a volume of 30 pitch × 30 pitch × 3mm (along the drift direction),

which includes the cathode, grid, pad and pixels of the anode. The geometries of MIMELI and GEM-modified grid are both presented in Fig.4. The copper pad located between the grid (MIMELI grid or GEM-modified grid) and anode is a cylinder with a radius of 75 microns and a height of 125 microns. The base cylinder has a radius of 150 microns and a height of 17 microns. Different from the MIMELI grid, the GEM-modified grid is made from a copper plate, which has some circular holes with a radius of 30 microns, and the center-center distance between two adjacent circular holes is 100 microns.

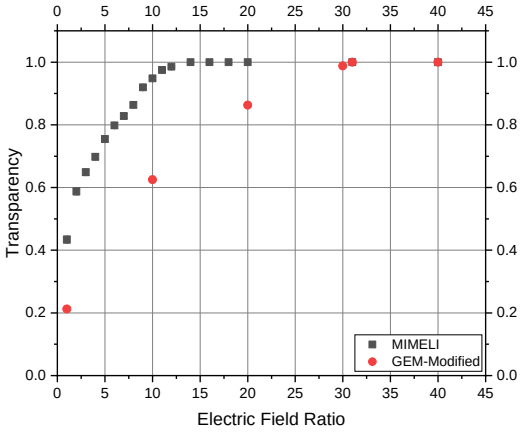

Figure 5: Electronic transparency at different electric field ratios (E_a/E_{drift})

The upper plane of the simulated volume is defined as the cathode, and the lower plane as the anode. The electric field between the cathode and the grid is fixed to 2 kV/cm, denoted as E_{drift}, and the electric field between the grid and the anode is denoted as E_a. The relationship between electronic transparency and electric field ratio (denoted as R), was studied by changing E_a, which is shown in Fig.5. In this work, 50,000 electrons are simulated for each E_a and the electrons collection position of MIMELI with pad at $R = 12$ are shown in Fig.6. The simulation results indicate that the transparency of MIMELI grid achieves 100% at $R = 12$ and the GEM-modified grid can achieve 100% at $R = 31$. Additionally, the GEM-modified grid is much more solid than MIMELI grid, so GEM-modified grid can be a potentially better candidate to replace the MIMELI grid in XEMIS2. More tests and experiments will be conducted to further investigate the performance of GEM-modified grid.

Scintillation light measurement calibration

In XEMIS2, scintillation signals can provide the information on the time and spatial pre-localization of gamma-ray interaction, which reduces TPC occupancy. The scintillation light detection chain consists of three

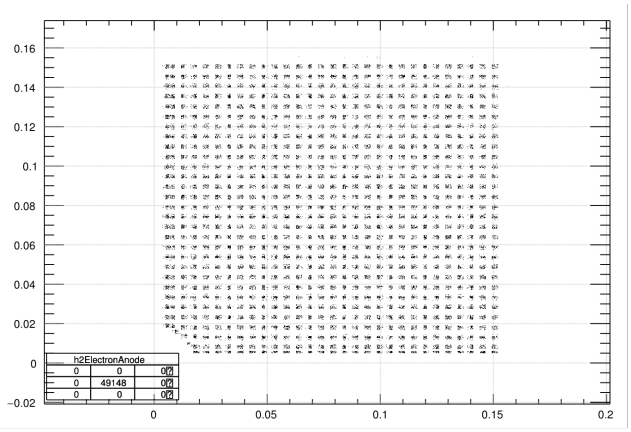

Figure 6: Electrons collection position of MIMELI at $R = 12$

parts: VUV sensitive PMT, XEMIS scintillation readout for extraction of time over threshold discrete electronics (XSRETOT) and XEMIS data concentrator (XDC). The 64 VUV sensitive PMTs that work at the liquid xenon temperature can measure the interaction time and the number of photoelectrons. The output signals of each PMT are filtered, shaped and then amplified by XSRETOT. The output data of XSRETOT is collected and concentrated by XDC. A detailed study on the electronics response for each part of the scintillation signal detection chain is necessary to characterize the detector performance.

In XEMIS2, time over threshold (TOT) method is applied to detect the number of photoelectrons since the front-end readout circuit based on the TOT readout method has various advantages in simple circuit structure: high efficiency, flexible design, low cost, and low power consumption.

In the present work, a calibration protocol of light detection chain is proposed, which consists of the following steps: i) selecting the appropriate threshold, ii) defining the equivalent charge to threshold, iii) converting the TOT into an equivalent number of photoelectrons, iv) correct the time walk effect and v) adjusting the high voltage applied to each PMT. These five steps are necessary to the camera acquisition calibration. The satisfying calibration results show that the scintillation light measurement chain is ready for the future experiments. One of the calibration results reveals the dependence of the number of photoelectrons on the TOT for a threshold of 1 photoelectron, which is shown in Fig.7. TOT varies as expected, which means that the number of collected photoelectrons can be easily distinguished from TOT.

Conclusion

The GEM-modified grid can replace the MIMELI grid according to simulation results and thus has been installed in XEMIS2 at CHU. Nevertheless, further experiments are necessary to validate its performance.

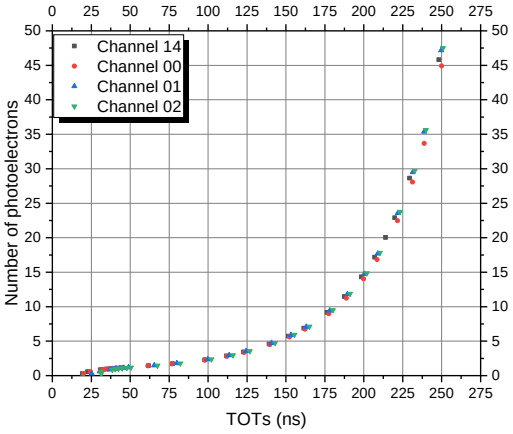

Figure 7: Dependence of the number of photoelectrons on the Time Over Threshold (TOT) for a threshold of 1 photoelectron

Moreover, the present work uses a new calibration protocol, which predicts the normal function of scintillation light acquisition chain. New simulations and experiments are ongoing to correct the conversion between TOT and equivalent number of photoelectrons. Furthermore, the XEMIS2 detector is scheduled to be operational in 2023 and will be used for future experiments.

References

[1] A. Hans Vija, Introduction to xSPECT* Technology: Evolving Multi-modal SPECT to Become Context-based and Quantitative, 11.(2015) Siemens Healthcare GmbH.

[2] S. R. Cherry, Total-body imaging: Transforming the role of positron emission tomography, Science Translational Medicine VOL.9, NO.381

[3] Suleman Surti, Joel S. Karp, Advances in time-of-flight PET, Physica Medica, Volume 32, Issue 1,2016,Pages 12-22,ISSN 1120-1797, https://doi.org/10.1016/j.ejmp.2015.12.007.

[4] Ito, M., Hong, S.J. & Lee, J.S. Positron emission tomography (PET) detectors with depth-of- interaction (DOI) capability. Biomed. Eng. Lett. 1, 70 (2011).

[5] L. R. MacDonald and M. Dahlbom, "Parallax correction in PET using depth of interaction information," in IEEE Transactions on Nuclear Science, vol. 45, no. 4, pp. 2232-2237, Aug. 1998, doi: 10.1109/23.708354.

[6] Y. Xing. Studies and optimization of ionization signal measurement for the 3-gamma imaging XEMIS2 liquid xenon Compton camera. Nuclear Experiment [nucl-ex]. Ecole nationale supérieure Mines-Télécom Atlantique, 2021. English. ffNNT : 2021IMTA0249ff. fftel-03373202f

[7] Y. Zhu, Studies and optimization of scintillation light measurements for the development of the 3-gamma medical imaging XEMIS2 liquid xenon Compton camera, Nuclear Inst. and Methods in Physics Research, A 1047 (2023) 167794.

[8] Y. Zhu. Development of the XEMIS2 liquid xenon Compton camera for 3-gamma imaging : studies and optimization of scintillation light measurements. Nuclear Experiment [nucl-ex]. Ecole nationale supérieure Mines-Télécom Atlantique, 2021. English. ffNNT : 2021IMTA0247ff. fftel-03374269f

[9] J. P. Cussonneau, et al., 3 gamma Medical Imaging with a Liquid Xenon Compton Camera and 44Sc Radionuclide, Acta Phys. Polon. B 48 (2017) 1661-1667.

[10] L. G. Manzano, "Optimization of a single-phase liquid xenon compton camera for 3γmedical imaging," Ph.D. dissertation, Ecole des Mines de Nantes, 2016.

[11] Y. Xing, et al., XEMIS: Liquid Xenon Compton Camera for 3γ Imaging, Springer Proc. Phys. 213 (2017) 154-158.

[12] Y. Xing, et al., Direct Measurement of Ionization Charges in Single-phase Liquid Xenon Compton Telescope for 3γ Medical Imaging, in: 2019 IEEE Nuclear Science Symposium and Medical Imaging Conference, NSS/MIC, 2019.

[13] C. GRUPEN, Particle detector, second edition, Cambridge University Press.

[14] AC/DC Module User's Guide, pp. 75-84. COMSOL MultiphysicsÂ® v. 6.1. COMSOL AB, Stockholm, Sweden. 2022.

Systematic effects and magnetic field uniformity in the n2EDM experiment.

Thomas Bouillaud

LPSC, Universite Grenoble Alpes, CNRS/IN2P3, Grenoble, France.

Abstract — Measurements of electric dipole moments (EDMs) of spin 1/2 particles such as the neutron are sensitive probes for CP violation beyond the standard model, a key to solving the baryon asymmetry problem. In this article I give a brief overview of n2EDM, an experiment aiming to measure the neutron EDM with a sensitivity of $1 \times 10^{-27} e$cm. I then focus on two areas of my PhD work related to magnetic field uniformity in n2EDM: magnetic mapping of the coil system, and calculation of a systematic effect generated by field non-uniformities.

Introduction

One of the fundamental issues of the Standard Model is that sources of CP violations, in both the weak and the strong sector, predict a baryon asymmetry in the universe that falls short of cosmological observations by several orders of magnitude. Fortunately there exist theories beyond the Standard Model that provide sizeable CP violation. These predict CP violating couplings such as electric dipole moments (EDMs) that are within the range of experimental sensitivities [1],[2]. Among experiments able to probe these new physics is n2EDM [3], which seeks to improve its previous $1 \times 10^{-26} e$cm upper limit [4] on the neutron EDM by one order of magnitude.

The main idea of the n2EDM experiment is to measure the neutron precession frequency f_n of polarized ultracold neutrons when subjected to a weak magnetic field B and a strong electric field E. These two interactions are described by the hamiltonian

$$H = -\mu_n \sigma \cdot B - d_n \sigma \cdot E, \tag{1}$$

with μ_n the neutron magnetic moment, d_n the sought-after electric dipole moment, and σ the Pauli matrices vector. In order to extract d_n, the experiment is operated in parallel ($B = B_0 e_z$, $E = E_0 e_z$) and anti-parallel ($B = B_0 e_z$, $E = -E_0 e_z$) configurations. The difference of precession frequencies

$$f_n = \frac{\mu_n}{\pi\hbar} B_0 \pm \frac{d_n}{\pi\hbar} E_0 \tag{2}$$

in opposite configurations then gives the electric dipole moment. Even with a low magnetic field ($B_0 = 1\mu$T) and a strong electric field ($E_0 = 15$kV.cm^{-1}), the electric dipole moment contribution to the precession frequency is incredibly difficult to detect. So as to maximize its sensitivity, the n2EDM experiment uses ultracold neutrons (UCNs) that are easier to store, in a large cell-volume (two cylindrical chambers of radius $R = 40$ cm and height $H = 12$ cm working in opposite configurations), isolated from external magnetic fields by both an active magnetic shield and a passive magnetic shield. A sketch of the apparatus is shown in figure 1. The ultra cold neutrons are polarized by a 5T superconducting magnet, travel through neutron guides to the precession chambers and then back towards the detectors thanks to the UCN switch, where they are counted using a spin-sensitive detection system. The $1\,\mu$T vertical magnetic field that allows the neutrons to precess inside the two chambers is applied using the main component of the coil system, the B_0 coil. Furthermore, in a process known as mercury co-magnetometry, a mercury gas is injected in the precession chambers alongside the neutrons and the mercury atoms precession frequency f_{Hg} is extracted. By taking the ratio of mercury and neutron precession frequencies $\mathcal{R} = f_n / f_{\mathrm{Hg}}$ instead of the neutron frequency alone,

$$\mathcal{R} = \left| \frac{\gamma_n}{\gamma_{\mathrm{Hg}}} \right| \pm \frac{E_0}{\pi\hbar f_{\mathrm{Hg}}} d_n, \tag{3}$$

where $\gamma = 2\mu/\hbar$, this process provides a measurement of d_n free of fluctuations of the magnetic field B_0.

Still, one of the main challenges of the n2EDM experiment is the control of the magnetic field uniformity. In order to maximize sensitivity we require in particular that the vertical magnetic field gradient stays below a certain value:

$$\left| \frac{\partial B_z}{\partial z} \right| < 0.6 \text{ pT/cm}. \tag{4}$$

Requirements on the magnetic field uniformity such as this one are addressed both during data-taking with mercury and cesium magnetometers, and before data-taking through a thorough mapping of the coil system. The first part of this article will focus on the latter.

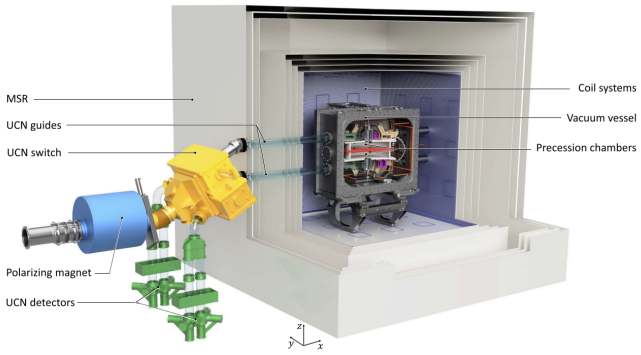

Figure 1: The n2EDM experimental setup [3]. The ultracold neutrons are polarized and transported inside two precession chambers by the apparatus on the left, which are stored in vacuum inside a magnetic shielding room (MSR).

The second part will deal with a systematic effect that is generated by non-uniformities in the magnetic field in combination with a relativistic effect impacting mercury atoms.

Mapping of the coil system

In n2EDM the magnetic field is described using a harmonic parametrization. In cylindrical coordinates, it is written

$$B(\rho,\varphi,z) = \sum_{l,m} G_{l,m} \begin{pmatrix} \Pi_{\rho,l,m}(\rho,\varphi,z) \\ \Pi_{\varphi,l,m}(\rho,\varphi,z) \\ \Pi_{z,l,m}(\rho,\varphi,z) \end{pmatrix}, \qquad (5)$$

where the $\Pi_{l,m}$ are products of polynomials of order l in ρ and z, and $\cos(m\varphi)$ for $m \geq 0$ or $\sin(m\varphi)$ for $m < 0$. The explicit form of these functions is found by requiring that that they satisfy stationary Maxwell's equation, which amounts to solving Laplace's equation for a potential Φ with $B = \nabla\Phi$ [5]. The magnetic field is then entirely described by its harmonic spectrum, which is the set of G_{lm} coefficients.

A magnetic map in n2EDM consists in the measurement of the magnetic field in three directions at several positions in space. Measurements are performed by a robot which carries a fluxgate at any cylindrical coordinate. The harmonic spectrum is then extracted from the measurements through a two-step fit. Consider a high-resolution map of the B_0 coil such as the one shown in figure 2 (B_z only). First we fit each ring (a set of points at a given ρ and z) with a Fourier series. Second we fit the fitted Fourier coefficients over the entire map with a polynomial in ρ and z given by the harmonic parametrization [5]. The fit parameters obtained from the second fit are the harmonic coefficients G_{lm}.

A direct application of field mapping is the qualification of the B_0 coil. In particular, we require that this coil matches condition (4), which in terms of the harmonic expansion translates to a requirement on the coefficient G_{10}. The first measurements of G_{10} for both

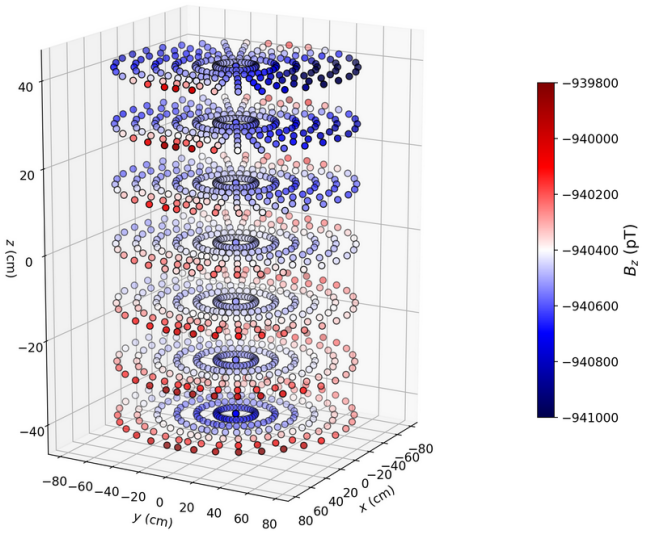

Figure 2: Vertical projection of a magnetic field map taken by the robotized fluxgate inside the vacuum vessel, with the B_0 coil in the negative polarity. Each point in this plot corresponds to the average value of B_z around a point of cylindrical coordinates (ρ,φ,z), with a φ averaging step of 10°.

B_0 coil polarities, plotted on figure 3 as the rightmost red and blue points, were far above the 0.6 pT/cm requirement. COMSOL [6] simulations performed by Pierrick Flaux [7] indicated that a vertical displacement of the coil with respect to the MSR would generate a vertical gradient proportional to the displacement δz, with $G_{10}/\delta z = 6.45(\text{pT/cm})/\text{mm}$ (page 74 of [7]). Therefore it was decided to move the coil down, by first 1 mm, in order to test this claim. Data recorded after moving the coil yielded the second set of points shown in figure 3, which confirmed the hypothesis as the slope of the linear fit (in purple) matched Pierrick's prediction. The coil was moved again by 2 mm in order to reach the satisfactory values shown as the last set of points in figure 3.

False EDM

Non-uniformities in the magnetic field also reveal problematic systematic effects. When combined with a relativistic effect arising when particles move inside an electric field and referred to as a *motional field*, which here concerns both neutrons and mercury atoms, the non-uniform field generates a shift in the precession frequency of both particles. This shift is given by spin-relaxation theory [8] as

$$\delta\omega = \frac{\gamma^2}{2}\int_0^\infty d\tau\, \mathrm{Im}\left[e^{i\omega\tau}\,\langle b(0)^* b(\tau)\rangle\right], \qquad (6)$$

where in our case $b(t) = \left[B(r(t)) + E\times \dot{r(t)}c^2\right]\cdot[e_x + ie_y]$ describes the transverse field fluctuations in the complex plane [9]. Because the neutron EDM is extracted from (3) by taking the difference of $+E$ and

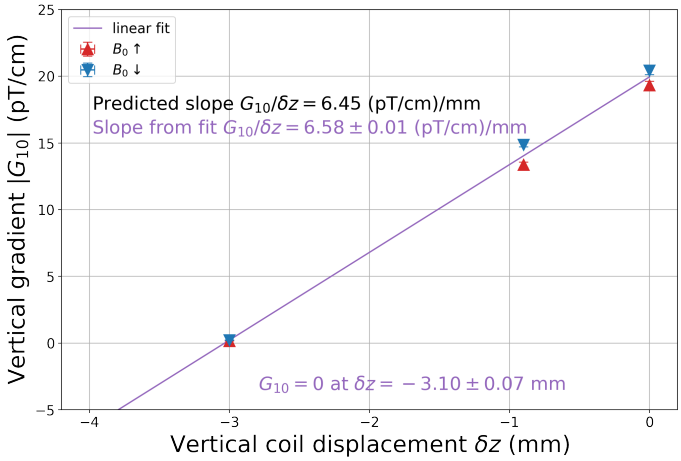

Figure 3: The triangle points show measurements of the vertical gradient, in both polarities of the coil, at three different positions (from right to left in chronological order). The slope of the linear fit matches Pierrick Flaux's prediction in [7]. The final leftmost values of 0.28 ± 0.4 pT/cm for $B_0 \uparrow$ and 0.1 ± 0.4 pT/cm for $B_0 \downarrow$ fulfill requirement (4).

$-E$ configurations, terms linear in E_0 in these frequency shifts will generate unwanted contributions to the EDM that are appropriately named *false EDM*s. Equation (6) shows that, indeed, only a combination of non-uniformities and a motional field will generate a false EDM. In this non-optimal scenario, equation (3) becomes:

$$\mathcal{R} = \left| \frac{\mu_n}{\mu_{\mathrm{Hg}}} \right| \pm \frac{E_0}{\pi \hbar f_{\mathrm{Hg}}} \left(d_n + d_n^{\mathrm{false}} + d_{n\leftarrow\mathrm{Hg}}^{\mathrm{false}} + \dots \right). \quad (7)$$

The largest of these two and the one that we will focus on is the mercury-induced false neutron EDM $d_{n\leftarrow\mathrm{Hg}}^{\mathrm{false}}$. Its expression is given by expanding $b(t)$ inside equation (6) and keeping linear in E_0 terms:

$$d_{n\leftarrow\mathrm{Hg}}^{\mathrm{false}} = \frac{\hbar \left|\gamma_n \gamma_{\mathrm{Hg}}\right|}{2c^2} \int_0^\infty d\tau \cos(\omega\tau) \frac{d}{d\tau} \left\langle x(\tau) B_x(0) + y(\tau) B_y(0) \right\rangle, \quad (8)$$

with $\omega = \gamma_{\mathrm{Hg}} B_0$. The initial approach, used for the previous version of the experiment (nEDM) and presented in [3], is to consider that in the working field $B_0 = 1\,\mu$T, the mercury atoms responsible for this effect are in a so-called *low-frequency regime* $\omega\tau_c \ll 1$, where τ_c is the correlation time of these particles. In other words the mercury atoms, which compared to cold neutrons are fast-moving particles, precess more slowly in a $B_0 = 1\,\mu$T field than their correlation time. In this regime equation (8) simplifies to an average over the volume of the precession chambers, which can be expressed using coefficients of the harmonic expansion and the geometrical parameters of the apparatus:

$$d_{n\leftarrow\mathrm{Hg}}^{\mathrm{false}} = -\frac{\hbar \left|\gamma_n \gamma_{\mathrm{Hg}}\right|}{2c^2} \langle x B_x + y B_y \rangle \quad (9)$$

$$= \frac{\hbar \left|\gamma_n \gamma_{\mathrm{Hg}}\right|}{8c^2} R^2 \left[G_{10} - G_{30} \left(\frac{R^2}{2} - \frac{H^2}{4} \right) + \dots \right]. \quad (10)$$

This analytical approach allows us to compute the exact false EDM, on the condition that the harmonic coefficients G_{lm} are measured accurately. The requirements on systematics therefore weigh entirely on online magnetometry and offline mapping.

A novel approach discussed in [10] proposes to try and cancel this systematic effect instead of measuring it. A numerical calculation of the correlation function $\langle x(\tau) B_x(0) + y(\tau) B_y(0) \rangle$ is performed using a Monte-Carlo simulation of the mercury atoms' trajectories inside the precession chambers. This function is then fitted with a double-exponential model $Fe^{-f\tau} - Se^{-s\tau}$, which is plugged into equation (8) and integrated analytically in order to obtain the false EDM as a function of the applied magnetic field B_0. The results of this numerical-analytical method when considering a first-order vertical gradient field configuration are shown as the blue curve in figure 4. This plot shows that the false EDM crosses the x-axis at a single value of B_0 of about ten times the working value of $1\,\mu$T, which we call the *magic field value*. Tuning the applied vertical field to this value ($B_m = 11.3\,\mu$T) would then cancel $d_{n\leftarrow\mathrm{Hg}}^{\mathrm{false}}$ entirely for this specific field configuration, although other requirements on field uniformity and stability, which scale with the applied field, need to be fulfilled with this one order of magnitude higher B_0.

One limitation of the magic field approach is that it is biased by the arbitrary correlation function fit. With that in mind we wished to evaluate the consistency of this numerical-analytical calculation of the false EDM with an alternative calculation method, based on the connection between the correlation functions of a signal $b(t)$ and its power spectral density. This connection is given by the Wiener-Khinchin theorem [11]

$$S_{ij}(\omega) = \int_{-\infty}^{+\infty} d\tau \left\langle b_i(0) b_j^*(\tau) \right\rangle e^{-i\omega\tau}, \quad (11)$$

where the power spectral density is defined as

$$S_{ij}(\omega) = \lim_{T\to\infty} \frac{1}{2T} \left\langle \left(\int_{-T}^{T} dt_1\, b_i(t_1) e^{-i\omega t_1} \right)^* \left(\int_{-T}^{T} dt_2\, b_j(t_2) e^{-i\omega t_2} \right) \right\rangle. \quad (12)$$

In the case of a linear vertical gradient field, we can express the false EDM as a function of the power spectral density:

$$d_{n\leftarrow\mathrm{Hg}}^{\mathrm{false}}(\omega_0) = -\frac{\hbar \left|\gamma_n \gamma_{\mathrm{Hg}}\right|}{4\pi c^2} \int_{-\infty}^{+\infty} d\omega\, \omega \frac{S_{B,x}(\omega) + S_{B,y}(\omega)}{\omega - \omega_0} \quad (13)$$

Plugging (12) in (13) and using the same Monte-Carlo simulation that allowed the calculation of the correlation function in (8), we were able to determine a numerically computable expression of the false EDM. The results of this method are shown for several values of B_0 as orange points in figure 4. The magic value thus obtained in this preliminary configuration ($B_m = 11.2 \pm 0.2\,\mu$T) was found to be compatible with the one given by the initial method. We thus confirmed the validity of the first method while also finding a way to compute the false EDM directly for any given value of the B_0 field, albeit for a simplified magnetic configuration.

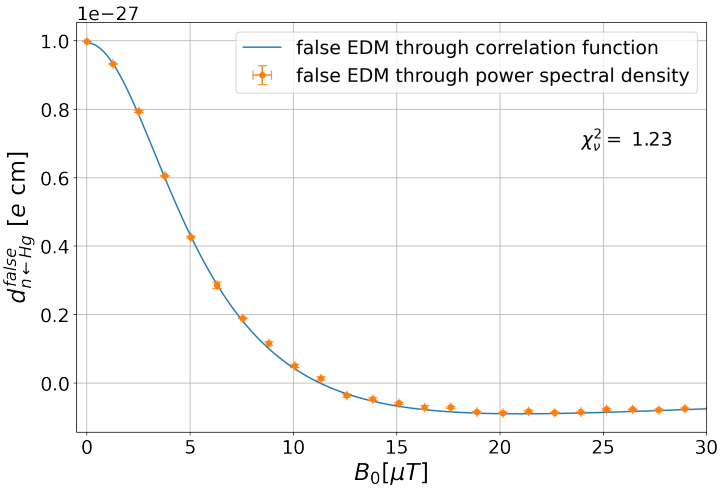

Figure 4: False mercury-induced neutron EDM as a function of the applied vertical field, for a first-order vertical gradient field configuration $B(\rho, \varphi, z) = G_{10}\Pi_{10}(\rho, \varphi, z)$ ($G_{10} = 78$ fT/cm). The false EDM is calculated from a Monte-Carlo simulation of the trajectory of mercury atoms using two seperate methods. The blue curve corresponds to the numerical-analytical approach where the simulated correlation is fitted with a double exponential model, while the orange dots correspond to $N = 20$ iterations of a direct numerical calculation of the false EDM using the Wiener-Khinchin theorem. The zero-crossing (magic value) is found at $B_0 = 11.3\,\mu$T for the former, and $B_m = 11.2 \pm 0.2\,\mu$T for the latter.

Conclusion

Ultimately the choice to either measure the false EDM at $B_0 = 1\,\mu$T, or suppress it at the magic value, relies on how well we are able to measure the generalized gradients $G_{10}, G_{30}, G_{50}, \ldots$ involved in (10). In the current state of the experiment, the offline extraction of the harmonic spectrum with the mapper is deemed reliable enough that the innacuracy on the measurement of the false EDM with the first option outweighs the scaling of the requirements on field production at the high B_0 value demanded by the second option. Nevertheless, both of these alternatives will be implemented for data-taking as a valuable check of the consistency of our false EDM correction.

References

[1] *Electric dipole moments as probes of new physics*, M. Pospelov, A. Ritz, Annals of Physics 318, 1, 119-169 (2005).

[2] *Electric dipole moments of nucleons, nuclei, and atoms: The Standard Model and beyond*, Progress in Particle and Nuclear Physics 71, 21-74 (2013).

[3] *The design of the n2EDM experiment*, N.J. Ayres et al., European Physics Journal C, 81.512 (2022).

[4] *Measurement of the Permanent Electric Dipole Moment of the Neutron*, C. Abel et al., Phys. Rev. Lett. 124, 081803 (2020).

[5] *Magnetic-field uniformity in neutron electric-dipole-moment experiments*, C. Abel et al., Phys. Rev. A 99, 042112 (2019).

[6] COMSOL Multiphysics v. 6.1. www.comsol.com. COMSOL AB, Stockholm, Sweden.

[7] *Measurement of the neutron electric dipole moment at the Paul Scherrer Institute: production of magnetic fields*, P. Flaux (2019).

[8] *On the Theory of Relaxation Processes*, G. Redfield, IBM J. Res. Dev. 1(1), 19 (1957).

[9] *Frequency shifts and relaxation rates for spin-1/2 particles moving in electromagnetic fields*, G. Pignol, M. Guigue, A. Petukhov, R. Golub, Phys. Rev. A 92, 053407 (2015).

[10] *A magic magnetic field to measure the neutron electric dipole moment*, G. Pignol, Phys. Lett. B 793, 440-444 (2019).

[11] *Time Series*, N. Wiener, M.I.T. Press, Cambridge, Massachusetts. (1964).

Machine learning and imaging approaches to improve the AGATA position resolution

Mojahed Abushawish

Université de Lyon 1, CNRS/IN2P3, UMR5822, IP2I, F-69622 Villeurbanne Cedex, France

Abstract — In-beam gamma-ray spectroscopy with high-velocity recoil nuclei requires very accurate Doppler correction. The Advanced GAmma Tracking Array (AGATA) is a new generation gamma-ray spectrometer that is capable of tracking gamma-rays in the detector, resulting in unprecedented position resolution and Doppler correction efficiency. AGATA is made of high-purity germanium crystals assembled to form a sphere. Each crystal is electrically segmented into 36 segments. To determine the gamma-ray interaction positions, the signals are processed by the Pulse Shape Analysis (PSA) algorithm. This algorithm estimates the interaction point positions by comparing the measured signals to a database of simulated signals. The PSA precision is a key point in the AGATA analysis. A way to improve its capabilities is to use experimental data to build the PSA databases instead of simulated ones. Such a database has been created in Strasbourg, but the current algorithm used to treat these data is very time-consuming. This work will present a new approach to improve the existing analysis using machine learning techniques. Finally, to characterise the improvement of the PSA, a new method based on gamma-ray imaging will be presented.

Introduction

In in-beam experiments, the high velocity of recoil nuclei leads to Doppler shift of the gamma-rays measured energy.

The Doppler shift depends on the emission angle of the gamma-ray that can be measured using the nuclei velocity along with the first interaction position of the gamma-ray. In case of large uncertainties on the emission angle, this shift results in the broadening of the photo-peak degrading the resolution. Previous generations of gamma-ray spectrometers are not inherently capable of tracking gamma-ray. Arrays like Euroball[1] and Gammasphere[2] used physically segmented Germanium detectors (clovers) to reduce the opening angle of each crystal therefore constraining the interaction position within the crystal and improving the Doppler correction. AGATA[3] (Advanced Gamma Tracking Array) and GRETA[4] (Gamma-Ray Energy Tracking Array) are new generation of gamma-ray spectrometers that are capable of tracking gamma-ray with resolution up to few mm.

AGATA is made of high-purity germanium crystals (about 50 available so far) assembled to form a sphere with the goal to cover 4π (180 required). Each crystal is electrically segmented into 36 segments. This high segmentation of crystals allows for high position resolution of up to 5mm[5].

The gap that has been achieved with these new generation gamma tracking arrays relies on two main algorithms that will be explained in the following: the Pulse Shape Analysis (PSA), which determines the positions of each gamma-ray interaction in Germanium, and the tracking, that allows to reconstruct the path of the gamma-rays within the detectors.

PSA

The current PSA algorithm[6] of AGATA works by comparing the 37 signals (36 segments and the central contact) with simulated ones to find the simulated signal that conforms with the measured one. The simulations are done using the AGATA Detector Library code (ADL)[7] producing a 2mm Cartesian grid that covers the full volume of the crystal, this grid is called the signal basis of the crystal. The bases are produced for all the AGATA crystals due to differences in geometry.

A so called "adaptive grid search" is done to find the most similar signal to the measured one[6]. A first evaluation is done using a wide grid with a large voxel size (6mm), and then a thin grid search (2mm voxels) on the most similar wide voxel.

Tracking

Gamma-ray interacts with matter in three main ways, photoelectric absorption, Compton scattering, and pair production. At energies up to 1.5MeV, photoelectric absorption and Compton scattering are the most probable interactions. During photoelectric absorption, the entire energy of the gamma-ray is transferred to an electron within the crystal, whereas in Compton scattering, only a portion of the energy is transferred, and the

gamma-ray may undergo additional scatterings or photoelectric absorption to dissipate the remaining energy.

In the case of Compton scattering, it is thus required to fully track the gamma-ray to recover the first interaction point in the direction of incidence of the incoming gamma-ray.

The Orsay forward tracking (OFT)[8] algorithm is used for the tracking of the gamma-ray; it works by applying the Compton diffusion formula on the different combinations of interaction points and building a figure of merit(FOM) for each combination. The FOM is then evaluated to determine the track of the gamma-ray and the position of the initial interaction; the FOM is based on comparing actual and calculated interaction energies, rather than the complementary scattering angles from the Compton-scattering formula.

Scanning tables

The PSA performance can be improved by having more and more realistic simulated bases.

To do that we need to have a full scan of the crystal, this is done by measuring a signal at every voxel of the crystal. This can be done by means of a so called scanning table.

The prototype crystal S001 was scanned by the nuclear physics group of the Institut pluridisciplinaire Hubert Curien Strasbourg (IPHC Strasbourg). The used scanning table is shown on figure 1. The scanning process consisted of two 2D scans, performed horizontally and vertically. For each scan, the crystal was fixed to the table structure and irradiated by a highly collimated source of ^{137}Cs. To get the 3D scan, the pulse shape coincidence scan (PSCS) technique is applied on the two scans[9].

The PSCS method depends on the fact that signals induced in the same position should have the same pulse shape, and by comparing the signals from the two scans we can identify those coming from the crossing point of the two scans. The comparison is done using a χ^2-like formula given below:

$$\chi^2 = \frac{\sum_{i=0}^{N}(v_i - h_i)^2}{\sigma.N}, \qquad (1)$$

where v_i and h_i are the samples of two pulses coming from the vertical and horizontal datasets respectively, N is the total number of samples of each signal (it is implied that both are sampled at the same rate) and σ is the measured noise level of the signals coming from the scanned detector. The signals with the lowest χ^2 are the most similar and are likely coming from the crossing point.

Machine learning

In this study, we used machine learning to extract a 3D basis from the two 2D scans, replacing the PSCS method. Machine learning is a fast and effective approach that has been used extensively to solve complex problems in nuclear instrumentation[10].We used a neural network with 2 long short-term memory(LSTM) layers coupled with 4 dense layers. LSTM layers are used for processing sequential data since it can learn and remember information for long periods of time, and are commonly used for natural languages and time series analysis. In addition, our tests demonstrated that LSTM layers are very robust to time misalignment when processing pulse signals[11].

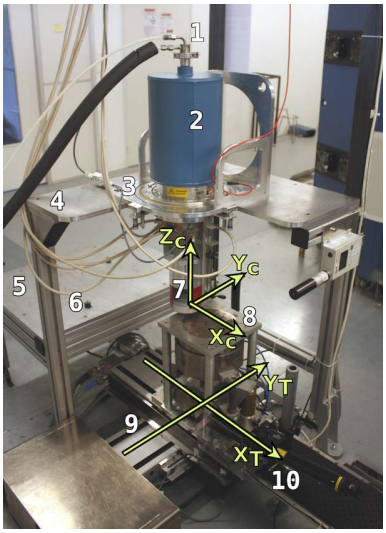

Figure 1: Picture of the scanning table: (1) LN2 pipes, (2) test-cryostat Dewar, (3) adjustment frame, (4) holding plate for vertical positioning, (5) holding plate for horizontal positioning, (6) fixing studs, (7) end cap of the detector, (8) collimator, (9) scanning table motorized axes, (10) alignment laser. The reference frame of the table $[X_T, Y_T]$ and the reference frame of the detector (crystal) $[X_C, Y_C, Z_C]$ are shown in green. Picture taken from [9]

Conventionally, supervised machine learning requires input (signal) and ground truth (3D position) for the training of the model, but since we do not have the 3D position of the measured signals we had to adapt a different training paradigm. We trained the model using the two known axes of each scan. For example, for the vertical scan, the (X,Y) positions are known, so the model will take the signal as input and predict a 3D position, then the loss function will be calculated only for the two known axes of this prediction since the third axis is unknown. This way the model will learn how to predict the (X,Y) position from the vertical scan and (X,Z) position from the horizontal scan, and the knowledge between the two is transferable since signals coming from the same position are very similar. Therefore, after training the model on both scans it will be able to give 3D position predictions.

The neural network was constructed using the TensorFlow[12] python library, and it was trained on Nvidia RTX6000 graphical processing unit(GPU). To assure the homogeneity of the training dataset only 10 signals per voxel were used for training; which are 3.5% out of the full dataset. The training took around

30 minutes while the inference of the full dataset took around 1 hour.

Imaging

It is possible to produce images from the results of the tracking of gamma-ray. This can be done using the position and the energy of the first and the second interactions, from this information you can build a cone of response where the source of the gamma-ray can be anywhere on the surface of the cone. The conventional imaging technique used in medical imaging is to build a 3D histogram and fill the surface of the cone of response of every gamma-ray in the dataset, but this technique is computationally expensive. In this study, we developed a fast imaging method aimed to characterize the PSA. After the photons go through Compton interaction, they scatter by an angle θ which is given in the following equation:

$$cos(\theta) = 1 - \frac{E_1 \times 511}{E_{tot} \times (E_{tot} - E_1)}, \qquad (2)$$

where E_{tot} is the gamma-ray energy and E_1 is the electron energy deposited in the detector by the interaction. The scattering angle can also be calculated using the results of the tracking algorithm and the position of the gamma-ray. Therefore, minimizing the difference between the two angles with respect to the position of the source will result in the real position of the gamma-ray source.

We used RootDataFrame[13] for data preparation and the scipy python library for the minimization[14]. The minimization method used is the Nelder-Mead method[15]. An example of the imaging result is given on Figure 2, representing the source position calculation projected on the Z axis for a ^{152}Eu source located at roughly (0,0,-55)mm; the positioning of the source was done manually, therefore the error in the source position is few mm. The position resolution obtained is of 3.8 mm (FWHM).

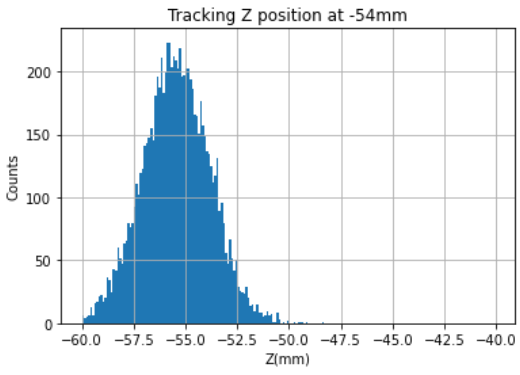

Figure 2: Source position calculation projected on the Z axis for a ^{152}Eu source located at (0,0,-55)mm. This measurement was conducted during the GANIL campaign in the autumn of 2021.

Results and discussion

Evaluating the accuracy of the neural network results poses a challenge as we do not have the full ground truth(3D positions of the signals). Therefore, we tried to assess the results by evaluating the distribution of the signals as well as comparing the signals predicted to be at the same position.

The error in the prediction of the two known axes of each scan can be a first indicator of the neural network performance, figure 3 and figure 4 show the predicted positions with respect to the scan position for the horizontal and the vertical scan respectively. Both figures display that most of the neural network predictions have less than a 2mm error. It also shows that there is a small portion of signals that gives a high error, this can be due to bad signals like multiple hits in the same segment, or very noisy signals. In addition, the figures do not show any dependence of the error on the position of the signal, due to this we will consider only the signals that show less than 1mm error in the two known axes.

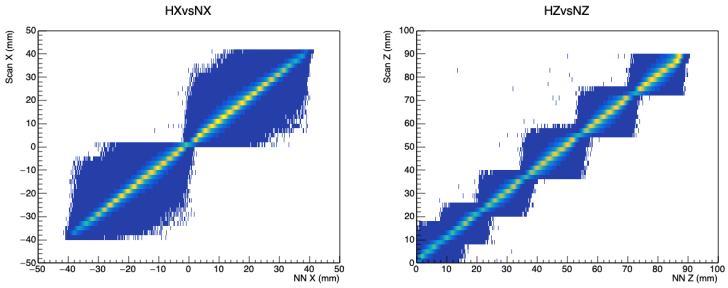

Figure 3: Predicted positions using the neural network with respect to the scan position for the horizontal scan.

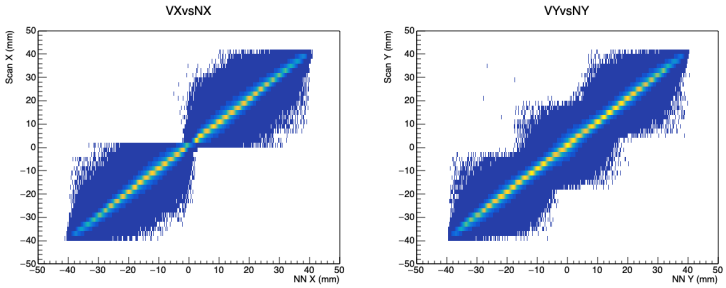

Figure 4: Predicted positions using the neural network with respect to the scan position for the vertical scan.

As explained in the scanning tables section, the scans were done using a highly collimated gamma-ray source directed on one side of the crystal, therefore, we expect to find an attenuation effect shown in the distribution of the signals. Figure 5 illustrates the signals distribution of the prediction of the unknown axis with respect to one of the known axes. the distribution of both scans is coherent with the expected attenuation effect of the gamma-ray. For instance, figure 5b shows

the signals distribution of the Z-axis predicted by the neural network with respect to the known Y-axis. The attenuation of the statistics with depth illustrates that the source was placed below the crystal.

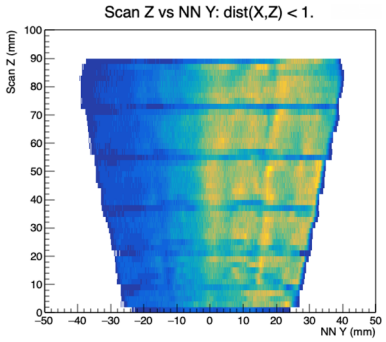

(a) Horizontal scan.

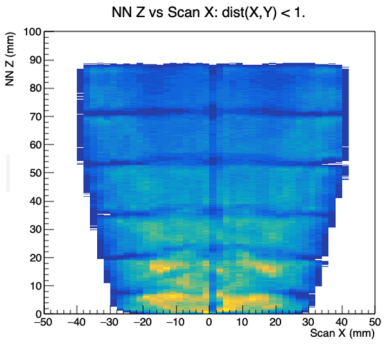

(b) Vertical scan.

Figure 5: Distribution of the neural network predictions of (a)Y-axis with respect to the known Z-axis (b)Z-axis with respect to the known X-axis.

To assess the consistency of the neural network we chose a specific position at (X=26mm, Y=0mm, Z=64mm), and we compared the predicted signals from both scans and the ones calculated using the PSCS method. This comparison is represented in Figure 6 by the mean of the signal of the fired segment along with the four neighboring segments, as well as the core signal. The figure shows that the signals predicted to be at the position are consistent between the neural network prediction and the PSCS method; however, the PSCS method shows a larger standard deviation from the mean shown in the segments A5, and A3 by the light green area around the mean. This can indicate that the neural network is more selective than the PSCS method in predicting the 3D position of the signals.

Conclusions and prospects

Experimental databases for a prototype AGATA crystal were produced in Strasbourg. The PSCS method used to analyse this database is a limiting factor in the scanning process due to the long computational time of around 5 days. This work is aimed to investigate the possibility of replacing the PSCS method with a neural network to accelerate the scanning process.

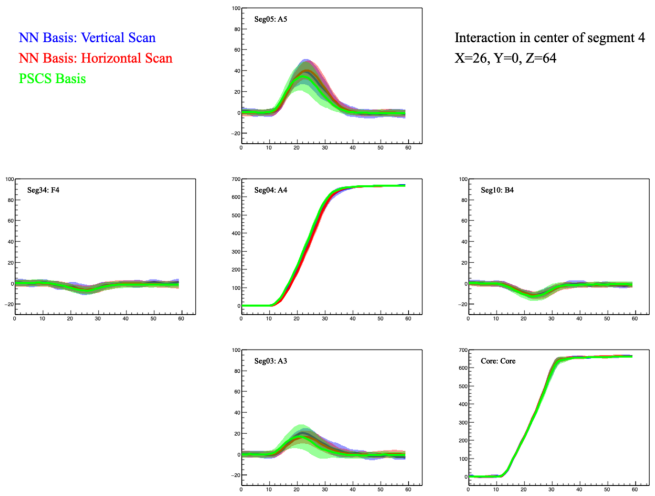

Figure 6: The mean of the signal of the fired segment along with the four neighboring segments, as well as the core signal located at (X=26, Y=0, Z=64) predicted by the neural network and calculated by the PSCS method.

We trained a neural network based on LSTM layers to predict the 3D position of the scanned signals, the training of the network took 30 minutes and the inference of the full dataset took 1 hour. The results of the neural network indicate that the network was able to learn how to predict the 3D position of a signal even though the 3D position was not provided as ground truth for the training.

The neural network prediction is also consistent with the PSCS method when we compare signals predicted to be at the same position; however, the neural network appears to be more precise.

Finally, we developed a fast imaging technique that will allow us to characterise the PSA. In the future, we plan to use the PSA with the bases produced by the PSCS, and the neural network and apply the imaging technique to evaluate both methods.

This work opens the door to developing a neural network based PSA, since practically the neural network we developed is functioning as a PSA in the very specific case of only one interaction per event in the detector.

References

[1] P.J. Nolan, F.A. Beck, D.B. Fossan, Annu. Rev. Nucl. Sci. 45 (1994) 561.

[2] I.-Y. Lee, Nuclear Phys. A 520 (1990) 641c.

[3] S. Akkoyun, et al., Nucl. Instrum. Methods A 668 (2012) 26-58.

[4] S. Paschalis, et al., Nucl. Instrum. Methods A 709 (2013) 44-55.

[5] PA Söderström, et al., Nucl. Instrum. Methods A 638(1) (2011) 96-109.

[6] R. Venturelli and D. Bazzacco, LNL Annual Report 2004 (2004).

[7] B. Bruyneel, B. Birkenbach, and P. Reiter, Eur. Phys. J. A 52, 70 (2016).

[8] Lopez-Martens, et al., Nucl. Instrum. Methods A 533, 454 (2004).

[9] B. de Canditiis, PhD thesis (2020)

[10] Boehnlein, Amber, et al. "Colloquium: Machine learning in nuclear physics." Reviews of Modern Physics 94.3 (2022): 031003.

[11] Fabian, X., et al. Nucl. Instrum. Methods A 986 (2021): 164750.

[12] M. Abadi, et al. (2015), software available from tensorflow.org.

[13] `https://root.cern/doc/master/classROOT_1_1RDataFrame.html`

[14] Virtanen, Pauli, et al. Nature methods 17.3 (2020): 261-272.

[15] Gao, F. and Han, L. 2012. Computational Optimization and Applications. 51:1, pp. 259-277

Part VI

Nuclear Physics & Multidisciplinary Topics

session chaired by Valérian GIRARD-ALCINDOR

The Impact of Nuclear Data on Decay Heat Uncertainty Quantification

Yohannes Molla ***with Lydie Giot***

Subatech, IMT-Atlantique, Nantes Université, CNRS-IN2P3, F-44307, Nantes, France

Abstract — Decay heat is a thermal power which continues to be generated after the shut-down of a nuclear power reactor. This is due to the radioactive decay of fission products, minor actinides, and delayed fission of fissile nuclide. A proper characterization of decay heat is essential for safety at all stages of the fuel cycle: design of decay heat removal systems, spent fuel transportation and repository management. It can be calculated either using standards or by the summation method. This latter approach uses computational tools that have the capability to simulate the fuel inventory as a function of cooling time to calculate the decay heat contribution of the depleted fuel components at a given time. The nuclear data required for the calculation, i.e., decay constants, fission yield data, and energy data, have uncertainties which needs to be propagated during the fuel depletion calculation, and to be taken into account in the decay heat uncertainty calculation. The objective of my PhD is to develop some tools to do so and to analyze the impact of these uncertainties on decay heat calculation. A Monte Carlo method was chosen to propagate the nuclear data uncertainties and their impact on decay heat calculations. As a first step, a benchmark comparison was performed on a PWR assembly sample to estimate the spent fuel nuclide inventory at different cooling times and later on to estimate the uncertainties on the inventory calculation. The chosen sample for this purpose is the ARIANE GU3 sample, which is part of an ongoing international benchmark evaluation coordinated by the Nuclear Energy Agency.

Introduction

The recoverable energy in nuclear fission reactors is mostly generated from the kinetic energy of the fission product nuclides. In addition, the kinetic energy of prompt neutrons and prompt gamma rays also have a significant contribution to the energy production. Moreover, about 6% of the recoverable energy on average is generated due to the β^- and γ decay of fission products. This delayed energy that is emitted as a form of heat is known as decay heat. Decay heat generated from spent nuclear fuel has to be efficiently removed from reactors and radioactive waste management facilities to avoid core damage and radioactive accidents. Therefore, the design and operation of such facilities have to be complacent to national regulations regarding temperature and radioactivity safety before commissioning. Moreover, proper decay heat estimation is an important parameter for Gen IV reactors safety system and their innovative fuel design.

Decay heat calculations have to be associated with uncertainties that propagate from nuclear data uncertainties (such as decay constants, fission yields, and mean energies), modeling codes and methods as well as the operational history of the spent nuclear fuel. Quantifying the uncertainties is essential to optimize the design margin of safety systems in new reactor concepts, and Spent Nuclear Fuel (SNF) disposal casks. For this PhD, a stochastic approach known as Total Monte Carlo (TMC) method is chosen to quantify decay heat uncertainties. This method is chosen due to its significant accuracy in predicting quantities of interest, and more realistic error estimation. TMC is a method based on random sampling of input parameters within their uncertainty range (in this case decay data), and producing a set of responses, in this case decay heat. Then, the probabilistic distribution of the set of responses represent the mean value and uncertainty margins.

The decay heat per isotope $DH_i(t)$ at a given time (t) can be calculated as the mean energy $(\bar{E}_i)$ released due to the radioactive decay of the nucleus multiplied by the decay rate $\lambda_i n_i(t)$ [1]. Then, the sum of decay heat produced by each isotope gives the total decay heat, represented by the following formula, known as the Summation Equation 1.

$$DH(t) = \sum_i N_i \lambda_i(t) \bar{E}_i \tag{1}$$

In the summation equation, the decay constants and the mean energies are nuclear decay data. Whereas, the concentration of isotopes can be estimated by depletion simulation codes. Depletion codes employee the Bateman equations (Eqn. 2), which give the time evolution of nuclide concentration of the production and disappearance terms by taking into account reaction decays:

$$\frac{dN_i(t)}{dt} = \sum_j (b_{j\to i}\lambda_j + \sigma_{j\to i}\phi)\cdot N_j(t) - (\lambda_i + \sigma_i\phi)\cdot N_i(t) \quad (2)$$

where, N_i and N_j are the atomic densities of nuclides i and j, λ_i and λ_j are the radioactive decay constant of i and j, $b_{j\to i}$ the branching ratio of j to produce the i, σ_i and $\sigma_{j\to i}$ the cross-sections of reactions of production or disappearance of the nuclide i, and ϕ the flux of particles.

From Eqn. 1 and Eqn. 2 it is evident that the uncertainties of the evolution calculation have an impact on decay heat and associated uncertainties calculation. Hence, it is worthwhile to investigate uncertainties related to fuel depletion estimation as well as decay heat uncertainties. In this context, the depletion calculation presented in the following sections is performed on the ARIANE GU3 sample as a contribution for NEA Working Party on Nuclear Criticality Safety (WPNCS) subgroup 10. This subgroup is delegated to investigate the computational uncertainties associated with SNF inventory that propagate from nuclear data, simulation tools, and methods. The three main objectives of the working group are: to list and compare method that can be used for uncertainty quantification of UO_x fuel depletion calculation, to assess the impact of nuclear data uncertainties on the overall uncertainties of depletion calculation, and to validate computational code by comparing calculation outputs with experimental results.

Section 2 of this proceeding states about the ARIANE program. Section 3 presents the assembly model of GU3 sample. Power normalization is explained in Section 4. In Section 5 the relative difference of computation and experiment comparison are discussed. Finally, conclusion and outlooks are given in Section 6.

The ARIANE program

The ARIANE program is an international collaboration that is dedicated to improve the isotopic measurement database, including the associated uncertainties for fission products and actinides in MOX and UO_2 SNF. The program was coordinated in 2001 by Belgonucleaire, a Belgian nuclear research institute, and it involved research centers from seven different countries. The motivations for such measurement are: firstly, measuring the isotopic assay is important to validate the isotopic inventory and enhance the confidence margin in measurement data [2]. Second, the measurement gives a valuable information for licensing of criticality safety, transportation, storage and reprocessing of SNF from highly enriched fuels. Thirdly, it can be used to validate computational codes, especially for high burnup conditions (above $50GWd/MTU$).

The ARIANE GU3 sample is one of the fuel rods measured in this program. It was irradiated for three cycles in a PWR reactor in Gosgen, Switzerland. This sample is chosen as a study case to analyze uncertainties in depletion calculation that are associated with nuclear data uncertainties. It is selected due to its well documented experimental data with uncertainties and the simple assembly design of the reactor in order to minimize modeling uncertainties. The experimental measurement data of the sample is taken from the NEA SFCOMPO - 2.0 database [3].

ARIANE GU3 assembly model

In order to compare the isotope inventory from depletion calculation with experimental measurement, a 2D model of the ARIANE assembly with reflective boundary condition was created based on the given specification by NEA/ WPNCS/ SG10 [4]. A Monte Carlo depletion code SERPENT2 is used to compute the nuclide concentration of a spent nuclear fuel sample. SERPENT2 is a continuous-energy Monte Carlo reactor physics burnup calculation code, which has been developed at VTT Technical Research Center of Finland since 2004 [5]. The code is capable of running both particle transport and burnup simulations. The nuclear libraries used for the simulation were JEFF3.2 and ENDF7.1. In this case, two libraries were implemented to investigate that may arise from using different nuclear data libraries.

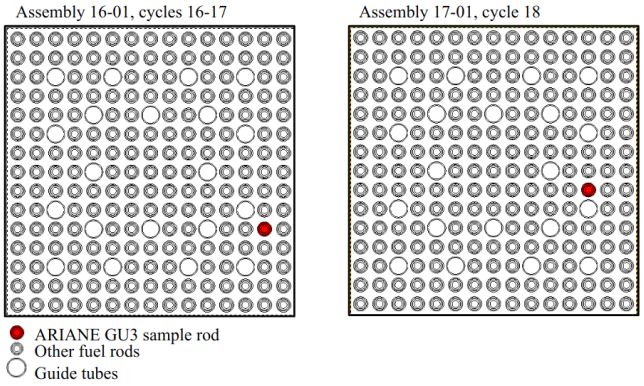

Figure 1: Radial locations of the GU3 sample.

The ARIANE GU3 fuel assembly where the GU3 sample was taken from has a 15 X 15 design, with a total of 205 UO_2 fuel rods of $4.1wt\%^{235}U$ initial enrichment. The three irradiation cycles are simulated separately by taking into account the position change of the sample between the second and third cycles, as shown in Fig. 1. The cycle average fuel temperatures assigned for each cycle are: 1200K, 1000K, and 900K respectively. Whereas, the moderator and cladding temperature is an average 600K for all cycles. Furthermore, the power history used for the assembly simulation is as shown in Fig. 2.

Power normalization

The power density is normalized to reproduce the experimental burnup values. Burnup is the amount of

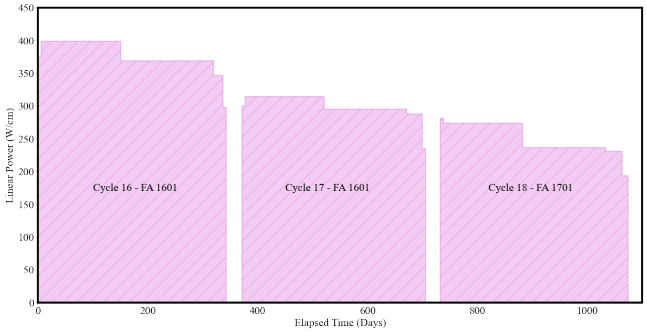

Figure 2: ARIANE GU3 sample irradiation history [4].

power generated per the mass of fuel. The burnup at a given step can be estimated by analyzing the concentration of the burnup indicator isotopes. These are fission products (such as ^{148}Nd, ^{137}Cs and ^{144}Ce) that have linear relationship with respect to burnup.

In most cases, ^{148}Nd is a preferred indicator due to the following characteristics [6].Nd is a direct fission product and it has a long decay time. It has also low fission and capture cross-sections, independent of the neutron energy. Moreover, it is not volatile. Therefore, local burnup estimation is possible. Its fission yield is nearly independent of the neutron energy and of fissionable isotope. For example, the behavior of Nd isotopes, calculated from the ARIANE GU3 depletion case, as a function of burnup is plotted in Fig. 3. From the figure, ^{145}Nd and ^{146}Nd are slightly non-linear as a function of burnup. However, the summation of the two isotopes tends to be linear, because both nuclides are stable [7].

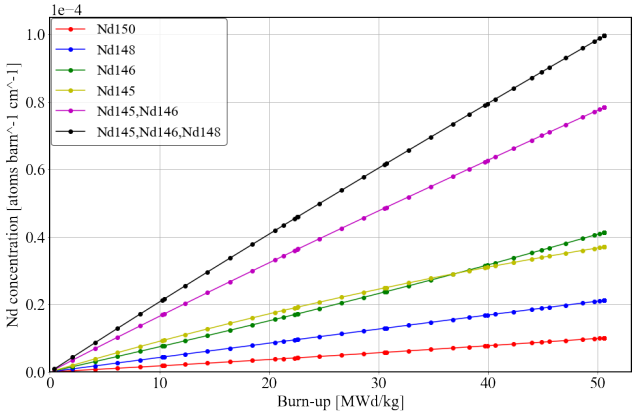

Figure 3: ARIANE GU3 sample Nd evolution before power adjustment.

As mentioned above, one of the purposes of this work is to perform validation of a depletion code using an experimental value. In general, during such comparison works, the focus is to evaluate the relative differences of isotopic inventory between the two. Hence, the first step is to check whether the computational burnup matches the given experimental burnup. In cases where the burnups of computation and experiment are not equivalent, the computation burnup value can be iteratively corrected by normalizing the irradiation history using burnup indicators.

The normalization requires the calculation of a global constant, which is applied to the power density steps. After each iteration, the simulation is performed and the normalization constant is calculated for the next power history correction. Due to the linear relationship between the tracer and burnup, the number of iterations to get a converged normalization constant is limited to a maximum of two steps, and the range of correction factor is within a range of 1 or 2 percentage [7]. However, if the correction factor is a higher percentage value or if it took more than two iteration steps to converge, then it may be taken as a suggestion to check the quality of the irradiation history or the simulation input file.

The most common method of calculating a correction factor is based on, ^{148}Nd as shown in Eqn 3.

$$Correction_{BU\,148} = \frac{C_{148_{Nd}}}{E_{148_{Nd}}} \tag{3}$$

On the other hand, a research work for EPR fuel burnup credits indicates that the burnup correction using only ^{148}Nd has a slight underestimation of the calculated burnup correction factor [8]. Hence, the formula used in the present work adopts the latter, which was suggested by the PhD work of CHAMBON A., as shown in Eqn 4.

$$Correction_{BU} = \frac{2 \cdot \frac{C_{145_{Nd}}+C_{146_{Nd}}}{E_{145_{Nd}}+E_{146_{Nd}}} + \frac{C_{148_{Nd}}}{E_{148_{Nd}}} + \frac{C_{150_{Nd}}}{E_{150_{Nd}}}}{4} \tag{4}$$

For the ARIANE GU3 simulations executed with JEFF3.2 the power history correction factor calculated to be 1.002, and for the ENDF7.1 library it was 0.9608.

Results

In this section, the percentage relative difference of fission product nuclide concentrations between SERPENT2 simulations and experimentally measured values are presented. In addition, a comparison of preliminary results among participants of the NEA working group is also illustrated.

Relative difference comparison

The SNF nuclide concentration comparison of calculation versus experiment was done based on the measurement data given in the NEA specification [4]. The results given here are obtained after normalization of the power history, based on the approach described in the previous section.

Fig. 4 shows the percentage differences for fission product nuclides of interest. Among the fission product nuclide, large discrepancy between experiment and computation was seen for ^{103}Rh, and ^{147}Pm in both nuclear data libraries. The differences for these isotopes using JEFF3.2 are: 26.84%, and 16.84% respectively. Similarly, the results from ENDF7.1 are: 29.23%, and

15.31%. These differences could partially be attributed to experimental measurement uncertainties [2]. The measurement uncertainties for $^{242}Am_m$, ^{237}Np, ^{103}Rh, and ^{147}Pm are: 10.60%, 20.60%, 9.77%, and 18.01% respectively. However, the computational result, for most important fissile isotopes such as ^{235}U and ^{239}Pu, are in acceptable agreement with experimental values. For instance, for the JEFF3.2 library, the relative difference between computation and experiment for ^{235}U and ^{239}Pu is 3.18% and -3.43% respectively (after power adjustment). On the other hand, a relatively large variation was seen for some minor actinides. The percentage difference for $^{242}Am_m$, ^{241}Am and ^{237}Np using JEFF3.2 is -23.98%, 15.19% and -10.02% after power correction. In the case of ENDF7.1 library, the difference for ^{235}U and ^{239}Pu is 1.46% and -1.18%. Whereas, for $^{242}Am_m$, ^{241}Am and ^{237}Np it is -22.85%, 17.23% and -10.99%.

Moreover, the comparisons after burnup normalization of the Neodymium isotopes, show significant improvement. For instance, the JEFF3.2 comparison for these isotopes is found to be in good agreement with the experiment, within a range of -1.44% to 1.13% difference. The trend is similar with the ENDF7.1 the differences are in a range of -0.64% to 3.04%. In particular, the prominent burnup indicator ^{148}Nd deviates from measurement only by 0.16%. The output for ^{148}Nd from the ENDF7.1 is also in good agreement, with a narrow 0.97% relative difference.

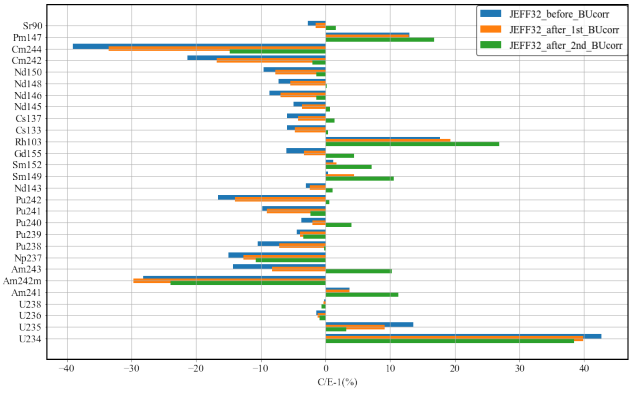

Figure 4: ARIANE GU3 sample $(C/E) - 1\%$ comparison for JEFF3.2 data library using SERPENT2.

Furthermore, as shown in Fig. 5 the comparison among participants indicates the computed ^{234}U isotope has a significant discrepancy with the experiment. This cab be attributed to its low percentage in the initial fuel composition. Also, the Am isotope inventory from the simulation output of the participants show differences among themselves and from the experimental measurement. This is mainly because of the low concentration of Am and high experimental uncertainty. The computational output differences for the ^{149}Sm are understood to be from statistical uncertainty due to the low concentration of the isotope in the depleted fuel. Otherwise, most actinides that are experimentally measured, such as U and Pu are well replicated by most of the computational codes used by the participants.

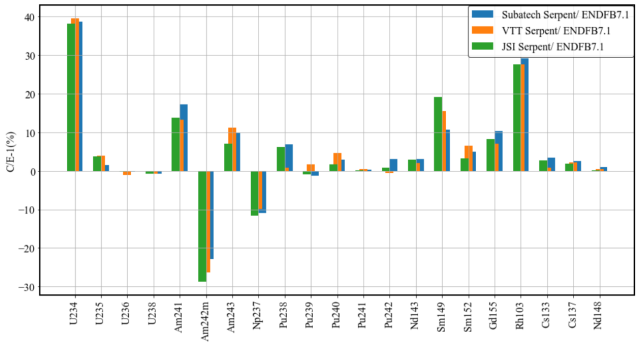

Figure 5: First comparison among NEA participants.

Conclusion and outlooks

The comparisons of the relative differences of computational and experimental results observed using both JEFF3.2 and ENDF7.1 are within acceptable range. The large differences observed in the actinides (i.e. ^{234}U, $^{242}Am_m$, and ^{244}Cm) are believed to be due to their smaller statistics (nuclide population) in Monte Carlo simulation and uncertainties associated to measurements.

The uncertainties propagated from estimating the SNF nuclide concentration have significant impact, in addition to the nuclear decay data, on the uncertainties in decay heat. In this regard, the work done so far on depletion calculation is one of the milestones of the thesis work. Moreover, validating the computed values to experimental results was found to be beneficial to understand the origins of difference between the two. Hence, a Monte Carlo code COCONUST (LPSC, Grenoble) that evaluates cross-section uncertainties in depletion calculation, will be used to calculate the uncertainties of isotopic concentration in the ARIANE GU3 sample. In continuation to the started work, the next step will be to perform another Monte Carlo simulation of the ARIANE assembly using an open source code known as OpenMC and compare the results. This helps to analyze the significance of uncertainty values that come from using different computational codes.

In addition, there will be a code development work that is related to the uncertainty analysis of decay data. A Python based Monte Carlo code coupled to SERPENT2, known as COCODRILO, have been in development since 2020. At its current stature, the code is capable of sampling from fission yield data using the Gaussian sampling method. Hence, the current work is to upgrade its capacity so that sampling from decay constant and mean energy data can be possible. Then, the code will be employed to analyze uncertainties of decay data on fission pulses of ^{235}U and ^{239}Pu. Provided that the coupled code successfully calculate decay heat uncertainties of fission pulses, it will be tested on the ARIANE GU3 benchmark. The end goal is to use COCONUST and COCODRILO to calculate decay heat with the associated uncertainties in the Molten Salt Fast Reactor (MSFR) concept.

References

[1] Luca Fiorito *et al.*, "Decay heat uncertainty quantification of MYRRHA", 2017, EPJ Web of Conf., vol. 146, doi: 10.1051/epjconf/201714609021

[2] Germina Ilas *et al.*, "Analysis of Experimental Data for High Burnup PWR Spent Fuel Isotopic Validation-ARIANE and REBUS Programs (UO_2 Fuel)", URL: www.nrc.gov/docs/ML1008/ML100850211.pdf

[3] SFCOMPO2.0, "Spent Fuel Isotopic Composition", URL: https://www.oecd-nea.org/jcms/pl_21515/sfcompo-2-0-spent-fuel-isotopic-composition

[4] WPNCS-SG10 NEA, "specifications (WPNCS SG7 Report, pending publication)-3"

[5] Serpent, "A Continuous-energy Monte Carlo neutron and photon transport code", URL: https://serpent.vtt.fi/serpent

[6] Soumia Azzaoui, "SCALE-6 fuel depletion analyses:Application to the ARIANE program", URL: https://publications.sckcen.be

[7] Wim Haeck *et al.*, "Experimental validation of VESTA 2.1", 2013, DOI: 10.1051/snamc/201403603

[8] Amalia Chambon, "Le Credit Burnup des combustibles REP-MOx francais: methodologie et conservatismes associes a l'evaluation JEFF-3.1.1", URL: https://tel.archives-ouvertes.fr/tel-00956580

Dense matter within Relativistic Hartree-Fock approaches

Mohamad Chamseddine ***with Jérôme Margueron, Guy Chanfray, Hubert Hansen, Rahul Somasundaram***

Univ Lyon, Univ Claude Bernard Lyon 1, CNRS/IN2P3, IP2I Lyon, UMR 5822, F-69622, Villeurbanne, France

Abstract — Relativistic Hartree-Fock Lagrangians including a chiral potential are investigated in dense nuclear matter. We fully consider the contribution of the exchange Fock term to the energy and the self-energies, and we investigate the nucleon's compositeness and finite size effects (confinement and form factors) and short range correlations based on the Jastrow ansatz. The parameters of the model are adjusted to reproduce fundamental properties related to the QCD theory at low energy, such as the chiral symmetry breaking, Lattice-QCD predictions, and the quark model. In addition, two empirical properties at saturation are employed: binding energy and density. All other empirical parameters, e.g., symmetry energy, incompressibility modulus and effective mass are predictions of the models and can be used to evaluate the quality of the different approximation schemes. Bayesian statistics is employed in order to propagate parameter uncertainties in predictions for the nuclear matter properties.

Introduction

The theory of dense nuclear matter has a long history of challenging physicists in all aspects: be it on the theoretical side where Quantum Chromo-Dynamics (QCD) is non-perturbative and cannot be solved directly (e.g. the numerical part where the sign problem still poses an impenetrable barrier), and the experimental side since very few data still exists (see Ref. [1]). Thus effective nuclear modeling may be employed to tackle the problem and efforts have been made to connect those descriptions to the fundamental theory of QCD, in particular its chiral properties [2]. Being an effective approach, the model has a certain range of validity, usually low energy regime, whereas at higher energy, or equivalently higher densities, it faces a natural breakdown. Chiral EFT ($\chi-$ EFT) for example, has an expected breakdown between $n_{\rm sat}$ and $2n_{\rm sat}$, where $n_{\rm sat}$ is the nuclear saturation density ($n_{\rm sat} \approx 0.155$ fm^{-3}). One particular area of interest for nuclear physicists and astrophysicists as much, is the study of neutron stars. As can be seen in Fig. 1, these objects lie at very high chemical potentials (or high densities equivalently), and they are made of highly asymmetric matter, conditions that are very hard to access in laboratory experiments. Thus the exploration of the densest phase of nuclear matter requires extrapolations to higher densities than those available in ($\chi-$ EFT).

In this work, we follow-up on the previous study of *Somasundaram et al.* [4] for a relativistic mean-field model where spontaneous chiral symmetry breaking and confinement effects are incorporated (RMF-CC model). This model is based on two important concepts: the identification of the Walecka scalar σ meson

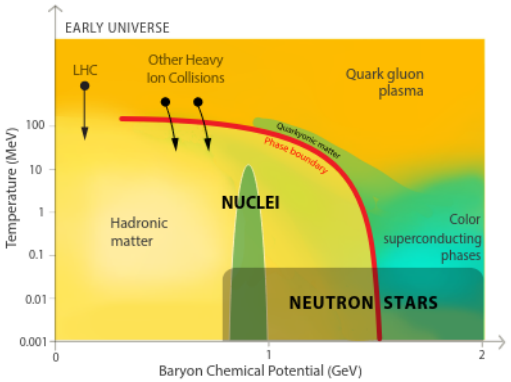

Figure 1: Schematic representation [3] of the hypothetical states of matter in the parameter space of of temperature against baryonic chemical potential. Neutron stars lie in the bottom right of the diagram, at low temperature and high chemical potentials.

with the radial fluctuation of the chiral quark condensate proposed in Ref. [5], and the inclusion of a nuclear "polarisation" as in Ref. [6]. This previous study was done at the Hartree level, and it was mentioned that this is not sufficient for a mean-field study of nuclear matter, for pions play a central role in such theories, and at the Hartree level they do not contribute. We will be analysing the same model, but this time going beyond the Hartree level, which requires the consideration of form factors (FF) at the interaction vertices, and the inclusion of short range correlations (SRC) due to the strong effect of the repulsive core interaction arising in the pion and ρ channels.

Formalism

The relativistic Lagrangian can generically be written as the sum of a kinetic fermionic term,

$$\mathcal{L}_\psi = \bar{\psi}\,(i\gamma^\mu - M_N)\,\partial_\mu\psi\,, \tag{1}$$

where the field ψ represents the nucleon spinor, and of meson-nucleon terms,

$$\mathcal{L}_m = \mathcal{L}_s + \mathcal{L}_\omega + \mathcal{L}_\rho + \mathcal{L}_\delta + \mathcal{L}_\pi\,, \tag{2}$$

collecting all mesonic contributions considered in a given model. Using notation of Ref. [7] these can be enumerated as,

$$\begin{aligned}
\mathcal{L}_s =& \big(M_N - M_N(s)\big)\bar{\psi}\psi - v(s) + \frac{1}{2}\partial^\mu s\partial_\mu s\,,\\
\mathcal{L}_\omega =& -g_\omega\omega_\mu\bar{\psi}\gamma^\mu\psi + \frac{1}{2}m_\omega^2\omega^\mu\omega_\mu - \frac{1}{4}F^{\mu\nu}F_{\mu\nu}\,,\\
\mathcal{L}_\rho =& -g_\rho\rho_{a\mu}\bar{\psi}\gamma^\mu\tau_a\psi + g_\rho\frac{\kappa_\rho}{2M_N}\partial_\nu\rho_{a\mu}\bar{\psi}\sigma^{\mu\nu}\tau_a\psi\\
&+\frac{1}{2}m_\rho^2\rho_{a\mu}\rho_a^\mu - \frac{1}{4}G_a^{\mu\nu}G_{a\mu\nu}\,,\\
\mathcal{L}_\delta =& -g_\delta\delta_a\bar{\psi}\tau_a\psi - \frac{1}{2}m_\delta\delta_a\delta_a + \frac{1}{2}\partial^\mu\delta_a\partial_\mu\delta_a\,,\\
\mathcal{L}_\pi =& \frac{g_A}{2f_\pi}\partial_\mu\varphi_{\pi a}\bar{\psi}\gamma^\mu\gamma^5\tau_a\psi - \frac{1}{2}m_\pi^2\varphi_{\pi a}\varphi_{\pi a}\\
&+\frac{1}{2}\partial^\mu\varphi_{\pi a}\partial_\mu\varphi_{\pi a}\,,
\end{aligned} \tag{3}$$

where the symbols have their usual meaning. In Eq. (3), two quantities are of particular interest to us, the scalar potential $v(s)$ and the s-field dependent nucleon mass $M_N(s)$. We study the relativistic Hartree-Fock approach including chiral symmetry breaking through the chiral potential $v(s)$ and confinement (RHF-CC), in light of the RMF-CC in [4], hereafter called ($\mathrm{RH_{CC}}$). The leading order effect of confinement at low energy is incorporated in $M_N(s)$ from its contribution to the nucleon polarisability in dense matter at the linear response approximation. We extend this model to include the finite-size effect through form factors (FF) as well as short-range correlations (SRC) from the Jastrow ansatz.

The effective chiral potential $v(s)$ in the scalar field s has a typical Mexican hat shape which breaks chiral symmetry. We consider in this study the expression provided by the linear sigma model (LσM),

$$\begin{aligned}
v(s) &= \frac{\lambda}{4}\{,\big((f_\pi + s)^2 - v^2\big)^2 - f_\pi m_\pi^2\, s\\
&\equiv \frac{m_\sigma^2}{2}\,s^2 + \frac{m_\sigma^2 - m_\pi^2}{2\,f_\pi}\,s^3 + \frac{m_\sigma^2 - m_\pi^2}{8\,f_\pi^2}\,s^4
\end{aligned} \tag{4}$$

See Ref [4], for instance, for more details on this effective chiral potential.

Based on a microscopic modeling of the nucleon substructure in terms of the MIT bag model [8], it was shown that the nucleon polarisability adds up to the in-medium nucleon mass from the LσM as,

$$M_N(s) = M_N + g_s\,s + \frac{1}{2}\,\kappa_{NS}\left(s^2 + \frac{s^3}{3\,f_\pi}\right). \tag{5}$$

generating a density dependent scalar susceptibility,

$$\tilde{\kappa}_{NS}(s) = \frac{\partial^2 M_N}{\partial s^2} = \kappa_{NS}\left(1 + \frac{s}{f_\pi}\right), \tag{6}$$

which vanishes at full chiral restoration, i.e., $\bar{s} = -f_\pi$, where $\bar{s}$ is the ground state value taken by the s field.

In addition to the scalar s and vector ω fields contributing to the Hartree and Fock terms in symmetric matter, the Fock term brings a contribution from the δ and ρ mesons. A very important point is that the meson-nucleon coupling constants are fixed to all available Lattice-QCD data and hadronic phenomenology, along the lines originally proposed in [6]. We however need two additional quantities to determine all coupling constants, which are taken to be $n_{\rm sat}$ and $E_{\rm sat}$. The delta meson is supposed to weakly couple to nucleons and we fix $g_\delta = 1$. The parameters considered in the present study are shown in Tab. 1.

By fitting the model to the parameters in Tab. 2, i.e. using the connection to Lattice QCD parameters a_2 and a_4 from the following relations (see Ref. [6]):

$$g_s = \frac{a_2 m_s^2}{f_\pi} \quad \text{and} \quad C = \frac{f_\pi g_s}{M_N}\left[\frac{3}{2} + \frac{a_4 m_s^4}{f_\pi g_s}\right], \tag{7}$$

and reproducing the NEP $E_{\rm sat}$ and $n_{\rm sat}$, the following model parameters m_s, g_ω, g_s and C can be fixed. Note that we use Bayesian statistics to propagate the parameter uncertainties into the model parameters.

It should be remarked that, as argued in Ref. [4], m_s has no direct relation with the broad resonance $f_0(600)$, but instead to the inverse of the vacuum scalar susceptibility which puts it to a value slightly larger than the one usually considered (about 500 MeV). It is therefore running from about 600 up to about 800 MeV. As for g_s, a value of around 10 can be predicted from the LσM, see Ref. [7] for instance, giving a reference value that we use for the comparison of our fits.

Nucleon finite size and short range correlations

In this section, we consider both the nucleon finite size, with FF, and the short-range correlations (SRC). Taking into account the finite size of the nucleon can be done by introducing form factors to each meson-nucleon vertex, and for simplicity, we consider monopole form factors (FFs) for meson α,

$$F_\alpha(\mathrm{q}) = \left(\frac{\Lambda_\alpha^2}{\mathrm{q}^2 + \Lambda_\alpha^2}\right), \tag{8}$$

Table 1: Model parameters (masses and coupling constants) which are fixed constant in the present analysis. The nucleon-ρ vector coupling is fixed to the nucleon-ω vector one by the following relation, $g_\rho = g_\omega/3$ in agreement with the quark model. We consider the strong ρ^T model with κ_ρ=6.6 suggested by scattering data [9].

M_N	m_ρ	m_δ	m_ω	m_π	g_ρ	κ_ρ	g_δ	g_A	f_π
MeV	MeV	MeV	MeV	MeV					MeV
938.9	779.0	984.7	783.0	139.6	$g_\omega/3$	6.6	1	1.25	94.0

Table 2: The remaining parameters g_s, m_s, g_ω and C are adjusted to reproduce the properties given in this table: the parameters a_2 and a_4 from lattice-QCD and the nuclear Empirical Parameters $E_{\rm sat}$ and $n_{\rm sat}$. For the Lattice parameters the average and standard deviation refers to the profile of a uniform distribution, while for the NEP they correspond to a Gaussian distribution.

Parameters	Ref.	centroid	std. dev.
a_2 (10^{-3} GeV^{-1})	L1 [10]	1.553	0.136
a_4 (10^{-9} GeV^{-3})	L1 [10]	-0.509	0.054
$E_{\rm sat}$ (MeV)	[11]	-15.8	0.3
$n_{\rm sat}$ (fm^{-3})	[11]	0.155	0.005

where Λ_α may vary with meson α. The interaction elements are modified as follows:

$$V_\alpha(\mathrm{q}) \longmapsto V_\alpha^{FF}(\mathrm{q}) = \frac{1}{\mathrm{q}^2+m_\alpha^2}\left(\frac{\Lambda_\alpha^2}{\mathrm{q}^2+\Lambda_\alpha^2}\right)^2 = D_\alpha(\mathrm{q})F_\alpha^2(\mathrm{q}), \quad (9)$$

where $D_\alpha(\mathrm{q})$ is the meson's α propagator.
As for SRC, note that we introduce them only for the ρ^T and π meson for practical reasons, but in principle, all mesons exchange potentials could potentially carry corrections at short distance from SRC. These correlations are introduced as a modification of the interactions by folding them with a two body correlation function $G(\mathbf{r}-\mathbf{r}')$ which forbids the presence of two nucleons at the same point, by imposing the following property $G(\mathbf{r}=\mathbf{r}')=1$. The two body correlation function $G(r)$ is identified with the Jastrow function, $G(r) \equiv j_0(\mathrm{q_c}r)$, with j_0 the Bessel function of the first kind and $\mathrm{q_c}$ a parameter controlling the shape of the correlation function. The detailed calculations can be found in [12]. Their effect is to again modify the interaction as follows:

$$V_\alpha^{FF,SRC}(\mathrm{q}) = V_\alpha^{FF}(\mathrm{q}) - V_\alpha^{FF}(\mathrm{q}\to\sqrt{\mathrm{q}^2+\mathrm{q}_c^2}) \quad (10)$$

In this way, the short range properties of the interaction in the π and ρ-tensor channels can be optimized by fixing the parameter q_c. The Jastrow approach allows to incorporate SRC in a smooth way by varying the parameter q_c. In the present study, we fix the value of the parameter q_c to reproduce the microscopic prediction for the interaction element $V(\mathrm{q})$ based on the Unitary Correlation Operator Method (UCOM) approach [13]. This is illustrated in Fig. 2 where we compare the UCOM prediction for the ρ^T and π meson exchange to a Jastrow approximation of the same interaction element for values of q_c = 800, 900 and 1000 MeV. Note that in this case, we have employed the same FF as in Ref. [13]. In the following, we fix q_c = 1000 MeV, since it reproduces very well the microscopic prediction from the UCOM approach for the two channels ρ^T and π.

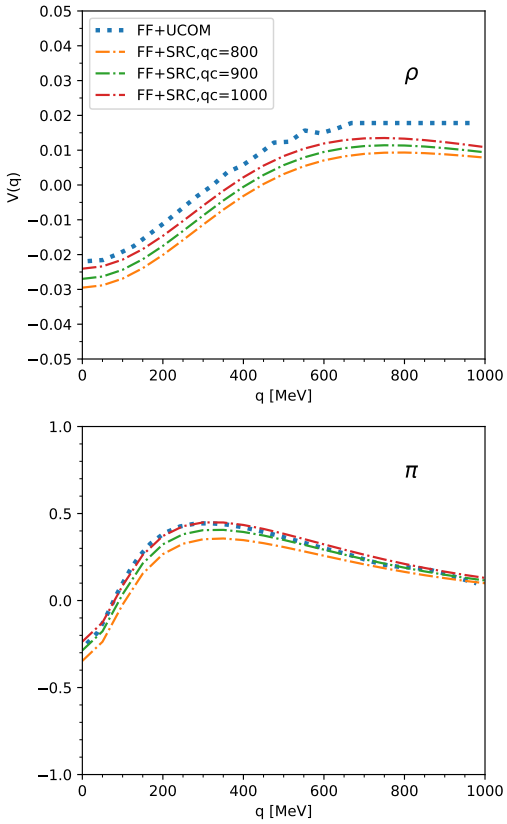

Figure 2: The tensor ρ and π meson interaction in the case of the UCOM method (see Ref. [13]) compared to their interaction in the case of the Jastrow function. We vary the value of q_c until we reproduce the same interaction, corresponding to a value of q_c = 1 GeV. The FF were all taken to have the same form and the same cut-off as in Ref. [13]

.

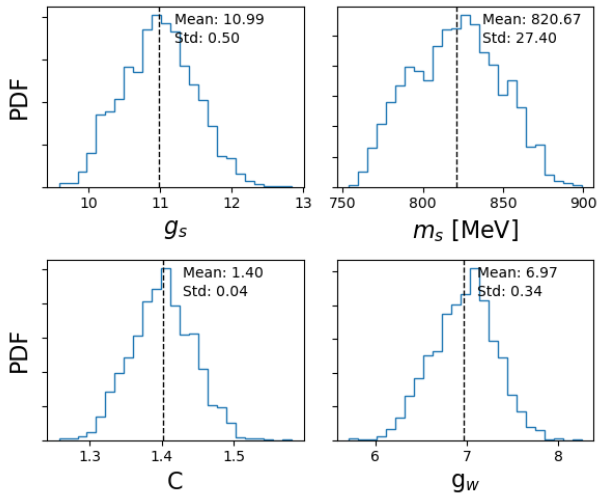

Figure 3: Probability Distribution Function (PDF) for the fit parameters for the case κ_ρ=6.6, adjusted to reproduce the saturation properties $n_{\rm sat}$ and $E_{\rm sat}$ of Tab. 2.

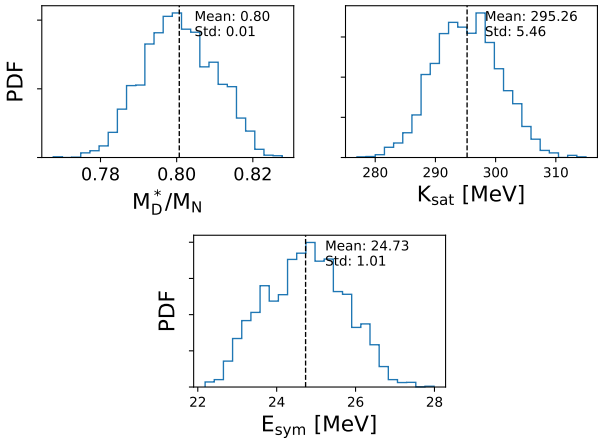

Figure 4: Probability Distribution Function (PDF) for the NEP parameters M^*_{DN}, the incompressibility modulus $K_{\rm sat}$ and the symmetry energy $E_{\rm sym}$ for the case κ_ρ=6.6, adjusted to reproduce the saturation properties $n_{\rm sat}$ and $E_{\rm sat}$ of Tab. 2.

Results

As mentioned before, the four parameters a_2, a_4, g_ω and m_s will be fixed by LQCD data and the two saturation properties $n_{\rm sat}$ and $E_{\rm sat}$(Table. 2). The uncertainties on the NEP and Lattice parameters help us investigate the sensitivity of our model's parameters to experimental errors by extracting a Probability Distribution Function (PDF). This is done with a Bayesian method using Markov-Chain Monte-Carlo (MCMC) approach. The prior distribution for the Lattice parameter a_2 and a_4 is a flat one. We aim to minimise the posterior which is the product of the prior and the χ^2 function by the Bayes theorem.

The PDFs obtained for the fit parameters m_s, g_s, g_ω and C are shown in Fig 3. The g_ω distribution peaks at 6.97 and the m_s at around 821 MeV. This value is in agreement with the one discussed in the formalism section. This is also the case for g_s and C. We can now also study the NEP parameters that are especially of interest for dense matter, e.g. the Dirac mass M^*_{DN}, the incompressibility modulus $K_{\rm sat}$ and the symmetry energy $E_{\rm sym}$. The results are shown in Fig. 4 with the Dirac mass being peaked at $(0.80 \pm 0.01)M_N$ and $K_{\rm sat}$ at (295±5)MeV, larger than the expected empirical value around 230-250 MeV [11], and even larger than what was found in [4]. And finally for $E_{\rm sym}$, the peak is at $\approx (25 \pm 1)$MeV, lower than the expected empirical value of 30-34 MeV [11], however it is an improvement over the low value at the Hartree level of ≈18 MeV, a result that was predicted in [4].

Conclusion

In this paper, we went beyond the standard RHF approaches to study nuclear matter. We studied the effects brought upon by the introduction of FF to take into account the finite size of the nucleon, and the SRC that compensate effects that can be missing in our effective model at higher energy regimes. A Bayesian analysis was performed to incorporate parameters uncertainty of the L-QCD parameters.

We were able to confront the fitted parameters to their values predicted from the LσM, but to also see the evolution of the NEP compared to a calculation only at the Hartree level. We found that there was an improvement in the symmetry energy, while the incompressibility modulus was pushed to higher values.

The SRC were included in a convenient, yet non-microscopic way. Using an approach such as the one in [13] should be important for future works, but also including higher order corrections, known as the pion cloud, which could further bring down the values of the couplings to a more "natural" value, and bridge the gap between the obtained and experimental values for the NEP.

Finally, a more microscopic treatment of the chiral potential, derived from an NJL model, is to be treated in future works.

References

[1] Ablyazimov, T., et al., Eur. Phys. J. A 53 (3), 60 (2017).

[2] S.Weinberg, Phys. Lett. B 251, 288 (1990).

[3] Anna L. Watts, et al., Rev. Mod. Phys. 88, 021001 (2016).

[4] Somasundaram, R., Margueron, J., Chanfray, G. et al, Eur. Phys. J. A 58 (5), 84 (2022).

[5] G. Chanfray, M. Ericson and P.A.M. Guichon, Phys. Rev C 63 (2001)055202.

[6] G. Chanfray and M. Ericson, Eur. Phys. J. A 25 (2005).

[7] E. Massot, G. Chanfray, Phys. Rev. C 78, 015204 (2008).

[8] P. A. M. Guichon, Phys. Lett. B200, 235 (1988).

[9] G. Hohler and E. Pietarinen, Nucl. Phys. B95, 210 (1975).

[10] D.B. Leinweber, A.W. Thomas, R.D. Young, Phys. Rev. Lett. 92, 242002 (2004).

[11] J. Margueron, R. Hoffmann Casali, F. Gulminelli, Phys. Rev. C 97(2), 025805 (2018).

[12] M. Chamseddine, J. Margueron, G.Chanfray, to be published .

[13] J. Hu, H. Toki, W. Wen, H. Shen, The European Physical Journal A 43(3), 323 (2010).

[14] M.C. Birse, Phys. Rev. C 53, R2048 (1996).

[15] G. Chanfray, M. Ericson, Phys. Rev. C 83, 015204 (2011).

[16] G. Chanfray, D. Davesne, M. Ericson, M. Martini, Eur. Phys. J. A 27, 191 (2006).

Part VII

Standard Model

session chaired by Olivier DAVIGNON

Angular analysis of the $\Lambda_b^0 \to \Lambda(1520)\mu^+\mu^-$ decays at LHCb

Felicia Volle

Laboratoire de Physique des 2 infinis Irène Joliot-Curie (IJCLab)

Abstract — The LHCb experiment reported tensions with the Standard Model in $b \to s\ell^+\ell^-$ transitions, observing a coherent and consistent pattern in different exclusive decay modes of b-hadrons produced at the LHC. Those measurements have been performed in B^+, B^0 and B_s^0 decays. Studies of b-baryon decays can provide additional and complementary information. Angular analyses of $b \to s\ell^+\ell^-$ transitions allow the characterization of potential NP affecting the decay properties. An angular fit to the $\Lambda_b^0 \to \Lambda(1520)\mu^+\mu^-$ decays is presented, which aims to extract observables sensitive to New Physics.

Motivation

The Standard Model (SM) of Particle Physics contradicts cosmological and astrophysical observables as it does not provide a dark matter candidate or describe the observed matter-antimatter asymmetry in the universe. New Physics (NP) is required to address these puzzles, and studying processes at higher scales could help reveal the nature and characteristics of that NP. Therefore, it is essential to shape the landscape of possible NP scenarios. While the direct searches at colliders are limited by the centre-of-mass energy, rare processes are suitable for indirect searches of NP. Among them, the $b \to s\ell^+\ell^-$ transitions are highly sensitive to NP effects and accessible with the existing data.

The LHCb experiment reported tensions with the SM in rare b-hadron decays. Most of these measurements are performed in rare b-meson decays. Rare b-baryon decays possess a different hadronic environment and their study offer a cross-check of the measured tensions. A Lepton Flavor Universality test has been performed in $\Lambda_b^0 \to pK^-\ell^+\ell^{-1}$ and was found to be compatible with the SM and at the same time with the other rare b-meson decays [1]. The following work aims to learn more about the SM and possible NP by performing an angular analysis in the rare Λ_b^0 decay. To deal with the rare occurrence of $\Lambda_b^0 \to pK^-\ell^+\ell^-$ decays and its large resonant structure, the focus is set on the narrow and abundant $\Lambda(1520)$ resonance, for which SM predictions for the angular observables exist [2, 3].

[1] Charge conjugation is implied throughout this document unless stated otherwise.

LHCb experiment

Protons are highly accelerated at the Large Hadron Collider (LHC) in Geneva and collided during the data-taking periods of Run I, 2011-12, and Run II, 2015-18, at centre-of-mass energies of 7, 8 and 13 TeV. An integrated luminosity of $9\,\text{fb}^{-1}$ was recorded by the LHCb experiment [4], situated at interaction point 8 of the LHC ring.

In view of the predominant production of $b\bar{b}$ pairs in the forward region, the LHCb detector is a single-arm forward spectrometer with a limited pseudo-rapidity range of $2 < \eta < 5$. The LHCb detector is composed of a tracking station around the beam pipe, the Vertex locator (Velo), which enables an excellent vertex and impact parameter resolution of about $\sigma_{\text{IP}} = 15 + 29/\text{p}_\text{T}\,\text{mm}$. The magnetic field provided by the dipole magnet causes a curvature of the track of charged particles depending on their momentum. Thanks to the various tracking stations Velo, TT, T1 - 3, the momentum of the charged particles can be inferred. For two-body decays, the momentum resolution is about $25\,\text{MeV}/c$. The electromagnetic calorimeter measures the energy of electromagnetically interacting particles, mainly electrons and photons. Hadrons are stopped in the hadronic calorimeter, where their energy is measured. It is the only place where neutral hadrons are measured. Muons depose only little energy in the calorimeters and are detected by the outer muon stations. The Ring Imaging Cherenkov detectors and the characteristical behaviour of the particles in the LHCb detector are used for particle identification. The efficiency of the particle identification is about 97-99%. In addition to precise detection and suitable particle identification, a versatile and efficient trigger is necessary for precision measurements.

$\Lambda_b^0 \to \Lambda(1520)\mu^+\mu^-$ decay

In the following analysis, the angular observables of the $\Lambda_b^0 \to \Lambda(\to pK^-)\mu^+\mu^-$ decay are studied for the first time. One of the dominant Feynman diagrams of this decay is depicted in figure 1. Even though the analysis

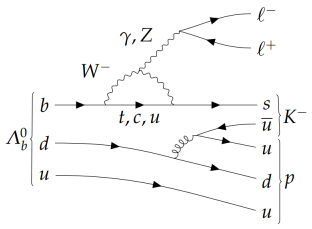

Figure 1: One of the dominant Feynman diagrams in the Standard Model of the $\Lambda_b^0 \to \Lambda(\to pK^-)\mu^+\mu^-$ decay [5].

of the rare decay uses the full Run I+II dataset, the sample size is limited. From the abundant tree-level decay $\Lambda_b^0 \to pK^- J/\psi(\to \mu^+\mu^-)$, the various Λ resonances in the pK^- mass spectrum are well-known [6]. To deal with the low occurrence of the rare decay, the focus is set on the dominant and narrow $\Lambda(1520)$ resonance by reducing the pK^- mass range to $\pm 50\,\mathrm{MeV}/c^2$ around the $\Lambda(1520)$ pole mass. Nevertheless, contributions of the two spin-1/2 resonances, $\Lambda(1405)$ and $\Lambda(1600)$, are present in the pK^- mass window under the spin-3/2 resonance. They need to be modelled in the angular fit. The idea is to separate the different Λ resonances due to their different angular distributions caused by their spin.

The dilepton invariant mass squared $q^2 = (2m_\ell)^2$ helps to distinguish the photon pole and the charmonia resonances from the rare mode. The charmonia resonances (J/ψ in $q^2 \in [8, 11]\,\mathrm{GeV}^2/c^4$ and $\psi(2S)$ in $q^2 \in [12.5, 15]\,\mathrm{GeV}^2/c^4$) are produced via the abundant tree-level decay $b \to c\bar{c}s$. Five q^2 bins are intended to be measured in the rare mode, namely $[0.1, 3], [3, 6], [6, 8], [11, 12.5], [1.1, 6]\,\mathrm{GeV}^2/c^4$, because there, NP particles could contribute to the penguin decay.

Theoretical description of the angular observables

In Effective Field Theories, long- and short-distance contributions are separated thanks to the factorization theorem. In the long-distance contributions, the hadronic matrix elements are hidden. Those are parameterised by form factors ff. The short-distance contributions are integrated out into Wilson Coefficients (WCs) at the energy scale corresponding to the Weak Effective Theory. The $b \to s\ell^+\ell^-$ transitions in the rare mode are, similar to the Fermi theory of beta decay, described by four-particle interaction operators. In the rare mode, the operators $\mathcal{O}_{7\ell\ell}$, $\mathcal{O}_{9\ell\ell}$ and $\mathcal{O}_{10\ell\ell}$ contribute. The WCs represent the corresponding coupling strengths $\mathcal{C}_{7\ell\ell}^{(\prime)}$, $\mathcal{C}_{9\ell\ell}^{(\prime)}$ and $\mathcal{C}_{10\ell\ell}^{(\prime)}$. In the presence of NP, the WCs deviate from the SM value. The WCs can be accessed by performing an angular analysis.

The $\Lambda_b^0 \to \Lambda(1520)\ell^+\ell^-$ decay is described by the decay angles $\vec{\Omega} = (\cos\theta_\ell, \cos\theta_p, \phi)$ in the helicity frame, defined as in figure 2. Theoretical predictions of the

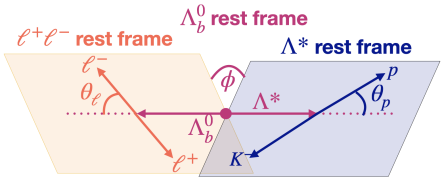

Figure 2: The definition of the decay angles of the Λ_b^0-baryon $\cos\theta_\ell, \cos\theta_p$ and ϕ in the helicity basis.

topology of the signal decay exist [7] and are presented in the following. The differential decay width of this decay can be written as

$$\frac{d^4\Gamma}{dq^2 d\vec{\Omega}} = \frac{9\pi}{32} \sum_i L_i(q^2, \mathcal{C}, ff) f_i(\vec{\Omega}). \tag{1}$$

The functions f_i represent polynomials of the decay angles. The angular coefficients L_i depend on the dilepton invariant mass squared, the WCs and the form factors. With the help of the angular coefficients of the Λ_b^0 and $\bar{\Lambda}_b^0$ decay, CP-symmetric angular observables are constructed via

$$S_i = \frac{L_i + \bar{L}_i}{d(\Gamma + \bar{\Gamma})/dq^2}. \tag{2}$$

The leptonic forward-backwards asymmetry, which is especially sensitive to NP effects, is defined as

$$A_{FB}^\ell = \frac{3(L_{1c} + 2L_{2c})}{2(L_{1cc} + 2(L_{1ss} + L_{2cc} + 2L_{2ss} + L_{3ss}))}. \tag{3}$$

A_{FB}^ℓ is measured using the Λ_b^0 and $\bar{\Lambda}_b^0$ decay together.

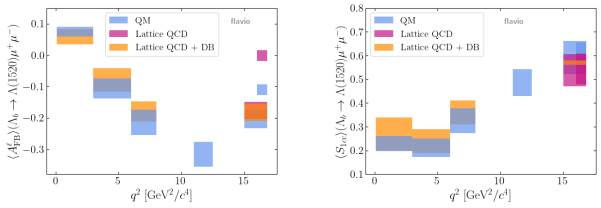

Figure 3: The theoretical predictions of the angular observables A_{FB}^ℓ and S_{1cc} in bins of dilepton invariant mass squared q^2 using non-relativistic Quark Model (QM), Lattice QCD and joint Lattice QCD and dispersive bound (Lattice QCD + DB) form factor predictions [7, 8, 9, 10]. Since the Lattice QCD prediction is only available in the $q^2 \in [16, 16.81]\,\mathrm{GeV}^2/c^4$ bin, it has been extrapolated to the $q^2 \in [15, 16.81]\,\mathrm{GeV}^2/c^4$ bin.

The theoretical values for different form factor pre-

dictions of the observables A_{FB}^{ℓ} and S_{1cc} in bins of q^2 are illustrated in figure 3. The Lattice QCD form factor prediction corresponds to an exact QCD calculation of the form factors on the lattice and is therefore the most accurate. The prediction is only situated in the $q^2 \in [16, 16.81]\,\mathrm{GeV}^2/c^4$ region [8] and has been extrapolated to the $q^2 \in [15, 16.81]\,\mathrm{GeV}^2/c^4$ bin. Because in the low-q^2 region, no light-cone sum rule form factor predictions are published yet, the SM predictions are not as advanced as in rare b-meson decays. To compare the future measurement to theory, the joint Lattice QCD and dispersive bound (Lattice QCD + DB) form factor predictions are used to predict the angular observables in the low-q^2 bins [9]. The non-relativistic Quark Model (QM) predictions are less accurate. They are based on a nuclear model [10]. Since the QM predicts no uncertainties, as proposed in Ref. [7], uncorrelated uncertainties of 10% on the form factors $f_{0,\perp,t}$ and uncorrelated 30% uncertainty on the f_g form factor are assumed.

One can conclude from figure 3 that the joint Lattice QCD and DB form factors are compatible with the QM predictions in the low-q^2 region, where the measurement is planned.

Development of the angular fit model

The angular Probability Density Function (PDF) of the spin $1/2 \to 3/2$ transition of the $\Lambda_b^0 \to \Lambda(1520)\ell^+\ell^-$ decay is predicted in Ref. [7]. The heavy-quark limit simplifies the angular PDF. Normalizing and CP-averaging it, the expression can be written as

$$\begin{aligned}&\frac{8\pi}{3}\frac{\mathrm{d}^4(\Gamma+\bar{\Gamma})}{\mathrm{d}q^2\mathrm{d}\cos\theta_\ell\mathrm{d}\cos\theta_p\mathrm{d}\phi} \\ &\simeq \frac{1}{4}\left(1+3\cos^2\theta_p\right) \\ &\times\left[\left(1-\frac{S_{1\mathrm{cc}}}{2}\right)\sin^2\theta_\ell + S_{1\mathrm{cc}}\cos^2\theta_\ell + \frac{4}{3}A_{\mathrm{FB}}^{\ell}\cos\theta_\ell\right].\end{aligned} \tag{4}$$

The expression of the PDF has no dependence on ϕ. The distribution of $\cos\theta_p$ is symmetric around zero.

Although the parities of the spin-1/2 resonances are opposite, the $\Lambda(1405)$ and $\Lambda(1600)$ can be described together by one angular PDF. A theoretical prediction is available for the $\Lambda_b^0 \to \Lambda^0\ell^+\ell^-$, with the ground-state spin-1/2 Λ resonance decaying weakly into $p\pi^-$ [11]. This PDF can be simplified because of the studied strong decay of the excited Λ resonances and rewritten as

$$\begin{aligned}&\frac{8\pi}{3}\frac{\mathrm{d}^4(\Gamma+\bar{\Gamma})}{\mathrm{d}q^2\mathrm{d}\cos\theta_\ell\mathrm{d}\cos\theta_p\mathrm{d}\phi} \\ &\simeq \frac{1-K_{1\mathrm{cc}}}{2}\sin^2\theta_\ell + K_{1\mathrm{cc}}\cos^2\theta_\ell + \frac{2}{3}A_{\mathrm{FB},1/2}^{\ell}\cos\theta_\ell. \\ &:= \mathrm{PDF}_{\mathrm{ang}}^{1/2}\end{aligned} \tag{5}$$

While the dependence on θ_ℓ is similar for eq. 4 and 5, there is no dependence on θ_p in the second PDF. Since both expressions are independent of ϕ, an angular fit is performed only on $\cos\theta_\ell$ and $\cos\theta_p$.

Since the strength of the interference terms cannot be predicted by theory, a realistic simulation sample generator was used to generate the angular distribution of interfering $\Lambda(1405)$, $\Lambda(1520)$ and $\Lambda(1600)$ resonances [12]. Six random samples were generated with different combinations of global complex phase differences $\Delta\varphi_X = \varphi_X - \varphi_{1520}$, $X \in \{1405, 1600\}$, of the spin-1/2 resonances with respect to the $\Lambda(1520)$, which are called phase combinations. Those different interference hypotheses have no impact on the $m(pK^-)$ and the $\cos\theta_\ell$ distribution, but cause a sizeable observed shift of the $\cos\theta_p$ distribution. Additional terms in $\cos\theta_p$ are introduced to cope with this effect. The total angular PDF combines eq. 4 and 5 with the scale factor $f_{3/2}$, which represents the fraction of $\Lambda(1520)$ events. Interference terms, j_1 and j_2, are introduced in the PDF. The formula for the combined angular PDF including the interferences is shown in eq. 6.

$$\begin{aligned}&\mathrm{PDF}_{\mathrm{ang}}^{\mathrm{total}} \\ &= f_{3/2}\left(\left(\frac{1}{4}-\frac{j_2}{3}\right) + j_1\cos\theta_p + \left(\frac{3}{4}+j_2\right)\cos^2\theta_p\right) \\ &\times\left[\left(1-\frac{S_{1\mathrm{cc}}}{2}\right)\sin^2\theta_\ell + S_{1\mathrm{cc}}\cos^2\theta_\ell + \frac{4}{3}A_{\mathrm{FB},3/2}^{\ell}\cos\theta_\ell\right] \\ &+ (1-f_{3/2})\times\mathrm{PDF}_{\mathrm{ang}}^{1/2}\end{aligned} \tag{6}$$

A fit of the pK^- mass spectrum is performed first. A relativistic Breit-Wigner is used to describe the $\Lambda(1520)$ baryon and a Chebychev Polynomial of the order 3 to model the spin-1/2 Λ resonances[2] The aim of this fit is to extract $f_{3/2}$, which is fixed in the angular fit.

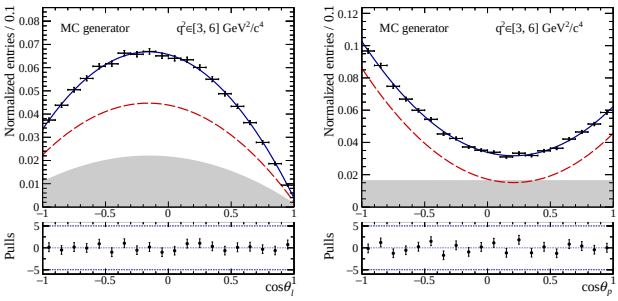

Figure 4: Angular fit to a realistic simulation sample with the differences of the strong phases $\Delta\varphi_{1405} = \Delta\varphi_{1520} = 0$ to the $\Lambda(1520)$ resonance in the $q^2 \in [3,6]\,\mathrm{GeV}^2/c^2$. Projection of the $\Lambda(1520)$ component in red, the spin-1/2 resonances in grey and the total fit in blue.

An exemplary fit to a realistic simulation sample with the phase differences $\Delta\varphi_{1405} = \Delta\varphi_{1600} = 0$ to the $\Lambda(1520)$ resonance in the $q^2 \in [3,6]\,\mathrm{GeV}^2/c^2$ bins is depicted in fig. 4. With the help of the interference terms, the angular fit can account for the shift in $\cos\theta_p$.

[2]Since in the mass distribution only interference's between resonances with the same spin and same parity appear, they do not need to be included in the pK^- mass fit.

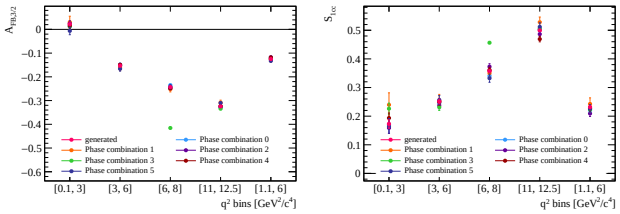

Figure 5: Resulting angular observables compared to the generated values (magenta) of the realistic simulation samples in the different q^2 bins.

After performing the fit on the different realistic simulation samples, the resulting fit values are shown as a function of the q^2 bin in fig. 5. The uncertainties are linked to the simulation sample size and are not scaled to the data expectations. The resulting fit values are close to the generated values, excluding the angular fit of phase combination 3 in the $q^2 \in [3,6]\,\mathrm{GeV}^2/c^4$ and the highest q^2 bin.

Selection and angular acceptance

In data as in simulation, a $\Lambda(1520)$-baryon candidate is reconstructed by combining two oppositely charged tracks emerging from a common vertex, if the tracks are assigned to one proton and one kaon candidate. Two tracks with opposite charges, identified as muons, are combined with the $\Lambda(1520)$ baryon candidate to form a Λ_b^0 baryon. Requirements on the quality of the Λ_b^0 decay vertex, the flight distances of the Λ_b^0 and $\Lambda(1520)$, as the consistency of the origin with the primary vertex are made to avoid wrong combinations.

$B_s^0 \to \phi(1020)(\to K^+K^-)\mu^+\mu^-$ decays with a kaon misidentified as a proton candidate, is suppressed by vetoing the narrow $\phi(1020)$ resonance. $B^- \to K^-\mu^+\mu^-$ decays, combined with a random proton, are rejected by a requirement on the B^- mass. The same decay with a kaon misidentification as a proton candidate is considered. $\Lambda_b^0 \to pD^0(\to K^-\pi^+)\pi^-$ decays, having two pions misidentified as muon candidates, are removed in the rare mode through a veto of the D^0 mass[3]. An additional veto rejects J/ψ decays, where a muon is misidentified as a hadron. The vetoes significantly remove the peaking backgrounds while keeping 91% of the signal. Contributions from $\Lambda_b^0 \to \Lambda_c^+(\to pK^-X)Y$ decays, where the X and Y represent either the hadronic ($\pi^\pm$) or leptonic ($\mu^\pm{}^{(-)}\nu_\mu$) decay products, were found to be negligible.

A Boosted Decision Tree (BDT) is implemented to remove the combinatorial background. As a signal proxy, simulated $\Lambda_b^0 \to \Lambda(1520)\mu^+\mu^-$ decays are used, and the upper mass sideband of the $pK^-\mu^+\mu^-$ data sample ($6 - 6.8\,\mathrm{GeV}/c^2$) is used as background proxy. The BDT is trained on the kinematic and topological information of the involved particles and optimized on the significance.

An exponential function describes the remaining combinatorial background in the $pK^-\mu^+\mu^-$ mass spectrum. A Hypathia function models Λ_b^0-baryon candidates, which shape is fixed to the fit of the simulation sample [13]. The *sPlot* technique is used to perform an angular fit on Λ_b^0-baryon candidates only [14].

Selection and corrections, applied to the simulation to match the data, shape the angular distributions, and especially momentum requirements on the final state particles. To account for this effect in the data sample, the angular acceptance is modelled by

$$\varepsilon(\cos\theta_\ell, \cos\theta_p, \phi) = \sum_{ijk} c_{ijk}\varepsilon_i(\cos\theta_\ell)\varepsilon_j(\cos\theta_p)\varepsilon_k(\phi).$$

Legendre Polynomials up to order five describe the angular acceptance of $\cos\theta_p$ and even ones up to order 4 $\cos\theta_\ell$. The ϕ angle is modelled by even Fourier Polynomials up to order 4.

An $\Lambda_b^0 \to \Lambda(1520)\mu^+\mu^-$ simulation sample, generated to be flat in the angles $\vec{\Omega}$, is used to extract the angular acceptance per event weights via the Method of Moments [15]. The angular acceptance event weights are applied to the data sample.

Results

To test the angular fit model on data, a fit on the tree-level $\Lambda_b^0 \to pK^-J/\psi(\to \mu^+\mu^-)$ control mode is performed.The angular fit converges, and the resulting fit value of A_{FB}^ℓ is compatible with zero within one standard deviation, as expected in the resonant mode.

The next step is to fit the angular distribution in the rare mode. We are looking forward to finalising the analysis and seeing it published. The expected statistical sensitivity is about $1/12^{\mathrm{th}}$ with respect to the $B^0 \to K^{*0}\mu^+\mu^-$ angular analysis.

Since the size of the $\Lambda_b^0 \to \Lambda(1520)\mu^+\mu^-$ sample is statistically limited, the increase of the luminosity expected in the coming years with the Run III data taking at the LHCb experiment would be highly beneficial for the analysis.

References

[1] LHCb collaboration, R.Aaij et al., *Test of lepton universality with $\Lambda_b^0 \to pK^-\ell^+\ell^-$ decays*, JHEP **55** (2020) 040.

[2] S. Descotes-Genon and M. Novoa-Brunet, *Angular analysis of the rare decay $\Lambda_b \to \Lambda(1520)(\to N\bar{K})\ell^+\ell^-$*, JHEP **06** (2019) 136 [Erratum: JHEP **06** (2020) 102].

[3] Y. Amhis, S. Descotes-Genon, C. Marín Benito, M. Novoa-Brunet and M. H. Schune, *Prospects for New Physics searches with $\Lambda_b^- \to \Lambda(1520)\ell^+\ell^-$ decays*, Eur. Phys. J. Plus **136** (2021) 614.

[3] Negligible in the resonant mode due to the tight requirements on the q^2 mass.

[4] LHCb collaboration, I. Bediaga et al., *Framework TDR for the LHCb Upgrade: Technical Design Report* (2012).

[5] V. Lisovskyi, *Study of rare b-baryon decays and test of lepton universality at LHCb*, Thesis, 2019.

[6] LHCb collaboration, R. Aaij et al., *Observation of $J/\psi p$ Resonances Consistent with Pentaquark States in $\Lambda_b^0 \to J/\psi K^- p$ Decays*, Phys. Rev. Lett. **115** (2015) 072001.

[7] S. Descotes-Genon and M. Novoa-Brunet, *Angular analysis of the rare decay $\Lambda_b \to \Lambda(1520)(\to NK)\ell^+\ell^-$*, JHEP **06** (2019) 136.

[8] S. Meinel and G. Rendon, $\Lambda_c \to \Lambda^*(1520)$ *form factors from lattice QCD and improved analysis of the $\Lambda_b \to \Lambda^*(1520)$ and $\Lambda_b \to \Lambda_c^*(2595, 2625)$ form factors*, Phys. Rev. D **105** (2022) 054511.

[9] Y. Amhis, M. Bordone and M. Reboud, *Dispersive analysis of $\Lambda_b \to \Lambda(1520)$ local form factors*, arXiv:2208.08937v2.

[10] L. Mott and W. Roberts, *Rare dileptonic decays of Λ_b in a quark model*, Int. J. Mod. Phys. A **27** (2012) 1250016.

[11] P. Böer, T. Feldmann and D. van Dyk, *Angular Analysis of the Decay $\Lambda_b \to \Lambda(\to N\pi)\ell^+\ell^-$*, JHEP **01** (2015) 155.

[12] A. Beck, T. Blake and M. Kreps, *Angular distribution of $\Lambda_b^0 \to pK^-\ell^+\ell^-$ decays comprising Λ resonances with spin up to $\leq 5/2$*, arXiv:2210.09988v2 (2022).

[13] D. Martínez Santos and F. Dupertuis, *Mass distributions marginalized over per-event errors*, NIM A **764** (2014) 150-155.

[14] M. Pivk and F. R. Le Diberder, *sPlot: a statistical tool to unfold data distributions*, Nucl. Instrum. Meth. A **555** (2005) 356-369.

[15] F. Beaujean, M. Chrząszcz, N. Serra and D. van Dyk, *Extracting Angular Observables without a Likelihood and Applications to Rare Decays*, Phys. Rev. D **91** (2015) 114012.

Angular analysis of the $B_s^0 \to \phi e^+ e^-$ decay at LHCb

Gaelle Khreich

Universite Paris-Saclay, IJCLab, Orsay

Abstract — One of the favored ways to search for signs of New Physics (NP) beyond the Standard Model (SM) is the study of $b \to s\ell^+\ell^-$ (ℓ= electron or muon) transitions which involve Flavour Changing Neutral Currents (FCNC) via box or loop diagrams. The LHCb experiment has recently published a set of measurements in tension with the SM predictions. The aim of this work is to perform an angular analysis on $B_s^0 \to \phi e^+ e^-$ decay in the low dielectron mass region to measure the photon polarization in $b \to s\gamma$ transitions.

Introduction

The Standard Model (SM) of Particle Physics is scientists' current best theory to describe the most basic building blocks of the universe, the elementary particles and their interactions. It explains three of the four fundamental interactions, namely electromagnetism (carried by the photon), the strong force (carried by gluons) and the weak force (carried by W and Z bosons).
Despite its success at describing hundreds of precise measurements, the SM does have limitations and many important questions remain unanswered (e.g. Dark Matter, gravity).
The study of flavour-changing neutral currents (FCNC) gives access to important tests of the SM and allows to search for hints of beyond the SM phenomena. These processes take a down (d, s, b) or up (u, c, t) type quark and transform it into another quark of the same type but of a different flavour. They are forbidden at tree level in the SM; hence they need to proceed at next-to-leading order, via loops, resulting in being rare. If heavy new particles exist, they may contribute to FCNC decay amplitudes, affecting the measurement of some observables such as angular observables.

The $B_s^0 \to \phi(\to K^+K^-)e^+e^-$ decay is a FCNC process. The angular distribution of the $K^+K^-e^+e^-$ system is particularly sensitive to contributions from non SM physics. The leading SM diagrams are shown in Fig. 1; the relative contribution of each of the diagrams varies with the dilepton invariant mass. The contribution from a virtual photon coupling to the lepton pair dominates in the region where the dilepton invariant mass is very small, allowing measurement of the helicity of the photon in $b \to s\gamma$ transitions. In the SM, this photon is predominantly left handed, with a small right-handed component arising from the mass of the s quark and long distance effects. In contrast, in many extension of the SM, NP may manifest as a large right handed current.

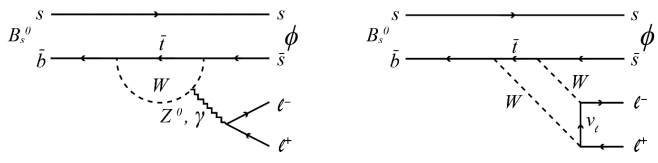

Figure 1: Dominant Standard Model Feymann Diagrams for $B_s^0 \to \phi e^+ e^-$ decay.

Experimentally, an analysis with muons rather than electrons in the final state produces a much higher yield at LHCb [1]. This is primarily due to the distinctive signature that muons provide, which is efficiently exploited in the online selection, together with the better mass and energy resolutions and higher reconstruction efficiency of dimuon decays. However, the choice of electrons as the final state leptons is driven by the fact that it allows to explore the photon pole, far below the dimuon mass threshold at $4m_\mu^2 = 0.05 GeV^2/c^4$. Moreover, one can take advantage of the increase of the branching fraction due to the photon pole.
In the decay $B_s^0 \to \phi e^+ e^-$, followed by $\phi \to K^+K^-$, the direction of the four outgoing particles can be described by three angles, shown in Fig. 2. The differential decay width can thus be written as a function of the three angles ($\cos\theta_l$, $\cos\theta_K$, ϕ) and the dilepton mass squared q^2. The angle θ_l is defined as the angle between the direction of the e^- and the direction of flight of the B_s^0 in the dielectron rest frame. The angle θ_k is defined as the angle between the direction of K^- and the direction of flight of B_s^0 in the K^-K^+ rest frame. The angle ϕ is defined as the angle between the plane containing the two leptons and the plane containing the two hadrons of the final state in the B_s^0 rest frame. ϕ is transformed such that $\tilde{\phi} = \phi + \pi$ if $\phi < 0$. This transformation simplifies the angular expression without any loss of sensitivity to the photon polarization observables and compensate the limited signal yield. In the limit of massless leptons, the $B_s^0 \to \phi e^+ e^-$ angular

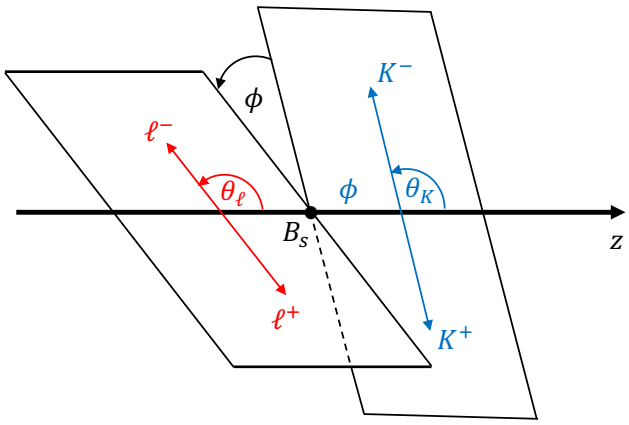

Figure 2: A sketch of the definition of the three angles θ_L, θ_K and ϕ for the $B_s^0 \to \phi e^+ e^-$ decay.

distribution reads as

$$\left\langle \frac{d^3\Gamma}{d\cos\theta_l d\cos\theta_k d\tilde{\phi}} \right\rangle = \frac{9}{16\pi}\left\{\frac{3}{4}(1-F_L)\sin^2\theta_k + F_L\cos^2\theta_k + \left[\frac{1}{4}(1-F_L)\sin^2\theta_k - F_L\cos^2\theta_k\right]\cos 2\theta_l + \frac{1}{2}(1-F_L)A_T^{(2)}\sin^2\theta_k\sin^2\theta_l\cos 2\tilde{\phi} + (1-F_L)A_T^{ReCP}\sin^2\theta_k\cos\theta_l + \frac{1}{2}(1-F_L)A_T^{ImCP}\sin^2\theta_k\sin^2\theta_l\sin 2\tilde{\phi}\right\}$$

The four angular observables $F_L, A_T^{(2)}, A_T^{ImCP}$ and A_T^{ReCP} are related to the transversity amplitudes. The observable F_L is the longitudinal polarisation of the ϕ and is expected to be small at low q^2. The observable A_T^{ReCP} is related to the lepton forward-backward asymetry. The observables $A_T^{(2)}$ and A_T^{ImCP} are the key observables to this analysis because they are related to the photon polarisation [2].

The LHCb detector and data set

The study reported here is based on pp collision data, corresponding to an integrated luminosiy of 9fb^{-1}, collected at the Large Hadron Collider (LHC) with the LHCb detector between the year 2011 to 2018.
LHCb [3] is a single-arm spectrometer covering the pseudorapidity range $2<\eta<5$. The choice of the detector geometry is motivated by the fact that at the high energies provided by the LHC, the production of a $b\bar{b}$ pair occurs mostly in a small forward or backward cone. The detector includes a tracking system [4] consisting of a vertex detector surrounding the pp interaction region and of tracking stations on either side of a 4 [Tm] dipole magnet. Charged particles are identified using information from two ring-imaging Cherenkov detectors (RICH) [5], electromagnetic (ECAL) and hadronic (HCAL) calorimeters and muon chambers. Particle identification is then achieved by combining the information from several sub-detectors.

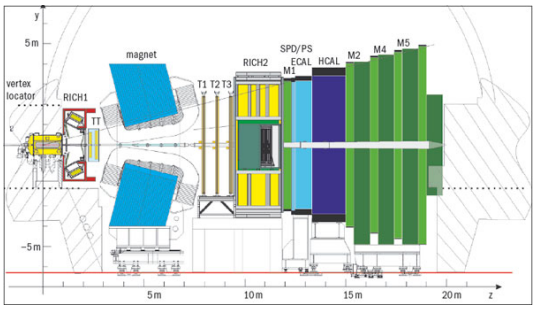

Figure 3: Schematic view of the LHCb detector

All candidates in the $K^+K^-e^+e^-$ final state are required to be well identified using particle identification information and pass some kinematics criteria (e.g. Energy and momentum requirements).
Simulated samples are used to determine the effect of reconstruction and selection on the angular distributions and to estimate the expected signal yields and the contamination from specific backgrounds.

Selection of $B_s^0 \to \phi e^+ e^-$ events

Oppositely charged electron pairs formed with p_T exceeding 500 MeV/c and with a good quality vertex are used to form signal candidates. The reconstructed e^+e^- invariant mass is required to be in the range 10-500 MeV/c^2. To be as close as possible to the true dielectron mass, the later is computed with the constraint that $m(K^+K^-e^+e^-)$ is equal to the B_s mass and that the signal candidates originate from the Primary Vertex (PV). This also serves to reduce the background from $B_s^0 \to \phi\gamma$ decays followed by a photon conversion in the material of the detector.
The ϕ mesons are reconstruced in the $\phi \to K^+K^-$ mode where the mass of the pair K^+K^- is around ± 12 MeV/c^2 of the ϕ invariant mass[6].
In order to maximize the signal efficiency while reducing the level of combinatorial background, a multivariante classifier based on a boosted decision tree (BDT) [7] is used. The signal training sample is composed of simulated $B_s^0 \to \phi e^+ e^-$ events and the background training sample is taken from the data's upper mass sideband ($m_{(K^+K^-e^+e^-)} > 5700 MeV/c^2$) of $B_s^0 \to \phi e^+ e^-$ candidates. The BDT uses the event's kinematics and geometrical properties. The BDT efficiency on the selected signal is $\sim 96\%$ while the background is reduced by half.

Backgrounds

Several sources of background are studied and are still under investigation using samples of simulated events, corrected to reflect the difference between data and simulation.
A possible source of contamination is the decay $B_s^0 \to$

$D_s^- e^+ \nu_e$ with $D_s^- (\to \phi e^- \bar{\nu}_e)$ which has a larger branching fraction than that of the signal. In the rare case where both neutrinos have low energies, this background is signal-like and can pass the selection. Knowing that $\cos(\theta_L)$ can be expressed as $\sim \frac{E_{e^+} - E_{e^-}}{E_{e^+} + E_{e^-}}$, this background tends to peak at $\cos(\theta_L) \pm 1$. For that reason, a requirement of $|\cos(\theta_L)| < 0.9$ is applied to suppress this background.

The radiative decay $B_s^0 \to \phi\gamma$, where the real photon converts into an e^+e^- pair in the material of the detector is an important background to the $B_s^0 \to \phi e^+ e^-$ decay having the exact same final state and a branching ratio of two orders of magnitude higher. The dielectron mass of $B_s^0 \to \phi\gamma$ is usually very small and removing events below 10 MeV/c^2 which is required by the dilepton mass range of the analysis already removes most of the converted photons. Nonetheless, a veto is designed to reject events where the dielectron pair may have originated from a photon that converted into an e^+e^- pair in the material of the detector by checking whether the vertex of the dielectron pair is consistent with a region in the detector that contains material and reduce this contamination to 1%.

Fit to the $K^+K^-e^+e^-$ mass

The analysis is performed blinding the angular fit to data. However, the mass fits to data are not blinded. A mass fit over a wide mass range from 4500 to 6300 MeV/c^2 is performed to estimate the size of the signal and the combinatorial background as shown in Fig. 3. The signal probability density function (PDF) is described by a Double Sided Crystal Ball (DSCB). The shape of the combinatorial background is parametrised by an exponential function. The mass shapes are fixed from MC. To account for MC/data differences, the signal shapes are allowed to be modified by a scale and shift factor. The fit to data is shown in Fig. 4 and the resulting signal yield is 85 ± 12.

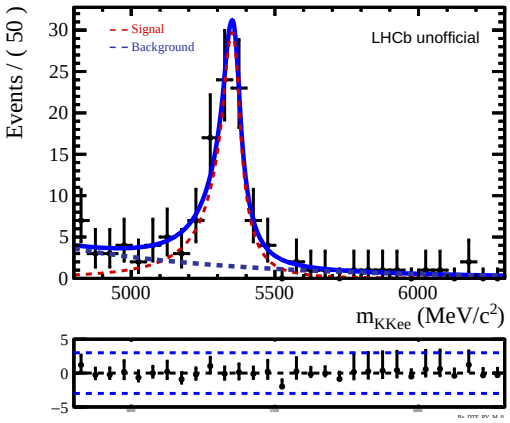

Figure 4: Invariant mass distribution for the $B_s^0 \to \phi e^+ e^-$ decay in the very low dilepton mass region.

Angular modelling

The angular acceptance can be expressed as $\epsilon(\cos\theta_l, \cos\theta_k, \tilde{\phi}) = \epsilon(\cos\theta_l)\epsilon(\cos\theta_k)\epsilon(\tilde{\phi})$. The three angular distributions for the $B_s^0 \to \phi e^+ e^-$ decay are distorted by the geometrical acceptance of the detector, the trigger, the event reconstruction and the selection. To study these effects, $B_s^0 \to \phi e^+ e^-$ simulated events are generated with no underlying physics but momentum conservation. Hence the three angles $\cos\theta_l, \cos\theta_k$ and ϕ are generated with a flat uncorrelated distribution. The full reconstruction algorithm as well as the full selection is then applied. The resulting distribution of $\cos\theta_l, \cos\theta_k$ and ϕ give access to the angular acceptance of the three angles.

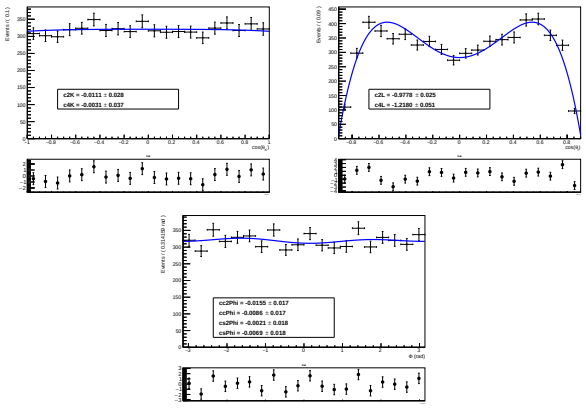

Figure 5: Angular acceptance curves of $\cos(\theta_K), \cos(\theta_L)$ and ϕ on a subset of $B_s^0 \to \phi e^+ e^-$ simulated events

The angular distribution of combinatorial events are described by the product of three independant distributions of $\cos\theta_l$, $\cos\theta_k$ and $\tilde{\phi}$. They are extracted from $B_s^0 \to \phi e^\pm e^\pm$ data. Due to the conservation of lepton flavor, this decay is forbidden in the SM. Therefore, when asking to reconstruct it, all candidates found must have selected a random track to form the $e^\pm e^\pm$ pair.

Prospects

In this contribution, I briefly discussed the ongoing angular analysis of the $B_s^0 \to \phi e^+ e^-$ decay in the very low dilepton mass region in order to measure the photon polarization. The aim is to determine the four observables $F_L, A_T^{(2)}, A_T^{ImCP}$ and A_T^{ReCP} by performing a four dimensional fit to the $B_s^0 \to \phi e^+ e^-$ signal candidates to the differential decay width discussed before and the $K^+K^-e^+e^-$ invariant mass. The fit will be validated using a large number of pseudo-expirements that include all the components of the fit.

Acknowledgements

My work is part of a project that has received funding from the European Research Council (ERC) under the European Union's Horizon 2020 research and innovation program (grant agreement No 101018181).

References

[1] LHCb collaboration, R.Aaij et al, Angular analysis of the rare decay $B_s \to \phi\mu^+\mu^-$, JHEP 11 (2021) 043.

[2] On the impact of meson mixing on $B_s \to \phi e^+ e^-$ angular observables at low q^2, arXiv: 2210.11995

[3] LHCb collaboration, I. Bediaga et al., Framework TDR for the LHCb Upgrade: Technical Design Report (2012).

[4] P. d'Argent et al., Improved performance of the LHCb Outer Tracker in LHC Run 2, JINST 12 (2017) P11016, arXiv:1708.00819.

[5] M. Adinolfi et al., Performance of the LHCb RICH detector at the LHC, Eur. Phys. J. C73 (2013) 2431, arXiv:1211.6759.

[6] R.L. Workman et al. (Particle Data Group), Prog. Theor. Exp. Phys. 2022, 083C01 (2022).

[7] L. Breiman, J. H. Friedman, R. A. Olshen, and C. J. Stone, Classification and regression trees, Wadsworth international group, Belmont, California, USA, 1984.

Test of lepton flavor universality using $B^0 \to D^{*-}\tau^+\nu_\tau$ decay at LHCb

Gaya Benane

Aix Marseille Univ, CNRS/IN2P3, CPPM, Marseille, France

Abstract — The Standard Model of particle physics (SM) states that the three charged leptons e, μ and τ have the same electroweak coupling (through $W^\pm$ and Z^0 bosons) and the only difference between them is their coupling to the Higgs field, i.e. their mass. Couple of independent experiments (BaBar, Belle and LHCb) have measured deviations from the SM prediction. One of the anomalies arises from the $b \to c\ell\nu$ transition called *charged anomalies*. The goal of my thesis is to study such anomalies by comparing the decays $B^0 \to D^*\tau\nu_\tau$ to $B^0 \to D^*\mu\nu_\mu$ where τ is reconstructed from $\pi^+\pi^-\pi^+(\pi^0)$, using data collected by the LHCb detector from 2011 to 2018. With this large statistical sample, we will be able to significantly reduce the uncertainty of the measurement.

Introduction

In the standard model of particle physics, Lepton Flavor Universality (LFU) stands for the symmetry between the three families of quarks and (charged) leptons. Namely, each member of a given family has associated particles in the others with which it shares the same quantum numbers, only their mass is different.

During previous years, flavor community started to have some doubts on the validity of the LFU assumption from the experimental side. Two possibility have cropped up: *flavor changing neutral currents* (FCNC) through the $b \to s\ell^+\ell^-$ quark transition and *flavor changing charged currents* (FCCC) through[1] the $b \to c\ell\nu$ quark transition, where ℓ is a charged lepton.

Multiple ways exist for the seak of testing LFU. In this paper, we present an FCCC test by comparing the two decays $B^0 \to D^{*-}\ell^+\nu_{\ell^+}$, where $\ell = \tau$ and μ. The Feynman diagram is depicted in fig. 1, where the decay $\bar{b} \to \ell^+\nu_{\ell^+}$ occurs via W^+ intermediate state. Because it involves an excited charm meson, the ratio between the branching fraction of the two decays is called $R(D^{*-})$:

$$R(D^*) = \frac{\mathcal{B}(B^0 \to D^{*-}\tau^+\nu_\tau)}{\mathcal{B}(B^0 \to D^{*-}\mu^+\nu_\mu)} \tag{1}$$

If we substitute the spectator d quark by c or the charm meson D by a charmed baryon Λ_c, we will get similar ratios $R(J/\Psi)$, $R(\Lambda_c)$.

There was multiple measurements of $R(D^*)$ from different experiments using different channels and techniques: BaBar [1] measuring the ratio $\frac{\mathcal{B}(B^0\to D^{*-}\tau^+\nu_\tau)}{\mathcal{B}(B^0\to D^{*-}\ell\nu_\mu)}$ with $\ell = \mu, e$, Belle [2, 3] with hadronic and leptonic τ channels and one-prong hadronic decay: $\tau \to \pi\nu_\tau$ and $\tau \to \rho\nu_\tau$ and finally LHCb with muonic decay [5] $\tau^- \to \mu^-\bar{\nu}_\mu\nu_\tau$ and the 3-prong hadronic τ (Run 1) [4].

[1] FCCC can happen at the tree level.

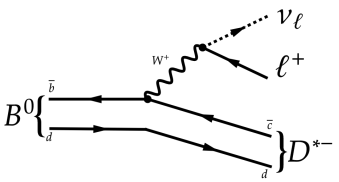

Figure 1: Feynman diagram of the B^0 to $D^{*-}\ell^+\nu_\ell$ transition.

The analysis is an extension of the Run 1 study done in [4], we present the $R(D^*)$ analysis using the hadronic τ reconstruction from the data collected between 2015 and 2016 at LHCb. The future work in my PhD thesis consist in adding the full Run 2 dataset (2015–2018).

The structure of the paper is the following: in chapter 30, we introduce the main channels and the relevant observables to measure $R(D^*)$. Then, we briefly explain the methods we use to characterise our backgrounds and to separate the signal and normalisation samples, in chapter 30. After what we discuss two control samples in chapter 30. The signal fit result is shown in chapter 30. And finaly, in chapter 30 before the conclusion, we give a short review of the $R(D^*)$ measurements and the possible candidates that could be at the origin of the LFU anomalies.

$R(D^*)$ hadronic τ analysis

The signal mode fig. 2 (left) corresponds to the decay $B^0 \to D^{*-}\ \tau^+\ \nu_\tau$, where the τ^+ decays into $3\pi^\pm(\pi^0)\bar{\nu}_\tau$ the D^{*-} gives $\pi^- D^0$, and $D^0 \to K^+\pi^-$. The decay $B^0 \to D^{*-}\ 3\pi^\pm$ fig. 2 (right) have the same visible final states as our signal, it has also the advantage to be fully reconstructed, whereas the signal is only partially reconstructed due to the missing neutrinos. In addition, taking the ratio between these two modes will help to cancel out systematic effects. The

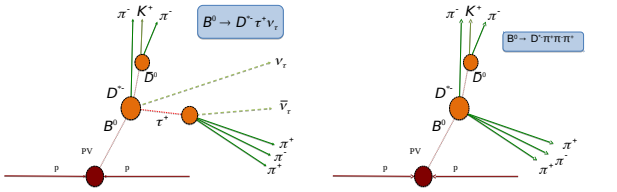

Figure 2: Signal (left) and normalisation (right) mode topology.

second mode will be taken as our normalisation mode.

We introduce $\mathcal{K}(D^{*-})$:

$$R(D^{*-}) \equiv \mathcal{K}(D^{*-}) \frac{\mathcal{B}(B^0 \to D^{*-} 3\pi^{\pm})}{\mathcal{B}(B^0 \to D^{*-} \mu^+ \nu_\mu)}, \qquad (2)$$

that we measure directly, it can be decomposed as follows:

$$\mathcal{K}(D^{*-}) = \frac{\mathcal{B}(B^0 \to D^{*-} \tau^+ \nu_\tau)}{\mathcal{B}(B^0 \to D^{*-} 3\pi^{\pm})}, \qquad (3)$$

$$= \frac{N_{\text{sig}}}{N_{\text{norm}}} \frac{\varepsilon_{\text{norm}}}{\varepsilon_{\text{sig}}} \frac{1}{\sum \mathcal{B}(\tau^+ \to 3\pi^{\pm}(\pi^0)\nu_\tau)}. \qquad (4)$$

The signal yield N_{sig} is determined from a three–dimensional binned template fit to: the momemtum transfered to the leptonic system $q^2 \equiv (p_B - p_{D^*})^2$, the τ^+ lifetime t_τ and the Anti–D_s^+ BDT, the normalisation yield N_{norm} is obtained from an unbinned fit to $m(D^* 3\pi^{\pm})$, the efficiences ε_{sig} and $\varepsilon_{\text{norm}}$ are extracted from simulated samples and the branching fractions are extracted from external measurements [6, 7] .

Selection

One of the main challenges of the analysis is to isolate the signal from the multiple backgrounds, for that we go through multiple selection stages. Initially we apply trigger and common requirements, and then we use boosted–decision–tree (BDT) classifiers applied to different sets of samples. The four BDT are listed below:

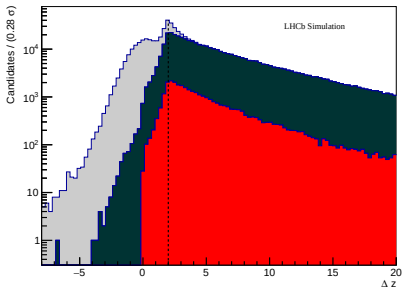

Figure 3: Detachment uncertainty distribution in logarithmic scale of the simulated signal (red), double charm background (black) and prompt background (grey), after the initial cuts.

- $3\pi^{\pm}$ *vertex detachment BDT* targets the 'prompt' background, where the three pion system come directly from the B^0 vertex. In fig. 3, we see the candidates distribution as function of Δz–the vertex displacement of the $3\pi^{\pm}$ system from the B^0 vertex. Most of the background candidates in gray and dark green are rejected after apply $\Delta z > 2$ cut.

- *Anti–combinatorial background BDT* tackles the background where D^{*-} and $3\pi^{\pm}$ from different hadrons.

- *Charged isolation BDT* removes candidates with extra charged tracks associated with signal ones. Namely, events where $B^0 \to D^{*-} D^0 K^+(X)$ with $D^0 \to K^- 3\pi^{\pm}$.

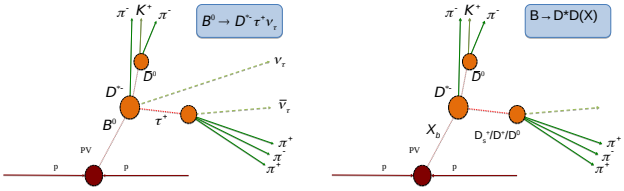

Figure 4: Signal (left) and normalisation (right) mode topology.

- After apply the three previous BDT, the double-charm decays remain the most dominant backgrounds. Thess backgrounds have the same topology with the signal as depicted in fig. 4. We apply *Anti–D_s BDT* to target the $B^0 \to D^{*-} D_s X$ events where $D_s \to 3\pi^{\pm} X$. This BDT is used in final fit.

Finally, in the last stage we apply final cuts to select samples enriched in the signal or normalisation modes.

Control samples

Before fitting the signal, it is important to check the agreement between simulated samples and real data. This step is also required to extract constraints for the parameters used in the signal fit.

We use the D_s decay model, and samples with double-charm dominated region $B^0 \to D^{*-} D_s(X)$, $B \to D^{*-} D^0 X$ and $B \to D^{*-} D^+ X$ as control samples, in what follows, we describe only the two former ones.

D_s decay model

As for the τ, the D_s can decay into $3\pi^{\pm}$, it can go through various intermediate resonante states: a_1^+, ρ^0, η, η', ϕ, ω with unknown branching fractions. To avoid misidentification of pions coming from τ from the one originating from a D_s, but also to correct simulated samples with respect to real data, we exploit the combination of two-pion systems mass: $\min m(\pi^+\pi^-)$, $\max m(\pi^+\pi^-)$, $m(\pi^+\pi^+)$ to identify the invariant mass of the intermediate state, and $m(3\pi^{\pm})$ to distinguish

exclusive $D_s \to 3\pi^{\pm}$ decays from inclusive ones. We perform a simultaneous maximum likelihood binned fit to the four variables aforementioned, to a $D_s \to 3\pi^{\pm}X$ sample with a D_s BDT requirement.

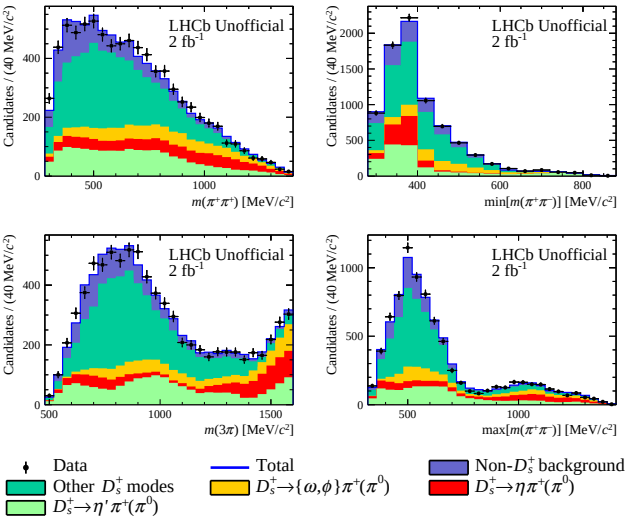

Figure 5: Projections of the $D_s \to 3\pi^{\pm}X$ components for the variables: $\min[m(\pi^+\pi^-)]$, $\max[m(\pi^+\pi^-)]$, $m(\pi^+\pi^+)$ and $m(3\pi^{\pm})$ in the fit to the control data samples. The components are: $D_s \to \eta'\,\pi^+\,(\pi^0)$ (green); $D_s \to \eta\,\pi^+\,(\pi^0)$ (red); $D_s \to \omega\,\pi^+\,(\pi^0)$ and $D_s \to \phi\,\pi^+\,(\pi^0)$ (orange); other D_s modes (yellow); non-D_s background (blue).

The result is shown in fig. 5, the fit shows a good agreement between the real data and the associated Probabily Density Function (PDF). We estimate the branching fraction of the $D_s \to a_1^+X$, and we apply correction factors on the simulated samples $B^0 \to D^{*-}\,D_s(X)$, to match the fitted fractions.

$B^0 \to D^{*-}D_s(X)$ control mode

After applying the selection cuts, the double–charm events are the remaining dominant backgrounds.

The fit is performed only to $m(D^*3\pi^{\pm})$. In fig. 6 we show the corresponding distribution from which we subtract $m(K^-\pi^+)$ and $m(3\pi^{\pm})$ for a better resolution (upper–left corner), in addition, we also present the composition of the three variables used for the signal fit. The fit shows simulation describe well the real data. The fraction obtained from this fit are used as Gaussian constraints for the extraction of the signal yield (*cf.* next section).

Signal fit

The signal yield is determined from a three–dimensional maximum likelihood binned fit to q^2 (8 bins), τ^+ lifetime t_τ (8 bins) and the anti-D_s BDT (6 bins). The PDF is a sum of 16 templates: 13 templates are obtained from simulation and 3 data-driven templates, the parameters are either free (4),

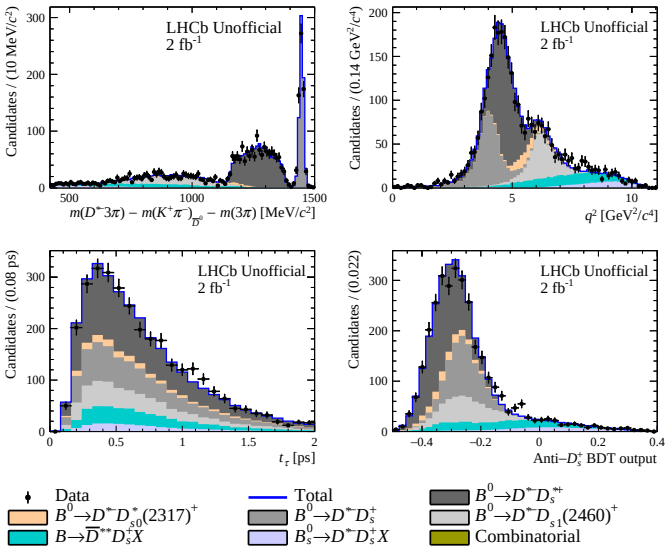

Figure 6: Data-fit projections of the $B \to D^{*-}\,D_s\,(X)$ components for the fit variable $m(D^{*-}3\pi^{\pm}) - m(K^-\pi^+)_{D^0} - m(3\pi^{\pm})$ and other variables q^2, t_τ and anti-D_s BDT output.

constrained (6) or fixed (6). The signal yield $N_{\rm sig}$ is blinded.

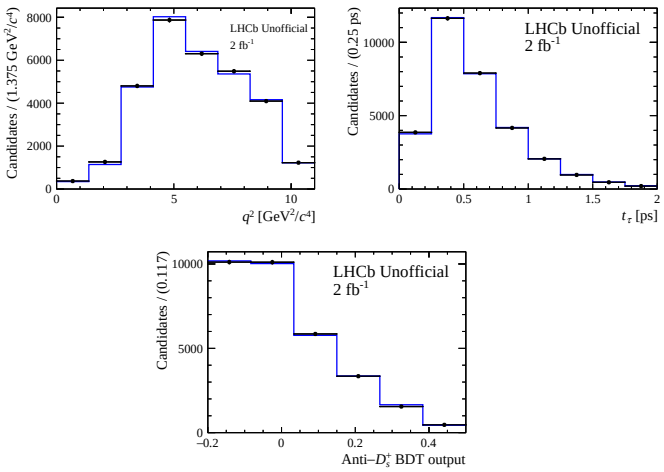

Figure 7: Signal fit projection on q2 (left), τ lifetime (middle) and the Anti-D_s BDT (right).

The projection on the three fitting variables are shown in fig. 7. We find a good agreement between the simulated samples and data.

From eq. (4), we have all the ingredients to determine $\mathcal{K}(D^*)$. However, the current analysis is still undergoing final steps of internal review at the LHCb collaboration, no results will be shown here.

Measurements of $R(D)$ and $R(D^*)$

As mentioned in the introduction, $R(D^*)$ ratios have been measured by three experiments. In fig. 8, we see the $R(D)$ and $R(D^*)$ results, the horizontal bands corresponds to $R(D^*)$ measurements and the combined measurements are shown in ellipses.

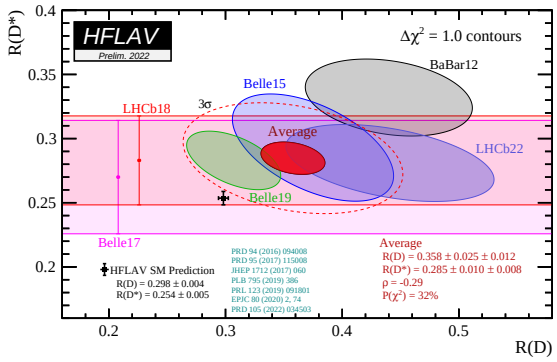

Figure 8: Summary of previous measurements of $R(D)$ and $R(D^*)$ [7].

The red ellipse correspond to the current world-average measured $R(D)$ and $R(D^*)$, which lies 3.2σ away from the Standard Model predictions.
In the literature, multiple theoretical scenarios could explain the lepton flavor violation: The Standard

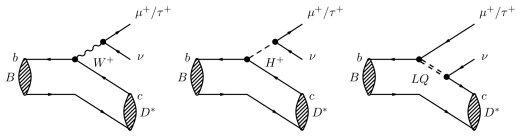

Figure 9: Beyond Standard model candidates to explain lepton flavor universality.

model contribution correspond to the left diagram, others possible candidates are the vector boson W' [8], the higgs-doublet model [9] (middle diagram) and leptoquark model [10, 11, 12] (right diagram) of fig. 9.

Conclusions

The Run 2 $R(D^*)_{\tau/\mu}$ hadronic analysis at LHCb is in the final stage of internal review. After couple of years of intense work, the collaborators arrived to build a solid understanding of the backgrounds.

The remaining tasks consist in including the full analysis of data collected during Run 1 (2011–2012) and Run 2 (2015–2018), to increase statistics and thus reduce systematic and statistical errors.

Multiple channels remains to explore. The $R(D)$ and $R(D^*)$ simultaneous measurement was done at LHCb [5] using the muonic channel. We still need to perform such measurements using the hadronic decay of the τ. It is worth to mention that some other analysis are planed like ratios $R(D^*)_{\tau/e}$ $R(D^*)_{\mu/e}$, B_s, B_c, J/Ψ, Λ_b ratios and, angular analysis that could characterise the type of new physics.

References

[1] BaBar collaboration, J. P. Lees et al., Evidence for an excess of $B^- \to D^{*0}\tau^-\nu_\tau$ decays, Phys. Rev. Lett. 109 (2012) 101802, arXiv:1205.5442.

[2] M. Huschle et al. Measurement of the branching ratio of $\mathcal{BR}(B \to D^*\tau^-\nu_\tau)$ relative to $\mathcal{BR}(B \to D^{(*)}\mu^-\nu_\mu)$ decays with hadronic tagging at Belle. Physical Review D, 92.7 (Oct. 2015). issn: 1550-2368. doi: 10.1103/physrevd.92.072014. url: http://dx.doi.org/10.1103/PhysRevD.92.072014

[3] The Belle Collaboration et al. Precise determination of the CKM matrix element $|V_{cb}|$ with $B^0 \to D^{*+}\ell^-\nu_\ell$ decays with hadronic tagging at Belle. 2017. arXiv: 1702.01521 [hep-ex]

[4] LHCb collaboration, R. Aaij et al., Measurement of the ratio of the $\mathcal{BR}(B^0 \to D^{(*-)}\tau^+\nu_\tau)$ and $\mathcal{BR}(B^0 \to D^{(*-)}\mu^+\nu_\mu)$ branching fractions using three-prong τ-lepton decays, Phys.Rev. Lett. 120 (2018) 171802, arXiv:1708.08856.

[5] LHCb collaboration, R. Aaij et al., TBD, LHCb-PAPER-2022-039, in preparation.

[6] Particle Data Group, R. L. Workman et al., Review of particle physics, Prog. Theor. Exp. Phys. 2022 (2022) 083C01.

[7] Averages of b-hadron, c-hadron, and τ-lepton properties as of 2021, Amhis, Y. and others, arXiv: 2206.0750 [hep-ex].

[8] S. Fajfer and N. Košnik. Vector leptoquark resolution of R_K and R_{D^*} puzzles. Physics Letters B, 755 (Apr. 2016), pp. 270-274. issn: 0370-2693. doi: 10.1016/ j.physletb.2016.02.018. url: http://dx.doi.org/10.1016/j.physletb. 2016.02.018

[9] Andreas Crivellin, Julian Heeck, and Peter Stoffer. Perturbed Lepton-Specific Two-Higgs-Doublet Model Facing Experimental Hints for Physics beyond the Standard Model. Physical Review Letters, 116.8 (Feb. 2016). issn: 1079-7114. doi: 10.1103/physrevlett.116.081801. url: http://dx.doi.org/10.1103/PhysRevLett.116.081801

[10] Andreas Crivellin, Dario Müller, and Toshihiko Ota. Simultaneous explanation of $R(D^*)$ and $b \to s\ell^+\ell^-$: the last scalar leptoquarks standing. Journal of High Energy Physics, 2017.9 (Sept. 2017). issn: 1029-8479. doi: 10.1007/jhep09(2017)040. url: http://dx.doi.org/10.1007/JHEP09(2017)040

[11] Admir Greljo, Gino Isidori, and David Marzocca. On the breaking of Lepton Flavor Universality in B decays. 2015. arXiv: 1506.01705 [hep-ph]

[12] Damir Bećirević et al. Leptoquark model to explain the B-physics anomalies, $R(K)$ and $R(D)$. Physical Review D, 94 (Aug. 2016). doi: 10.1103/PhysRevD.94.115021

Part VIII

Theoretical Physics

session chaired by Andreas GOUDELIS

Theoretical Physics Session Introduction

Andreas Goudelis

Laboratoire de Physique de Clermont (UMR 6533), CNRS/IN2P3, Univ. Clermont Auvergne, 4 Av. Blaise Pascal, F-63178 Aubière Cedex, France

Abstract — In this talk we briefly introduce two topics that will be discussed in more detail during the "Theoretical Physics" session: some elements of nuclear theory and extra dimensions. The aim is to present some useful notions in a pedagogical and accessible manner, focusing on some conceptual issues rather than on mathematical rigour.

Introduction

Theoretical physics is an extremely broad field. As such, it is not completely straightforward to define. There are, however, a few key elements that one can highlight and which permeate, to a lesser or a greater extent, the entire field of theoretical physics. The first one is *abstraction*: in theoretical physics we typically try to reduce complex real-world physical systems down to simpler, more tractable ones, and the physical laws that theorists formulate are typically deduced from (and intended to apply to) more than just one single physical phenomenon. Secondly, theoretical physics aims at establishing a *qualitative understanding* of the physical world surrounding us: we are not just interested in writing down equations and computing numbers, we are also interested in understanding what these equations mean and in developing some sort of intuition about them. Last but not least, theoretical physics also aims at developing a *quantitative description* of physical phenomena, by defining mathematical objects in order to describe the properties of physical systems and establishing relations among them.

In what follows I will try to briefly introduce two topics that will be discussed during today's session: first, I will introduce some notions which are useful for nuclear theory, mostly from the point of view of multi-body interactions. Secondly, I will briefly discuss and the concept of extra spacetime dimensions. Both of these fields are extremely active areas of research and, consequently, it is impossible to cover these topics in full detail. The focus will be on the introduction of some elements which will, hopefully, facilitate the speakers that follow.

Nuclear Theory

Microscopic, relativistic particles are described as excited states of fields, operator-valued functions of spacetime. The interactions between such fields can be encoded in a mathematical object called the *Lagrangian*. Consider, for example, a real scalar field ϕ described by a Lagrangian as

$$\mathcal{L} = (\partial_\mu \phi)(\partial^\mu \phi) - \frac{m^2}{2}\phi^2 + \frac{\lambda}{4!}\phi^4 \qquad (1)$$

where m is the mass of ϕ and λ is a dimensionless constant. The first two terms in the RHS of this equation correspond to the kinetic and the mass term for the ϕ field, respectively. The third term describes the way through which four fields interact with each other.

So how do we compute measurable quantities? In quantum physics observables are represented by operators. Quantities such as cross-sections, decay rates etc can be calculated as expectation values of such operators. The basic object that we (often, silently) employ when computing these expectation values is the so-called *path integral*. In particular, the expectation value of an operator $\mathcal{O}$ is

$$\langle \mathcal{O} \rangle \propto \int \mathcal{D}\phi \; e^{i \int d^4x \mathcal{L}[\phi]} \; \mathcal{O}[\phi] \qquad (2)$$

where $\mathcal{L}[\phi]$ (the Lagrangian) and $\mathcal{O}[\phi]$ are generalisations of ordinary functions (called *functionals*) and $\int \mathcal{D}\phi$ denotes integration over a functional space. The theory behind such expressions can be found in numerous excellent textbooks on quantum field theory, *e.g.* [1, 2]. In a nutshell, the path integral is an integral over all field configurations as well as all spacetime points.

Unfortunately, in the general case we do not actually know how to compute such objects. Assuming that the coupling λ in Eq.(1) is small, the usual solution that is adopted in particle physics involves separating the free from the interacting part in Eq.(2), calculate the free part (this is something that we do know how to do), Taylor-expand the exponential involving the interacting part[1] and end up with ordinary integrals that we do know how to compute.

However, in nuclear physics two major problems are encountered: first, the (equivalent of the) coupling λ is *not* small. Indeed, QCD in a hadronic environment is non-perturbative, since the strong coupling constant is

[1] This description is quite schematic. In reality, there are more rigorous methods from functional analysis that are employed.

large. Secondly, and contrary to particle physics where we are most often interested in the interaction cross-section of only two particles, nuclei are bound states of more than two objects, which implies that describing nuclei (and, even more so, nuclear collisions) requires solving a many-body problem. Unfortunately, the many-body problem in physics is another problem that we do not know how to tackle in full generality.

The first issue is typically addressed by choosing not to rely on QCD. Different potentials can be used in order to describe nuclei, some of which will be discussed during the talks that follow.

As for the second issue, fortunately, in the case of few-body systems there *do* exist methods in order to compute observables. In particular, as we will see in Pierre-Yves Duerinck's talk, there exist the so-called Fadeev equations which, in the case of a three-body system, read

$$\Phi = \Phi^0 + \begin{vmatrix} 0 & G_1 & G_1 \\ G_2 & 0 & G_2 \\ G_3 & G_3 & 0 \end{vmatrix} \Phi \tag{3}$$

where Φ is a vector representing the wavefunction of each component of the system, Φ^0 is a set of initial conditions and the G_i's describe the interactions of the components in pairs, and depend on the potential form that one chooses to describe the nucleus. These equations can be solved iteratively and allow one to recover the full solution of the Schrödinger equation. The application that we will see concerns the annihilation of an antiproton with a light nucleus.

As the number of nucleons increases, the situation becomes much more complicated. In particular, the traditional nuclear shell model, as successful as it might be in describing nuclear structure, is incapable of describing nuclear reactions due to the fact that it relies on an infinite well potential thus isolating the nucleus from its surroundings. As we will see in the talk by Jose Pablo Linares, this approximation fails especially for nuclei close to the proton or neutron drip lines where nuclei can become weakly bound or even unbound in the ground state. This shortcoming can be addressed by considering such nuclei as open quantum systems, a framework which further enables one to study nuclear reactions.

Theoretical nuclear physics allows us, often in conjunction with input from other fields of theoretical and/or experimental physics, to describe quantitatively systems as diverse as the reactions taking place in nuclear power plants, the way through which nuclei interact with human tissues during radiotherapy sessions, the structure and evolution of stellar objects and the evolution and abundance of light elements in the Universe. Moreover, from a more theoretical standpoint, as we said nuclei are multi-body quantum systems and studying them can have interesting implications for other physical systems as well. Given these elements, it becomes clear that nuclear theory is not just interesting, it is also practically useful for a large variety of applications.

Extra Dimensions

Our everyday experience suggests that we live in a world of 3+1 dimensions. However, both relativity and quantum mechanics have repeatedly shown us that our everyday experience need not be the end of the story. In this spirit, the idea that our world might be described by more than 3+1 spacetime dimensions dates (at least) back to the early 20th century with the works of Kaluza and Klein [3, 4, 5], who showed that by appropriately extending the number of spatial dimensions to 4, it is possible to obtain a unified description of General Relativity and Maxwell's equations.

But what would such a theory look like, from our usual $(3+1)$ - dimensional perspective? In order to understand this, let us consider a toy model involving a five - dimensional spacetime and a free scalar field ϕ which is allowed to propagate in all four spatial dimensions. The action of such a field reads

$$S[\phi] = \frac{1}{2}\int d^4x dy (\partial^A \phi \partial_A \phi - m^2\phi^2) \tag{4}$$

where $A = 1, \cdots, 5$. Further assume that the field ϕ is periodic along the fifth dimension, $\phi(y) = \phi(y + 2\pi R)$. Then, we can Fourrier-expand the scalar field as

$$\begin{aligned}\phi(x,y) = &\frac{1}{\sqrt{2\pi R}}\phi_0(x) \\ &+ \sum_{n=1}^{\infty}\frac{1}{\sqrt{\pi R}}\left[\phi_n(x)\cos\left(\frac{ny}{R}\right) + \hat{\phi}_n(x)\sin\left(\frac{ny}{R}\right)\right]\end{aligned} \tag{5}$$

where the modes $\phi_n(x)$, $\hat{\phi}_n(x)$ only depend on the (3+1)-dimensional spacetime coordinates. Then, if we plug this expression back in the action and integrate over the fifth dimension y, we obtain a four-dimensional effective action as

$$\begin{aligned}S[\phi] = &\sum_{n=0}^{\infty}\frac{1}{2}\int d^4x \left(\partial^\mu\phi_n\partial_\mu\phi_n - m_n^2\phi_n^2\right) \\ &+ \sum_{n=1}^{\infty}\frac{1}{2}\int d^4x \left(\partial^\mu\hat{\phi}_n\partial_\mu\hat{\phi}_n - m_n^2\hat{\phi}_n^2\right)\end{aligned} \tag{6}$$

This action describes an infinite set of particles of (increasing) mass $m^2 + n^2/R^2$. In other words, from a $(3+1)$ - dimensional perspective, the $(4+1)$ - dimensional scalar field of our example corresponds to an infinite *Kaluza-Klein tower of states* with appropriately increasing masses.

In practice, depending on the theory, different fields might be allowed to propagate in the entire $(4+N)$ - dimensional spacetime (the geometry of which also varies between models), or be confined to some subspace of it. The important thing to remember is that particles that are allowed to propagate in the extra dimensions will acquire a Kaluza-Klein tower of states, when viewed from a $(3+1)$ - dimensional perspective.

Extra dimensional theories are not just a theoretical curiosity: they can make numerous exciting phenomenological predictions *e.g.* for collider searches,

flavour physics experiments or cosmology. In the talk by Anna Chrysostomou, we will see that they can also predict interesting signatures for gravitational wave experiments.

Summary and conclusions

Theoretical physics is a very broad field and, each year, the topics covered during the Theoretical Physics session vary wildly. This is one of the factors that make this session interesting! One takeaway message from this talk is that even in its most abstract and speculative forms, theoretical physics is, above all, *physics*, *i.e.* it studies and tries to make sense out of the physical world.

Moreover, theoretical physics is *useful*: two of the most important discoveries of the 21st century, the Higgs boson and gravitational waves, started off long ago as theoretical predictions and motivated vast experimental campaigns in order to be, eventually, detected. Experimental physicists employ theoretical input on a regular basis, be it in the form of parton distribution functions in order to generate events for their analyses or using programs such as GEANT in order to model their detectors. And, as we will see during this session, nuclear theorists seek to model nuclear reactions that are studied by experimentalists, whereas cosmologists study models predicting signals that could be observed in current or future gravitational wave experiments. Experimentation and theory are as important for the development of physics. I hope you will enjoy the session!

References

[1] M. E. Peskin and D. V. Schroeder, "An Introduction to quantum field theory", Addison-Wesley

[2] M. Srednicki, "Quantum field theory", Cambridge University Press

[3] T. Kaluza, Sitzungsber. Preuss. Akad. Wiss. Berlin (Math. Phys.) **1921** (1921), 966-972, [arXiv:1803.08616 [physics.hist-ph]].

[4] O. Klein, Nature **118** (1926), 516

[5] O. Klein, Z. Phys. **37** (1926), 895-906

Nucleon-antinucleon annihilation from optical and coupled-channel models

Pierre-Yves Duerinck

Physique Nucléaire et Physique Quantique (CP 229), Université libre de Bruxelles (ULB), Brussels, 1050, Belgium - Institut Pluridisciplinaire Hubert Curien (IPHC), CNRS/IN2P3, Université de Strasbourg, Strasbourg, 67037, France

Abstract — In this work, the annihilation of an antiproton with a nucleon or with the deuteron is studied within the context of different models. For nucleon-antinucleon systems, the collision matrix is first computed with an optical potential to model the annihilation process. As an alternative approach, a coupled-channel potential is then considered, its parameters being adjusted to fit the results of the optical model. By solving the Faddeev equations for the deuteron-antiproton system, the complex scattering lengths and energies for the lowest hydrogenic states are computed with the optical model. Different nucleon-nucleon interactions are used for comparison.

Introduction

The development at CERN of the Extra Low Energy Antiproton ring (ELENA), providing low-energy antiproton beams, has revived the interest in physics of interactions between matter and antimatter and should enable the production of various exotic systems in which particles and antiparticles are bound together. These systems can constitute an efficient tool to determine the properties of antimatter. However, they can also be used to improve our knowledge of matter, which is the main motivation of the antiProton Unstable Matter Annihilation (PUMA) project [1]. This ambitious experimental project aims to study nucleus skin densities of short-lived nuclear isotopes, produced by the Isotope mass Separator On-Line (ISOLDE) facility at CERN, using low-energy antiprotons, transported from ELENA, as a probe. This is done in two steps, first by creating nucleus-antiproton bound systems, second by following the annihilation of the antiproton with either a neutron or a proton of the probed nucleus.

Low-energy antiprotons are expected to provide a quite unique sensitivity to the tail of the neutron and proton densities but a fully microscopic treatment of the antiproton-nucleus systems remains to be developed. In the present work, the nucleon-antinucleon interaction and the annihilation process are first discussed. The proton-antiproton collision is then studied by solving the coupled-channel Schrödinger equation with both an optical and a coupled-channel model. Finally, the deuteron-antiproton scattering is studied by solving the Faddeev equations [2]. The scattering lengths and energies are computed for several partial waves with different nucleon-nucleon (NN) interactions.

The $N\bar{N}$ interaction

Due to the complexity of the physics involved and the limited amount of experimental data, the interaction between nuclear matter and antimatter is not precisely known. Nevertheless, a qualitative picture of what will happen in the PUMA experiments is well known [1]. When a low-energy antiproton beam collides with an ion target, it does not necessarily annihilate directly. Instead, it can be captured in a highly excited Coulomb orbital to form an exotic atom or ion in a resonant state with a lifetime of the order of the nanosecond or even of the microsecond. This exotic atom or ion will decay via a cascade of X-ray and Auger electron emissions before its annihilation with a nucleon of the nucleus. The annihilation is followed by an emission of mesons, mostly pions, sharing the charge and momentum of the annihilated particles. The reconstruction of the total charge of the emitted mesons allows the experimental determination of the type of the nucleon (proton or neutron) which was annihilated with the antiproton.

The first step towards the description of the antiproton-nucleus annihilation is the establishment of the nucleon-antinucleon ($N\bar{N}$) interaction model. The $N\bar{N}$ interaction should describe not only the attractive/repulsive features between the two particles but also account for the annihilation. This annihilation is a complicated process involving complex dynamics and containing a multitude of meson-producing channels such as $N\bar{N} \to \pi\bar{\pi}, \rho\bar{\rho}, K\bar{K}, \pi\bar{\pi}\pi\bar{\pi}$. Given the large number of possibilities for the annihilation, the meson channels are in practice treated using phenomenological models. Since the PUMA project is based on the detection of annihilation products, it is of paramount importance to test the model-dependence of the scattering observables. For this reason, two models are considered for this study: the optical model and the

coupled-channel model. These are hereafter developed and applied to the description of the $p\bar{p}$ system.

Optical model

In the optical model framework, the $N\bar{N}$ potential $V_{N\bar{N}}$ is a complex quantity:

$$V_{N\bar{N}} = U_{N\bar{N}} + i\,W. \tag{1}$$

Within the meson exchange theory, the real part of the potential is related to the NN interaction via G-parity transform. Its imaginary part induces a loss of probability current in the $p\bar{p}$ channel, which simulates the effect of all annihilation channels. The charge exchange channel $p\bar{p} \to n\bar{n}$ is here explicitly included. In the present work, the Kohno-Weise potential [3] is considered: the imaginary part W is a Woods-Saxon potential whose parameters are adjusted to fit the experimental $p\bar{p} \to p\bar{p}$ and $p\bar{p} \to n\bar{n}$ cross sections. The $p\bar{p}$ system is studied by solving the multi-channel Schrödinger equation:

$$(E - H_0 - V)\begin{pmatrix} u_{p\bar{p}} \\ u_{n\bar{n}} \end{pmatrix} = 0, \tag{2}$$

where u_c is the radial wavefunction of channel c, H_0 is the kinetic energy (diagonal matrix) and V is given by

$$V = \begin{pmatrix} V_{p\bar{p}} & V_{\rm ce} \\ V_{\rm ce} & V_{n\bar{n}} \end{pmatrix}, \tag{3}$$

where $V_{\rm ce}$ is the charge exchange potential.

While the optical model is able to reproduce the experimental cross sections, it suffers from several drawbacks. The phenomenological term eliminates a part of the $N\bar{N}$ current, which baldly suppresses a part of the wavefunction. Due to this loss of flux, the collision matrix is not unitary. This may introduce non-physical properties for the description of bound states [4].

Coupled-channel model

In order to analyse the model-dependence of the scattering observables on the $N\bar{N}$ input, an alternative annihilation model is considered: the coupled-channel model [4]. In this case, the annihilation is simulated by the addition of effective meson-antimeson ($m\bar{m}$) channels coupled to $p\bar{p}$ and $n\bar{n}$ ones by short-range Yukawa potentials. One $m\bar{m}$ channel is added for each isospin component, i.e. one is related to the $p\bar{p}$ annihilation and another one to the $n\bar{n}$ annihilation. Within this framework, the $p\bar{p}$ system is described by solving the following coupled-channel Schrödinger equation

$$(E - H_0 - V)\begin{pmatrix} u_{m_1\bar{m}_1} \\ u_{m_2\bar{m}_2} \\ u_{p\bar{p}} \\ u_{n\bar{n}} \end{pmatrix} = 0, \tag{4}$$

where the potential matrix reads

$$V = \begin{pmatrix} 2\Delta_{mp} & 0 & V^{(a)}_{p\bar{p}} & V^{(a)}_{\rm ce} \\ 0 & 2\Delta_{mp} & V^{(a)}_{\rm ce} & V^{(a)}_{n\bar{n}} \\ V^{(a)}_{p\bar{p}} & V^{(a)}_{\rm ce} & V_{p\bar{p}} & V_{\rm ce} \\ V^{(a)}_{\rm ce} & V^{(a)}_{n\bar{n}} & V_{\rm ce} & V_{n\bar{n}} \end{pmatrix}. \tag{5}$$

For the simplicity of the model, the $m\bar{m}$ interaction is set to zero. The $N\bar{N}$ interaction is obtained via G-parity transform of the Brian and Phillips potential [5] and is smoothly extrapolated with a polynomial function close to the origin ($r < r_c$) to avoid singularities due to spin-orbit and tensor terms.

The annihilation potentials $V^{(a)}_{N\bar{N}}$ and $V^{(a)}_{\rm ce}$ are written as

$$V^{(a)}_{N\bar{N}}(r) = \frac{\hbar}{2}\,(\lambda_0 + \lambda_1)\,r^{-1}e^{-\frac{r}{r_a}}, \tag{6}$$

$$V^{(a)}_{\rm ce}(r) = \frac{\hbar}{2}\,(\lambda_0 - \lambda_1)\,r^{-1}e^{-\frac{r}{r_a}}, \tag{7}$$

where λ_0 and λ_1 denotes the amplitudes of the annihilation potential for the isospin components $T = 0$ and $T = 1$ respectively. The parameters of the coupled-channel potential are here adjusted to fit the low-energy collision matrix obtained with the optical model from S- to G-waves. Figures 1 and 2 show the real and imaginary part of the $p\bar{p}$ S-matrix elements for the $^1S_0$ and $^3P_1$ partial waves.

Despite the fact that this approach remains phenomenological, it provides a more realistic description of the annihilation process and includes very different dynamics in comparison to the optical model. Unlike the optical model for which the annihilation flux is lost, the presence of coupled channel involves nucleon-antinucleon re-emission possibilities. Moreover, since the potential is real, the full collision matrix remains unitary.

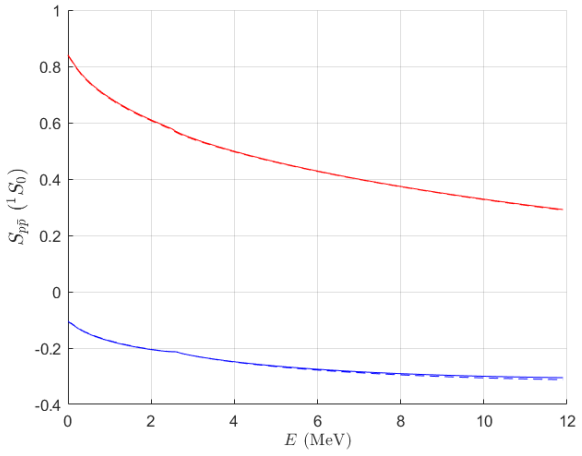

Figure 1: Real (red) and imaginary part (blue) of $S_{p\bar{p}}$ computed with the optical model (dotted line) and the coupled-channel model (solid line) for the partial wave $^1S_0$. Dotted and full lines overlap with each other and are almost indiscernible.

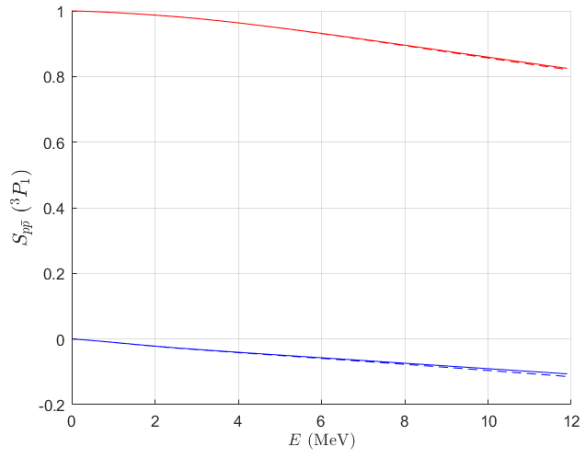

Figure 2: Real (red) and imaginary part (blue) of $S_{p\bar{p}}$ computed with the optical model (dotted line) and the coupled-channel model (solid line) for the partial wave $^3P_1$. Dotted and full lines overlap with each other and are almost indiscernible.

The three-body problem

Having at disposition $N\bar{N}$ potentials which approximately provide the same collision matrix, the dynamical effects and the model-dependence on the $N\bar{N}$ input are investigated by studying the deuteron-antiproton ($d\bar{p}$) annihilation. The $d\bar{p}$ system is considered as a system of three particles (n, p, $\bar{p}$) interacting via two-body interactions. The low-energy scattering properties of the $d\bar{p}$ are computed by solving the Faddeev equations in configuration space.

Faddeev equations

Let us consider a system of three particles with masses m_1, m_2, and m_3 and located at positions $\mathbf{r}_1$, $\mathbf{r}_2$, $\mathbf{r}_3$. The scattering wavefunction is solution of the three-body Schrödinger equation

$$(E - H_0 - V_{12} - V_{13} - V_{23})\Psi = 0, \tag{8}$$

with the appropriate boundary condition. H_0 is now the three-body kinetic energy operator and V_{ij} denotes the potential between particle i and j. To solve the Schrödinger equation, it is convenient to describe the system in terms of Jacobi coordinates defined as

$$\mathbf{x}_i = \sqrt{\frac{2\,m_j\,m_k}{(m_j+m_k)\,m_0}}\,(\mathbf{r}_k - \mathbf{r}_j)\,, \tag{9}$$

$$\mathbf{y}_i = \sqrt{\frac{2\,m_i\,(m_j+m_k)}{(m_i+m_j+m_k)\,m_0}}\left(\mathbf{r}_i - \frac{m_j\mathbf{r}_j + m_k\mathbf{r}_k}{m_j+m_k}\right), \tag{10}$$

where m_0 is a reference mass chosen for the coherence of the units. As shown in Figure 3, by considering cyclic permutations of the particle indices (i, j, k), three sets of Jacobi coordinates can be defined.

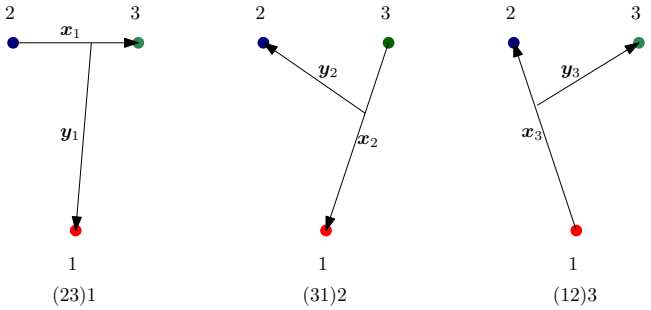

Figure 3: Jacobi coordinates for a three-body system.

The basic idea of the Faddeev formalism is to decompose the wavefunction as the sum of three contributions called Faddeev components, each of them being associated with a set of Jacobi coordinates, i.e. a partition of the system:

$$\Psi = \Psi_1(\mathbf{x}_1, \mathbf{y}_1) + \Psi_2(\mathbf{x}_2, \mathbf{y}_2) + \Psi_3(\mathbf{x}_3, \mathbf{y}_3). \tag{11}$$

The Faddeev components are solutions of the Faddeev equations:[2]

$$(E - H_0 - V_{23})\Psi_1 = V_{23}\,(\Psi_2 + \Psi_3)\,, \tag{12}$$
$$(E - H_0 - V_{13})\Psi_2 = V_{13}\,(\Psi_3 + \Psi_1)\,, \tag{13}$$
$$(E - H_0 - V_{12})\Psi_3 = V_{12}\,(\Psi_2 + \Psi_1)\,. \tag{14}$$

Since the Faddeev components are asymptotically decoupled, independent boundary conditions can be imposed for each component. The resolution of the Faddeev equations is carried out by considering a partial wave expansion of each component as

$$\Psi_i(\mathbf{x}_i, \mathbf{y}_i) = \sum_n \frac{\phi_n^{(i)}(x_i, y_i)}{x_i y_i}\,\mathcal{Y}_n(\hat{x}_i, \hat{y}_i), \tag{15}$$

where $\mathcal{Y}_n$ is a generalised bispherical harmonics including orbital and spin couplings. The index n includes the different orbital and spin quantum numbers (l_x, l_y, L, s_x, S) required to define a Faddeev amplitude characterised by the total angular momentum J and the parity π.

The radial wavefunctions $\phi_n^{(i)}(x_i, y_i)$ are computed by expanding them as a linear combination of Lagrange-Laguerre functions [6] with

$$\phi_n^{(i)}(x_i, y_i) = \sum_{\alpha,\beta} c_{n\alpha\beta}^{(i)}\,\hat{f}_\alpha\left(\frac{x_i}{h_x}\right)\,\hat{f}_\beta\left(\frac{y_i}{h_y}\right), \tag{16}$$

where h_x and h_y are scaling parameters. The calculation of the scattering wavefunction is then reduced to computation of the coefficients $c_{n\alpha\beta}^{(i)}$ via the resolution of an inhomogeneous linear system.

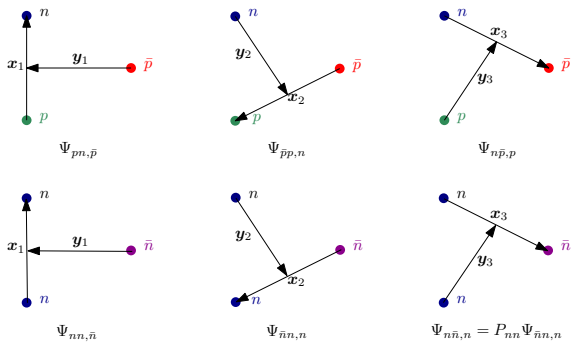

Figure 4: Faddeev components for the $d\bar{p}$ system (optical model). The operator P_{nn} performs cyclic permutations and is used to account for the symmetry between the components $\Psi_{\bar{n}n,n}$ and $\Psi_{n\bar{n},n}$ under the exchange of two neutrons.

The $d\bar{p}$ annihilation (optical model)

The study of the $d\bar{p}$ system requires an extension of this formalism to account for the coupling between the channels involved in the annihilation process. In the present work, the $d\bar{p}$ annihilation is studied in the optical model framework. Different kinds of Faddeev components are therefore defined, including the permutation of the different particles : $(p, \bar{p}, n)$ and $(n, \bar{n}, n)$. These components are illustrated on Figure 4. The number of equations can be reduced from six to five by exploiting the symmetry under the exchange of the neutrons in the components $\Psi_{\bar{n}n,n}$ and $\Psi_{n\bar{n},n}$. The Faddeev equations then read

$$(E - H_0 - V_{np})\Psi_{np,\bar{p}} = V_{np}\left(\Psi_{p\bar{p},n} + \Psi_{\bar{p}n,p}\right), \quad (17)$$

$$(E - H_0 - V_{nn})\Psi_{nn,\bar{n}} = V_{nn}\left(1 + P_{nn}\right)\Psi_{n\bar{n},n}, \quad (18)$$

$$(E - H_0 - V_{p\bar{p}})\Psi_{p\bar{p},n} = V_{p\bar{p}}\left(\Psi_{np,\bar{p}} + \Psi_{\bar{p}n,p}\right) + V_{\text{ce}}\left[\Psi_{nn,\bar{n}} + (1 + P_{nn})\Psi_{n\bar{n},n}\right], \quad (19)$$

$$(E - H_0 - V_{n\bar{n}})\Psi_{n\bar{n},n} = V_{n\bar{n}}\left(\Psi_{nn,\bar{n}} + P_{nn}\Psi_{n\bar{n},n}\right) + V_{\text{ce}}\left(\Psi_{np,\bar{p}} + \Psi_{p\bar{p},n} + \Psi_{\bar{p}n,p}\right), \quad (20)$$

$$(E - H_0 - V_{n\bar{p}})\Psi_{\bar{p}n,p} = V_{n\bar{p}}\left(\Psi_{np,\bar{p}} + \Psi_{p\bar{p},n}\right), \quad (21)$$

where P_{nn} is the cyclic permutation operator. By considering the appropriate asymptotic behaviour for the $\Psi_{np,\bar{p}}$ component, the scattering wavefunction and the scattering length have been computed for different partial waves. The results are shown in Table 1. Different models are considered for the nucleon-nucleon interaction: the Malfliet-Tjon potential which is central and the realistic Argonne V18 potential [9]. Table 1 also contains the complex energy shift ΔE corresponding to the energy difference between the $d\bar{p}$ Rydberg state and the $d\bar{p}$ quasi-bound system. This shift is computed from the scattering length with the Trueman relation [11]. These results stand as an updated version of Ref. [10] (Table 5) in which an error was detected. Table 1 shows a very small dependence on the nucleon-nucleon models, especially for S-waves. This indicates that the deuteron-antiproton system is dominated by the $N\bar{N}$ interaction and the strong imaginary part of the potential related to the annihilation process.

MT-I-III+KW

	a_0 (fm)	ΔE (keV)
$^2S_{1/2}$	$1.34 - 0.72\,\text{i}$	$1.92 - 0.89\,\text{i}$
$^4S_{3/2}$	$1.40 - 0.72\,\text{i}$	$1.99 - 0.88\,\text{i}$
	a_1 (fm^3)	ΔE (meV)
$^4P_{5/2}$	$0.75 - 2.68\,\text{i}$	$58.1 - 208\,\text{i}$

AV18+KW

	a_0 (fm)	ΔE (keV)
$^2S_{1/2}$	$1.34 - 0.72\,\text{i}$	$1.92 - 0.89\,\text{i}$
$^4S_{3/2}$	$1.39 - 0.72\,\text{i}$	$1.98 - 0.89\,\text{i}$
	a_1 (fm^3)	ΔE (meV)
$^4P_{5/2}$	$0.71 - 2.60\,\text{i}$	$54.8 - 202\,\text{i}$

Table 1: The $d\bar{p}$ scattering lengths and complex energy shifts obtained with the Kohno-Weise potential for different partial waves and NN interactions.

Conclusion and prospects

The aim of this work is to contribute to the theoretical understanding of the antiproton-nucleus systems that will be studied in the PUMA experiments. For this purpose, the two- and three-body Schödinger equations have been solved exactly (in the numerical sense) with realistic NN and $N\bar{N}$ interactions.

As an alternative approach to the traditional optical models, a coupled-channel potential has been developed, which to reproduces the results of the Kohno-Weise potential for low-energy $N\bar{N}$ observables.

Finally, the deuteron-antiproton scattering has been studied by computing the scattering length within the optical model framework. The main prospect is to carry out similar calculations with the coupled-channel model to investigated the model-dependence relative to the $N\bar{N}$ input. These calculations are however more involved, first due to the presence of additional channels, and second due to the three-body breakup in the meson channels. For this reason, the Faddeev equations will be solved in conjunction with the complex scaling method [12].

Acknowledgements

I would like to thank my PhD supervisors Jérémy Dohet-Eraly and Rimantas Lazauskas for their support and helpful remarks.

This work has received funding from the F.R.S.-FNRS under Grant Nos. 4.45.10.08. The author is a Research Fellow at F.R.S.-FNRS.

References

[1] T. Aumann, W. Bartmann, O. Boine-Frankenheim, A. Bouvard, A. Broche, *et al.* *The European Physical Journal A* **58** (2022) 88

[2] R. Lazauskas. *Few-body Systems* **54** (2012) 717

[3] M. Kohno and W. Weise. *Nuclear Physics A* **454** (1986) 429

[4] E. Ydrefors and J. Carbonell. *The European Physical Journal A* **57** (2021) 303

[5] R. A. Bryan and R. J. N. Phillips. *Nuclear Physics B* **5** (1968) 201

[6] D. Baye. *Physics Reports* **565** (2015) 1

[7] J. Carbonell, J.-M. Richard and S. Wycech. *Zeitschrift für Physik A* **343** (1992) 325

[8] R. A. Malfliet and J. A. Tjon. *Nuclear Physics A* **127** (1969) 161

[9] S. Veerasamy and W. N. Polyzou. *Physical Review C* **84** (2011) 034003

[10] R. Lazauskas and J. Carbonell. *Physics Letters B* **820** (2021) 136573

[11] T. L. Trueman. *Nuclear Physics* **26** (1961) 57

[12] R. Lazauskas. *Few-body Systems* **54** (2013) 967

Nuclear physics at the edge of stability

José Pablo Linares Fernández

Grand Accélérateur National d'Ions Lourds (GANIL), CEA/DSM - CNRS/IN2P3, BP 55027, F-14076 Caen Cedex, France

Abstract — Loosely bound nuclei are currently at the center of interest in low-energy nuclear physics. The deeper understanding of their properties provided by the shell model for open quantum systems changes the comprehension of many phenomena and offers new horizons for spectroscopic studies from the driplines to the well-bounded nuclei for states in the vicinity and above the first particle emission threshold. In this paper, we outline the open quantum system description of nuclear states and reactions based in the Gamow shell model theory which provides a comprehensive description of bound states, resonances and scattering many-body states in a single theoretical framework.

Introduction

Since its introduction by Meyer [1] and Jensen [2], the Shell Model (SM) has treated the nucleus as a closed quantum system where nucleons exists 'within their own universe', ignoring the environment around them. However, this approximation is at its best in the valley of stability of the nuclear chart. Close to the drip lines, the nuclei find themselves either loosely bound or even unbound. This means that we can no longer ignore the environment in which they reside. This calls for an open quantum system treatment of the atomic nucleus. An advantage of this approach is that nuclear structure and reactions, which have been traditionally studied separately, should come together in a unifying framework.

Resonances have always presented a major theoretical challenge. They are intrinsic properties of quantum systems that are associated with their natural frequencies and describe the decay of unbound systems. Experimentally, they appear as peaks and/or interference patterns in the cross-section. Both of these phenomena can be characterized by an energy and a width associated to a particular state of a nucleus. However, due to the unitarity condition in Hilbert space, one cannot properly define a resonant state, also known as a Gamow [3] or Siegert [4] state, within standard quantum mechanics. This issue can be solved by redefining quantum mechanics in the so-called rigged Hilbert space (RHS) [5, 6].

The properties of radioactive nuclei are also strongly affected by couplings to many-body continuum of scattering states and reaction channels. This calls for a unified theory which would involve a comprehensive description of bound states, resonances and scattering many-body states within a single theoretical framework. An attempt in this direction was done within the continuum shell model [7, 8, 9, 10], and has been extended to *ab initio* description of structure and reactions of light nuclei within the no-core shell model coupled with the resonating-group method [11] and the no-core shell model with continuum [12].

An alternative approach within a unifying framework has been proposed with the open quantum system formulation of the shell model, the Gamow Shell Model (GSM) [13, 14, 15]. GSM offers the most general treatment of couplings between discrete and scattering states, using Slater determinants defined in the Berggren ensemble of single-particle states. For the description of scattering cross-sections and reactions, GSM should be formulated in the representation of reaction channels (GSM-CC) [16].

Theoretical Framework

In this section, we will outline the formalism of Gamow Shell Model including also its formulation in coupled channel representation. First, we will introduce the single-particle Berggren basis. We will follow with its extension to the many-body problem as the GSM in the Slater determinant formulation. Finally, we will finish with the formulation of GSM in coupled-channels.

The Berggren basis

The skeleton of the SM is provided by single-particle eigenstates. Each state is labelled by several quantum numbers like angular momentum and parity. In the 60s, Newton derived the completeness relation in Hilbert space [17]. This completeness relation goes as follows:

$$\sum_n u_{\ell,n}(r)\tilde{u}^*_{\ell,n}(r') + \int_0^\infty dk\, u_\ell(k,r)\tilde{u}^*_\ell(k,r') = \delta(r-r'), \tag{1}$$

where $u_{\ell,n}(r)$ are bound states with positive imaginary momentum k and $u_\ell(k,r)$ scattering states with real momentum. Even though in principle it is possible to use the Newton completeness relation (1) to describe certain resonance phenomena, however its ap-

plication would be impossible in practical applications as it would require a very fine discretization of the integral [15]. Berggren improved upon this by instead taking a deformed contour in k-plane that would embed narrow resonances, i.e. the poles in the second Riemann sheet of the S-matrix [18] as can be seen in Fig. 1. The Berggren completeness relation reads:

$$\sum_n u_{\ell,n}(r)\tilde{u}^*_{\ell,n}(r') + \int_{L^+} dk\, u_\ell(k,r)\tilde{u}^*_\ell(k,r') = \delta(r-r'). \tag{2}$$

The difference with the Newton completeness relation is two-fold. First of all the sum contains not only bound states but also narrow resonances. Second, the contour integral over non-resonant scattering states is deformed into the fourth quadrant of the complex k-plane. This allows for the simultaneous treatment of bound, resonant and non-resonant scattering states.

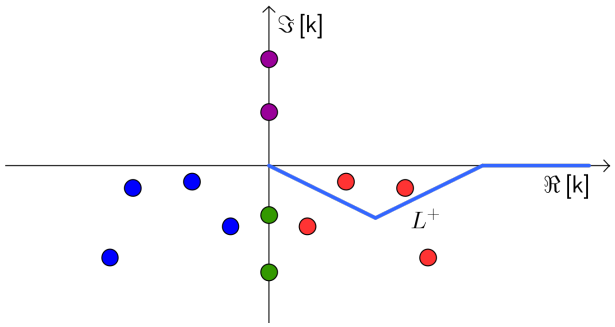

Figure 1: Representation of the complex k-plane. Positions of S-matrix poles corresponding to bound states, antibound states, decaying resonances and capturing resonances are shown in magenta, green, blue and red, respectively. The integration path of the Berggren completeness relation L^+ is also shown in the figure. The contour is chosen so that all important narrow resonances are contained within the contour.

The tilde in Eq. (1) and (2) corresponds to time reversal. Indeed, differently from standard quantum mechanics where the inner product takes the form $\langle u_f|u_i\rangle = \int dr\, u^*_f(r)u_i(r)$, the inner product is not the standard one. This requires a reformulation of quantum mechanics in RHS [5, 6, 19]. In the theory of RHS the inner product changes and all observables of unbound states are complex. Divergent integrals that appear in the calculations for resonant and scattering states have to be regularized. One method of regularization has been proposed by Zel'dovich [18, 20]. This method consisted in adding an exponential factor with a limit

$$\text{Reg} \int_0^\infty dr\, u_f(r)\hat{\mathcal{O}}(r)u_i(r) = \lim_{\epsilon\to 0}\int_0^\infty dr\, e^{-\epsilon r^2} u_f(r)\hat{\mathcal{O}}(r)u_i(r), \tag{3}$$

where $\hat{\mathcal{O}}$ is an arbitrary operator. This method though formally correct, in not usefull in practical applications as the convergence requires very large computational resources to obtain stable results. This is improved with a technique called complex rotation [21]. This method relies on the wave functions being regular in the first quadrant of the complex plane. Based on the Cauchy Theorem using the integration path shown in Fig. 2, this allows for a substitution $r \to R + \rho e^{i\theta}$ where θ is an angle that is chosen to ensure convergence [22]. In this way, we are able to construct numerically a Berggren basis of normalized single-particle eigenstates.

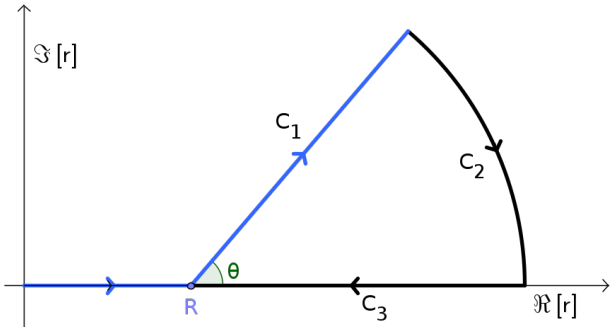

Figure 2: The path of integration in the complex plane corresponding to the complex rotation technique at a point R with an angle θ. R is large compared to the nuclear radius which means that the nuclear potential is negligible for $r > R$.

As any other completeness relation, the Berggren completeness relation can be used to expand other vectors. One typical application consist of expanding high energy, unbound single-particle states in a more stable basis generated by a binding potential [22]. Such an expansion of a one-body state u_{WS} in a basis generated by another potential $\{u_B\}$ is:

$$u_{WS}(r) = \sum_i c_{k_i} u_B(k_i,r) + \int_{L^+} dk\, c(k) u_B(k,r), \tag{4}$$

where, due to the basis being normalized, the overlap amplitudes follow the condition

$$\sum_i c^2_{k_i} + \int_{L^+} dk\, c^2(k) = 1. \tag{5}$$

For certain applications it is useful to use the well known properties of a harmonic oscillator state. For example, one can expand matrix elements in Berggren basis using the harmonic oscillator basis. This is particularly useful when calculating two-body matrix elements. Usually, one can go from relative to laboratory coordinates using a Talmi-Brody-Moshinsky [23, 24] transformation. This transformation is straightforward in the harmonic oscillator basis, however it is computationally demanding in any other basis. This has been solved by expanding the two-body matrix elements with a harmonic oscillator basis truncated to $N_{\max}$

$$\langle ab|\hat{V}|cd\rangle = \sum_{\alpha\beta\gamma\delta}^{N_{\max}} \langle\alpha\beta|\hat{V}|\gamma\delta\rangle \langle a|\alpha\rangle \langle b|\beta\rangle \langle c|\delta\rangle \langle d|\delta\rangle\,, \tag{6}$$

where the latin letters correspond to the Berggren basis, the greek letter to the harmonic oscillator basis and $\hat{V}$ is a generic interaction [25]. This method is not limited to the Hamiltonian matrix elements but can also

be conveniently used for the computation of electromagnetic operators.

Gamow Shell Model

The Gamow Shell Model is the generalization of the nuclear shell model in Berggren basis. Analogously to the standard SM, the many-body antisymmetric states are built with Slater determinants of single-particle basis states. The choice of the single-particle basis is the Berggren basis, however an approximation has to be made in the completeness relation. The infinite number of scattering states are approximated by the discretization of the integral in the completeness relation in Eq. (2):

$$\int_{L^+} u_\ell(k,r)\tilde{u}^*_\ell(k,r') \approx \sum_i^{N_d} u_{\ell,i}(r)\tilde{u}^*_{\ell,i}(r'), \qquad (7)$$

where we discretize the contour L^+ with a Gauss-Legendre quadrature for a number N_d of points with momentum $k_i \in L^+$ each [22]. This leaves us with a discrete Berggren basis $\{u_\ell\}$ that leads to the many-body completeness relation

$$\sum_n |\mathrm{SD}_n\rangle \langle\widetilde{\mathrm{SD}}_n| \approx 1 \quad |\mathrm{SD}\rangle = |u_{\ell_1 1} u_{\ell_2 2} ... u_{\ell_M M}\rangle\,. \quad (8)$$

The precision of this relation depends on the achieved precision of the discretized completenes relation (7). Also, the tilde keeps its meaning of time reversal.

An identification of resonances in GSM requires a special procedure. Even though there exists a Lanczos method for complex matrices, it cannot be used in GSM because the Lanczos algorithm yields the lowest energy eigenvalues. Hence, why it is so useful in the traditional SM. However, in GSM, we not only have bound and resonant states but also scattering states that are eigenvectors of the Hamiltonian. This means that resonances are embedded in a discretized continuum of scattering states and the scattering states may have lower energy than the resonance. One way to overcome this difficulty is by doing several calculations with different contours. The non-physical eigenvalues are going to move in the k complex plane, whereas physical resonances will be stationary.

This is not very practical so a different approach, the so-called overlap method, was developed. This method consist of doing a full diagonalization with an incomplete basis including only poles of the S-matrix (bound and resonance states) to extract a pivot $|\Psi_0\rangle$. Afterwards, one finds the many-body state $|\Psi\rangle$ with the full Berggren basis that optimizes the overlap $|\langle\Psi_0|\Psi\rangle|$ [22].

In a SM calculation, one removes the center-of-mass excitations using the Lawson method [26]. This method cannot be applied in the GSM [15]. One option is to use Jacobi coordinates, but its application is numerically demanding.

In most applications GSM is solved in the core + valence particle approximation. To deal with the problem, we transform the Hamiltonian from the laboratory coordinates to the relative cluster orbital shell model (COSM) coordinates [27]. The COSM coordinates are defined as

$$\mathbf{r}_i = \mathbf{r}_{i,\mathrm{lab}} - \mathbf{R}_{\mathrm{CM,core}} \ \text{ if } i \in \text{ val}, \qquad (9)$$

$$\mathbf{r}_i = \mathbf{r}_{i,\mathrm{lab}} \ \text{ if } i \in \text{ core}, \qquad (10)$$

where $\mathbf{r}_{i,\mathrm{lab}}$ is the coordinate of a nucleon in laboratory coordinates and $\mathbf{R}_{\mathrm{CM,core}}$ is the coordinate in laboratory of the center-of-mass of the core. This is interpreted as defining the coordinates of valence particles relative to the center-of-mass of the core. In particular, this is a translationaly invariant framework.

Phenomena that have been studied with GSM include among others: study of near-threshold spectroscopic properties in light nuclei associated with the presence of particle emission thresholds [28]; studies of the influence of antibound states, particularly related to halo nuclei like ^{6}He [29]; and studies of the Thomas-Ehrman shift in light nuclei [30].

Coupled Channel Formulation

In GSM, which is formulated in the Slater determinant representation, one cannot define reaction channels as the many-body scattering eigenstates are generally a linear combination of many channels. In order to do calculations of cross-sections and phase-shifts, one has to formulate the GSM in the representation of coupled channels. In GSM-CC, this allows the definition of entrance and exit channels with correct asymptotics and hence, calculate the reaction observables. In this representation, we can also calculate spectroscopic observables. This yields a unified theory of nuclear structure and nuclear reactions, which have traditionally been developed separately. In this way, we can use spectroscopical information to improve the reaction cross-sections calculations and vice-versa.

We begin with the definition of the channel wave functions

$$|c,r\rangle = \mathcal{A}\left\{|\Psi^{J_T}_T\rangle \otimes |\Psi^{J_P}_P\rangle\right\}^{J_A}_{M_A}, \qquad (11)$$

where the indices T and P refer to *target* and *projectile*, respectively. The quantum number $c \to \{Z-z, N-n, J_T; z, n, \ell, J_{\mathrm{int}}, J_P\}$ includes the quantum numbers of both target and projectile which are proton number, neutron number, and spin. In particular ℓ is the angular momentum of the projectile and J_{int} is the intrinsic spin of the projectile. The spins are coupled as $\boldsymbol{\ell}+\mathbf{J}_{\mathrm{int}} = \mathbf{J_P}$ and $\mathbf{J_T} + \mathbf{J_P} = \mathbf{J_A}$. Expanding the solution of an Hamiltonian for a particular nucleus with A nucleons one obtains:

$$|\Psi\rangle^{J_A}_{M_A} = \sum_c \int_0^\infty \frac{u_c(r)}{r}\,|c,r\rangle\; r^2 dr, \qquad (12)$$

where u_c is the radial amplitude that describes the relative motion of the projectile respect to the core with a total angular momentum J_A. With this expansion,

the Schrödinger equation can be written as

$$\sum_c \int_0^\infty \left[H_{cc'}(r,r') - E\, N_{cc'}(r,r')\right] \frac{u_c(r)}{r}\, r^2 dr = 0 \tag{13}$$

where $H_{cc'}(r,r') = \langle r,c|H|r'.c'\rangle$ and $N_{cc'}(r,r') = \langle r,c|r',c'\rangle$ are the interaction matrix elements and the overlap functions, respectively. Eq. (13) is called Hill-Wheeler equation. The channel states $|c,r\rangle$ are expanded in a one-body Berggren basis $|c,n\rangle$ to calculate the kernels $H_{cc'}(r,r')$ and $N_{cc'}(r,r')$. The many-body matrix elements $N_{cc'}$ are computed using the Slater determinant expansion of the cluster wave functions $|c,n\rangle$.

Eq. (13) is a non-standard eigenvalue problem which is solved by transforming it into a standard one. One starts by rewriting it in matrix form as

$$\mathcal{H}\mathcal{U} = \mathcal{E}\mathcal{N}\mathcal{U}. \tag{14}$$

By defining the following: $\mathcal{W} = \mathcal{N}^{1/2}\mathcal{U}$ and $\mathcal{H}_m = \mathcal{N}^{-1/2}\mathcal{H}\mathcal{N}^{-1/2}$, where $\mathcal{W}$ is a vector containing the orthogonal channel wave-function and $\mathcal{H}_m$ is the modified Hamiltonian [16], Eq. (14) becomes:

$$\mathcal{H}_m\mathcal{W} = \mathcal{E}\mathcal{W}. \tag{15}$$

After solving Eq (15) one obtains the physical channel wave functions:

$$u_c(r) = w_c(r) + \sum_{c'} r'^2 [\mathcal{D}]_{cc'}(r,r') \frac{w_{c'}(r')}{r'}\, dr', \tag{16}$$

where w_c are the orthogonal channel wave functions and $\mathcal{D} = \mathcal{N}^{1/2}[\mathcal{N}-1]\mathcal{N}^{1/2}$.

Once the kernels are calculated, the Hill-Wheeler equation (13) is solved using a numerical method based on a Berggren basis expansion of the Green's function $(H-E)^{-1}$. Details of this method can be found in Refs. [16, 31, 32].

The target and projectile can no longer interact at high energy due to the large difference in momenta. It is therefore convenient to express the Hamiltonian $\hat{H}$ as $\hat{H} = \hat{H}_T + \hat{H}_P + \hat{H}_{TP}$, where $\hat{H}_T$ and $\hat{H}_P$ are the target and projectile Hamiltonians, respectively. More specifically, $\hat{H}_T$ is the intrinsic Hamiltonian of the target. Moreover, $\hat{H}_P$ can be decomposed as $\hat{H}_P = \hat{H}_{\rm int} + \hat{H}_{\rm CM}$, where $\hat{H}_{\rm int}$ describes its intrinsic properties and $\hat{H}_{\rm CM}$ the dynamics of its center of mass.

The target wave-function is obtained by solving GSM in Slater determinant representation. In the applications with multi-nucleon projectiles, the projectile wave functions in calculated in no-core shell model [33]. Regarding the interaction, the inert core is mimicked by a one-body potential which is comprised of a Woods-Saxon potential with a spin-orbit term and a Coulomb field. The two-body part is an FHT [34] interaction which is a Gaussian interaction with central, spin-orbit and tensor parts. Moreover, the two-body Coulomb interaction is treated exactly by incorporating its long-range part in the basis potential.

GSM-CC has been applied to the calculation of the proton and deuteron scattering [16, 32], the radiative capture of nucleons [35] and the deuteron transfer reaction [36].

Outlook

The GSM allows to treat the atomic nucleus as an open quantum system. It is therefore ideal for nuclei close to the dripline where one-nucleon separation energies are very low. GSM studies have mainly concentrated in light nuclei. Studies of heavier systems are possible by selecting different cores, and is something that should be explored in the future.

There has been recent developments in *ab initio* methods with GSM, this is important as it allows for the inclusion of more realistic interactions. Moreover, no-core approaches are possible using a Berggren basis and allows for the studies of light nuclei, particularly those close to the driplines [37].

The GSM-CC approach allows the simultaneous calculation of spectra and cross-sections. Moreover, this model allows to include cluster entrance and exit channels. Many reactions of astrophysical interest including ^{3}He, ^{3}H and ^{4}He clusters can be studied in this approach. The GSM-CC can give insight into in the structure of states that are close to cluster emission thresholds [38], e.g. the famous Hoyle state in ^{12}C. Therefore, one would like to expand the range of calculations from deuteron to $A = 3, 4$ clusters.

Studies of nuclear clustering in the vicinity of cluster decay thresholds require the inclusion of more complex, multi-mass partitions, i.e. large number of different continua. This challenging project will open also the door for the systematic studies of transfer and knockout reactions.

References

[1] M.G. Mayer, Phys. Rev. **75**, 1969 (1949).

[2] O. Haxel, J.H.D. Jensen, and H.E. Suess, Phys. Rev. **75**, 1766 (1949).

[3] G. Gamow, Z. Phys. **51**, 204 (1928).

[4] A.J.F. Sieger, Phys. Rev. **56**, 750 (1939).

[5] I.M. Gel'fand and N.Y. Vilenkin, *Generalized Functions*, vol. 4 (Adademic Press, New York, 1961)

[6] A. Böhm and J. D. Dollard, *The Rigged Hilbert Space and quantum mechanics: lectures in mathematical physics at the University of Texas at Austin* (Springer, 1978).

[7] J. Okołowicz, M. Płoszajczak and I. Rotter, Phys. Rep. **374**, 271 (2003).

[8] K. Bennaceur, F. Nowacki, J. Okołowicz, and M. Płoszajczak, Nucl. Phys. A **671**, 203 (2000).

[9] J. Rotureau, J. Okołowicz, and M. Płoszajczak, Nucl. Phys. A **767** 13 (2006).

[10] A. Volya and V. Zelevinsky, Phys. Rev. Lett. **94**, 052501 (2005).

[11] S. Quaglioni and P. Navrátil, Phys. Rev. Lett. **101**, 092501 (2008).

[12] S. Baroni, P. Navrátil, and S. Quaglioni, Phys. Rev. Lett. **110**, 022505 (2013).

[13] N. Michel, W Nazarewicz, M. Płoszajczak, K. Bennaceur, Phys. Re. Lett. **89**, 042502 (2002).

[14] R. M. Id Betan, R.J. Liotta, N. Sandulescu, T. Vertse, Phys, Rev. Lett, **89**, 042501 (2002).

[15] N. Michel and M. Płoszajczak, *Gamow Shell Model, The Unified Theory of Nuclear Structure and Reactions*, Vol. 983 (Springer, 2021).

[16] Y. Jaganathen, N. Michel, and M. Płoszajczak, Phys. Rev. C **89**, 034624 (2014).

[17] R. G. Newton, Jour. of Math. Phys. **1**, 319 (1960).

[18] T. Berggren, Nucl. Phys. A **109**, 265 (1968).

[19] R. de la Madrid, Eur. Jour. of Phys. **26**, 287 (2005).

[20] Y. B. Zel'dovich, On the theory of unstable states, Sov. Phys. JETP **12**, 542 (1961).

[21] B. Gyarmati and T. Vertse, Nuclear Physics A **160**, 523 (1971).

[22] N. Michel, W. Nazarewicz, M. Płoszajczak, and J. Okołowicz, Phys. Rev. C **67** 054311 (2003).

[23] I. Talmi, Helv. Phys. Acta **25**, 185 (1952).

[24] M. Moshinsky, Nucl. Phys. **13**, 104 (1959).

[25] G. Hagen, M. Hjorth-Jensen and N. Michel, Phys. Rev. C **73**, 064307 (2006).

[26] R. Lawson, *Theory of the Nuclear Shell Model* (Clarendon, Oxford, 1980)

[27] Y. Suzuki and K. Ikeda, Phys. Rev. C **38** 410 (1988).

[28] N. Michel, W. Nazarewicz, and M. Płoszajczak, Phys. Rev. C **75**, 031301 (2007)

[29] N. Michel, W. Nazarewicz, M. Płoszajczak, Phys. Rev. C **89**, 034624 (2014)

[30] X. Mao, J. Rotureau, W. Nazarewicz, N. Michel, R.M. Id Betan, and Y. Jaganathen, Phys. Rev. C **102**, 024309 (2020).

[31] R. I. Betan, Phys, Lett. B **730**, 18 (2014).

[32] A. Mercenne, N. Michel, M. Płoszajczak, Phys. Rev. C **99**, 044606 (2019).

[33] B. Barret, P. Navrátil and J. Vary, Prog. in Part. and Nucl. Phys. **69** 131 (2013).

[34] H. Furutani, H. Horiuchi, and R. Tamagaki, Prog. Theor. Phys. 62, 981 (1979).

[35] K. Fossez, N. Michel, M. Płoszajczak, Y. Jaganathen, and R. I. Betan, Phys. Rev. C **91**, 034609 (2015).

[36] A. Mercenne, N. Michel, J.P. Linares Fernández, and M. Płoszajczak, Phys. Rev. C **107** L011603 (2023).

[37] G. Papadimitriou, J. Rotureau, N. Michel, M. Płoszajczak, and B. R. Barrett Phys. Rev. C **88**, 044318 (2013).

[38] Okołowicz, M. Płoszajczak, and W. Nazarewicz, Prog. Theor. Phys. Supp. **196**, 230 (2012)